Fluid Flow Processes at Mid-Ocean Ridge Hydrothermal Systems

by

Timothy Edmund Jupp

A dissertation submitted for the
Degree of Doctor of Philosophy
at the University of Cambridge

Pembroke College
Cambridge

September, 2000

Declaration

This dissertation describes my original work except where acknowledgement is made in the text. It does not exceed the page limit and is not substantially the same as any other work that has been, or is being, submitted to any other university for any degree, diploma or other qualification.

30th September 2000 Timothy Edmund Jupp

“Correlation does not imply causality”

P.E. & S.L. Jupp,
frequent *pers. comms.*,
since 1974

Summary

Fluid flow processes at mid-ocean ridge hydrothermal systems

by

Timothy Edmund Jupp

The subseafloor structure and temporal variability of mid-ocean ridge hydrothermal systems are examined from a largely theoretical standpoint.

The nature of tidal signals is considered in detail and there is a discussion of the mechanisms by which the tidal modulations observed at seafloor hydrothermal systems might be produced. A review of the known examples of tidal modulation at hydrothermal systems is presented, and a new procedure for the analysis of these tidally modulated time-series is proposed. Where possible, this new procedure is applied to datasets previously obtained at the seafloor and it is recommended for use in future analyses.

It is shown that the nonlinear thermodynamic properties of pure water are sufficient to impose a structure consistent with the known constraints on subseafloor convection cells. In particular, it is demonstrated that the properties of water limit seafloor vent temperatures to ~400°C, even when the energy source driving the convection cell is much hotter. A scaling analysis is presented to reveal how the lengthscales and timescales associated with a subseafloor convection cell depend on the bulk crustal permeability.

The equations of poroelasticity are reviewed to demonstrate how the nonlinear thermodynamic properties of water influence the response of a hydrothermal system to tidal loading at the seafloor. A selection of simple analytical solutions reveals the phase relationship of the effluent temperature and effluent velocity at the seafloor to the ocean tide. A numerical simulation illustrates the effect of tidal loading on a two-dimensional subseafloor convection cell incorporating the nonlinear properties of water.

Acknowledgements

Firstly, my profound thanks go to my supervisor, Prof. Adam Schultz. He took the rash step of engaging me in the first place, and then kept faith in me when logic probably dictated otherwise. Furthermore, he retained an unfailingly good sense of humour throughout, even when I managed to break (slay?) Medusa. I apologise for failing to have proved (or indeed disproved) some of his favourite theories. I hope that his future research students are more successful - and less stubborn - than me.

Next on my list of thanks are the public-spirited research workers who place their computer codes in the public domain for me to study and adapt. If I had faced the prospect of writing every subroutine which contributed to this dissertation, I should have given up before I began. In particular, I made extensive use of codes by Hans-Georg Wenzel (ETGTAB), Daniel Hayba (HYDROTHERM) and Richard Eanes (CSR). I have made every effort to acknowledge my use of these codes specifically, but an extra note of thanks is by no means out of place.

I was very grateful to take part in the PICO cruise off the Azores in 1998, and my thanks go to all on board the N/O Nadir for making the trip such a pleasure. My trip to the Lucky Strike vent site in the submersible Nautile was an unforgettable experience. I also thank the French football team for their impeccable timing – waiting until we had docked before winning the World Cup was a masterstroke.

My thanks are also due to Pembroke College for funding my participation in the 1999 InterRidge field course at the Troodos ophiolite in Cyprus. I am particularly grateful to the field trip leaders, Joe Cann and Kathy Gillis, who managed to explain real geology to me in such a patient fashion.

Enormous thanks go to Amy Davis and Aoife Mulhall – partly for being such splendid office mates, but particularly for the high quality of the proof reading to which I subjected them at such short notice. I also extend my gratitude to Jon Dale for correcting sections of the text.

The official page limit prevents me from mentioning by name everyone who has made the Department Of Earth Sciences such a happy place to work. Needless to say, I shall miss the wit and bonhomie generated around the coffee table and will always be looking for an excuse to return.

Graham Forsythe deserves a special mention for being a fellow tail-end Charlie – it would have been so much worse if I had been the only one.

Finally, my deepest thanks go to Anne-Marie Conkey whose moral support over the years was an indispensable component in the completion of this thesis.

Table of Contents

Chapter 1: Introduction

This dissertation is concerned with the flow of water through the subseafloor at mid-ocean ridge hydrothermal systems (Section 1.1). The crustal rock and sediment which constitute the subseafloor are both permeable. Consequently, flows of interstitial water can be induced by thermal buoyancy forces and non-hydrostatic pressure gradients. The buoyancy forces are derived from the heat of upwelling magma and drive a steady convective flow (Chapter 5). In addition to this steady flow, pressure gradients induced by tidal loading drive an oscillatory flow (Chapter 6).

As water flows through the subseafloor it exchanges heat and chemical elements with the surrounding rock. Consequently, hydrothermal convection is important because it contributes to the thermal balance of the oceanic crust and the chemical balance of the oceans (Elderfield & Schultz, 1996; Schultz & Elderfield, 1997). Furthermore, the advection of heat and chemical elements by hydrothermal flow affects the distribution of these quantities within the subseafloor. A principal aim of this dissertation is to explain the subseafloor structure of hydrothermal convection cells. It is proposed that the nonlinear thermodynamic properties of water are sufficient to impose this structure (Chapter 5).

Tidally induced flows *below* the seafloor are important because they lead to observable consequences *on* the seafloor. Tidal signals have been recorded in time-series measurements of the temperature, flow rate and composition of hydrothermal fluid emerging from the seafloor. Understanding the mechanism which causes these tidal modulations is of intrinsic scientific interest, but it may also allow constraints to be placed on the properties of the subseafloor. The ocean tide constitutes an accurately known 'input signal' to a physical process whose 'output signals' are the observed tidal modulations in temperature, flow rate and composition. If the physical process and the input and output signals can all be quantified, constraints can be placed on the properties of the subseafloor. Consequently Chapter 2 is devoted to a detailed study of the characteristic features of tidal phenomena while the aim of Chapter 3 is to derive optimal techniques for extracting information from tidal signals. The principles and techniques of these two chapters are then applied to seafloor data in Chapter 4. Chapter 5 is devoted to a discussion of the steady state structure of subseafloor convection cells. Finally, in Chapter 6, the discussion returns to the subject of

tidal modulation and a model of the physical process which links the 'input' and 'output' signals is proposed.

1.1 Mid-Ocean Ridge hydrothermal systems

Mid-ocean ridges form boundaries between the rigid plates that constitute the ocean basins (Figure 1.1). Upwelling magma from the Earth's mantle creates new crust at mid-ocean ridges, and the plates are forced apart. Heat is transported to the oceans as the magma solidifies and the crust cools.

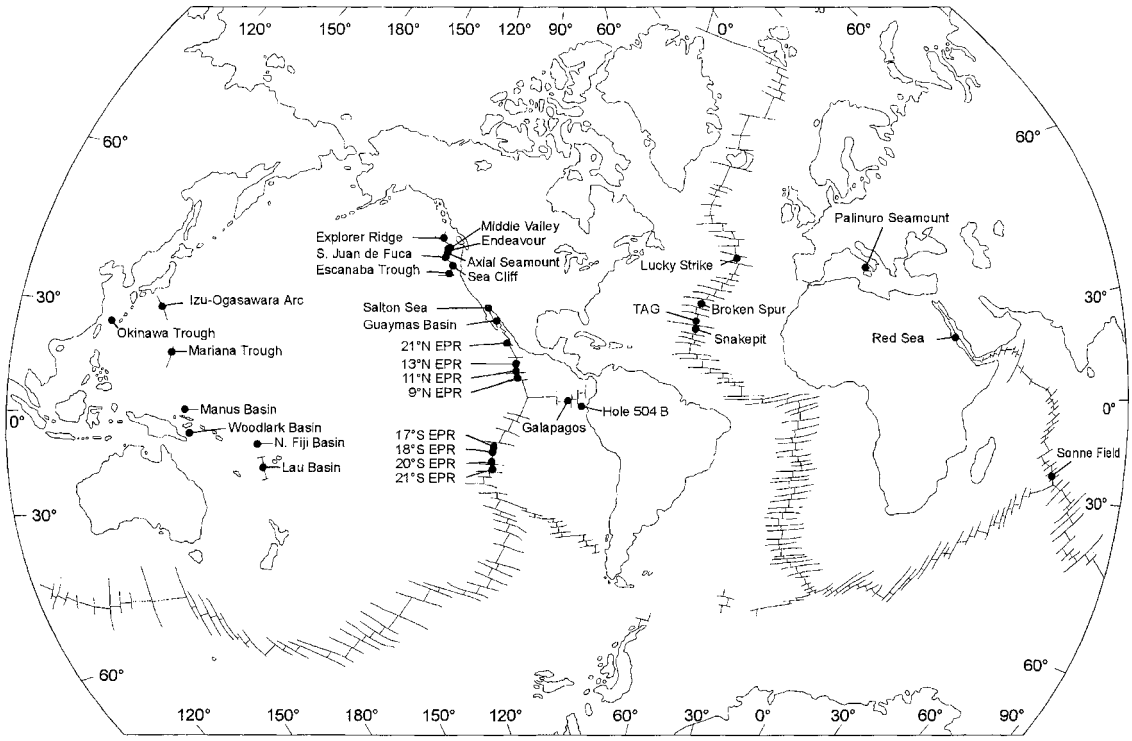

Figure 1.1: The mid-ocean ridge system. A selection of the currently known hydrothermal systems and polymetallic massive sulphide deposits is also shown. Diagram from Herzig & Hannington (1995).

The oceanic crust cools as it is carried away from mid-ocean ridges by the motion of the plates. Typically the plates diverge at speeds between 1 $cm.yr^{-1}$ and 10 $cm.yr^{-1}$, and so cover a distance between 10 km and 100 km every million years. Consequently, distances from the ridge are often expressed as crustal ages in millions of years.

There are two mechanisms which cool the crust – conduction and advection. The conductive transfer of heat is induced by spatial gradients in temperature and occurs throughout the crust. The conductive heat flux is greatest near mid-ocean ridges - where the lithosphere is

thin - and decays with distance away from the ridge. Advective heat transfer is a consequence of the buoyancy-driven flow of seawater within the subseafloor. The most vigorous convection occurs at the ridge axis where it is known as 'active circulation'. However, there is also significant advective heat transport in the ridge flanks - known as 'passive circulation' - for crustal ages up to 65 Ma (Stein & Stein, 1992; Stein & Stein, 1994).

This dissertation is concerned principally with the 'active' circulation which occurs in young (<1 Ma) oceanic crust. Evidence from a number of different sources suggests that a typical hydrothermal convection cell at a mid-ocean ridge has the general structure shown in Figure 1.2. In broad terms, the structure can be summarised as follows. Seawater percolates down through the crust towards a magma chamber, interacting with the surrounding rock as it flows. The interaction is both chemical and thermal. Temperature generally increases with increasing depth below the seafloor and so the fluid becomes hotter as it harvests heat from the crust. Furthermore, an exchange of chemical elements between the percolating water and the rock occurs. The fluid gains some elements and loses others, with the exact nature of the chemical transfer being temperature dependent. The fluid reaches its greatest temperature in the region above the magma chamber and begins a buoyancy-driven ascent to the seafloor. The hot fluid expelled at the seafloor is usually divided into three categories.

Firstly, the hottest fluid emerges from the seafloor through structures known as black smokers which are characterised by temperatures between 300°C and 400°C. These vents are so named because of the black "smoke" which forms when the vent water cools and mixes with cold seawater. The "smoke" is in fact due to the precipitation of metal sulphides dissolved in the vent fluid. Over time, precipitation of minerals such as anhydrite, pyrite and chalcopyrite leads to the formation of chimney structures through which the effluent fluid issues. A typical black smoker chimney has an internal diameter of ~10 cm and is a few metres in height. In the prototype example shown in Figure 1.2, several black smokers are shown within a "central black smoker complex" of a hydrothermal mound formed by the precipitation of anhydrite and metal sulphides.

Secondly, a lower temperature form of focussed flow emerges from structures known as white smokers which are characterised by temperatures below 300°C. In this case, the white "smoke" is produced by the precipitation of sulphates, amorphous silica and zinc sulphides.

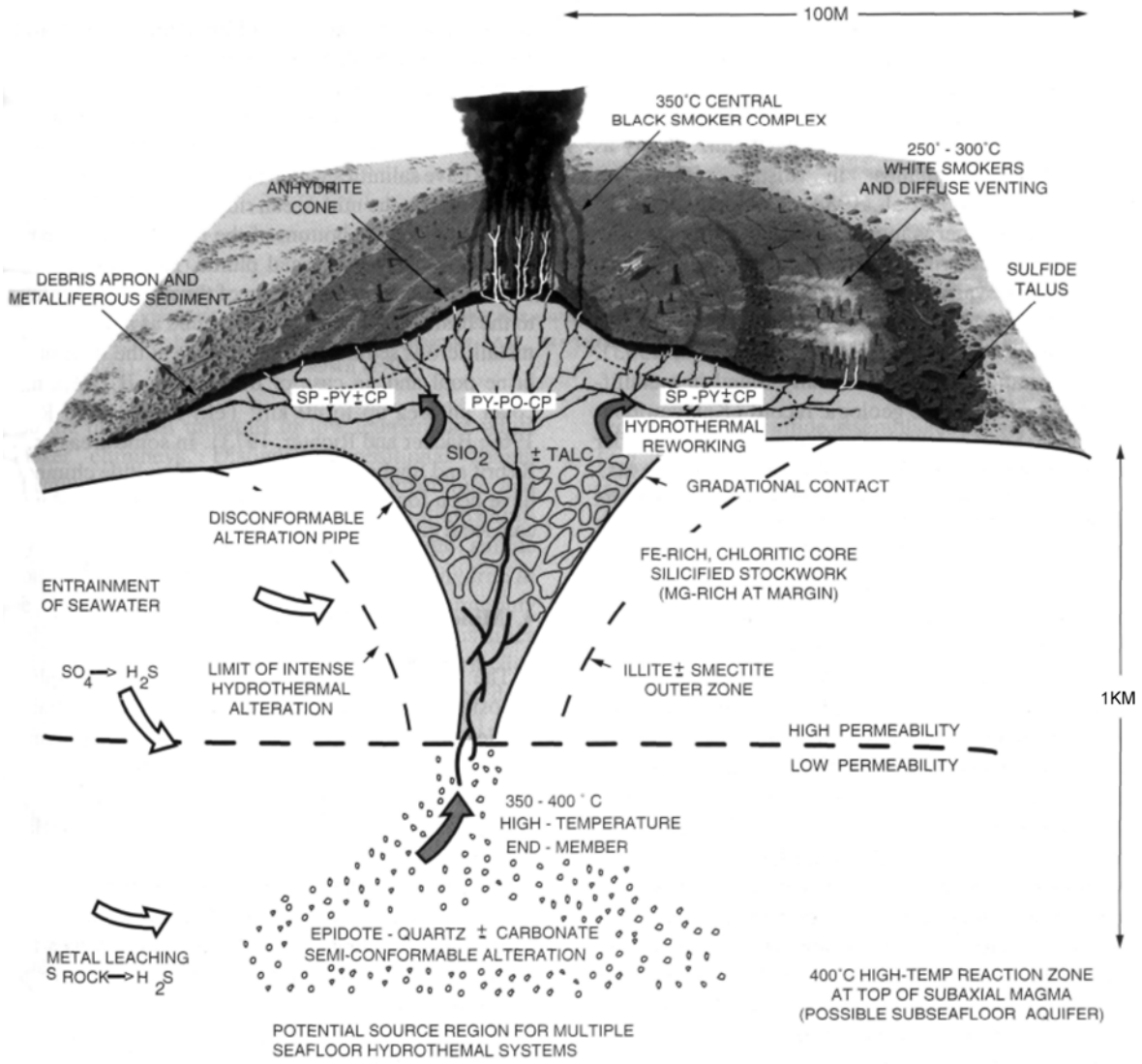

Figure 1.2: Cross section through the seafloor, showing the principal components of a typical seafloor hydrothermal system. Diagram from Herzig & Hannington (1995).

Thirdly, the term "diffuse flow" is applied to the flow of low temperature (typically < 50°C) water which emerges from broad areas of the seafloor in the vicinity of black and white smokers. An individual area of diffuse flow typically covers an area of at most a few square metres and is identified by the appearance of "shimmering" water just above the seafloor.

The schematic picture of subseafloor structure in Figure 1.2 is derived from evidence obtained at active hydrothermal systems on the seafloor and at fossil hydrothermal systems exposed on land. At active systems, the temperature and chemistry of seafloor effluent can be measured and used to infer the conditions below the seafloor (e.g. Von Damm *et al.*, 1985). In addition, seismic studies can be used to constrain the depth of the magma chamber

below the seafloor (Morton, 1984; Morton & Sleep, 1985; Detrick *et al.*, 1987; Vera & Diebold, 1994). At fossil systems, relict hydrothermal convection cells are sometimes exposed in cross section and the subseafloor structure is revealed by examination of the metamorphic mineral assemblages (Gillis & Roberts, 1999) and by fluid inclusion geothermometry (Cowan & Cann, 1988).

1.2 Aims and dissertation outline

This dissertation is concerned with (1) the temporal variability and (2) the spatial structure of active seafloor hydrothermal systems. The spatial structure is considered on the lengthscale of an individual convection cell while the temporal variability is considered on a timescale ranging from hours to months. Spatial structure is considered in Chapter 5, while temporal variability is considered in Chapters 2, 3, 4 and 6.

The aims of this dissertation are:

1) to develop an optimal technique for analysing the tidal component of time-series collected at seafloor hydrothermal systems.
2) to apply this technique to existing seafloor datasets and assess its usefulness.
3) to develop the simplest model of hydrothermal circulation which is sufficient to explain the known subseafloor structure of convection cells.
4) to develop theoretical models of a mechanism which causes tidal modulation of the observable quantities at hydrothermal systems.

Chapter 2 contains a review of the theory of tides and tidal signals. All tidal signals share a common cause – the well known astronomical motions of the sun and moon – and it is helpful to consider the features which all tidal signals are expected to share. There are two obvious mechanisms by which the tides might deform the seafloor and influence hydrothermal systems. Firstly, the direct action of tidal forces on the seafloor causes a deformation known as the solid tide. Secondly, the rise and fall of the ocean surface (the ocean tide) imposes a time-dependent load on the seafloor. This causes a deformation known as the load tide. Order of magnitude calculations suggest that the load tide produces much larger strains in oceanic crust than the solid tide. It is therefore expected that the tidal signals observed at hydrothermal systems are correlated with the load (i.e. ocean) tide rather than the solid tide. This expectation is tested in Chapter 4. A third mechanism by which tidal processes might influence hydrothermal systems is provided by tidal streams - the lateral motion of ocean waters induced by the ocean tide. The characteristic features of each of the

three plausible 'input signals' – solid tide, ocean tide and tidal streams – are considered in turn from a theoretical standpoint. Consequently the tidal component of any seafloor time-series (the 'output signal') can be compared with each of the postulated 'input signals' in order to constrain the physical process linking input and output.

Chapter 3 is concerned with finding the best way to extract useful information from a time-series with a tidal component. Methods of time-series analysis are divided into two classes – parametric and non-parametric. Non-parametric methods are used to estimate the power spectrum of a time-series. Most previous analyses of tidal modulation at seafloor hydrothermal systems have relied on non-parametric methods based on the periodogram. However, it is argued that the multiple window method (Thomson, 1982) is much better suited to the analysis of the short noisy datasets which are typically obtained at the seafloor. It is therefore recommended that the multiple window method should be used in all future analyses. Parametric methods are used to derive parameters which describe the information content of a time-series, if it is assumed that the time-series takes a particular functional form. Previous analyses of hydrothermal time-series data have used a discrete Fourier series (referred to as the Harmonic Method) as a parametric model for tidal data. It is argued here that the Admiralty Method is simpler and likely to yield more useful information from a limited dataset. The Admiralty Method has long been used to describe the nature of the ocean tides in the world's ports (Doodson & Warburg, 1941; Admiralty Tidal Handbook, No. 1; Admiralty Tidal Handbook, No. 3). It is recommended here that the Admiralty Method should be used to describe the tidal component of time-series obtained at the seafloor. Previously, the Harmonic Method has been combined with a Bayesian technique for removing the drift from a time-series to produce a parametric algorithm for tidal analysis (Tamura *et al.*, 1991). Here the Bayesian drift removal technique is instead combined with the Admiralty Method to produce a new parametric algorithm for tidal analysis. This algorithm has been combined with the robust data analysis technique of Huber weighting (Chave *et al.*, 1987) to produce a new computer code – HYBRID – which is recommended for the parametric analysis of tidally modulated time-series from seafloor hydrothermal systems.

Chapter 4 presents a review of the tidally modulated signals which have been obtained at seafloor hydrothermal systems. In the cases where these data are readily available, they are examined in the light of the theory presented in Chapter 2, by using the techniques described in Chapter 3. Some of the data discussed in Chapter 4 is presented here for the first time. In

addition, previously published data are re-examined. In some cases, the conclusions based on the theory of Chapters 2 and 3 are different to those of the authors who originally analysed the data. The results of the data analysis are used to determine which 'input signal' (solid tide, ocean tide, tidal streams) is most likely to have caused the tidal modulations in the data. Finally, the efficacy of the techniques recommended in Chapter 3 is discussed in the light of their application to real data.

Chapter 5 examines the structure of hydrothermal convection cells. A simple model of subseafloor convection - incorporating the full nonlinear thermodynamic properties of water - is examined using numerical simulations and analysis of the governing equations. It is argued that the nonlinear thermodynamic properties of water are sufficient to explain the structure of convection cells and the observed upper limit to black smoker temperatures (~400°C). A scaling analysis is derived to quantify how the lengthscales and timescales of a subseafloor convection cell depend on the bulk crustal permeability.

Chapter 6 draws together the concepts of the previous chapters. The convection cell structure derived in Chapter 5 is considered in the context of tidal loading of the seafloor. The equations of poroelasticity are reviewed in order to examine how the thermodynamic properties of water influence the response of a hydrothermal system to an applied tidal load. An analytical solution describing the diffusion of fluid pressure in a tidally loaded one-dimensional halfspace is reviewed (Van der Kamp & Gale, 1983). This solution is then extended in a number of ways. Firstly, expressions for the tidally induced variations in temperature and flow are derived from the established expression for the pressure variations. Secondly, analogous expressions are derived for a layer of finite thickness. Thirdly, the theory is extended to two-dimensions where it is illustrated with numerical simulations. These simulations are used to show how the convection cell derived in Chapter 5 is affected by tidal loading of the seafloor.

Finally, Chapter 7 contains a summary of the preceding chapters and a brief discussion of the suggested directions for future research.

Chapter 2: The nature of tidal signals

2.1 Introduction

Much of this study is concerned with the identification and analysis of tidal signals in hydrothermal systems associated with mid-ocean ridge. Consequently, it is appropriate to define the term tidal signal before proceeding any further. An observer at rest on the Earth experiences a force per unit mass due to the gravitational attraction of celestial bodies. This is known as the tide-generating force and is the spatial gradient of a function known as the tidal potential (W) (Melchior, 1983).

A tidal signal can then be defined to be any time-series, or component of a time-series, whose cause is the tidal potential. Generally, time-series are influenced by many physical processes, some of which are independent of the tidal potential. It is often helpful to decompose an empirical time-series into two parts: a tidal signal; and a residual signal containing the contributions of noise, instrumental drift and other physical processes. (In Chapter 3, an explicit formalism for splitting the residual into a drift signal and a noise signal is discussed.)

There are many observable consequences of the tidal potential - of which the rise and fall of the oceans (the ocean tide) and associated horizontal currents (tidal streams) are the most commonly known. Less obviously, the Earth's crust is deformed directly by the tide-generating force (to produce the solid tide) and by the weight of the shifting oceans (to produce the load tide). All of these phenomena produce tidal signals. In every case there is a well-understood physical mechanism by which the tidal potential causes the observable time-series. In addition, each of these signals has a frequency spectrum which is similar to that of the tidal potential, in the sense that it contains power at the same discrete set of frequencies and in roughly the same proportions. It must be stressed that tidal signals are not required, by definition, to have these typically tidal spectra. Nonetheless, it appears that many of them do. This is because their dependence on the tidal potential is approximately linear.

In particular, it is often the case that the physical process linking the local tidal potential ($W(t)$) to an observable time-series ($\zeta(t)$) can be well approximated by a time-domain convolution with a response function $r(t)$ (Munk & Cartwright, 1966):

$$\zeta(t) = \int_{\tau=-\infty}^{\infty} r(\tau) \cdot W(t-\tau) d\tau \tag{2.1}$$

By taking Fourier transforms:

$$\hat{\zeta}(f) = \int_{t=-\infty}^{\infty} \zeta(t) \cdot e^{2\pi i f t} dt, \quad R(f) = \int_{t=-\infty}^{\infty} r(t) \cdot e^{2\pi i f t} dt, \quad \hat{W}(f) = \int_{t=-\infty}^{\infty} W(t) \cdot e^{2\pi i f t} dt \tag{2.2}$$

the convolution can be transformed into a multiplication in the frequency domain:

$$\hat{\zeta}(f) = R(f) \cdot \hat{W}(f) \tag{2.3}$$

Hence, provided that the admittance ($R(f)$) is a reasonably smooth function of frequency (f) the process $\zeta(t)$ will have a similar spectrum to the tidal potential $W(t)$.

Regardless of whether a time-series ($\zeta(t)$) really does depend on the tidal potential in this linear fashion it is of interest to examine its frequency spectrum. A spectrum containing power at the typical tidal frequencies may be taken as strong evidence that the signal under analysis is influenced by the tidal potential.

The tidal potential has a highly distinctive power spectrum, which can be calculated to great precision. It is reasonable to expect that any tidal signal will exhibit similar behaviour. For this reason, it is of great benefit to review the nature of the tidal potential in considerable detail, before considering any data which might be affected by it.

The next step is to identify, *a priori*, some plausible physical mechanisms by which the tidal potential might affect seafloor hydrothermal systems. The first order effects of the tidal potential (the solid, ocean and load tides, as well as tidal streams) are examined in turn. Qualitative estimates are then made of how these first order effects might lead to the second order effects (variations in temperature, flow rate and effluent chemistry) observed at hydrothermal systems.

2.2 The Tidal Potential of a celestial body

By definition, all tidal phenomena on Earth are caused by the gravitational fields of celestial bodies. Every astronomical object creates tidal forces on Earth, but it is the contributions from the moon and the sun which are, by far, the most important (Doodson & Warburg, 1941). Consequently, it is only the lunar and solar tides which are considered here.

At any fixed point on the Earth's surface, the tidal potential changes over time as the moon and the sun move with respect to the rotating Earth. Two spherical co-ordinate systems are commonly used to describe this motion – the ecliptic system and the equatorial system. Their relationship is summarised in Figure 2.1.

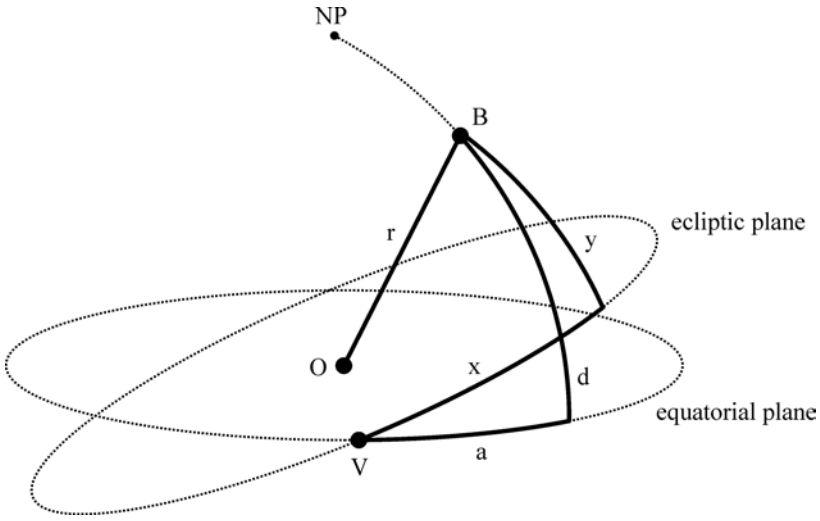

Figure 2.1: The position of a tide-raising body, *B*, relative to the centre of the Earth, *O*, and the vernal equinox, *V*. The point *NP* is the celestial North Pole. In equatorial coordinates, the point *B* is described by the triple (*r,a,d*). In ecliptic coordinates, it is described by the triple (*r,x,y*). Coordinates are named as follows: *r* - distance from the centre of the Earth, *a* - right ascension, *d* – declination, *x* – ecliptic longitude, *y* – ecliptic latitude. Figure adapted from Doodson & Warburg (1941).

Consider the tidal potential at a point *P* due to a single tide-raising body *B* of mass M_B (Figure 2.2). The tide-raising body lies at a distance r_B from the centre of the earth, and at a declination *d* above the equator.

The tidal potential at *P*, W(r,λ,Z), can be written as a sum of spherical harmonic functions. For practical purposes, $W(r,\lambda,Z)$ is approximated to sufficient accuracy by the first term in this series, the second order spherical harmonic function $W_2(r,\lambda,Z)$ (Melchior, 1983; Doodson & Warburg, 1941).

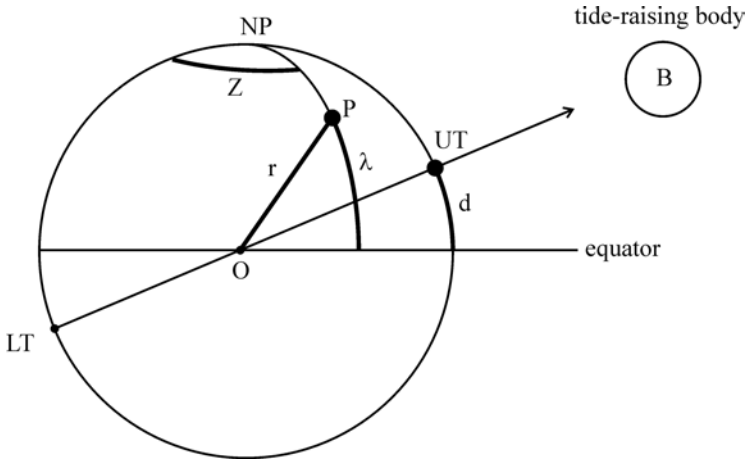

Figure 2.2: The tidal potential W at a point P on the Earth's surface, due to a single tide-raising body B with declination d. NP is the North Pole. UT is the point of upper transit, directly below the tide-raising body. The location of P can described by (r,λ,Z), where r is distance to the centre of the Earth, λ is (terrestrial) latitude and Z is the angle between the meridian of lower transit (LT) and the meridian of the point P. The tidal potential at P is $W(r,\lambda,Z)$ as described in the text. Figure adapted from Doodson &Warburg (1941).

If G is the gravitational constant, $W_2(r,\lambda,Z)$ is defined by:

$$W_2(r,\lambda,Z) = \frac{3}{4}\left[GM_B\frac{r^2}{r_B^3}\right]\begin{Bmatrix}\cos^2(\lambda)\cos^2(d)\cos(2Z)\ldots\\ \ldots-\sin(2\lambda)\sin(2d)\cos(Z)\ldots\\ \ldots+3\left(\sin^2(\lambda)-\frac{1}{3}\right)\cdot\left(\sin^2(d)-\frac{1}{3}\right)\end{Bmatrix} \quad (2.4)$$

It is very important that the tidal potential due to a tide-raising body varies over two separate timescales. Firstly, there is a short timescale associated with the rotation of the Earth. The angle ($Z(t)$) between the meridian of the tide-raising body and the meridian of the point P increases at a rate of ~15º per hour (or ~360º per day). Consequently, the tidal potential at P displays diurnal ($\cos(Z)$) and semi-diurnal ($\cos(2Z)$) periodicity. Secondly, there is a long timescale, associated with the oscillations in declination $d(t)$ and distance $r_B(t)$ of the tide-raising body. These oscillations have a period of ~1 month when the tide-raising body is the moon, and ~1 year when it is the sun. The interaction of periodic processes on these short (daily) and long (monthly and yearly) timescales leads to the characteristic spectral nature of tidal phenomena (Section 2.3.4).

Time-series measurements of hydrothermal systems often span a time interval intermediate between these short and long timescales (Chapter 4). In Chapter 3, it is shown that this has important implications for the extraction of tidal information from a seafloor dataset.

2.3 Decomposition of the Tidal Potential

2.3.1 Decomposition by species

Defining M_E to be the mass of the Earth, and r_E to be the radius of the Earth, the gravitational acceleration at the Earth's surface (g) is given by:

$$g = \frac{GM_E}{r_E^2} \tag{2.5}$$

Hence, the tidal potential at the Earth's surface, due to a single tide-raising body, is:

$$W_2\big|_{r=r_E} = gr_E \frac{3}{4}\left[\frac{M_B}{M_E}\left(\frac{r_E}{r_B}\right)^3\right]\begin{cases}\cos^2(\lambda)\cos^2(d)\cos(2Z)\ldots \\ \ldots - \sin(2\lambda)\sin(2d)\cos(Z)\ldots \\ \ldots + 3\left(\sin^2(\lambda)-\frac{1}{3}\right)\cdot\left(\sin^2(d)-\frac{1}{3}\right)\end{cases} \tag{2.6}$$

This can be split into three species by considering the three terms on the right hand side of equation (2.6).

The first species, known as the long-period species, consists of the term:

$$gr_E \frac{3}{4}\left[\frac{M_B}{M_E}\left(\frac{r_E}{r_B}\right)^3\right]3\left(\sin^2(\lambda)-\frac{1}{3}\right)\cdot\left(\sin^2(d)-\frac{1}{3}\right) \tag{2.7}$$

This expression changes over time because of the long timescale changes in the distance $r_B(t)$ and declination $d(t)$ of the tide-raising body. The exact formulae for $r_B(t)$ and $d(t)$ need not be quoted here. It is sufficient to note that they have been calculated to great precision for both the moon and the sun (Doodson & Warburg, 1941), and are available in public domain computer codes such as ETGTAB and CSR. (Further details of these and other computer codes used in this dissertation are given at the end of the References section.)

There are two short timescale species, known as the diurnal and semi-diurnal species. The diurnal species of the tidal potential consists of the term:

$$-gr_E \frac{3}{4}\left[\frac{M_B}{M_E}\left(\frac{r_E}{r_B}\right)^3\right]\sin(2\lambda)\sin(2d)\cos(Z) \tag{2.8}$$

Here, the presence of the earth rotation term cos(Z) means that a short timescale diurnal oscillation interacts with the long timescale changes in $r_B(t)$ and $d(t)$. It is helpful to think of the diurnal species as being a diurnal oscillation (cos(Z)) whose amplitude is modulated over the long timescale by the declinational term sin(2d). (The changes in distance ($r_B(t)$) have a similar but less significant effect.) It follows that the diurnal part of the tidal potential is greatest when the declination of the tide-raising body is greatest (Section 2.3.2).

Finally, the semi-diurnal species of the tidal potential consists of the term:

$$gr_E \frac{3}{4}\left[\frac{M_B}{M_E}\left(\frac{r_E}{r_B}\right)^3\right]\cos^2(\lambda)\cos^2(d)\cos(2Z) \tag{2.9}$$

The semi-diurnal species can be considered to be a semi-diurnal oscillation (cos(2Z)), whose amplitude is modulated over the long timescale by the declinational term cos^2(d). Therefore, the semi-diurnal part of the tidal potential is greatest when the declination of the tide-raising body is zero (Section 2.3.2).

2.3.2 Frequency Modulation by declinational changes

The decomposition of the tidal potential into species (Section 2.3.1) is conceptually useful when considering tidal phenomena over a timescale of a few days. On such a timescale, changes in the distance and declination of a tide-raising body can give the tidal potential a non-stationary appearance (Figure 2.3).

In the example shown in Figure 2.4, the lunar declination (d) is zero approximately 11 days into the time interval (Figure 2.3). At this time, the semi-diurnal species (with its cos^2(d) term) dominates over the diurnal species (with its sin(2d) term) in the tidal potential. Consequently, the tidal potential appears to be strongly semi-diurnal when viewed over the course of a few cycles at the centre of the observation period. However, at the beginning and end of the time interval, the lunar declination is large and the tidal potential has a dominantly diurnal appearance. The tidal potential as a whole can therefore be considered to be frequency-modulated by declinational changes. (In this example, attention has been focussed solely on the lunar declination because it varies appreciably over the course of 20 days. In principle, changes in solar declination have a similar effect. However, the period of change of solar declination is one year, and so the solar declination is therefore approximately constant.)

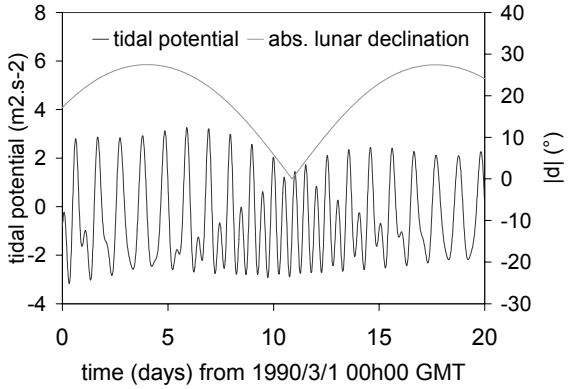

Figure 2.3: 'Frequency Modulation' of the tidal potential due to changes in lunar declination (d). The absolute value of the lunar declination ($|d|$) is plotted over a period of 20 days in March 1990. Also shown is the tidal potential, W, at (45°N, 0°E) over the same time interval. When the lunar declination is zero, the tidal potential is dominated by the semi-diurnal species. Conversely, the diurnal species dominates when the lunar declination is large. Data calculated using ETGTAB.

This phenomenon has important consequences for the interpretation of tidal data from hydrothermal systems. For example, if an observed seafloor time-series spans no more than a few days, it would be unwise to conclude that a frequency spectrum obtained from the dataset were typical. A dataset collected the following week might have a markedly different spectrum simply because of changes in lunar declination.

It is reasonable to suppose that any tidal signal will display some degree of diurnal/semi-diurnal frequency modulation, and it is of interest to see how such modulation correlates with the well-known astronomical forcing. For example, an observed tidal signal might display its greatest semi-diurnal character a few days *after* the lunar declination is zero. This would be evidence for a considerable time lag in the physical mechanism by which the tidal potential gave rise to the tidal signal.

2.3.3 Amplitude Modulation by lunar phase – spring and neap tides

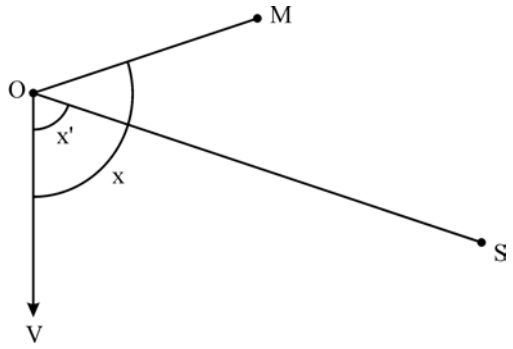

Figure 2.4: The positions of the sun (*S*) and moon (*M*) projected onto the ecliptic plane. The point *O* is the centre of the Earth. The moon and sun have ecliptic longitudes *x* and *x'* respectively, measured positive eastwards from the vernal equinox, *V*. A lunar phase parameter (Φ_L) can be defined by $\Phi_L=|\cos(x-x')|$.

For simplicity, the tidal potential due to a *single* tide-raising body is considered above (Section 2.3.1). However, the interaction of the lunar and solar tides creates an important phenomenon - the amplitude modulation of the tidal potential according to the phases of the moon (Doodson & Warburg, 1941).

When the moon is new or full, the lunar and solar potentials are in phase and produce spring tides which exhibit a larger range than normal. At half-moon, the tidal potentials are out of phase and produce neap tides, with a smaller range than normal. For this reason it is useful to define a lunar phase parameter (Φ_L) as a numerical measure of the phase of the moon.
If *x* is the ecliptic longitude of the moon, and *x'* is the ecliptic longitude of the sun (Figure 2.4), then Φ_L can be defined as follows:

$$\Phi_L = \left|\cos(x - x')\right| \tag{2.10}$$

Hence, the tidal potential displays spring tides at new and full moon when $\Phi_L=1$, and neap tides at half moon when $\Phi_L=0$. The interval between springs and neaps is about 7.38 days (Doodson & Warburg, 1941).

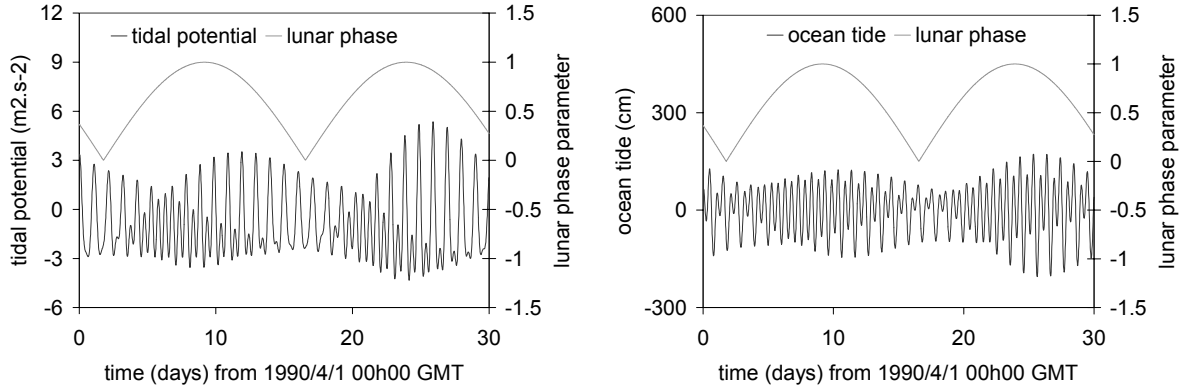

Figure 2.5: 'Amplitude Modulation' of the tidal potential and ocean tide due to changes in the lunar phase parameter (Φ_L) defined in the text, and in Figure 2.4. (a) The tidal potential, W, at the TAG hydrothermal site (26.13°N, 44.82°W). Time-series generated by the ETGTAB code. (b) The ocean tide at the TAG hydrothermal site, generated by the CSR code.

It is important to stress that spring tides *in the oceans* may not occur at the same time as spring tides in the tidal potential. This effect is due to the finite hydrodynamic response time of the oceans. The time lag between Φ_L=1 and oceanic spring tides is known as the age of the tide and varies with location. For example, the tides in British coastal waters generally have an age of about 1.5 days (Manual of Tidal Prediction, 1958). An example of the amplitude modulation caused by lunar phases is presented in Figure 2.5. Unless otherwise stated, the estimates of ocean tide presented in this dissertation have been made using the CSR code, which is derived from satellite altimetry (Schrama & Ray, 1994).

It is reasonable to assume that any tidal signals will display a springs/neaps cycle to some extent. Therefore, when analysing tidal behaviour in a dataset it is important to identify evidence of amplitude modulation, and to correlate this with the springs/neaps cycle in the local ocean tide and tidal potential.

2.3.4 Decomposition into harmonic series

In Sections 2.3.1 – 2.3.3, the tidal potential is viewed as a *non-stationary* mixture of diurnal and semi-diurnal oscillations. This non-stationarity is manifest as amplitude- and frequency modulation of the basic diurnal and semi-diurnal frequencies. However, when viewed over a much longer timescale (~1 year or more) tidal signals can be regarded as *stationary*

harmonic series. In this alternative viewpoint, a tidal signal is decomposed into cosine waves of constant amplitude and frequency.

The relationship between the two viewpoints is exemplified by the following identity (Doodson & Warburg, 1941):

$$f(t) = \underbrace{\left(A + B\cos(\Omega t)\right)}_{L(t)} \cdot \underbrace{\cos(\omega t)}_{S(t)} = \underbrace{A\cos(\omega t)}_{f1(t)} + \underbrace{\tfrac{1}{2}B\cos((\omega+\Omega)t)}_{f2(t)} + \underbrace{\tfrac{1}{2}B\cos((\omega-\Omega)t)}_{f3(t)} \qquad (2.11)$$

Equation (2.11) illustrates how the function $f(t)$, defined by the product $L(t)S(t)$, can be decomposed into the sum $f1(t)+f2(t)+f3(t)$.

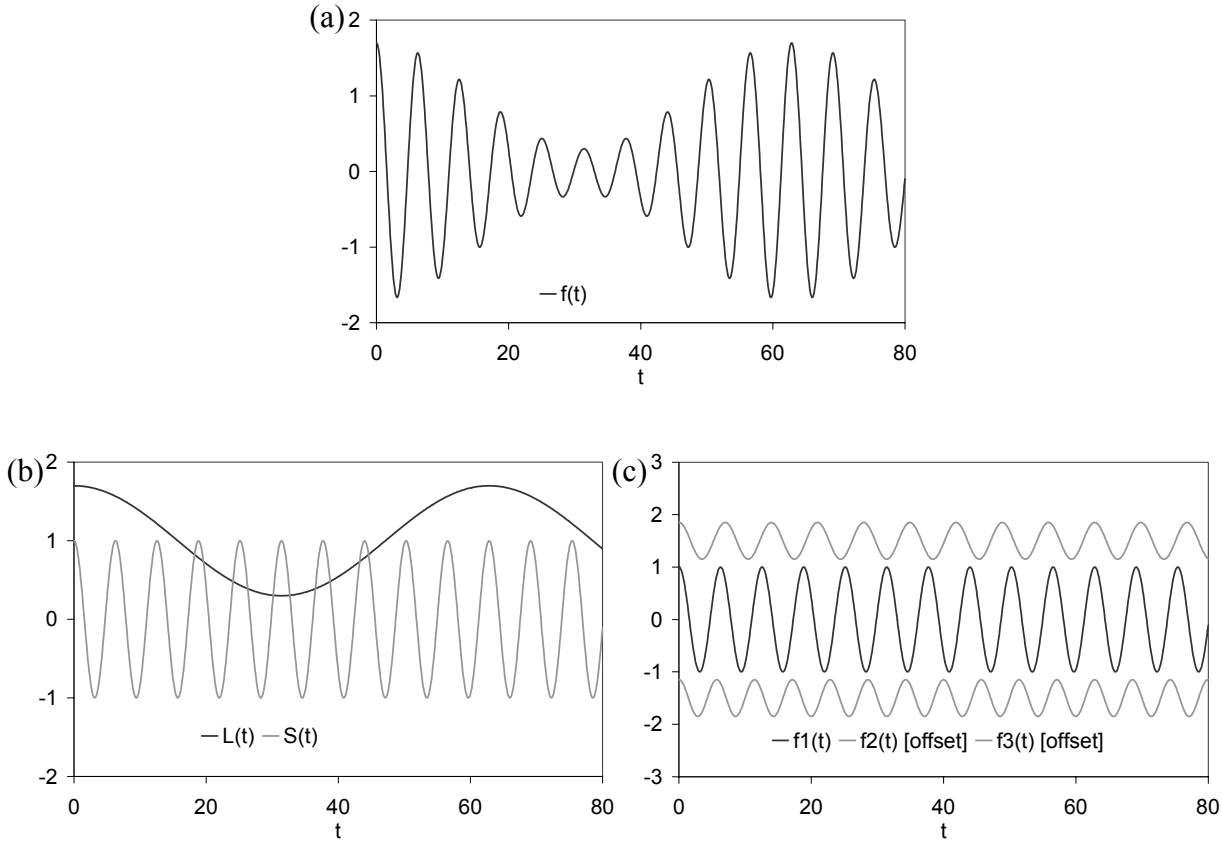

Figure 2.6: The interaction of periodic processes on long and short timescales, illustrated by equation (2.11). (a) The function $f(t)$, which can be decomposed in two ways. (b) Decomposition into a product: $f(t)=L(t)\cdot S(t)$. (c) Decomposition into a sum: $f(t)=f1(t)+f2(t)+f3(t)$. (For clarity, $f2(t)$ and $f3(t)$ have been offset on the y-axis.)

Suppose that $\Omega << \omega$, and that $0<B<A$. The function $f(t)$ is then, in effect, a short timescale process, $S(t)$, (e.g. the daily rotation of the earth), which amplitude-modulated by a long timescale process ($L(t)$) (e.g. monthly changes in lunar declination). Thus, when viewed over a timescale greater than $\sim 1/\Omega$, $f(t)$ is naturally interpreted as an oscillation of angular frequency ω, whose amplitude is not constant, but varies with angular frequency Ω (Figures 2.6a,b). This viewpoint corresponds to the non-stationary species decomposition of Section 2.3.1.

By contrast, the decomposition $f1(t)+f2(t)+f3(t)$ expresses $f(t)$ as a sum of three harmonic terms, each of constant frequency and amplitude (Figure 2.6c).

Thus, the modulation of a short timescale signal of angular frequency ω by a long timescale signal of angular frequency Ω produces a harmonic series of terms with frequencies ω, $(\omega+\Omega)$, and $(\omega-\Omega)$.

This principle lies behind the decomposition of the tidal potential into harmonic components. The (well-known) long-period frequencies of lunar and solar motion combine with the diurnal and semi-diurnal Earth-rotation frequencies to produce a set of N tidal frequencies $\{\omega_1,...,\omega_N\}$. The number of frequencies in a particular decomposition (N) depends on the number of tide-raising bodies included, and the accuracy with which their motions are considered. For example, Doodson (1921) has N=378, Cartwright & Edden (1973) have N=505, and Tamura (1987) has N=1200. A typical tidal spectrum is shown in Figure 2.7.

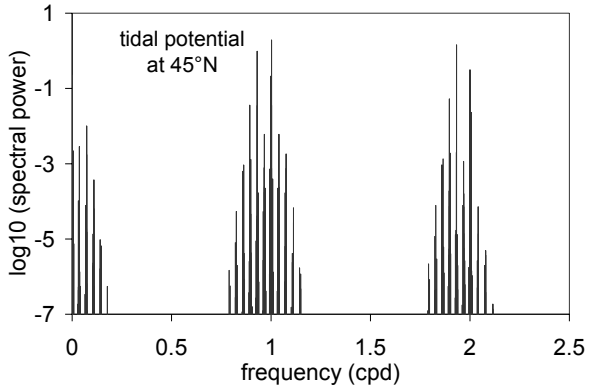

Figure 2.7: A typical tidal power spectrum, calculated from the harmonic constants used in the creation of the time-series in Figure 2.3. The power H_j^2 in each harmonic line is plotted as a function of frequency $\omega_j/2\pi$. Note the logarithmic scale on the y-axis. Data produced using ETGTAB.

After harmonic decomposition, the tidal potential W_2 (at some fixed point on the Earth's surface) is written as a cosine series:

$$W_2(t) = \sum_{j=1}^{N} H_j \cos(\omega_j t - g_j) \tag{2.12}$$

Given a set of tidal frequencies $\{\omega_1,...,\omega_N\}$, the information in the tidal signal $W_2(t)$ is completely described by the set of N amplitudes $\{H_1,...,H_N\}$ and the set of N phase-lags $\{g_1,...,g_N\}$.

The same information can be expressed in complex number notation as follows:

$$W_2(t) = \mathrm{Re}\left(\sum_{j=1}^{N} A_j \exp(i\omega_j t) \right) \tag{2.13}$$

Here, the signal is completely described by the set of N complex numbers $\{A_1,...,A_N\}$.

The amplitude/phase notation and the real/imaginary notation are linked according to:

$$\begin{cases} \mathrm{Re}(A_j) = H_j \cos(g_j) \\ \mathrm{Im}(A_j) = -H_j \sin(g_j) \end{cases} \tag{2.14}$$

The frequency spectrum of $W_2(t)$ is obtained by graphing the power ($H_j^2=|A_j|^2$) in each spectral line against its frequency ($\omega_j/2\pi$). The spectrum in Figure 2.7 is typical and displays the features common to most tidal signals. The spectral lines are clustered into three bands corresponding to the three species of Section 2.3.1 – long-period, diurnal and semi-diurnal. Within each band, certain frequencies tend to contain a greater proportion of the power, and have been assigned names (Doodson & Warburg, 1941). Table 2.1 lists the principal tidal frequencies, along with their names (Doodson & Warburg, 1941).

In the diurnal band, the most significant spectral lines of the tidal potential are *K1*, *O1*, *P1* and *Q1*; and in the semi-diurnal band, they are *M2*, *S2*, *N2* and *K2* (Schwiderski, 1980). The *M2*, or 'principal lunar' component, with a period of 12.42 hours, is usually the most significant component of a tidal signal. For this reason, initial testing of a dataset should involve identification of significant power at ~1.932 cpd which is characteristic of all tidal signals.

Among the harmonic components of the long-period band is a fortnightly component, *Mf*. It is very important to distinguish conceptually between this fortnightly *harmonic component* and fortnightly *modulations*. For example, the springs/neaps cycle is a prominent tidal phenomenon with a period of ~14 days. However, it is caused by the beating of the *M2* and

S2 components, and *not* by the *Mf* component which has an amplitude typically less than 5% of the *M2* component (Schwiderski, 1980).

Consequently, when looking for long-period phenomena in hydrothermal datasets it is more practical to identify long-period modulations than the long-period harmonic components themselves.

name	f (cpd)	T (days)	T (hrs)	name	f (cpd)	T (days)	T (hrs)
M0S0	0.0000	-	-	*J1*	1.0390	0.9624	23.0985
Sa	0.0027	365.2301	8765.5223	*SO1*	1.0705	0.9342	22.4202
Ssa	0.0055	182.6150	4382.7611	*OO1*	1.0759	0.9294	22.3061
STA	0.0082	121.7532	2922.0779	*V1*	1.1122	0.8991	21.5782
MSm	0.0314	31.8120	763.4883	*3N2*	1.8234	0.5484	13.1622
Mm	0.0363	27.5548	661.3149	*ε2*	1.8283	0.5470	13.1273
MSf	0.0677	14.7652	354.3656	*2N2*	1.8597	0.5377	12.9054
Mf	0.0732	13.6608	327.8599	*μ2*	1.8645	0.5363	12.8718
MSTm	0.1046	9.5569	229.3651	*N2*	1.8960	0.5274	12.6583
MTm	0.1095	9.1329	219.1901	*ν2*	1.9008	0.5261	12.6260
MSQm	0.1409	7.0958	170.2989	*γ2*	1.9274	0.5188	12.4519
2Q1	0.8570	1.1669	28.0062	*α2*	1.9295	0.5183	12.4382
σ1	0.8618	1.1603	27.8484	*M2*	1.9323	0.5175	12.4206
Q1	0.8932	1.1195	26.8684	*β2*	1.9350	0.5168	12.4030
ρ1	0.8981	1.1135	26.7231	*δ2*	1.9377	0.5161	12.3855
O1	0.9295	1.0758	25.8193	*λ2*	1.9637	0.5092	12.2218
τ1	0.9350	1.0695	25.6681	*L2*	1.9686	0.5080	12.1916
M1	0.9664	1.0347	24.8333	*2T2*	1.9945	0.5014	12.0329
χ1	0.9713	1.0295	24.7091	*T2*	1.9973	0.5007	12.0165
π1	0.9945	1.0055	24.1321	*S2*	2.0000	0.5000	12.0000
P1	0.9973	1.0027	24.0659	*R2*	2.0027	0.4993	11.9836
S1	1.0000	1.0000	24.0000	*K2*	2.0055	0.4986	11.9672
K1	1.0027	0.9973	23.9345	*ξ2*	2.0369	0.4909	11.7825
ψ1	1.0055	0.9946	23.8693	*η2*	2.0418	0.4898	11.7545
φ1	1.0082	0.9919	23.8045	*M3*	2.8984	0.3450	8.2804
θ1	1.0342	0.9670	23.2070	*M4*	3.8645	0.2588	6.2103

Table 2.1: The principal harmonic components of the tidal potential, derived from the ETGTAB code, listed in order of increasing frequency (f). The corresponding period (T=1/f) is also shown.

This concept can cause much confusion. For example, Rinehart (1972a, 1972b) attempted to correlate geyser activity with 'the 18.6-year tidal component'. In reality, his study compared geyser activity with the slowly changing amplitude envelope of the tidal oscillations.

It should be stressed that the fixed set of tidal angular frequencies in a particular harmonic decomposition ($\{\omega_1,...,\omega_N\}$) is derived directly from tidal potential – the particular, accurately known signal which gives rise to all tidal phenomena. The harmonic decomposition of *other* tidal signals depends on the assumption that they contain power at precisely the same set of frequencies. Under this assumption, the arbitrary tidal signal $\zeta(t)$ would be written:

$$\zeta(t) = \sum_{j=1}^{N} H_j \cos(\omega_j t - g_j) \tag{2.15}$$

Thus, all of the information in the signal is expressed by the set of N amplitudes $\{H_1,...,H_N\}$ and the set of N phase-lags $\{g_1,...,g_N\}$, collectively known as the harmonic constants of the signal. Unfortunately, for real data, it is rarely possible to determine accurate estimates for all of these harmonic constants. Even if the dataset is free from errors and noise, its finite length will limit the ability to discriminate between individual spectral lines. From Fourier transform theory, it is only possible to separate harmonic components at angular frequencies ω_1 and ω_2 in a time-series whose length exceeds $2\pi/(\omega_1-\omega_2)$ (Press *et al.*, 1986). For example, to separate the *M2* component (period 12.42 hours) from the *S2* component (period 12 hours) requires a time-series of at least 14.8 days duration. The longer the time interval spanned by the dataset the more spectral lines can be extracted. However, to resolve *all* of the spectral lines in a standard harmonic decomposition requires an impractically long time-series of 18.6 years duration, which is the period of revolution of the moon's nodes (Doodson & Warburg, 1941).

The impossibility of resolving all spectral lines from a time-limited dataset renders the classical harmonic decomposition inappropriate for the short, noisy datasets obtained from hydrothermal systems. Consequently, it is important to develop methods of extracting the maximum amount of tidal information from limited datasets. This process is discussed in Chapter 3.

2.4 The Solid Tide

2.4.1 Definition of the Solid Tide

One immediate consequence of the tidal potential is the solid tide, sometimes known as the earth tide. This is defined as the flexing of the solid earth due to the direct influence of the tide-generating force. Of course, the presence of oceans creates an additional tidal strain, due to the changing pressure field which the oceans exert on the seafloor. However, the term tidal loading is reserved for the latter mechanism and it is considered separately, in Section 2.5.4.

2.4.2 The nature of the Solid Tide

It can be shown (Bredehoeft, 1967; Melchior, 1983) that the vertical displacement of the Earth's surface due to the solid tide is:

$$\zeta_s = \frac{h}{g} W_2 \big|_{r=r_E} \tag{2.16}$$

Here, h is a 'Love number' derived from the elastic properties of the Earth and g is gravitational acceleration.

Furthermore, the volumetric dilatation of the crust at the Earth's surface, due to the solid tide, is given by:

$$\varepsilon = \left(\frac{1-2\nu}{1-\nu} \right) \frac{(2h-6l)}{g r_E} W_2 \big|_{r=r_E} \tag{2.17}$$

where ν is a Poisson's ratio, r_E is the radius of the Earth, g is gravitational acceleration and h and l are Love numbers.

The values quoted by Bredehoeft (1967): ν=0.25, h=0.60 and l=0.07, give:

$$\varepsilon \approx \frac{1}{2 g r_E} W_2 \big|_{r=r_E} \tag{2.18}$$

This allows two important conclusions to be drawn. Firstly, the displacements and strains of the solid tide are exactly proportional to, and in phase with, the tidal potential. Secondly, an estimate can be made of the magnitude of the crustal strains due to the solid tide. Oscillations in the tidal potential, W_2, have magnitude ~3 m^2s^{-2} (Figure 2.3). Using $g \sim 9.8$ ms^{-2} and $r_E \sim 6.4 \cdot 10^6$ m suggests that the strain, ε, should have magnitude ~$2.4 \cdot 10^{-8}$. Therefore, the solid tide can be expected to produce strain values of the order of a few tens of nanostrain. Although very small, these strain values are sufficient to cause measurable fluctuation of the water level in wells (Bredehoeft, 1967; Marine, 1975, Rojstaczer & Agnew, 1989).

Furthermore, there is some evidence that the solid tide may influence the periodicity of geysers (Ingebritsen & Rojstaczer, 1993; Ingebritsen & Rojstaczer, 1996). It would therefore seem plausible - *a priori* - that crustal strains created by the solid tide might have an important effect on seafloor hydrothermal systems.

It is important to note that this theory considers the response of the whole Earth to the tide-generating force (Bredehoeft, 1967). The theory does account for changes in the elastic properties of the Earth with depth, but it does not allow for any localised inhomogeneities which might complicate the local strain response.

It is possible to predict the solid tide for any point on the Earth's surface, given values for the Love numbers and Poisson's ratio, since it is proportional to the tidal potential. There are several publicly available codes which perform this calculation, including ETGTAB (H.-G. Wenzel, *pers. comm.*, 1997), and the SPOTL suite of programs (Agnew, 1997)

2.5 The Ocean Tide

2.5.1 Definition of the Ocean Tide

The ocean tide at any particular place ($\zeta_O(t)$) can be defined as the vertical deviation of the sea-surface from its average position due to tidal effects.

2.5.2 The Equilibrium Tide

The equilibrium tide is the ocean tide which would occur on Earth, if two highly idealised conditions were met (Doodson & Warburg, 1941). These conditions are:

(1) There is a single ocean, of constant mean depth, covering the entire globe.

(2) The surface of this ocean achieves instant equilibrium with the tide-raising force. In other words, it is assumed that the ocean surface is always a potential surface, positioned perpendicular to the local effective gravity.

Each of these assumptions represents a considerable departure from the truth, and therefore the equilibrium tide is very different to the true ocean tide in both amplitude and phase.

It can be shown (Doodson & Warburg, 1941) that the equilibrium tide ($\zeta_{eq}(t)$) is simply another scaled version of the tidal potential:

$$\zeta_{eq} = \frac{1}{g} W_2 \big|_{r=r_E} \tag{2.19}$$

The equilibrium tide is very simple to compute, and in the past it has been used as an estimate of the real ocean tide (Thomson *et al.*, 1986). However, there is now such good

knowledge of the true ocean tide (Section 2.5.3), that there is no longer any need to resort to the equilibrium tide.

2.5.3 The Ocean Tide

The real ocean tide observed on Earth is considerably more complex than the equilibrium tide (Schwiderski, 1980). There are many factors which contribute to this complexity, including the topography of the seafloor, the dynamical response of the oceans, friction, Coriolis forces and the presence of coastal boundaries. Nonetheless, the global ocean tide is now known to considerable accuracy. Direct hydrodynamic modelling of the oceans (Le Prevost *et al.*, 1994) and data from satellite altimetry (Schrama & Ray, 1994; Le Prevost *et al.*, 1995) can be combined with data from deep-sea and coastal tide gauges (Egbert at al., 1994) to produce cotidal maps for the principal tidal harmonic components. The maps reproduced in Figure 2.8 are typical, and present a useful summary of the magnitudes of the main tidal components in the world oceans. (Computer codes to predict the ocean tide at any location are currently available at http://podaac-www.jpl.nasa.gov/toppos/toppos_tides.html.)

It is possible to draw some general conclusions about the nature of the ocean tide at different hydrothermal sites, from an analysis of global ocean tide maps (Figure 2.8). For each component of the ocean tide, Coriolis forces create amphidromic points - where the magnitude of the ocean tide is zero - in the open oceans. Amphidromic points are a graphic demonstration of the fact that tides in the middle of the ocean can be very different from those at the coast.

For example, hydrothermal sites on the Mid-Atlantic Ridge, Atlantic Ocean, such as TAG (26.1°N, 44.8°W) and Lucky Strike (37.3°N, 32.3°W), are situated close to the North Atlantic amphidromes and experience much smaller ocean tides than ports on the Atlantic coasts of Europe. In contrast, on the Juan de Fuca Ridge, Pacific Ocean, the Endeavour hydrothermal field (47.8°N, 129.0°W) is situated close to the coast where the ocean tides are reasonably large. There is also a general difference in the spectral nature of the ocean tide in the Atlantic and Pacific Oceans. The natural frequency of oscillation of the Atlantic Ocean is close to two cycles per day. Consequently, the components of the ocean tide in the semi-diurnal frequency band are amplified (Doodson & Warburg, 1941; Figure 2.8). Therefore, the ocean tides of the Atlantic are generally semi-diurnal.

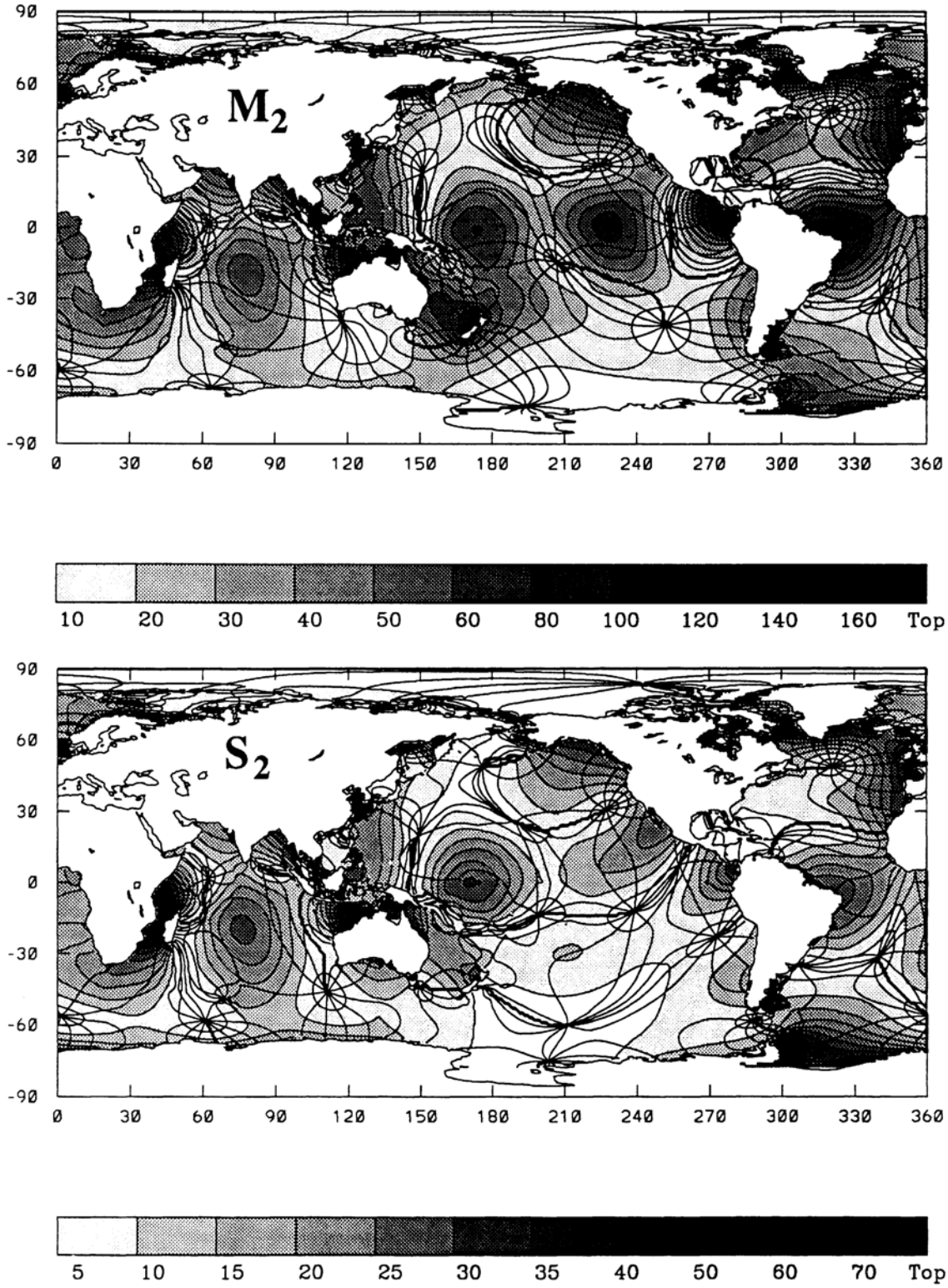

Figure 2.8: (a) Cotidal maps for the semi-diurnal components *M2* and *S2*. Amplitudes are in cm. Cophase lines are drawn at intervals of 30° with the thick line corresponding to the Greenwich passage of the tidal potential. (From Le Prevost *et al.*, 1994).

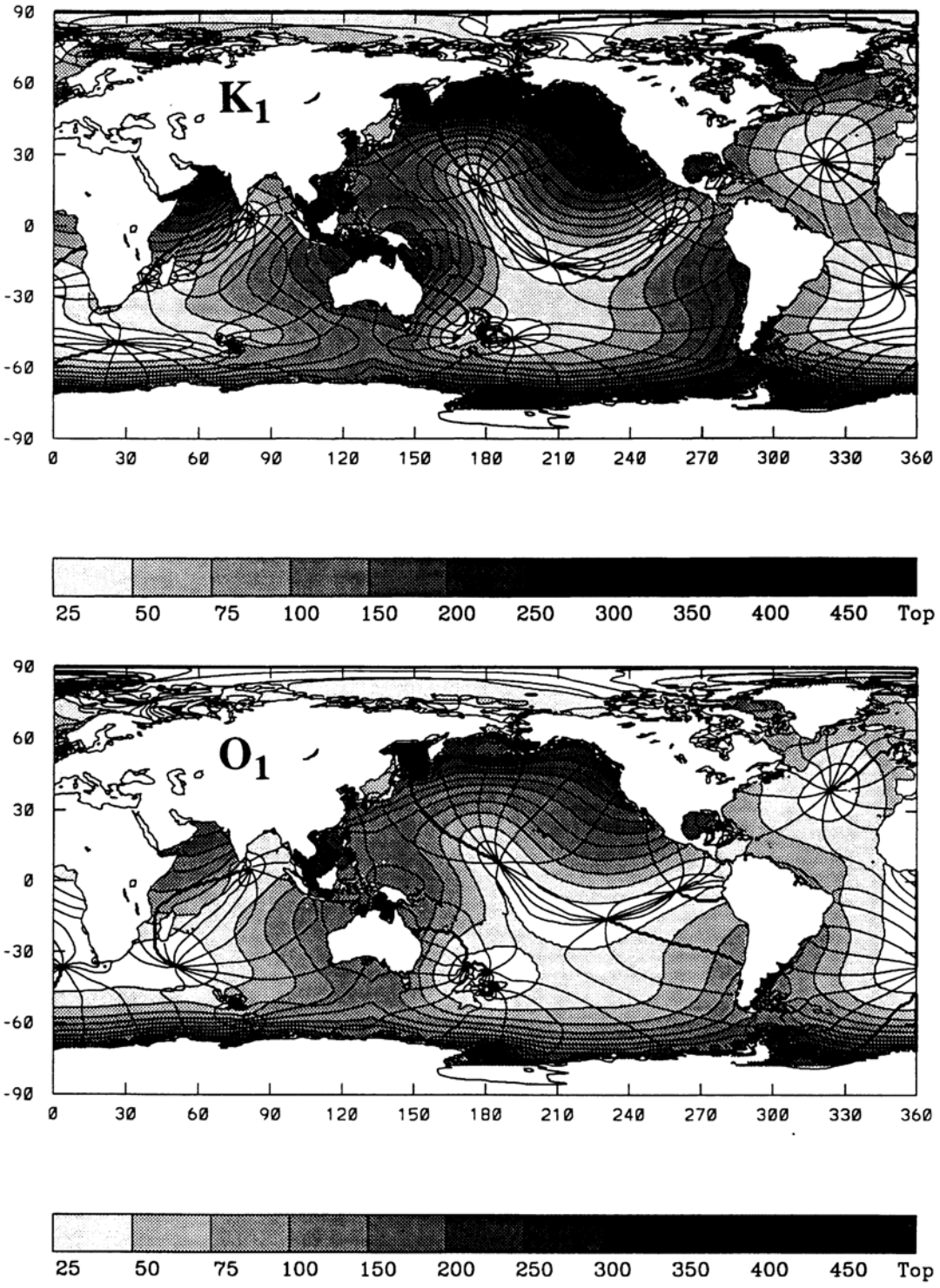

Figure 2.8: (b) Cotidal maps for the diurnal components *K1* and *O1*. Note that amplitudes are in mm, unlike those in Figure 2.8a. Cophase lines are drawn at intervals of 30º with the thick line corresponding to the Greenwich passage of the tidal potential. (From Le Prevost *et al.*, 1994).

Although the frequency modulation of Section 2.3.2 does occur, the small amplitude of the diurnal components renders it insignificant in many cases. In contrast, the Pacific Ocean does not display any particular semi-diurnal resonance. As a result, the diurnal components of the ocean tide are generally much larger in the Pacific Ocean than the Atlantic Ocean (Figure 2.8).

Ideally, direct measurements of the ocean tide could be made, using seafloor pressure sensors, whenever time-series data are acquired from hydrothermal sites. Such sensors would record all changes in seafloor pressure including those which are not tidal in origin, such as the effects of atmospheric pressure and wind. However, where direct measurements are not available, computer simulations of the ocean tide provide a reasonable alternative.

The ocean tides in the open ocean generally have an amplitude of ~1 m, and can be expected to influence hydrothermal systems by imposing a changing pressure field on the seafloor (Section 2.5.4) and by creating horizontal water motion across the seafloor (Section 2.6).

2.5.4 The Load Tide

The ocean tide ($\zeta_O(t)$) (Section 2.5.3), creates a changing pressure field ($\rho_0 g\zeta_O(t)$) on the seafloor, where ρ_0 is the average density of seawater. This generates additional strain and displacement in the Earth's crust - known as the load tide - in addition to the solid tide of Section 2.4. The load tide at any point on the Earth's surface is calculated by evaluating a convolution integral of the ocean tide with the appropriate Green's function over the entire global seafloor (Longman, 1962, 1963; Farrell, 1972a, 1972b, 1973). Thus, the load tide at any point depends on the ocean tide for the whole globe. However, mid-ocean ridge hydrothermal systems are located on the seafloor where the convolution is overwhelmingly dominated by the local ocean tide (Francis & Mazzega, 1990). Therefore, it is an acceptable approximation to assume that load tides on the seafloor are in phase with, and proportional to, the local ocean tide.

For a seawater density $\rho_0 \sim 10^3$ kg.m^{-3}, ocean tides of amplitude ~1 m will create an oscillating seafloor pressure field of amplitude ~10^4 Pa. Ingebritsen & Rojstaczer (1996) considered the crustal strain values expected in land-based hydrothermal systems. They compared the strain magnitude generated by the solid tide with that created by fluctuations in atmospheric pressure. Their argument can be adapted to the investigation of seafloor systems by considering the changing weight of the water column - rather than atmospheric pressure - as the source of the surface load to the crust. Ingebritsen & Rojstaczer (1996) assumed a typical rock compressibility of ~10^{-10} Pa^{-1}, which would suggest that an ocean tide of ~1 m should produce crustal strains of magnitude ~10^{-6}. This is two orders of magnitude greater

than the strains of magnitude ~10^{-8} which are expected to result from the solid tide (Section 2.4). Consequently, it is to be expected that seafloor hydrothermal systems will suffer much more deformation from the load tide (which is proportional to the ocean tide) than from the solid tide (which is proportional to the tidal potential). This expectation is tested in Chapter 4 by comparing hydrothermal time-series with both the local tidal potential and the local ocean tide.

2.6 Tidal Streams

The vertical motion of the sea-surface, defined as the ocean tide ($\zeta_O(t)$), is accompanied by horizontal movement of water within the oceans, which is termed tidal streams (Doodson & Warburg, 1941). Ideally, current meter data would be collected at hydrothermal vent sites concurrently with measurements of temperature, flow rate, pressure and chemistry, but this has not always been possible. In the absence of direct current measurements it is necessary to estimate the tidal streams at hydrothermal vent sites using knowledge (or an estimate) of the ocean tide.

For simplicity, the following sections will consider the tidal stream due to a single tidal component (e.g. the *M2* component), of angular frequency ω. The aim is to summarise the inferences that can be made about tidal streams on the seafloor, given an estimate of the local ocean tide.

2.6.1 Rectilinear travelling waves in the open oceans

In the open oceans the sea-surface displacement due to a particular tidal component takes the form of a travelling wave, progressing rotationally about an amphidrome as illustrated on global co-tidal charts (Figure 2.8). However, for the purposes of this discussion it is sufficient to consider a surface wave in two dimensions (Figure 2.9).

If the wave travels along the x-axis with amplitude A, the displacement of the water surface $\zeta(x,t)$ is given by:

$$\zeta = A\cos(kx - \omega t) \tag{2.20}$$

The dispersion relation is (Lamb, 1932):

$$\omega^2 = gk\tanh(kh) \tag{2.21}$$

and the horizontal and vertical components of the water velocity are:

$$u = A\omega \frac{\cosh(kz + kh)}{\sinh(kh)} \cos(kx - \omega t) \tag{2.22}$$

$$w = A\omega \frac{\sinh(kz + kh)}{\sinh(kh)} \sin(kx - \omega t) \tag{2.23}$$

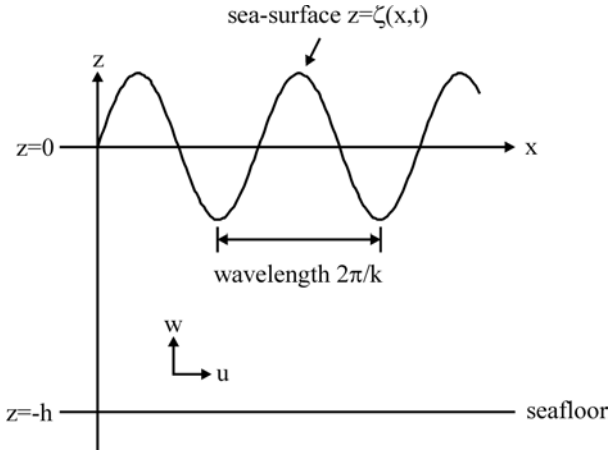

Figure 2.9: The ocean tide ($\zeta(x,t)$) in water of depth h results in a wave of wavenumber k. As described in the text, the nature of the induced tidal stream (u,w) depends on whether this is a standing wave or a travelling wave. The velocity is $u(x,z,t)$ in the x-direction, and $w(x,z,t)$ in the z-direction.

In the open oceans, h is typically ~1 km, while the wavelength $2\pi/k$ is typically ~10^2 – 10^4 km. Hence, kh<<1, and so $\sinh(kh) \approx kh$ and $\tanh(kh) \approx kh$. Under this shallow water approximation, it follows that the horizontal stream, u, on the ocean floor $z = -h$, is an oscillation of magnitude:

$$\frac{A\omega}{\sinh(kh)} \approx A\sqrt{\frac{g}{h}} \tag{2.24}$$

Thus, for a typical ocean tide of amplitude $A \approx 1$ m, in an ocean of depth $h \approx 1000$ m, with $g \approx 10$ m.s^{-2}, the tidal streams would have a magnitude $|u| \sim 0.1$ m.s^{-1}. The surface displacement (ζ) and the horizontal velocity (u) are both dependent on time via the term $\cos(kx-\omega t)$. Therefore peak tidal streams on the ocean floor coincide with low and high tide. This result seems to contradict common experience that slack water occurs at high and low tide, and that peak tidal streams coincide with half-tide. The apparent confusion results because common experience is based on the standing waves found in small gulfs and

estuaries rather than the travelling waves found in the open oceans (Doodson & Warburg, 1941).

2.6.2 Rectilinear standing waves in small gulfs

In a short gulf, for example the Gulf of California (Little *et al.*, 1988), the surface displacement (ζ) due to a particular tidal component often takes the form of a standing wave. The pattern of cophase lines on a cotidal chart (Figure 2.8) reveals whether the surface wave generated by a particular tidal component is a standing wave or a travelling wave. A standing wave of amplitude A can be written as the sum of two travelling waves:

$$\zeta = A\left[\frac{1}{2}\cos(kx-\omega t)+\frac{1}{2}\cos(kx+\omega t)\right] = A\cos(kx)\cos(\omega t) \tag{2.25}$$

By linearity, and using the theory of Section 2.6.1, it follows that the horizontal component of velocity (u) is given by:

$$u = A\omega\frac{\cosh(kz+kh)}{\sinh(kh)}\sin(kx)\sin(\omega t) \tag{2.26}$$

Thus, assuming $kh<<1$, the magnitude of the streams on the seafloor is the same as for travelling waves:

$$\frac{A\omega}{\sinh(kh)} \approx A\sqrt{\frac{g}{h}} \tag{2.27}$$

However, the phase relationship between the ocean tide and tidal streams is very different. The surface displacement (ζ) depends on time via the term $\cos(\omega t)$, but the horizontal velocity (u) depends on time via the term $\sin(\omega t)$. It therefore follows, in agreement with common experience, that peak streams occur at half-tide for standing waves. The interaction of standing and travelling waves in the Gulf of California is discussed in greater detail in Chapter 4.

2.6.3 The frequency spectrum of a rectilinear tidal stream

Consider the horizontal velocity (u) of a rectilinear tidal stream along the x-axis, due to a single tidal component of angular frequency ω, so that $u\sim\sin(\omega t)$. The rate of heat transfer from the seafloor to the ocean is proportional to the speed ($|u|$) of the stream. In contrast, the pressure drop due to flow over a hydrothermal edifice, caused by the Bernoulli effect, is proportional to the square of the speed ($|u|^2$) (Schultz & Elderfield, 1997). Both of these processes might be expected to affect hydrothermal systems, and it is useful to consider the expected spectral nature of signals which depend on them. The square of the speed of the tidal stream is:

$$|u|^2 \sim \sin^2(\omega t) = \frac{1}{2} - \frac{1}{2}\cos(2\omega t) \tag{2.28}$$

Hence, any process which depends linearly on the Bernoulli effect will have all power concentrated at angular frequency 2ω, or twice the angular frequency of the surface displacement.

In contrast, the speed of the tidal stream is:

$$|u| \sim |\sin(\omega t)| = \frac{2}{\pi}\left[1 - 2\sum_{n=1}^{\infty}\frac{1}{(2n+1)(2n-1)}\cos(2n\omega t)\right] \tag{2.29}$$

Hence, any physical process which depends linearly on the rate of heat transfer from the seafloor to the ocean will have spectral power at all of the angular frequencies $\{2\omega, 4\omega, 6\omega, \ldots\}$.

Thus, careful examination of the power spectrum of a seafloor tidal signal can be used to distinguish $|u|$-dependent processes from $|u|^2$-dependent processes. However, it must be stressed that the situation is considerably more complicated if the effects of more than one tidal component are significant.

2.6.4 Rotating tidal streams

In many cases, the seafloor tidal streams associated with a particular tidal component are rotating rather than rectilinear (Doodson & Warburg, 1941). In such a case, the vector representing the tidal stream in the horizontal plane traces an elliptical path during each tidal period. If the *x*- and *y*-axes are placed along the major- and minor-axes of this ellipse, then the components of the tidal stream velocity are:

$$u = a\cos(\omega t) \tag{2.30}$$

$$v = b\sin(\omega t) \tag{2.31}$$

It then follows that the square of the speed of the tidal stream is given by:

$$u^2 + v^2 = \frac{1}{2}(a^2 + b^2) + \frac{1}{2}(a^2 - b^2)\cos(2\omega t) \tag{2.32}$$

which has all power concentrated at angular frequency 2ω, as for the rectilinear case (equation (2.28)).

In contrast, the speed of the stream is given by:

$$\sqrt{u^2 + v^2} = \sqrt{\frac{1}{2}(a^2 + b^2) + \frac{1}{2}(a^2 - b^2)\cos(2\omega t)} \tag{2.33}$$

The exact Fourier series representation of this expression is not known, but it is clear that it must contain spectral lines at the angular frequencies $\{2\omega, 4\omega, 6\omega, \ldots\}$ in the same manner as

equation (2.29). Hence, the same general conclusions can be drawn for the case of rotating streams as for rectilinear streams. In principle, $|u|$-dependent processes could be distinguished from $|u|^2$-dependent processes by examining the spectral power at the even harmonics of the fundamental frequency.

2.7 Conclusions

A tidal signal is defined to be the part of a time-series which is caused by the tidal potential. Several first order tidal signals have been described – the solid tide, ocean tide, load tide and tidal streams, and their potential influence on hydrothermal systems has been discussed.

The solid tide is in phase with the tidal potential and easily predictable using public domain computer codes. It is expected to lead to crustal strains of magnitude $\sim 10^{-8}$ (i.e. tens of nanostrain).

The global ocean tide is extremely complex, but a combination of satellite altimetry, hydrodynamic modelling and pressure gauge data means that it is known to considerable accuracy in most of the world's oceans. There are public domain computer codes which predict the ocean tide at any location. Ocean tides generally have an amplitude of ~1 m. The ocean tide creates a changing pressure field on the seafloor which gives rise to crustal strain – the load tide.

To a reasonable approximation, the load tide at a point on the seafloor is in phase with, and proportional to, the local ocean tide. The crustal strains due to the load tide can be as large as 10^{-6}, two orders of magnitude greater than the solid tide. It is therefore expected that the ocean tide will have a greater influence on hydrothermal systems than the solid tide. This expectation is tested in Chapter 4.

The tidal streams which accompany the ocean tide typically have a magnitude ~0.1 $m.s^{-1}$ in the open ocean. If tidal streams influence hydrothermal systems, it might be informative to examine the power spectrum of hydrothermal tidal signals. A spectrum containing the 4^{th} and 6^{th} harmonics of the tidal frequencies would suggest that the hydrothermal system is influenced by the speed of the water (via heat transfer from the seafloor) rather than the speed squared (via the Bernoulli effect).

The nature of the tidal potential has been examined in some detail, as it is expected that tidal signals in hydrothermal systems will display similar behaviour. When considered over a long time interval (perhaps a year or more), it is reasonable to view tidal signals in terms of their stationary harmonic decomposition, or Fourier series. However, the number of spectral lines which can be resolved from a short dataset (of a few days to a few months) is severely limited. Accordingly, when considering tidal phenomena over the course of a few semi-diurnal cycles it is conceptually useful to view the tidal potential as a mix of diurnal and semi-diurnal frequencies which is frequency- and amplitude-modulated by lunar and solar motions.

The tidal potential can be considered to be amplitude-modulated by the phases of the moon, and frequency-modulated by the lunar and solar declinations. It is informative to look for similar behaviour in time-series obtained from hydrothermal systems (Chapter 4). The astronomical positions of the sun and moon are accurately known, and are expected to influence *all* tidal signals in a similar way. Consequently, it is efficient to use this astronomical knowledge to develop data analysis techniques which are specifically designed for use with tidal time-series. Chapter 3 is concerned with the development of these techniques.

Chapter 3: The analysis of tidal data

3.1 Introduction

Chapter 2, above, is devoted to a discussion of the tidal potential and its immediate consequences – the solid and ocean tides. These tidal signals can be considered to be the inputs to a physical system – a hydrothermal convection cell – whose outputs are the observed variations in effluent temperature, chemistry and flow rate. The input signals are easily predicted, and their characteristic features are discussed in detail in Chapter 2. It would be advantageous to have an equally precise knowledge of the measured output signals, but this is rarely possible. Collecting data on the seafloor is difficult and expensive, so the datasets are often limited in length to a few days or weeks. Furthermore, the resulting time-series tend to be rather noisy. Consequently, the aim of this chapter is to compare the different methods of extracting information from a limited, imperfect hydrothermal time-series.

The analysis of tidal signals has been a subject of great interest for many years. Originally, the motivation was to establish the nature of the ocean tide at a particular port, to ensure the safety of shipping. The sea level in the port was measured with a tide-gauge over a period of time and a harmonic decomposition of the resulting time-series was used to extract the harmonic constants of the port. The number of harmonic constants which can be determined increases with the length of the time-series (Doodson & Warburg, 1941). Given suitable data, this method produces an accurate and theoretically sound description of oceanic tidal signals. Furthermore, it has successfully been applied to the study of earth tides, where the data to be analysed include time-series of gravity, strain and tilt (Melchior, 1983).

It must be stressed, however, that traditional harmonic methods are ill suited to the analysis of hydrothermal time-series. The first reason for this is that data from the seafloor are constrained to span limited short time intervals. In contrast, land-based equipment such as tide gauges can obtain very long time-series at minimal cost. For example, Munk & Cartwright (1966) were able to analyse 19 years of tide observations in order to establish the harmonic constants of the ocean tide at Newlyn and Honolulu. The second obstacle to the application of harmonic methods is that hydrothermal time-series tend to be much noisier

than traditional tidal signals - such as those from tide-gauges or strain meters - which appear smooth in the time-domain. To a good approximation, these smooth tidal signals contain spectral power only at the tidal frequencies. A hydrothermal time-series, on the other hand, often has a significant amount of power in a smooth background spectrum, in addition to power in line components at the tidal frequencies.

In summary, the task of extracting tidal information from hydrothermal time-series is made difficult by the fact that the datasets tend to be (1) short and (2) noisy. The implications of these problems are discussed in this chapter by dividing the techniques of time-series analysis into two classes – parametric and non-parametric.

Among non-parametric techniques, the periodogram spectral estimator has been widely used in the interpretation of hydrothermal time-series despite the fact that it is demonstrably ill suited to short and noisy data. The multiple window method (Thomson, 1982) is much better suited to the problem, and is recommended as the best non-parametric technique for hydrothermal time-series. The MWPS code which implements this technique (A. Chave, *pers. comm.*, 1999) is applied to hydrothermal time-series data in Chapter 4.

Among parametric techniques, the traditional Harmonic Method is of limited use with a short time-series, and it is recommended that the Admiralty Method (Admiralty Tidal Handbook, No. 3) be used in its place. Furthermore, to combat the problems of noise, the Admiralty Method can be made more robust (Chave *et al.,* 1987), and combined with a technique which removes drift from the data signal (Tamura *et al.,* 1991). The subsequent hybrid technique is recommended as the optimal parametric technique for extracting information from hydrothermal time-series. This technique has been implemented in the new computer code HYBRID. It is applied to hydrothermal time-series data in Chapter 4.

3.2 Non-parametric analysis

Many hydrothermal time-series clearly have the appearance of tidal signals when viewed in the time-domain because they display diurnal and semi-diurnal periodicity (Chapter 4). However, it should not be assumed that a signal is tidal without further supporting evidence. Consequently, the first step in the examination of a time-series should be an impartial, non-parametric analysis of the data, in which the prejudice of the analyst plays no part. An attempt to fit the data with a parametric model should only be made if evidence of tidal modulation has previously been uncovered by a non-parametric analysis.

A hydrothermal time-series can be considered to be a finite sample from a stationary process. The problem is then to make an estimate of the power spectrum of this process, using the information from the finite dataset. It must be stressed that the true power spectrum of the process can never be deduced from a finite amount of data (Thomson, 1982). However, the data can be used to construct several different *estimates* of the true power spectrum (Section 3.2.1).

Once an estimate of the power spectrum has been made, it can be examined to see if there is evidence of significant power at the tidal frequencies. The principal components of the tidal potential are *M2* (period 12.42 hours), *S2* (period 12 hours), *K1* (period 23.94 hours) and *O1* (period 25.82 hours) (Table 2.1). It is likely that *any* tidal signal has significant spectral power at these frequencies. In most tidal signals the *M2* component dominates (Schwiderski, 1980). Consequently, an initial test of whether a signal is influenced by the tides is simply to see if it has significant spectral power at ~1.93 cpd (equivalent to a period of ~12.42 hours).

It must be stressed that the presence of spectral power at ~1.93 cpd does not *prove* that a time-series is tidally modulated. It may be that there is some other physical process – entirely independent of the moon - which causes modulation at this frequency. For the purposes of this dissertation, however, it is supposed that this is not the case. Consequently it is assumed that all signals whose spectra are *correlated* with tidal processes are in fact *caused* by tidal processes.

3.2.1 Simple Fourier transform methods

3.2.1.1 The periodogram

The simplest spectral estimate is the periodogram, which is based on the discrete Fourier transform (Press *et al.,* 1986). Given a time-series dataset $\{x_0,\ldots,x_{N-1}\}$, the periodogram estimate $\hat{S}_P(f)$ of the power at frequency f is:

$$\hat{S}_P(f) = \left| \sum_{n=0}^{N-1} x_n e^{2\pi i f n / N} \right|^2 \qquad (3.1)$$

Normally, this spectral estimate is made at the discrete set of frequencies $\{f_j = j/(N\Delta t)\}$, where Δt is the sampling interval between successive data-points in the time-domain, and j lies in the range $\{-N/2,\ldots,0,\ldots,N/2\}$. (It is assumed, for convenience, that N is even.) Unfortunately, the periodogram $\hat{S}_P(f)$ is not a good estimator of the true spectrum $S(f)$.

The Fejer kernel $K_F(f)$ is defined by:

$$K_F(f) = \frac{1}{N^2}\left[\frac{\sin(\pi f)}{\sin(\pi f/N)}\right]^2 \tag{3.2}$$

It can be shown that the periodogram estimate $\hat{S}_P(f)$ is equal to the convolution of the true spectrum $S(f)$ with the Fejer kernel $K_F(f)$ as follows:

$$\hat{S}_P(f) = \int_{s=-\infty}^{\infty} K_F(s)S(f-s)ds \tag{3.3}$$

Consequently, the periodogram estimate $\hat{S}_P(f_j)$ of the power at frequency f_j is a weighted average of the true power at *all* other frequencies. For this reason, the periodogram is said to be biased by spectral leakage.

3.2.1.2 Local and broadband bias

The bias can be divided into two parts by defining a bandwidth W in the frequency domain. Leakage from frequencies in the range $(f_j\text{-}W, f_j\text{+}W)$ is termed local bias, while leakage from the other more distant frequencies is termed broadband bias. The bandwidth can be expressed in non-dimensional form, as the time-bandwidth product $NW\Delta t$. This is often chosen to be an integer, in which case it represents the number of frequency bins, on either side of f_j, which contribute to the local bias in the estimate at frequency f_j. Consequently the local bias in the estimate at f_j consists of the spectral leakage from the frequencies $\{f_{j-NW\Delta t}, \ldots, f_{j+NW\Delta t}\}$ (Thomson, 1982).

3.2.1.3 The windowed periodogram

The periodogram estimate of equation (3.3) suffers very badly from broad band bias, because the side-lobes of the Fejer kernel fall away slowly (equation (3.2)). The problem can be addressed by multiplying the dataset $\{x_0, \ldots, x_{N-1}\}$ by a data window $\{w_0, \ldots, w_{N-1}\}$ before performing the Fourier transformation (Press *et al.,* 1986). This produces a spectral estimate known as the windowed periodogram estimate $\hat{S}_{WP}(f)$, defined by:

$$\hat{S}_{WP}(f) = \left|\sum_{n=0}^{N-1} w_n x_n e^{2\pi i f n/N}\right|^2 \tag{3.4}$$

In this case, the estimate $\hat{S}_{WP}(f)$ is the convolution of the true spectrum $S(f)$ with a spectral window $W_S(f)$:

$$\hat{S}_{WP}(f) = \int_{s=-\infty}^{\infty} W_S(s)S(f-s)ds \tag{3.5}$$

The data window $\{w_0,\ldots,w_{N-1}\}$ is usually normalised so that:

$$\sum_{n=0}^{N-1} w_n^2 = N \tag{3.6}$$

It then follows that the spectral window $W_S(f)$ is given by:

$$W_S(f) = \left| \sum_{n=0}^{N-1} w_n e^{2\pi i f n / N} \right|^2 \tag{3.7}$$

Many data windows are in common use, and the choice of a particular data-window is made according to the desired bias properties of its spectral window $W_S(f)$.

3.2.1.4 Discrete prolate spheroidal sequences

A family of data windows known as the discrete prolate spheroidal sequences (or DPSS's) is of particular interest. Given a choice of the time-bandwidth product ($NW\Delta t$) it is possible to define an ordered set of N DPSS's $\{\{v_n^{(0)}\},\ldots,\{v_n^{(N-1)}\}\}$ (Thomson, 1982). For a particular value of the time-bandwidth product ($NW\Delta t$), the first DPSS ($\{v_n^{(0)}\}$) can be shown to have the smallest local bias of all possible data windows (Slepian, 1978).

This optimality of the DPSS's - in particular the first such window $\{v_n^{(0)}\}$ - makes them a natural choice as the data windows for use in windowed periodograms. The choice of time-bandwidth product should be made individually for each problem, by weighing up the likely effects of local and broad-band bias and the desired resolution of the spectral estimate.

The preceding remarks have important consequences for the analysis of tidal signals from the noisy, short datasets which are obtained at hydrothermal systems. The true spectrum of the tidal potential is known to consist of a large number of closely-spaced harmonic lines, and it is expected that all tidal signals will have similar line components in their spectra, in addition to the background noise from other processes. When spectral estimates are made, the large concentrations of power in the harmonic lines will tend to leak into adjacent frequencies, making it difficult to distinguish individual lines. The problem gets worse as the time-interval spanned by the dataset ((N-1)Δt) decreases, because the separation between adjacent frequency bins is $1/(N\Delta t)$. For example, a dataset spanning a time-interval of 14 days gives a frequency bin separation of ~0.07 cpd. The set of tidal harmonic lines in the semi-diurnal frequency band covers a bandwidth of about ~0.3 cpd and would therefore contain only 4 frequency bins. This is clearly insufficient to resolve the location of a useful number of harmonic lines (Figure 2.7).

The bias problems of the unwindowed periodogram (equation (3.1)) are severe, and it should not be used in tidal analysis. Nonetheless, many studies of hydrothermal tidal signals contain little or no discussion of the spectral estimators which are employed, and it is quite possible that they rely on unwindowed periodograms (Johnson & Tunnicliffe, 1985; Little *et al.,* 1988; Chevaldonné *et al.,* 1991; Johnson *et al.,* 1994; Copley *et al.,* 1999). Windowed periodograms are an improvement, and a DPSS should be used as the data window to minimise bias, with the time-bandwidth product chosen to suit the particular problem.

Even with a DPSS as the data window, the windowed periodogram estimate (equation (3.4)) is not optimal for application to hydrothermal time-series. Periodogram estimates are not statistically efficient, in the sense that the variance of the estimate does not decrease as the number of data-points (N) increases. The two traditional methods of countering this problem are band-averaging and section-averaging (Press *et al.,* 1986; Chave *et al.,* 1987), but both have the undesirable side effect of reducing resolution in the frequency domain. This can ill be afforded in the analysis of short tidal signals.

3.2.1.5 Band-averaging

In band-averaging, a windowed periodogram estimate $\hat{S}_{WP}(f)$ is smoothed in the frequency domain by taking its convolution with a suitable function $K(f)$. Therefore the band-averaged spectral estimate $\hat{S}_{BA}(f)$ is:

$$\hat{S}_{BA}(f) = \int_{s=-\infty}^{\infty} K(s)\hat{S}_{WP}(f-s)ds \tag{3.8}$$

The convolution in equation (3.8) has the effect of smearing the power from tidal harmonic lines into neighbouring frequencies and therefore leads to a loss of resolution in the frequency domain. Consequently, band-averaging is not recommended for the analysis of hydrothermal time-series.

3.2.1.6 Section-averaging

In section averaging, the time-domain dataset $\{x_0,\ldots,x_{N-1}\}$ is split into M subsections, which may overlap with each other. For each section m, a windowed periodogram is used to produce a spectral estimate $\hat{S}_m(f)$. The section-averaged spectrum $\hat{S}_{SA}(f)$ is then calculated by taking an average of the spectral estimates obtained from each section. The averaging process can be done in several ways (Chave *et al.,* 1987), but the most obvious method is simply to take the arithmetic mean:

$$\hat{S}_{SA}(f) = \frac{1}{M}\sum_{m=1}^{M}\hat{S}_m(f) \tag{3.9}$$

Regardless of the details of the averaging process, this approach inevitably reduces resolution in the frequency domain, because the individual spectra ($\hat{S}_m(f)$) are obtained from subsections which are shorter than the original time-series. Consequently, section-averaging is not recommended for the spectral analysis of hydrothermal time-series.

3.2.1.7 Conclusion

In summary, methods based on the periodogram suffer from severe problems as means of extracting tidal information from hydrothermal time-series, although they have been used extensively for this purpose. The unwindowed periodogram of equation (3.3) is badly biased, while the windowed periodogram of equation (3.4) must be smoothed, by band- or section-averaging, to make it reasonably efficient. However, both of these methods lead to reduced resolution in the frequency domain, making it difficult to separate individual line components. It is strongly recommended that the periodogram methods of Section 3.2.1 should *not* be used to analyse hydrothermal time-series.

3.2.2 Multiple Window Power Spectra

The optimal non-parametric technique for analysing hydrothermal time-series is arguably the multiple window (or multiple taper) method of Thomson (1982), which makes use of the DPSS data windows discussed in Section 3.2.1. A brief synopsis of the method is provided here.

The first step is to choose a value for the time-bandwidth product $NW\Delta t$. The choice is influenced by the length of the time-series $(N\text{-}1)\Delta t$ and by the desired accuracy of the spectral estimate in the frequency domain. Inherent in this choice is a trade-off between efficiency and spectral resolution. A small time-bandwidth product allows closely spaced lines to be separated, but at the cost of low efficiency. Conversely, a large time-bandwidth product increases efficiency at the cost of smearing adjacent line components together. In the case of hydrothermal time-series, it is helpful that the spacing of the tidal harmonic lines in the frequency domain is known *a priori*.

As discussed in Section 3.2.1, a particular choice of time-bandwidth product $NW\Delta t$ defines a set of DPSS's $\{\{v_n^{(0)}\},\ldots,\{v_n^{(N-1)}\}\}$. In the multiple window method, each DPSS is used as the data window in a separate windowed periodogram of the entire time-series. This creates a

set of N separate spectral estimates $\{\hat{S}_0(f),\ldots,\hat{S}_{N-1}(f)\}$ which are known as the eigenspectra. The multiple window spectral estimate $\hat{S}_{MWPS}(f)$ is then obtained by taking a weighted average of the eigenspectra at each frequency. It can be shown that it is acceptable to restrict attention solely to the first $K=2NW\Delta t$ eigenspectra (Thomson, 1982). Consequently, $\hat{S}_{MWPS}(f)$ is given by an expression of the form:

$$\hat{S}_{MWPS}(f) = \sum_{k=0}^{K-1} d_k(f)\hat{S}_k(f) \tag{3.10}$$

The weights $d_k(f)$ are calculated from the data in a manner described by Thomson (1982). It is important to note that this method relies on windowed periodograms of the *entire* data sequence, and does not perform any convolutional smoothing in the frequency domain. Thus, unlike band- or section-averaging, it achieves statistical efficiency without sacrificing any spectral resolution. This is clearly desirable when seeking to identify closely spaced tidal harmonic lines in short time-series.

3.2.2.1 Identification of line components

The multiple window method is particularly well suited to tidal analysis as it incorporates an explicit procedure for the identification of significant line components in the spectrum. Firstly, the complex harmonic constants for the time-series are estimated, by regression over the eigenspectra, for each frequency bin (f_j). It must then be decided whether the estimated power of the harmonic constants represents a statistically significant line component. To this end, an F-statistic is constructed for the estimated harmonic constants in each frequency bin. It can be shown that this statistic is distributed as $F_{2,2K-2}$ for Gaussian data. Consequently, an unusually large value of the F-statistic is interpreted as evidence that there is a significant line component at the frequency under consideration. For a time-series of N data-points, Thomson (1982) suggests that the F-statistic should be considered significant if its value exceeds the $100*(N-1)/N$ percentage point of the $F_{2,2K-2}$ distribution. In Chapter 4, this criterion is used to decide if line components in the spectrum are significant.

Once the significant line components have been identified, a residual time-series is constructed by subtracting the signal generated by the significant line components from the original time-series. The power spectrum of the residual time-series is then calculated using the multiple window method. Of course, with the power in the significant line components removed from the residual signal, its spectrum is much less prone to distortion by spectral leakage. Finally, the power in the significant line components is added to the spectrum of the residual time-series to give the overall spectral estimate.

A computer code to perform these calculations, MWPS (A. Chave, *pers. comm.*, 1999) is used for the non-parametric analysis of seafloor data in Chapter 4.

From the point of view of hydrothermal time-series, the multiple window method offers reasonable solutions to the two key problems which afflict seafloor data - shortness and noisiness. Firstly, by retaining the highest possible resolution in the frequency domain, it makes maximum use of the limited length of the dataset, unlike the band- and section-averaged periodogram methods. Secondly, by identifying significant line components, and removing them before calculating the background spectrum, it reduces the effect of spectral leakage from the powerful tidal harmonic lines into the surrounding spectrum.

The multiple window method is very well suited to the analysis of data with a tidal component. It is therefore surprising, and disappointing, that it seems to have been used only once for this purpose (Thomson *et al.,* 1986). Nonetheless, it is proposed here that it should be the non-parametric method of choice for all subsequent analysis of seafloor hydrothermal time-series.

3.3 Parametric analysis

Non-parametric analysis (Section 3.2) can be used to examine a time-series without prejudice as to its nature or cause. If non-parametric analysis suggests that the time-series may have a tidal component, the next step is to postulate a parametric model for the time-series and estimate the values of the parameters. The underlying objective is to extract as much useful information from the data as possible, given the parametric form assumed for the data. The choice of a particular parametric model is made according to the expected structure of the time-series. It must be remembered, therefore, that each parametric model contains an implicit set of assumptions, or prejudices, about the nature of the time-series.

The Harmonic Method (Section 3.3.1) relies on fewer assumptions than the Admiralty Method (Section 3.3.2). In a Harmonic Method decomposition, the sole assumption is that all tidal signals have spectral lines at the same discrete set of frequencies as the tidal potential. The disadvantage of the Harmonic Method is that a large number of harmonic constants must be estimated to yield a reasonably accurate description of the tidal signal. This requires a long time-series (~1 year or more) and so the Harmonic Method is unsuitable for the short time-series obtained at the seafloor.

In contrast, the Admiralty Method of Section 3.3.2 requires only 8 harmonic constants to describe a tidal signal, and the values of these parameters can be estimated from relatively short time-series (~7 days). However, these advantages come at the cost of making extra assumptions about the nature of tidal signals. In common with the Harmonic Method, it is assumed in the Admiralty Method that all tidal signals have harmonic lines at the same discrete set of tidal frequencies. In addition it is supposed that certain magnitude and phase relationships which hold between selected harmonic components of the tidal potential hold good for all other tidal signals. The Admiralty Method is very successful in describing the ocean tides in the world's ports, which suggests that these assumptions are justified.

The Bayesian method of drift removal, discussed in Section 3.3.3, relies on the assumption that the drift component of a time-series is smooth. It yields parameter estimates which are maximum likelihood estimates when the drift has a particular stochastic structure.

Finally, the Hybrid Method of Section 3.3.4 combines the ideas of the earlier sections in a new computer code (HYBRID) designed for the parametric analysis of tidal signals. The code decomposes a time-domain dataset into subsections and analyses each subsection separately. The code removes the non-tidal part of the data within each subsection in one of two ways, with the choice being made by the user. In the first method, the mean value of the subsection is removed. The Admiralty Method harmonic constants are then estimated by solution of the appropriate normal equations. In the second method, a Bayesian estimate of the non-tidal drift in the signal is made concurrently with the estimates of the Admiralty Method harmonic constants. The estimated Admiralty Method harmonic constants for each subsection are then combined in a robust manner (Chave *et al.,* 1987) to give an overall estimate of the tidal component of the original data signal.

3.3.1 The Harmonic Method

It is assumed in the Harmonic Method (Section 2.3.4) that an arbitrary tidal signal $\zeta(t)$ can be written as a sum of harmonic terms at the N tidal frequencies $\{\omega_1,\ldots,\omega_N\}$, plus an error term $\varepsilon(t)$:

$$\zeta(t) = \sum_{j=1}^{N} \hat{H}_j \cos\left(\omega_j t - \hat{g}_j\right) + \varepsilon(t) \tag{3.11}$$

Thus, given the set $\{\omega_1,\ldots,\omega_N\}$ *a priori*, equation (3.11) can be postulated as a parametric model for a time-series exhibiting tidal modulation. The set of harmonic constants $\{\hat{H}_1,\ldots,\hat{H}_N$

, $\hat{g}_1,\ldots,\hat{g}_N\}$ is then chosen to provide the best-fitting model for a given time-series. Usually, the harmonic constants are chosen to minimise the least-squares expression:

$$\int [\varepsilon(t)]^2 \, dt = \int \left[\zeta(t) - \sum_{j=1}^{N} \hat{H}_j \cos(\omega_j t - \hat{g}_j) \right]^2 dt \qquad (3.12)$$

The harmonic constants which minimise the error of equation (3.12) can be found directly by solving the appropriate normal equations (Press *et al.,* 1986).

Unfortunately, the Harmonic Method is not a good means of extracting tidal information from a short time-series, for the reasons outlined in Chapter 2. It is only possible to separate harmonic components at angular frequencies ω_1 and ω_2 with a time-series whose length exceeds $2\pi/(\omega_1-\omega_2)$. Consequently, a prohibitively long time-series is required to estimate the harmonic constants at a useful number of tidal frequencies.

3.3.2 The Admiralty Method

The Admiralty Method of tidal analysis represents a distinct improvement over the Harmonic Method for seafloor hydrothermal systems because it can extract reasonably accurate harmonic constants from much shorter time-series (Doodson & Warburg, 1941; Admiralty Tidal Handbook, No. 1; Admiralty Tidal Handbook, No. 3). There are, in fact, two related versions of the Admiralty Method, but only one of them is considered in detail here. The first version is the Annual Grouping Method (Admiralty Tidal Handbook, No.1) which is designed for use with time-series longer than one year. Hydrothermal time-series are rarely as long as this, so the Annual Grouping Method will not be considered further. The second version of the Admiralty Method (Admiralty Tidal Handbook, No.3) is designed for the analysis of time-series of one month's duration or less. It is this version of the method which is considered here.

Given a tidally modulated time-series $\zeta(t)$ the task is to derive a finite set of parameters which summarises the tidal information contained within the signal. In a Harmonic Method decomposition (Section 3.3.1), the time-series $\zeta(t)$ is written as the sum of N harmonic components, plus an error term $\varepsilon(t)$, as follows:

$$\zeta(t) = \sum_{j=1}^{N} \hat{H}_j \cos(\omega_j t - \hat{g}_j) + \varepsilon(t) \qquad (3.13)$$

It is conceptually useful to consider the sum in equation (3.13) to be a sum of N basis functions:

$$\left\{\hat{b}_j(t) = \cos(\omega_j t)\right\} \tag{3.14}$$

In equation (3.13), the basis functions of equation (3.14) are time-shifted by the phase-lags $\{\hat{g}_j\}$ and scaled by the amplitudes $\{\hat{H}_j\}$ to create a synthetic tidal signal. Consequently, it is the set of $2N$ numbers $\{\hat{H}_j,\hat{g}_j\}$ which describes the tidal component of the time-series $\zeta(t)$.
In the Admiralty Method, the tidal signal is written in a manner analogous to equation (3.13), as a sum of components, plus an error term $\varepsilon(t)$:

$$\zeta(t) = \sum_{j=1}^{4} H_j F_j(t)\cos\left(\phi_j(t) - g_j\right) + \varepsilon(t) \tag{3.15}$$

The advantage of the Admiralty Method is that it has only four basis functions, defined by:

$$\left\{b_j(t) = F_j(t)\cos\left(\phi_j(t)\right)\right\} \tag{3.16}$$

The functions $F_j(t)$ and $\varphi_j(t)$ are of great importance as they endow each Admiralty Method basis function with a degree of non-stationarity. The presence of $F_j(t)$ and $\varphi_j(t)$ in equation (3.16) shows that the Admiralty Method basis functions are not pure sinusoidal functions of time like the basis functions of the Harmonic Method (equation (3.14)). Rather, they might be described as *pseudo*-sinusoidal functions whose amplitude is modulated by the function $F_j(t)$ and whose phase is controlled by the function $\varphi_j(t)$. It is shown in Sections 2.3.1 – 2.3.3 that the tidal potential can be viewed as a non-stationary mixture of diurnal and semi-diurnal oscillations whose magnitude and phase vary according to the positions of the sun and moon. The functions $F_j(t)$ and $\varphi_j(t)$ are calculated from astronomical theory at any time t and impose the same astronomical non-stationarity on all functions which are linear combinations of Admiralty Method basis functions (equation (3.16)). Consequently, the use of the Admiralty Method basis functions ensures automatically that the expected astronomical non-stationarity is present in all tidal signals. Daily values of the functions $F_j(t)$ and $\varphi_j(t)$ – valid at 00h00 GMT - are published annually in Table VII of the Admiralty Tide Tables under the heading 'Tidal Angles and Factors'. The values at intermediate times are found by interpolation. The four Admiralty Method basis functions $\{b_1(t),b_2(t),b_3(t),b_4(t)\}$ are shown over a period of 20 days in 1994 in Figure 3.1

The parameters in an Admiralty Method decomposition are the amplitudes $\{H_1,...,H_4\}$ and phase-lags $\{g_1,...,g_4\}$ which must be applied to the four basis functions of equation (3.16). The parameter set $\{H_1,\ldots,H_4,g_1,\ldots,g_4\}$ describing the signal $\zeta(t)$ is usually chosen - according to a least-squares criterion - to minimise:

$$\int\left[\varepsilon(t)\right]^2 dt = \int\left[\zeta(t) - \sum_{j=1}^{4} H_j f_j(t)\cos\left(\phi_j(t) - g_j\right)\right]^2 dt \tag{3.17}$$

It is important to note the limits which are placed on the amplitudes and phase-lags. The amplitudes must be non-negative

$$H_j \in [0, \infty) \tag{3.18}$$

while the phase-lags are constrained as follows:

$$g_j \in [0, 2\pi) \tag{3.19}$$

This means that although the basis function $b_j(t)$ can be scaled arbitrarily (equation 3.18), it can only be shifted in phase by one cycle (equation 3.19).

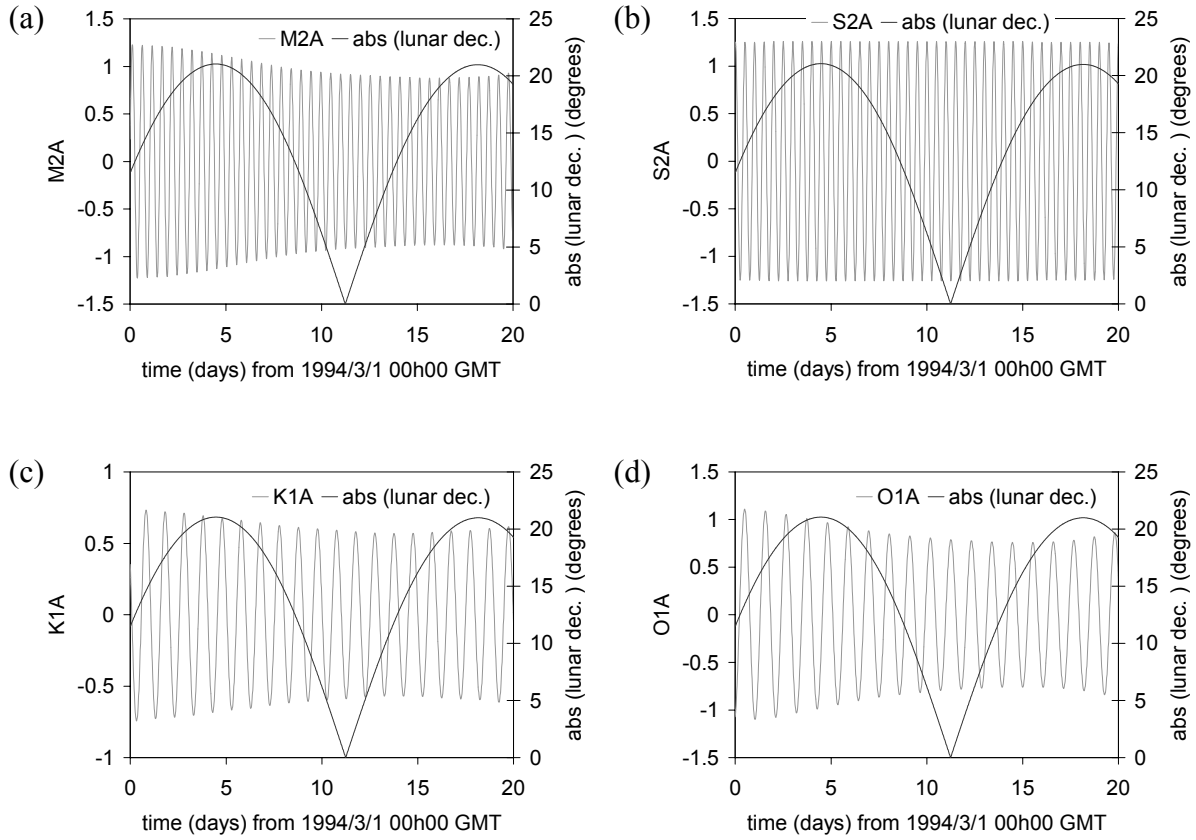

Figure 3.1: The four basis functions of the Admiralty Method (equation 2.16) as functions of time over a period of 20 days in 1994. The non-stationarity of these basis functions is controlled by the positions of the sun and the moon. The absolute lunar declination is shown for comparison. (a) The *M2A* basis function $b_1(t)$. (b) The *S2A* basis function $b_2(t)$. (c) The *K1A* basis function $b_3(t)$. (d) The *O1A* basis function $b_4(t)$.

It should be noted that in equation (3.19) the phase lag g_j is expressed in radians. The usual convention in the tidal literature (Doodson & Warburg, 1941) is to express angles in degrees. Both conventions are used in this dissertation.

3.3.2.1 Derivation of the Admiralty Method basis functions $\{b_j(t)\}$

The basis functions of the Admiralty Method (equation (3.16)) are derived from a subset of the basis functions of the Harmonic Method (equation (3.14)). Since the Admiralty Method is designed for use with time-series shorter than one month, it cannot extract harmonic constants equivalent to the long-period species of the Harmonic Method. The Admiralty Method is only capable of extracting information from the diurnal and semi-diurnal frequency bands. Under a Harmonic Method decomposition of the tidal potential, the most significant diurnal components are *K1* and *O1*, and the most significant semi-diurnal components are *M2* and *S2*. Each of these four principal components {*M2*,*S2*,*K1*,*O1*} is associated with a group of harmonic components with similar frequencies (Table 3.1). Consequently, the 20 most important Harmonic Method components are organised into four groups.

Admiralty Method component	Harmonic Method component	period (hours)	relative magnitude within group
M2A or $b_1(t)$	*2N2*	12.90	0.02534
	μ2	12.87	0.03057
	N2	12.66	0.19146
	ν2	12.63	0.03636
	M2	12.42	1.00000
	λ2	12.22	0.00738
	L2	12.19	0.02827
S2A or $b_2(t)$	*T2*	12.02	0.05861
	S2	12.00	1.00000
	K2	11.97	0.27215
K1A or $b_3(t)$	*π1*	24.13	0.01939
	P1	24.06	0.33093
	K1	23.94	1.00000
	φ1	23.81	0.01424
	J1	23.09	0.05591
O1A or $b_4(t)$	*2Q1*	28.02	0.02534
	σ1	27.84	0.03056
	Q1	26.87	0.19146
	ρ1	26.73	0.03637
	O1	25.83	1.00000

Table 3.1: The derivation and naming of the four Admiralty Method basis functions is based on four groups of Admiralty Method basis functions. Table from Admiralty Tidal Handbook, No.3.

The four Admiralty Method basis functions represent the overall, combined behaviour of the Harmonic Method components within each group in Table 3.1. For this reason, it is conceptually useful to refer to the four Admiralty Method basis functions $\{b_1,b_2,b_3,b_4\}$ by using the notation $\{M2A,S2A,K1A,O1A\}$. However, it is very important to stress the difference between the set $\{M2,S2,K1,O1\}$ of Harmonic Method basis functions and their Admiralty Method counterparts $\{M2A,S2A,K1A,O1A\}$. The former set consists of stationary, sinusoidal basis functions of the form $\left\{\hat{b}_j(t)=\cos(\omega t)\right\}$ (equation (3.14)). The latter set consists of the non-stationary, *pseudo*-sinusoidal basis functions $\left\{b_j(t)=F_j(t)\cos(\varphi_j(t))\right\}$.

In summary, the Admiralty Method of decomposing a tidal signal makes use of the fact that the astronomical motions of the sun and moon are well known and are expected to affect all tidal signals in a similar manner. This assumption allows tidal signals to be described by a set of 8 harmonic constants which can be extracted from reasonably short (~7 days) time-series

3.3.2.2 The information content of a tidal signal

Consider a (synthetic) tidal signal created using the 1200 components of the Tamura tidal potential catalogue (Tamura, 1987) by the ETGTAB code (Figure 3.2a). Admiralty Method harmonic constants can be extracted from the original data series (sampling interval Δt = 15 min, series length $N\Delta t$ = 7 days) according to the least-squares criterion of equation (3.17). The set of 8 Admiralty Method harmonic constants $\{H_1,\ldots,H_4,g_1,\ldots,g_4\}$ which are obtained can be expressed in complex number form by the set of 4 complex numbers $\{A_1,\ldots,A_4\}$, defined by:

$$\begin{cases}\mathrm{Re}(A_j)=H_j\cos(g_j)\\ \mathrm{Im}(A_j)=-H_j\sin(g_j)\end{cases} \tag{3.20}$$

The set of complex harmonic constants $\{A_1,\ldots,A_4\}$ can then be graphed in the complex plane and labelled according to the corresponding basis functions $\{M2A, S2A, K1A, O1A\}$ (Figures 3.2b,c). The magnitudes $\{H_1,\ldots,H_4\}$ of the components are represented graphically by the length of the phasors. The phase lags $\{g_1,\ldots,g_4\}$ are represented by the angles, measured positive *anticlockwise*, between the real axis and the phasor. It is important to stress the

physical meaning of these phase lags. They represent the phase lag of each component relative to the corresponding component of the tidal potential on the Greenwich meridian. The time-series analysed in Figure 3.2 is an estimate of the tidal potential on the 30°W meridian. Semi-diurnal components of the tidal potential travel westwards round the globe at 30° per hour, while diurnal components of the tidal potential travel westwards at 15° per hour. This explains why the semi-diurnal components have phase lags of 60° (Figure 3.2b) while the diurnal components have phase lags of 30° (Figure 3.2c). This illustrates an important feature of Admiralty Method harmonic constants.

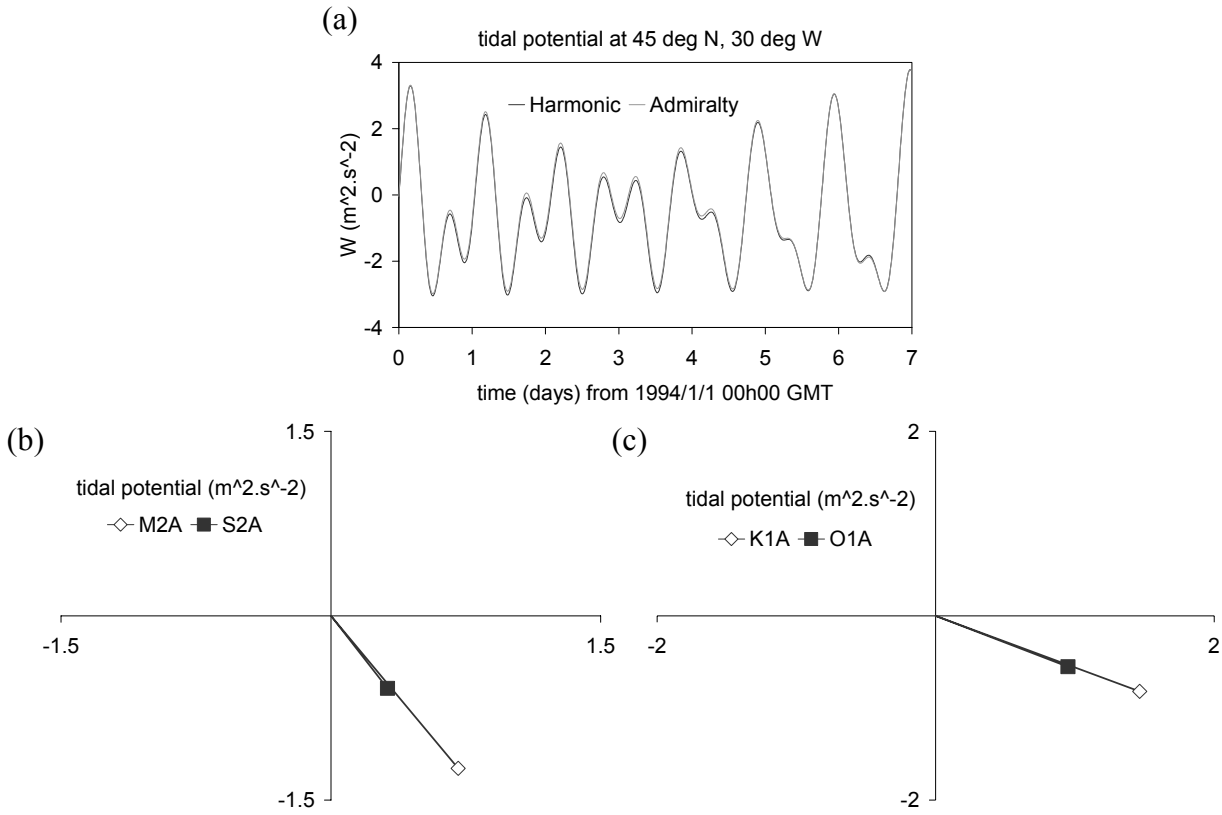

Figure 3.2: The extraction of Admiralty Method harmonic constants from a tidal potential generated using 1200 components of a Harmonic Method decomposition. (a) The tidal potentials generated by the Harmonic Method and the Admiralty Method in the time domain. (b) The semi-diurnal Admiralty Method harmonic constants in the complex plane. (c) The diurnal Admiralty Method harmonic constants in the complex plane. Original time-series generated using the ETGTAB code.

For the tidal potential and the solid tide, the Admiralty Method harmonic constants have distinctive phase lags. The phase lags for the diurnal components (g_3 and g_4) equal the

westward longitude, while those for semi-diurnal components (g_1 and g_2) equal twice the westward longitude. As a consequence, it is a striking feature of the diagrams that the two semi-diurnal components have the same phase lag (i.e. $g_1 = g_2$ in Figure 3.2b), and the two diurnal components have the same phase lag (i.e. $g_3 = g_4$ in Figure 3.2c). In general these phase lag equalities do not occur for the ocean tide (Figure 3.3). Consequently, if plots of the Admiralty Method harmonic constants for a time-series show that $g_1 \approx g_2$ and $g_3 \approx g_4$ then this constitutes evidence that the time-series is more closely correlated to the solid tide than the ocean tide.

It is of interest to compare the original time-series generated by the Harmonic Method harmonic constants $\{\hat{H}_1,\ldots,\hat{H}_{1200},\hat{g}_1,\ldots,\hat{g}_{1200}\}$ with the time-series generated by the Admiralty Method harmonic constants $\{H_1,\ldots,H_4,g_1,\ldots,g_4\}$ (Figure 3.2a). The time-series generated by the 8 parameters of the Admiralty Method does not match the original perfectly, but the fit is nonetheless remarkably good. It is tempting to conclude that a parametric description with 2400 degrees of freedom has been replaced by a parametric description with 8 degrees of freedom, but this is not so. The harmonic decomposition of a *tidal* signal into N Harmonic Method components does not have $2N$ degrees of freedom, because certain magnitude and phase relationships always hold between some of the components for all tidal signals. This should not be too surprising. The working definition of a tidal signal is 'a time-series whose fundamental physical cause is the tidal potential'. It is shown in Section 2.3 that the harmonic decomposition of the tidal potential is derived from the simpler long-period/diurnal/semi-diurnal decomposition. The essence of the Admiralty Method is the assumption that the astronomical motions of the sun and moon impose the same constraints on all tidal signals. It must be stressed that this is only a hypothesis, but it is one that has been shown to be justified in the many applications of the Admiralty Method to the description of ocean tides in the world's ports.

Figure 3.3 shows the Admiralty Method harmonic constants extracted from an estimate of the ocean tide at 45°N, 30°W. The estimate of the ocean tide is made using the CSR code which is based on the results of satellite altimetry (Schrama & Ray, 1994). Figure 3.3a shows that the 8 Admiralty Method harmonic constants reproduce the original signal remarkably well. Figures 3.3b,c demonstrate that the phase lags for the ocean tide are not generally as simple as those for the solid tide (Figures 3.2b,c). For the ocean tide, it is not generally true that $g_1 \approx g_2$ or $g_3 \approx g_4$.

3.3.2.3 Astronomical and intrinsic non-stationarity

By definition, every tidal signal is the output from some physical system whose input is the tidal potential. The tidal potential exhibits astronomical non-stationarity due to the motions of the sun and moon (Sections 2.3.1 – 2.3.3). Consequently, if the physical mechanism linking the tidal potential to the observable time-series does not change over time, it is to be expected that the observable time-series will exhibit the same astronomical non-stationarity.

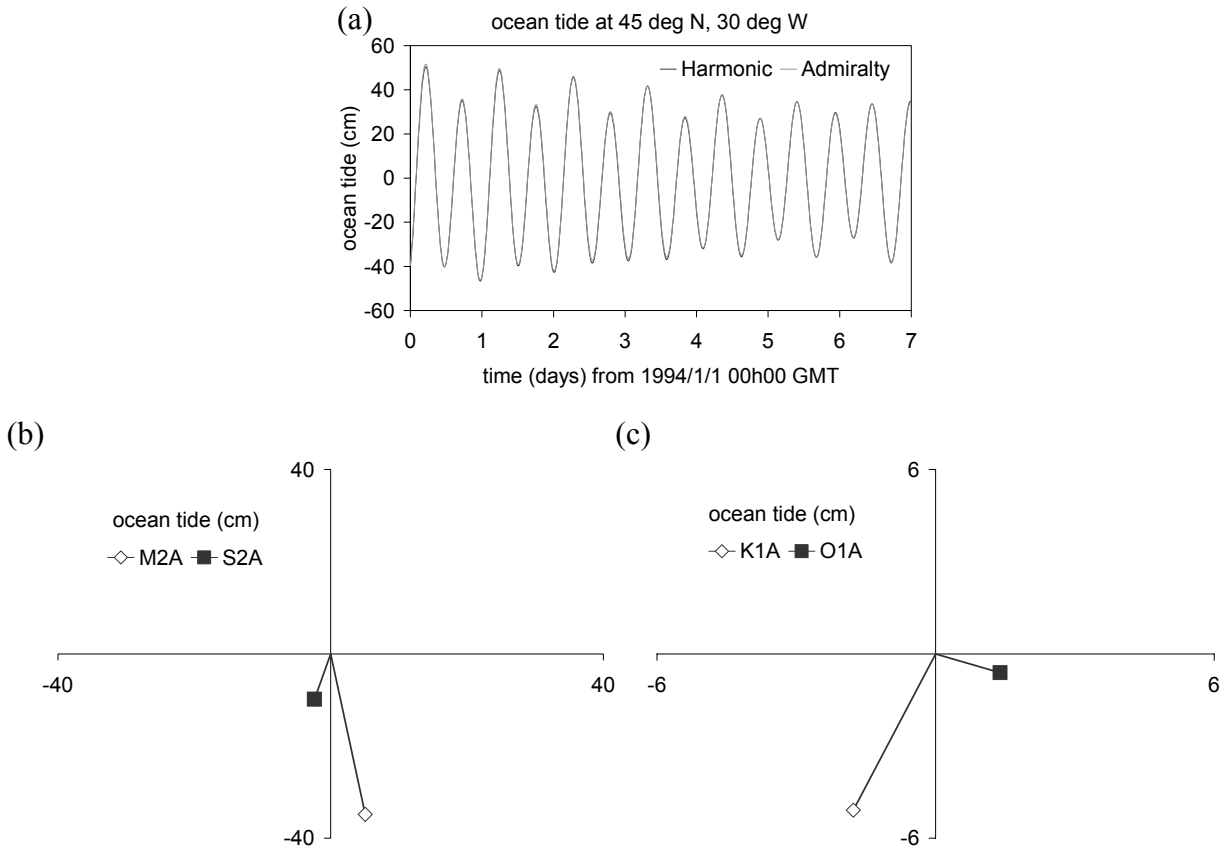

Figure 3.3: The extraction of Admiralty Method harmonic constants from an estimate of the ocean tide generated from a Harmonic Method decomposition. (a) The ocean tide signals generated by the Harmonic Method and the Admiralty Method in the time domain. (b) The semi-diurnal Admiralty Method harmonic constants in the complex plane. (c) The diurnal Admiralty Method harmonic constants in the complex plane. Harmonic Method ocean tide time-series generated using the CSR code.

Astronomical non-stationarity is easily predicted from astronomical formulae and is explicitly accommodated in the basis functions of the Admiralty Method (equation (3.16)). As an example, consider the parametric analysis of a tidal signal of two weeks duration. The time-series could be split into disjoint sections, each a week long, which are to be analysed separately. The set of $2N$ parameters extracted in a Harmonic Method decomposition $\{\hat{H}_1,\ldots,\hat{H}_N\ ,\ \hat{g}_1,\ldots,\ \hat{g}_N\}$ changes from one week to the next because of the astronomical non-stationarity induced by declinational changes (Figure 2.3). However, an Admiralty Method decomposition yields the *same* set of 8 parameters $\{H_1,\ldots,H_4,g_1,\ldots,g_4\}$ for both weeks. For this reason, the Admiralty Method is immune to astronomical non-stationarity.

However, there is a second type of non-stationarity which might be present in a time-series, to which the Admiralty Method is not immune. This can be labelled intrinsic non-stationarity, and occurs if the physical mechanism linking the tidal potential to the observable time-series is *itself* subject to change over the observation interval. For example, if the observable time-series is the temperature of hydrothermal effluent, a change in seafloor hydrology could lead to a change in the spectral character of the temperature signal. Other examples would be drift caused by an erratic instrumental power supply, or by hydrothermal precipitation on seafloor sensors.

If a time-series dataset is split into subsections, each can be analysed separately using the Admiralty Method. If the harmonic constants obtained from these analyses change significantly between the subsections, it can be surmised that there is an intrinsic non-stationarity in the time-series.

3.3.2.4 Robustification of the Admiralty Method

Since hydrothermal time-series are noisy, it is of interest to consider how the estimation of Admiralty Method harmonic constants could be made more robust. In general a data section of ~7 days length is sufficient to yield accurate estimates of the Admiralty Method harmonic constants. Consequently, a time-series longer than ~7 days can be split into shorter subsections for which the Admiralty Method harmonic constants are estimated separately. Chave *et al.* (1987) suggest a manner in which power spectrum estimates from the separate subsections can be combined in a robust manner to yield an overall estimate. Their method is here adapted to the case of estimating Admiralty Method harmonic constants. As an example, consider the estimation of the (complex) harmonic constant A_1 associated with the *M2A* component (equation (3.20)). Suppose that the original time-series is split into M

subsections, and that the estimate of A_1 obtained from the m^{th} subsection is labelled $A_{1,m}$. The technique of Huber weighting can be used to derive an overall estimate from the set $\{A_{1,m}\}$ of estimates obtained from the separate subsections. The real and imaginary parts of A_1 are estimated in the same manner, and so estimation of the real part only is described here. Firstly, the median μ and interquartile distance σ of the set $\{\mathrm{Re}(A_{1,m})\}$ are calculated. (The median and interquartile distance are robust equivalents of the mean and standard deviation). The scaled distance of the m^{th} estimate from the median is given by:

$$x_m = \frac{\mathrm{Re}\left(A_{1,m}\right) - \mu}{\sigma} \tag{3.21}$$

The purpose of the robustification is to downweight the influence on the overall estimate of outlier subsection estimates for which $\left|x_m\right|$ is large. Consequently a set of weights $\{w_m\}$ is defined by:

$$\begin{aligned} w_m &= 1 && \left|x_m^2\right| \le k \\ w_m &= \sqrt{\frac{2k}{\left|x_m^2\right|} - \frac{k^2}{x_m^2}} && \left|x_m^2\right| > k \end{aligned} \tag{3.22}$$

Chave *et al.* (1987) suggest that k = 1.5 gives good results. The overall estimate of the real part of the harmonic constant is then given by:

$$\mathrm{Re}\left(A_1\right) = \sum_{m=1}^{M} w_m \,\mathrm{Re}\left(A_{1,m}\right) \tag{3.23}$$

Furthermore, this robust section averaging technique can be used to estimate jack-knife confidence limits for the estimate $\mathrm{Re}(A_1)$ on the assumption that the real and imaginary parts of A_1 are normally distributed.

Robust estimates of Admiralty Method harmonic constants are made using this technique for the data presented in Chapter 4. For sufficiently long time-series, robust section averaging is used and 95% confidence limits can be placed on the harmonic constants in the complex plane.

3.3.3 Drift Removal by Bayesian methods

In many cases, the time-series obtained from a hydrothermal system appears to be the sum of three separate signals - a tidal signal, a background drift signal and residual high frequency noise. For example, the temperature measurements obtained at TAG on the Mid-Atlantic Ridge (Schultz *et al.,* 1996) show tidal variations of ~0.5 °C superimposed on a slow drift whose amplitude is ~10 °C. (Figure 4.11). It is desirable to have a well-defined method of decomposing a time-series into a drift signal, a parametrised tidal signal and residual error. An interesting method, whose heuristic justification relies on techniques from Bayesian

statistics, is proposed by Tamura *et al.* (1991). In their original method, the tidal signal is represented parametrically by a Harmonic Method decomposition. In order to apply their method to short hydrothermal time-series, it is adapted here to incorporate an Admiralty Method decomposition. Accordingly, what follows is a summary of the theory presented by Tamura *et al.* (1991) and Akaike (1980), modified where necessary to incorporate the Admiralty Method.

Suppose that the time-series to be analysed consists of the data $\{x_1,\ldots,x_N\}$, collected at times $\{t_1,\ldots,t_N\}$. The objective is then to estimate a drift signal $\{d_1,\ldots,d_N\}$ and a set of Admiralty Method harmonic constants $\{H_1,\ldots,H_4,g_1,\ldots,g_4\}$ which generate a tidal signal $\{\zeta_1,\ldots,\zeta_N\}$ according to:

$$\zeta_i = \sum_{j=1}^{4} H_j F_j(t_i)\cos\left(\phi_j(t_i) - g_j\right) \tag{3.24}$$

Consequently, the original time-series $\{x_1,\ldots,x_N\}$ can be decomposed into a tidal signal (ζ_i), a drift signal (d_i), and a residual error signal (ε_i) as follows:

$$x_i = \zeta_i + d_i + \varepsilon_i \tag{3.25}$$

It is reasonable to demand two properties of the extended parameter set $\{d_1,\ldots,d_N,H_1,\ldots,H_4,g_1,\ldots,g_4\}$ which is to be estimated from the data $\{x_1,\ldots,x_N\}$. Firstly, the drift $\{d_i\}$ should be smooth, and secondly the resulting error $\{\varepsilon_i\}$ should be small. The smoothness of the drift is quantified by the expression:

$$\sum_{i=3}^{N} \left| d_i - 2d_{i-1} + d_{i-2} \right|^2 \tag{3.26}$$

A small value of this quantity is desirable to ensure that the drift is smooth.

The size of the error can be quantified by the expression:

$$\sum_{i=1}^{N} \left|\varepsilon_i\right|^2 = \sum_{i=1}^{N} \left| x_i - d_i - \zeta_i \right|^2 \tag{3.27}$$

A small value of this quantity is desirable to ensure that the error is small.

In order to achieve the simultaneous requirements of smooth drift and small error, the extended parameter set $\{d_1,\ldots,d_N,H_1,\ldots,H_4,g_1,\ldots,g_4\}$ is obtained by finding the values which minimise the penalised least-squares expression:

$$\sum_{i=1}^{N} \left| x_i - d_i - \zeta_i \right|^2 + \nu^2 \sum_{i=3}^{N} \left| d_i - 2d_{i-1} + d_{i-2} \right|^2 \tag{3.28}$$

Equation (3.28) shows that the relative importance of smooth drift and small error is controlled by a hyperparameter ν whose value must be chosen before the least-squares

solution is found. (Later, an analogy with Bayesian statistics will provide an explicit criterion for selecting the optimal value of v.)

The penalised least squares minimisation of equation (3.28) can be written in matrix form by defining an extended data vector $\underline{X}$ (of dimension $2N$-2), and an extended parameter vector $\underline{P}$ (of dimension N+8) as follows:

$$\underline{X} = \begin{pmatrix} x_1 \\ \vdots \\ x_N \\ 0 \\ \vdots \\ 0 \end{pmatrix} \quad , \quad \underline{P} = \begin{pmatrix} d_1 \\ \vdots \\ d_N \\ H_1 \cos(g_1) \\ H_1 \sin(g_1) \\ \vdots \\ H_4 \cos(g_4) \\ H_4 \sin(g_4) \end{pmatrix} = \begin{pmatrix} \underline{d} \\ \underline{\theta} \end{pmatrix} \tag{3.29}$$

For later convenience the vector $\underline{P}$ is split into two parts: $\underline{d}=(d_1,\ldots,d_N)$ and $\underline{\theta}=(H_1\cos(g_1),\ldots,H_4\sin(g_4))$. It should be noted that the set of Admiralty Method harmonic constants $\{H_1,\ldots,H_4,g_1,\ldots,g_4\}$ is easily recovered from the elements of $\underline{\theta}$. Therefore the vector $\underline{d}$ represents the drift signal while the vector $\underline{\theta}$ represents the parameters which generate the estimated tidal part of the signal.

The N-by-8 matrix T is defined by:

$$T = \begin{bmatrix} f_1(t_1)\cos(\phi_1(t_1)) & f_1(t_1)\sin(\phi_1(t_1)) & \cdots & f_4(t_1)\cos(\phi_4(t_1)) & f_4(t_1)\sin(\phi_4(t_1)) \\ \vdots & \vdots & \ddots & \vdots & \vdots \\ f_1(t_N)\cos(\phi_1(t_N)) & f_1(t_N)\sin(\phi_1(t_N)) & \cdots & f_4(t_N)\cos(\phi_4(t_N)) & f_4(t_N)\sin(\phi_4(t_N)) \end{bmatrix} \tag{3.30}$$

The (N-2)-by-N matrix D is defined by:

$$D = \begin{bmatrix} 1 & -2 & 1 & & 0 \\ & 1 & -2 & 1 & \\ & & \ddots & \ddots & \ddots \\ 0 & & & 1 & -2 & 1 \end{bmatrix} \tag{3.31}$$

The (2N-2)-by-(N+8) matrix A is defined by:

$$A = \begin{bmatrix} I_N & T \\ vD & O \end{bmatrix} \tag{3.32}$$

where I_N is the N-by-N identity matrix and O is an (N-2)-by-8 matrix of zeroes.

It then follows that the solution $\underline{P}^*=(\underline{d}^*,\underline{\theta}^*)$ of the penalised least squares minimisation of equation (3.28) is the value of $\underline{P}$ which minimises the matrix norm:

$$\left\| A\underline{P} - \underline{X} \right\|^2 \tag{3.33}$$

For a given value of the hyperparameter v, the solution $\underline{P}^*$ which minimises this norm can be found explicitly by constructing and solving the appropriate normal equations (Press *et al.,* 1986). The solution is:

$$\underline{P}^* = \left(A^T A\right)^{-1} A^T \underline{X} \tag{3.34}$$

A criterion for deciding the optimal value of the hyperparameter v is now constructed by analogy with Bayesian statistics.

Consider the idealised case where the drift can be represented stochastically by an integrated random walk. Suppose that the $\{E_I\}$ is a set of random variables, drawn independently from a zero-mean normal distribution of variance σ^2/v^2. The drift is then given by:

$$d_i = 2d_{i-1} + d_{i-2} + E_i \tag{3.35}$$

In the language of Bayesian statistics, equation (3.32) defines a prior distribution for the drift signal, given by:

$$\pi\left(\underline{d}|\sigma^2, v\right) = \left(\frac{1}{2\pi\sigma^2}\right)^{N/2} \left(\det\left(v^2 D^T D\right)\right) \exp\left(\frac{-v^2}{2\sigma^2} \underline{d}^T \left(D^T D\right) \underline{d}\right) \tag{3.36}$$

It is now supposed that the error terms $\{\varepsilon_i\}$ of equation (3.25) are drawn independently from a zero-mean normal distribution of variance σ^2. It follows that the data distribution is proportional to:

$$f\left(\underline{x}|\underline{d}, \sigma^2, v, \underline{\theta}\right) = \exp\left(\frac{-1}{2\sigma^2} \left\|\underline{x} - \underline{d} - T\underline{\theta}\right\|^2\right) \tag{3.37}$$

From equations (3.36) and (3.37), the posterior distribution for the data $\underline{x}$ is proportional to:

$$\begin{aligned} &f\left(\underline{x}|\underline{d}, \sigma^2, v, \underline{\theta}\right) \pi\left(\underline{d}|\sigma^2, v\right) = \\ &\left(\frac{1}{2\pi\sigma^2}\right)^{N/2} \left(\det\left(v^2 D^T D\right)\right) \exp\left(\frac{-1}{2\sigma^2} \left(\left\|\underline{x} - \underline{d} - T\underline{\theta}\right\|^2 + \left\|vD\underline{d}\right\|^2\right)\right) \end{aligned} \tag{3.38}$$

Given the stated assumptions, it is reasonable to define estimates of σ^2 and $\underline{\theta}$ which maximise the posterior likelihood (equation (3.38)) to be optimal. It can be shown that equation (3.38) is maximised with respect to $\underline{\theta}$ and σ^2 by setting $\underline{\theta}=\underline{\theta}^*$ (the solution from equation (3.34)) and by setting $\sigma^2 = \sigma_B^2$, where σ_B^2 is defined by:

$$\sigma_B^2 = \frac{1}{N} \left\|A\underline{P}^* - \underline{X}\right\|^2 \tag{3.39}$$

Consequently:

$$\begin{aligned} &f\left(\underline{x}|\underline{d}, \sigma_B^2, v, \underline{\theta}^*\right) \pi\left(\underline{d}|\sigma_B^2, v\right) = \\ &\left(\frac{1}{2\pi\sigma_B^2}\right)^{N/2} \left(\det\left(v^2 D^T D\right)\right)^{1/2} \exp\left(\frac{-N}{2}\right) \exp\left(\frac{-1}{2\sigma_B^2} \left(\underline{d} - \underline{d}^*\right)^T \left(I + v^2 D^T D\right) \left(\underline{d} - \underline{d}^*\right)\right) \end{aligned} \tag{3.40}$$

Finally, the posterior marginal likelihood $L(\nu)$ is defined by integrating equation (3.40) with respect to $\underline{d}$:

$$L(\nu) = \int f\left(\underline{x}|\underline{d}, \sigma_B^2, \nu, \underline{\theta}^*\right)\pi\left(\underline{d}|\sigma_B^2, \nu\right)d\underline{d} \tag{3.41}$$

It can be shown that:

$$L(\nu) = \left(\frac{1}{2\pi\sigma_B^2}\right)^{N/2}\left(\det\left(\nu^2 D^T D\right)\right)^{1/2}\left(\det\left(I + \nu^2 D^T D\right)\right)^{-1/2}\exp\left(\frac{-N}{2}\right) \tag{3.42}$$

The optimal value of the hyperparameter ν is now to defined to be the value which *maximises* the posterior marginal likelihood $L(\nu)$ of equation (3.42). Equivalently, the optimal value of ν is the value which *minimises* the quantity -2log($L(\nu)$), defined by:

$$-2\log\left(L(\nu)\right) = N + N\log\left(2\pi\sigma_B^2\right) + \log\left(\det\left(I + \nu^2 D^T D\right)\right) - \log\left(\det\left(\nu^2 D^T D\right)\right) \tag{3.43}$$

When comparing different values of the hyperparameter ν in a particular problem, equation (3.31) shows that the matrix D remains unchanged. It follows that $\log(\det(\nu^2 D^T D)) = N\log(\nu^2) + constant$ in equation (3.43). Consequently, the optimal value of ν in a particular problem is defined to be the value which minimises the quantity:

$$ABIC(\nu) = N + N\log\left(2\pi\sigma_B^2\right) + \log\left(\det\left(I + \nu^2 D^T D\right)\right) - N\log\left(\nu^2\right) \tag{3.44}$$

The quantity $ABIC(\nu)$ is known as 'Akaike's Bayesian Information Criterion' (Tamura *et al.,* 1991).

In practice, a computer can be programmed to vary the value of ν, obtaining a solution from equation (3.34) each time, until the least value of $ABIC(\nu)$ is found. The final estimate of the drift $\underline{d}$ and the Admiralty Method harmonic constants $\underline{\theta}$ are the solutions obtained from equation (3.34) when ν minimises $ABIC(\nu)$.

3.3.4 The HYBRID code – a parametric method for analysing tidal data

The ideas of the previous sections are combined in a new method of parametric analysis, which is specifically designed to extract tidal information from hydrothermal time-series. This method is implemented by the new HYBRID code which is used for parametric data analysis in Chapter 4.

The HYBRID code is designed to estimate Admiralty Method harmonic constants from hydrothermal time-series. For sufficiently long time-series, the time-series is split into separate subsections which are analysed independently. For the analysis of tidal signals, a subsection length of 1 week is often used as this is sufficiently long to allow accurate estimates to be made of the four complex harmonic constants $\{A_1, A_2, A_3, A_4\}$ (equation

(3.20)). In order to make clear their meaning, these harmonic constants are labelled according to the Admiralty Method basis function to which they correspond {*M2A*, *S2A*, *K1A*, *O1A*}. The HYBRID code analyses the individual data subsections in one of two ways, with the choice being made by the user. The first method is labelled 'mean removal', and involves the subtraction of the mean value of the subsection before the harmonic constants are estimated. This technique is simple and works well when the time-series does not suffer from excessive drift. The second method is labelled 'Bayesian drift removal'. This technique (Section 3.3.3) is much more computationally intensive, and is designed to decompose the time-series into (1) a smooth drift signal, (2) a tidal signal generated by the Admiralty Method harmonic constants, and (3) residual noise. Use of this method in Chapter 4 suggests that it works very well when the time-series follows closely the parametric form assumed in Section 3.3.3. However, for very noisy time-series, better results are obtained by using 'mean removal' in each subsection.

Finally, the harmonic constants estimated for each subsection are combined using Huber weighting to yield an overall robust estimate for the Admiralty Method harmonic constants. 95% jackknife confidence limits are provided for these estimates on the assumption that the real and imaginary parts of the harmonic constants are independently normally distributed.

3.4 Conclusions

The aim of this chapter is to explain the techniques for analysing hydrothermal time-series which are implemented in Chapter 4.

The first test of a time-series is to examine it in the time domain. In many cases diurnal and semi-diurnal periodicities are immediately apparent and it can be suspected that the time-series is tidally modulated. It is of interest to decide whether the tidal modulations are caused by the ocean tide or the solid tide and so it may be useful to graph these 'input signals' alongside the data signal in the time domain.

The next stage in the investigation of a time-series is to obtain a non-parametric estimate of its frequency spectrum. In the past, many authors have used the periodogram to estimate the power spectrum of seafloor time-series in order to establish whether it is tidally modulated. It is argued here, in Section 3.2.1, that the periodogram is an extremely bad estimator of the true power spectrum and should not be used. It is suggested instead that the multiple window method of Thomson (1982) should be used in the non-parametric analysis of tidal signals in

seafloor hydrothermal systems. Consequently, the MWPS code (A. Chave, *pers. comm.*, 1999) is used in Chapter 4 to obtain spectral estimates for hydrothermal time-series. This code incorporates an explicit method for the identification of significant line components in the spectrum. If significant line components are identified at the known tidal frequencies (in particular at ~1.93 cpd corresponding to the *M2* component) then it can be concluded with confidence that the time-series is tidally modulated.

In the cases where non-parametric analysis reveals tidal modulation of the time-series, a parametric analysis can be attempted in order to summarise the nature of the tidal signal. It is suggested that the Admiralty Method is the optimal parametric description of tidal signals since it requires only 8 harmonic constants to describe an arbitrary tidal signal. Furthermore, the harmonic constants for any time-series can be extracted from a fairly short data section of ~7 days. The Admiralty Method is able to describe tidal signals using so few parameters because much of the information content of a tidal signal is due to the well known astronomical motions of the sun and moon and is the same for *all* tidal signals.

A new computer code – HYBRID – for the parametric analysis of tidally modulated signals is described (Section 3.3.4). The HYBRID code is designed to estimate the Admiralty Method harmonic constants of a tidally modulated signal. It incorporates a Bayesian technique for drift removal (Section 3.3.3) and robust section averaging (Section 3.3.2.4). The HYBRID code is used extensively in Chapter 4 to quantify the tidal part of a number of seafloor time-series.

The (complex) harmonic constants extracted from a time-series using the Admiralty Method can be plotted in the complex plane for ease of interpretation. In Chapter 4, the harmonic constants of a seafloor time-series are compared with the harmonic constants of the solid and ocean tides in order to establish whether the ocean tide or the solid tide is responsible for the tidal modulation of the time-series.

Chapter 4: Evidence of tidal modulation at seafloor hydrothermal systems

4.1 Introduction

Over the last twenty years, many attempts have been made to acquire time-series measurements at seafloor hydrothermal systems. The aims and techniques of these studies are diverse, as are the locations at which the data were collected. There is no reason to suppose - *a priori* - that the same physical process causes the tidal modulation in all of these data. Nonetheless, in order to obtain an overview of tidal modulation in hydrothermal systems, it is useful to collate all of the published seafloor time-series which have been examined with tidal effects in mind. Consequently this chapter is devoted to an examination of the current evidence concerning tidal modulation of seafloor hydrothermal systems

The data which have been collected on the seafloor cover a wide range of hydrothermal sites. Accordingly, the time-series discussed in this chapter are classified into sections according to seafloor location. There are several further ways in which the datasets can be distinguished. Measurements have been made (1) above the seafloor, (2) on the seafloor and (3) below the seafloor. Furthermore, the settings for the measurements cover (1) high temperature vents (350°C - 400°C), (2) areas of warm diffuse flow (typically <50°C), and (3) cooler regions on the ridge flanks. At the most fundamental level, the various time-series can be classified according to the physical quantity which they record. Broadly, the four physical quantities which have been measured with tidal influence in mind are – (1) pressure, (2) temperature, (3) effluent velocity, and (4) fluid composition.

Pressure measurements at the seafloor have been made by Sato *et al.* (1995) and Fujioka *et al.* (1997) who used a hydrophone to measure pressure pulses. The pressure pulses are taken to be indicators of hydrothermal activity and their frequency of occurrence is correlated with the ocean tides. The other pressure data discussed below were made in sealed boreholes (Davis & Becker, 1994; Davis *et al.,* 1995; Davis & Becker, 1999) and are a measure of the fluid pressure in igneous rock lying below a layer of comparatively impermeable sediment. Although it is desirable to have direct time-series measurements of the ambient pressure on the seafloor, this information is rarely collected at hydrothermal sites. Consequently the

seafloor pressure in the open oceans is often estimated by an ocean tide model such as the CSR code (Schrama & Ray, 1994).

The measurements of temperature discussed below were obtained in a wide variety of settings. Firstly, below the seafloor, time-series of temperature have been collected at depths of up to 400 m within boreholes (Davis & Becker, 1994; Davis *et al.,* 1995; Davis & Becker, 1999). Temperatures have also been measured within 1 m of the seafloor using geothermal probes (Kinoshita *et al.,* 1996, 1998). Secondly, on the seafloor, there have been measurements of the temperature of diffuse effluent (Schultz *et al.,* 1992; Schultz *et al.,* 1996), the temperature of mussel beds around hydrothermal vents (Johnson *et al.,* 1994; Chevaldonné *et al.,* 1991), and the temperature of the hydrothermal vents themselves (Fornari *et al.,* 1998). Thirdly, above the seafloor, time-series of temperature have been collected in the water column at hydrothermal vent sites. The location of these measurements ranges from 3 cm above diffuse flow (Little *et al.,* 1988, 1989), to over 100 m above sites of focussed discharge (Wetzler *et al.,* 1998; Rudnicki *et al.,* 1994). Measurements have also been made at a lateral distance of a few metres from black smokers, at a height of 2 m above the seafloor (Fujioka *et al.,* 1997).

The measurements of the velocity of hydrothermal effluent discussed below were made using the Medusa hydrothermal effluent monitoring system (Schultz *et al.,* 1992; Schultz *et al.,* 1996) on areas of diffuse hydrothermal flow (<100°C).

Time-series measurements of the composition of hydrothermal effluent can take several forms. Firstly, the optical transmissivity of the water can be measured in order to estimate the turbidity or quantity of suspended particulate matter (Johnson & Tunnicliffe, 1985; Fujioka *et al.,* 1997). Secondly, chemical samples of effluent fluid can be collected at successive times for later analysis in the laboratory (Kadko, 1994; Cooper, 1999; Cooper *et al.,* 2000).

The aim of this chapter is to quantify the tidal signals observed in datasets obtained at seafloor hydrothermal systems. The observable signals (pressure, temperature, effluent velocity and effluent composition) are considered to be the output signals from a physical process whose inputs are the solid tide, the ocean tide and tidal streams. Where sufficient data are available the analysis of each output signal follows a strict sequence. Firstly, the

time-series is plotted alongside an estimate of the local ocean tide. For clean data, the tidal modulation of the output signal is sometimes immediately apparent in the time-domain. Secondly, a non-parametric estimate of the power spectrum of the time-series is made using the MWPS code. This procedure contains a statistical test for the presence of significant line components in the spectrum. Evidence for tidal modulation of the time-series is provided by the presence of line components at the known tidal frequencies (Table 2.1, Figure 2.7). For a tidally modulated time-series, the strongest line component is expected to occur at the *M2* frequency (1.932 cpd). Thirdly, if the time-series displays evidence of tidal modulation, a parametric estimate of the tidal component of the time-series can be made. The HYBRID code (Section 3.3.4) is used to estimate the Admiralty Method harmonic constants which describe the tidal component of the signal.

One of the objectives of this chapter is to establish which of the input signals (ocean tide, solid tide, tidal streams) causes the tidal modulation observed in the output signals (pressure, temperature, effluent velocity, composition). To this end, the estimated Admiralty Method harmonic constants for the output signal are compared with those for the solid and ocean tides. It should be noted that the Admiralty Method harmonic constants for the ocean and solid tides are obtained with negligible error. Synthetic time-series for the ocean tide can be generated by the CSR code, while time-series for the tidal potential are generated by the ETGTAB code. The solid tide is simply a scaled version of the tidal potential, by equation (2.18). The Admiralty Method harmonic constants for the input signals are then obtained by analysing the synthetic time-series with the HYBRID code. In contrast, the harmonic constants for the output time-series are known to much lower precision because the time-series are contaminated by noise.

In summary, this chapter contains a detailed and critical study of all reported tidally modulated time-series observed at seafloor hydrothermal systems. The separate data sets are compared with the tidal potential and the ocean tide in an attempt to uncover a coherent picture of tidal modulation in hydrothermal systems. It should be stressed that not all hydrothermal time-series display evidence of tidal modulation (Fornari *et al.,* 1998). However, there is no doubt that tidal modulation of hydrothermal systems does occur in many cases, and there is considerable interest in discovering the mechanism (or mechanisms) which causes this modulation.

4.2 Juan de Fuca Ridge

Several time-series measurements have been made at hydrothermal sites on the Juan de Fuca Ridge off the northwestern coast of the USA where the ocean tides have a significant diurnal component. The Admiralty Method harmonic constants at the Endeavour Segment (47.8°N, 129.0°W) are typical; those for the tidal potential and ocean tide are listed in Table 4.1 and graphed in Figure 4.1.

Endeavour	H_1 (*M2A*)	g_1 (*M2A*)	H_2 (*S2A*)	g_2 (*S2A*)	H_3 (*K1A*)	g_3 (*K1A*)	H_4 (*O1A*)	g_4 (*O1A*)
potential ($m^2.s^{-2}$)	1.28	257°	0.60	257°	1.60	129°	1.13	129°
ocean (m)	0.89	240°	0.26	272°	0.42	243°	0.26	226°

Endeavour	$(H_1+H_2)/(H_3+H_4)$	H_1/H_2	g_2-g_1	H_3/H_4	g_4-g_3
potential ($m^2.s^{-2}$)	0.687	2.14	< 1°	1.41	< 1°
ocean (m)	1.69	3.42	32°	1.62	-17°

Table 4.1: The Admiralty Method harmonic constants for the tidal potential and the ocean tide at the Endeavour Segment (47.8°N, 129.0°W). Estimates made using the HYBRID code.

4.2.1 Endeavour Segment (1)

The first seafloor time-series from a seafloor hydrothermal system to exhibit tidal modulation were obtained at a low temperature (56°C) vent on the Endeavour Segment (47.8°N, 129.0°W) of the Juan de Fuca Ridge (Johnson & Tunnicliffe, 1985). A camera was placed next to the vent and still photographs were obtained at a sampling interval of Δt = 42 min over a period $N\Delta t$ = 5 days. The photographs were analysed to produce estimated time-series of lateral water motions and the suspended particulate load or turbidity. The time-series of seafloor current was inferred from the deflection of vestimentiferan worms in the photographs. Johnson & Tunnicliffe (1985) report that this current is semi-diurnal and 'nearly in phase' with the semi-diurnal component of the ocean tide. Their spectral analysis of this inferred current data reveals a large semi-diurnal peak at about 1.90 cpd, but no evidence of a diurnal peak. Two further time-series - of suspended particulate load - were estimated by measuring the transmittance of light through the photographic slides. These two turbidity time-series - labelled *A* and *B* - were obtained from different regions of the photographs. Johnson & Tunnicliffe's (1985) spectral analysis of the first turbidity time-series (*A*) suggests that it was predominantly diurnal. Consequently, they infer a spectral

contrast between the *diurnal* variations in turbidity and the *semi-diurnal* variations in current, concluding that there is no causal link between turbidity and seafloor current.

It is instructive to re-examine this conclusion in the light of the theory discussed previously (Chapters 2 and 3). The first step is to consider the nature of the ocean tide at the vent site. The Admiralty Method harmonic constants for this site are given in Table 4.1, and graphed in Figure 4.1.

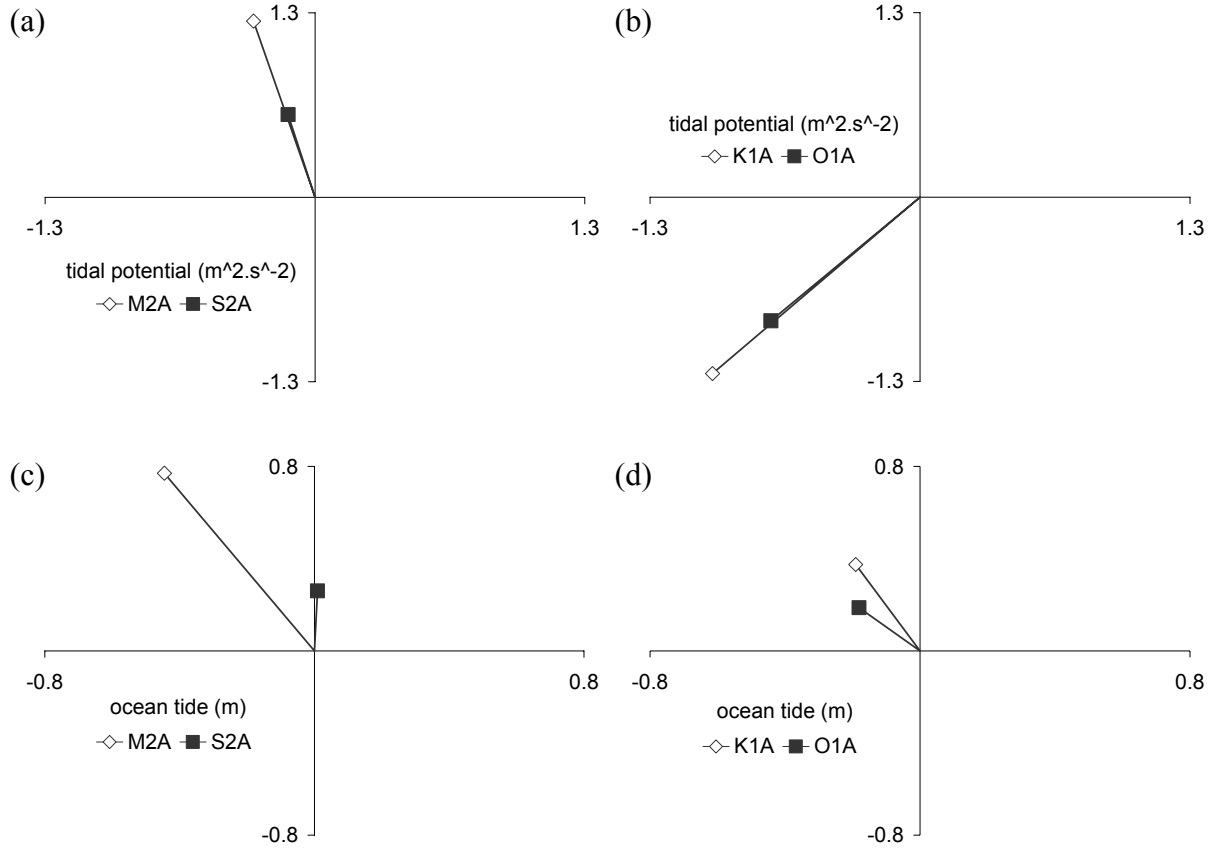

Figure 4.1: The (complex) Admiralty Method harmonic constants of the tidal potential and ocean tide at the Endeavour Segment (47.8°N, 129.0°W) extracted using the HYBRID code.

The harmonic constants show that the ocean tide at the Endeavour Segment has a significant diurnal component. The next step is to consider the nature of the tide over the observation period (from 1984/9/1 to 1984/9/6). Figure 4.2b shows that the lunar declination was relatively large at this time, and so the tide would have been *particularly* diurnal in character. This is confirmed in the time-domain view of the ocean tide at the time the observations were made (Figure 4.2a).

The two particulate load signals (*A*, *B*) are reproduced in Figure 4.2a together with a prediction of the ocean tide. Johnson and Tunnicliffe (1985) do not publish a prediction of the ocean tide for the observation period, but claim that the 'turbidity maxima are in phase

with the relevant component of the ocean surface elevation'. It is hard to discern strong evidence of this claim in Figure 4.2a.

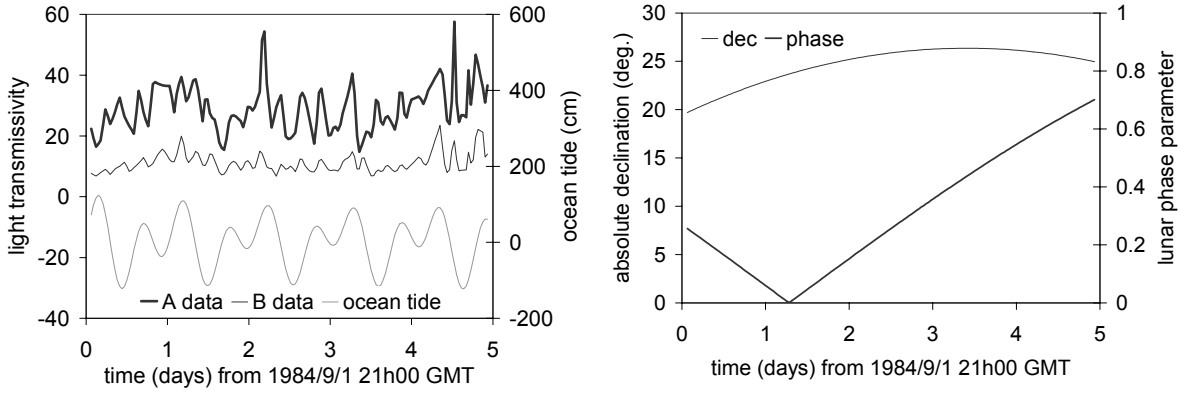

Figure 4.2: (a) Light transmissivity data (*A*, *B*) collected at the Endeavour Segment (47.8°N, 129.0°W) by Johnson & Tunnicliffe (1985). The local ocean tide is shown for comparison. (b) The lunar phase parameter, and absolute lunar declination for the same period, calculated using the CSR code.

A power spectrum estimate for the first turbidity time-series (*A*) is given by Johnson & Tunnicliffe (1985) but there is no discussion of the method by which it was obtained. The power spectra shown in Figure 4.3 were obtained from the turbidity time-series using two different methods and illustrate how the choice of spectral estimator influences the estimated spectrum (Section 3.2). The upper spectrum in Figure 4.3 is an unwindowed periodogram of the data following subtraction of the mean (Equation 3.1). The lower spectrum in Figure 4.3 was obtained using the MWPS code with a time-bandwidth product of 1 and 2 eigenspectra. An autoregressive pre-whitening filter of length 36 points (25.2 hours) was applied, and lines significant above the 95% level were removed. A significant line was found for the frequency bin at 1.948 ± 0.130 cpd. This frequency range encompasses the *M2* tidal component at 1.932 cpd. No significant lines were found in the diurnal band.

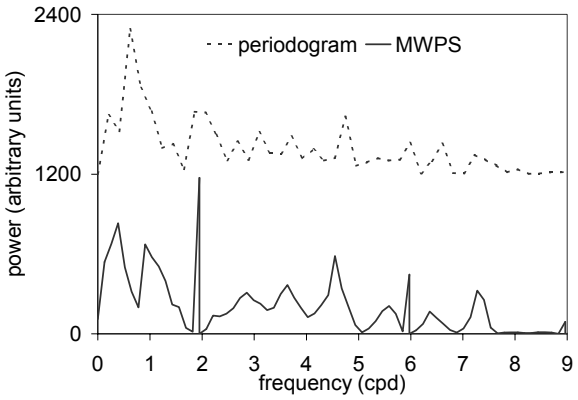

Figure 4.3: Power spectra for the turbidity time-series (*A*) (Johnson & Tunnicliffe, 1985) obtained using an unwindowed periodogram, and the MWPS code. For clarity, the periodogram estimate is offset by 1200 units on the vertical axis.

Figure 4.3 shows that the choice of spectral estimator has a profound effect on the estimated spectrum. The unwindowed periodogram estimate appears to have a greater concentration of power in the diurnal frequency band in agreement with the conclusions of Johnson & Tunnicliffe (1985). In constrast, the MWPS estimate has a statistically significant line component in the semi-diurnal band, but no significant line components in the diurnal band. The assertion that the turbidity time-series is predominantly diurnal can therefore be challenged. Figure 4.2a shows that the turbidity time-series (*A*) exhibits strong semi-diurnal oscillations in the time-domain, while the high lunar declination (Figure 4.2b) suggests that diurnal signals were at their strongest during the observation period. It is therefore likely that the time-series would appear even more strongly semi-diurnal at times of smaller lunar declination.

In summary, a re-examination of the data using the multiple window method casts doubt on the assertion that the turbidity signal is predominantly diurnal (Johnson & Tunnicliffe, 1985), and the subsequent conclusion that the turbidity and lateral currents are unconnected. It may simply be that the observed changes in turbidity are due to lateral current motions.

4.2.2 Endeavour Segment (2)

Time-series measurements of effluent temperature and velocity were obtained on the Endeavour Segment (47.95°N, 129.10°W) between 1988/7/15 and 1988/9/2 by Schultz *et al.* (1992). The measurements were made on an area of warm (7°C to 13°C) diffuse flow, where

the vertical effluent velocities ranged from 0.07 to 0.15 $m.s^{-1}$. Schultz *et al.* (1992) used a robust section-averaging method (Chave *et al.,* 1987) to estimate power spectra for the temperature and velocity signals. The spectra reveal a significant semi-diurnal peak for the temperature time-series. In contrast, the power spectrum of the velocity time-series appears 'white' with no obvious spectral peaks. It is suggested here that the choice of a section-averaged periodogram as the non-parametric spectral estimator (Section 3.2.1.6) may have a significant bearing on the spectra obtained. The data were collected at a sampling interval Δt=5 min, and a total of N=12,107 data points were used in the spectral analysis. Thus, the total length of the analysed time-series is about 42 days. However, in order to use a section-averaging approach, Schultz *et al.* (1992) were forced to divide the time-series into shorter subsections. They decomposed the series into five overlapping sections of 3,766 points, each of which spans a time interval of about 13 days. The disadvantage of this approach is that these short data subsections lead to decreased resolution in the frequency domain (Section 3.2).

It is therefore suggested that a higher resolution estimate of the power spectra would be obtained by applying the MWPS method of Section 3.2.2 to the data of Schultz *et al.* (1992).

4.2.3 Middle Valley

The boreholes of the Ocean Drilling Program (ODP) provide a number of tidally modulated time-series at seafloor hydrothermal systems (Davis & Becker, 1999). These boreholes have a diameter of 30 cm and are typically drilled to extend several hundred metres below the seafloor. The boreholes considered here are drilled in sedimented ridge-crest and ridge-flank environments. Consequently, the upper sections of the boreholes (corresponding to the sediment layer) are lined with cement to prevent hydraulic communication between the borehole and the sediment. The lower sections of the boreholes (corresponding to the igneous basement layer) are left open. Vertical arrays of thermistors are lowered into the boreholes to measure the temperature at selected depths, and a pressure sensor is placed near the top of each borehole. The tops of the boreholes are sealed to prevent hydraulic communication with the ocean, and time-series of pressure and temperature are collected. For each borehole, the pressure time-series is a measure of the pressure in the basement rock, since the cement lining isolates the borehole from the ocean and the sediment layer. Davis & Becker (1999) note that it can take more than a year for the pressure and temperature in a borehole to reach steady state. However, in addition to such long period trends in the time-series, there are also clear tidal signals.

Time-series of pressure and temperature were collected at ODP holes 857D and 858G (48.45°N, 128.72°W) in the Middle Valley of the Juan de Fuca ridge (Davis & Becker, 1994). Three weeks of data were collected at 857D in September 1991. No tidal modulation of temperature was observed, but the pressure variations were seen to be in phase with the local ocean tide and attenuated by a factor of 0.15. Davis & Becker (1994) explain this pressure data by appealing to the theory of poroelasticity, which is discussed in detail in Chapter 6. Hole 858G yielded 10 months of data beginning at September 1991. Again, there was a clear tidal modulation of the pressure signal, which was observed to be in phase with the local ocean tide. However, in this case, the pressure signal was attenuated by a factor which varied between 0.18 and 0.70 over the observation interval. All of the thermistor time-series displayed evidence of tidal modulation with a typical magnitude of 1°C. For all thermistors (i.e. all depths within the borehole) except one, the lowest temperatures occurred when the seafloor pressure was high. In contrast, the 'anomalous' thermistor recorded high temperatures when the seafloor pressure was high. In other words, for all thermistors except one the subseafloor temperature lags the ocean tide by 180°. One of the explanations proposed by Davis & Becker (1994) is that water is driven up the borehole when the seafloor pressure is high. Normally, the temperature can be expected to increase with depth below the seafloor and so it is argued that peak upflow will generally be associated with high temperatures. Davis & Becker (1994) suggest that the 'anomalous' thermistor lies in a region of inverse thermal gradient. The suggestion that high temperatures should coincide exactly with peak upflow is challenged in Chapter 6. In Section 6.3.1.3 an analytical poroelastic model is used to suggest that high temperatures lag the vertical velocity by a phase angle in the range [45°, 90°]. However this model also predicts that seafloor temperatures lag the ocean tide by an angle in the range [135°, 225°] which is consistent with the observations of Davis & Becker (1994).

Johnson (1998) reports measurements showing tidal modulation in the conductive heat flow through the seafloor at the Baby Bare Seamount (47.7°N, 127.8°W) which lies on the flank of the Juan de Fuca Ridge. The mean heat flow measured with a thermal blanket was found to be 7 $W.m^{-2}$, and bottom water temperatures were found to vary with a quarter-diurnal period. (This variation may be due to quarter-diurnal variations in the magnitude of the tidal stream as discussed in Section 2.6). The time-series of seafloor heat flow also displays tidal modulation. After the effect of the quarter-diurnal variations in bottom water temperature are

removed, there still remains a semi-diurnal heat flow variation of ±0.1 $W.m^{-2}$ which is attributed to the tidal modulation of the flow beneath the seafloor.

4.2.4 Cascadia Accretionary Prism

Borehole data have been collected on the Cascadia accretionary prism, at ODP hole 892B (44.68°N, 125.12°W) (Davis *et al.,* 1995). Pressure and temperature time-series were obtained for the first 10 months of 1993. The temperature time-series show no evidence of tidal modulation, but the pressure within the sealed hole exhibits distinct tidal periodicity. The pressure signal leads the local ocean tide by 0.3 hours, and is attenuated by a factor of 0.5. Davis *et al.* (1995) show that these observations are consistent with the presence of a layer containing 2% free gas lying above the open section of the borehole. The presence of gas alters the elastic response of the layer and leads to the phase shift, according to the theory of poroelasticity (Van der Kamp & Gale, 1983; Wang & Davis, 1996; Wang *et al.,* 1998). In Chapter 6, a similar investigation of the effect of spatially varying elastic parameters below the seafloor is presented, but with the difference that the spatial variation in elastic properties is caused by the temperature structure of a subseafloor convection cell (Chapter 5), rather than the presence of gas-bearing layers.

A feature of the time-series obtained below the seafloor in boreholes is the purity of the tidal modulation. In contrast, temperature time-series obtained above the seafloor tend to contain a lot of high-frequency noise in addition to any tidal modulation. It is possible that turbulent water motions just above the seafloor lead to this high frequency 'hiss' which often frustrates attempts to make reliable parametric estimates of the tidal modulation. However, the remarkable lack of noise in some of the subseafloor temperature measurements (Davis & Becker, 1994; Davis & Becker, 1999) means that these data would be very well suited to analysis by the Admiralty Method and the HYBRID code (Chapter 3).

4.2.5 The Pipe Organ Site and the Kolmogorov Hypothesis

Temperature measurements in the water column were made by Wetzler *et al.* (1998) at a location 100 m south of the Pipe Organ vent site on the Juan de Fuca Ridge (44.97ºN, 130.21ºW). The data were collected from a vertical instrument array tethered to a seafloor mooring. Water temperature was recorded at heights of 135 m, 165 m and 195 m above the seafloor, and lateral ocean currents were recorded by a sensor 164.5 m above the seafloor. The data span a period of 111 hours between 1997/9/24 and 1997/9/29. Wetzler *et al.* (1998) explain their observations with an advection-diffusion model suggesting that the plume from

the Pipe Organ vent is carried across their instrument array by the ocean currents. From the point of view of this dissertation, it is the possible presence of tidal signals in the time-series which is of interest. When viewed in the time-domain, the current and temperature time-series seem to exhibit a semi-diurnal periodicity. However, when Wetzler *et al.* (1998) calculated windowed periodograms of their time-series they discovered 'no indication of distinct spectral peaks'. It is suggested that use of the superior MWPS spectral estimator might reveal significant spectral lines at the principal tidal frequencies.

An interesting feature of the power spectra obtained by Wetzler *et al.* (1998) is their overall shape, or slope. The spectra lack any obvious peaks, but take the approximate form:

$$\hat{S}(f) = Af^{B} \quad \Leftrightarrow \quad \log\left(\hat{S}\right) = \log(A) + B\log(f) \tag{4.1}$$

for suitable constants A and B. (The value of B represents the slope of the spectrum when viewed on a log-log plot). The three temperature time-series collected at Pipe Organ yielded the values –1.53, –1.72, –1.76 for B. Wetzler *et al.* (1998) note that these values are close to the value of –5/3 suggested by the 'Kolmogorov hypothesis' (Phillips, 1966; Turner, 1973; Phillips 1991a). This hypothesis concerns the power spectrum of the velocity field of a turbulent fluid. If the turbulence is isotropic, dimensional analysis suggests that there is a frequency range over which the power spectrum of the velocity decays as $f^{-5/3}$. Data consistent with the Kolmogorov hypothesis have been found by measuring seawater temperature with a sensor towed behind a ship (Grant *et al.,* 1962). Similar isotropic turbulence might be expected to occur near a seafloor vent in the presence of oceanic currents. A temperature sensor near a hydrothermal vent experiences a relative flow of turbulent water in a manner analogous to the ship-towed sensors of Grant *et al.* (1962). For this reason, the overall shape of estimated power spectra is compared with the predictions of the Kolmogorov hypothesis in the following sections. Consequently, both the low- and high-frequency parts of power spectra obtained from seafloor data are of interest. The low-frequency section is examined for evidence of line components at the tidal frequencies while the high-frequency tail is compared with the predictions of the Kolmogorov hypothesis.

4.3 Gulf of California

4.3.1 Introduction

The hydrothermal activity in the Gulf of California is unique among the sites considered here because it occurs in a gulf rather than an open ocean. In the context of processes linked to the

ocean tides, this is significant because the ocean tide in a gulf may consist of standing waves, while the tide in the open oceans is always composed of travelling waves (Section 2.6). The phase relationship between the ocean tide and the associated tidal streams is therefore different for gulfs than for the open oceans, and care must be exercised when estimating tidal streams from an estimate of the ocean tide.

In Section 4.3.2, a seafloor temperature time-series collected by Little *et al.* (1988) is re-examined in the light of this observation. Little *et al.* (1988) correlated this time-series with a simplistic prediction of the seafloor currents. By making use of the theory of tidal streams (Section 2.6), a more sophisticated estimate of the likely seafloor currents is made.

4.3.2 Guaymas Basin

Little *et al.* (1988, 1989) collected a seafloor temperature time-series in the Guaymas Basin, Gulf of California (27°00'N, 111°24'W), using a thermistor placed 3 cm above an area of diffuse hydrothermal flow. The authors note that the local ocean tide is predominantly diurnal, but that the temperature time-series exhibits semi-diurnal periodicity. The tidal modulations in temperature are therefore unusual in demonstrating a frequency-doubling compared with the local ocean tide. (Other temperature time-series displaying semi-diurnal periodicity tend to occur in areas where the ocean tide is itself predominantly semi-diurnal.) Little at al. (1988) present a model to explain these data in which the thickness of the thermal boundary layer on the seafloor varies according to the magnitude of the tidal stream. The tidal stream is assumed to be proportional to the time derivative of the ocean tide at the town of Guaymas, located 100 km from the hydrothermal site. It is important to note the two assumptions inherent in this model – (1) that the ocean tide at the hydrothermal site is assumed to be the same as that on the coast, and (2) that the tidal streams are assumed to be given by the time derivative of the ocean tide. Both of these assumptions are open to question. The validity of the first assumption is examined in Table 4.3 and Figure 4.4.

The ocean tide at the town of Guaymas (27°55'N, 110°54'W) is predicted using Admiralty Method harmonic constants (Admiralty Tide Tables, Vol. 4). The harmonic constants published by the Admiralty refer to local time at Guaymas, which is 7 hours behind GMT. The waves of the tidal potential travel westwards around the Earth at an angular speed of ~15º per hour (diurnal components) and ~30º per hour (semi-diurnal components). Consequently, the published harmonic constants are here normalised to GMT by adding 105º to the phase-lags of the diurnal components and 210º to the phase-lags of the semi-diurnal components (Figure 4.4a,b).

The harmonic constants for the hydrothermal site itself (27°00'N, 111°24'W) are derived from a synthetic time-series created by the CSR code. Table 4.3 and Figure 4.4 show that the diurnal components of the tide vary little between the town of Guaymas and the hydrothermal site, but there is a slight difference in the phase of the semi-diurnal components. The time-domain graph gives a direct comparison of the two ocean tides over the period of the measurements (Figure 4.4e). The two tides are broadly similar, but the tide at the hydrothermal site has more pronounced double high waters in the first half of the time period.

Gulf of California	H_1 (*M2A*)	g_1 (*M2A*)	H_2 (*S2A*)	g_2 (*S2A*)	H_3 (*K1A*)	g_3 (*K1A*)	H_4 (*O1A*)	g_4 (*O1A*)
Ocean tide (m) at town of Guaymas	0.14	165°	0.11	137°	0.28	179°	0.19	176°
Ocean tide (m) at hydrothermal site	0.215	115°	0.153	120°	0.277	179°	0.178	167°

Gulf of California	$(H_1+H_2)/(H_3+H_4)$	H_1/H_2	g_2-g_1	H_3/H_4	g_4-g_3
Ocean tide (m) at town of Guaymas	0.532	1.273	-28°	1.474	-3°
Ocean tide (m) at hydrothermal site	0.809	1.405	5°	1.556	-12°

Table 4.2: Admiralty Method harmonic constants for the ocean tide at the town of Guaymas (27°55'N, 110°54'W) and at the Guaymas Basin hydrothermal site (27°00'N, 111°24'W).

The second assumption of Little *et al.* (1988, 1989) - that tidal streams are proportional to the time derivative of sea surface height - is examined below. The ocean tide $\zeta(t)$ can be written in terms of Admiralty Method harmonic constants $\{H_1,\ldots,H_4, g_1,\ldots,g_4\}$ as follows:

$$\zeta(t) = \sum_{j=1}^{4} H_j F_j(t) \cos\left(\phi_j(t) - g_j\right) \tag{4.2}$$

On a timescale of a few days, the factors $\{F_j(t)\}$ are approximately constant as functions of time, while the phases $\{\varphi_j(t)\}$ are approximately linear functions of time: $\varphi_j(t) \approx \omega_j t$. Thus:

$$\zeta(t) \approx \sum_{j=1}^{4} H_j F_j \cos\left(\omega_j t - g_j\right) \tag{4.3}$$

and so:

$$\frac{d\zeta}{dt} \approx \sum_{j=1}^{4} -\omega_j H_j F_j \sin\left(\omega_j t - g_j\right) = \sum_{j=1}^{4} \omega_j H_j F_j \cos\left(\omega_j t - \left(g_j - \frac{\pi}{2}\right)\right) \tag{4.4}$$

Equation (4.4) shows that if the ocean tide $\zeta(t)$ has harmonic constants $\{H_j, g_j\}$, then its time derivative has harmonic constants $\{\omega_j H_j, g_j - \pi/2\}$.

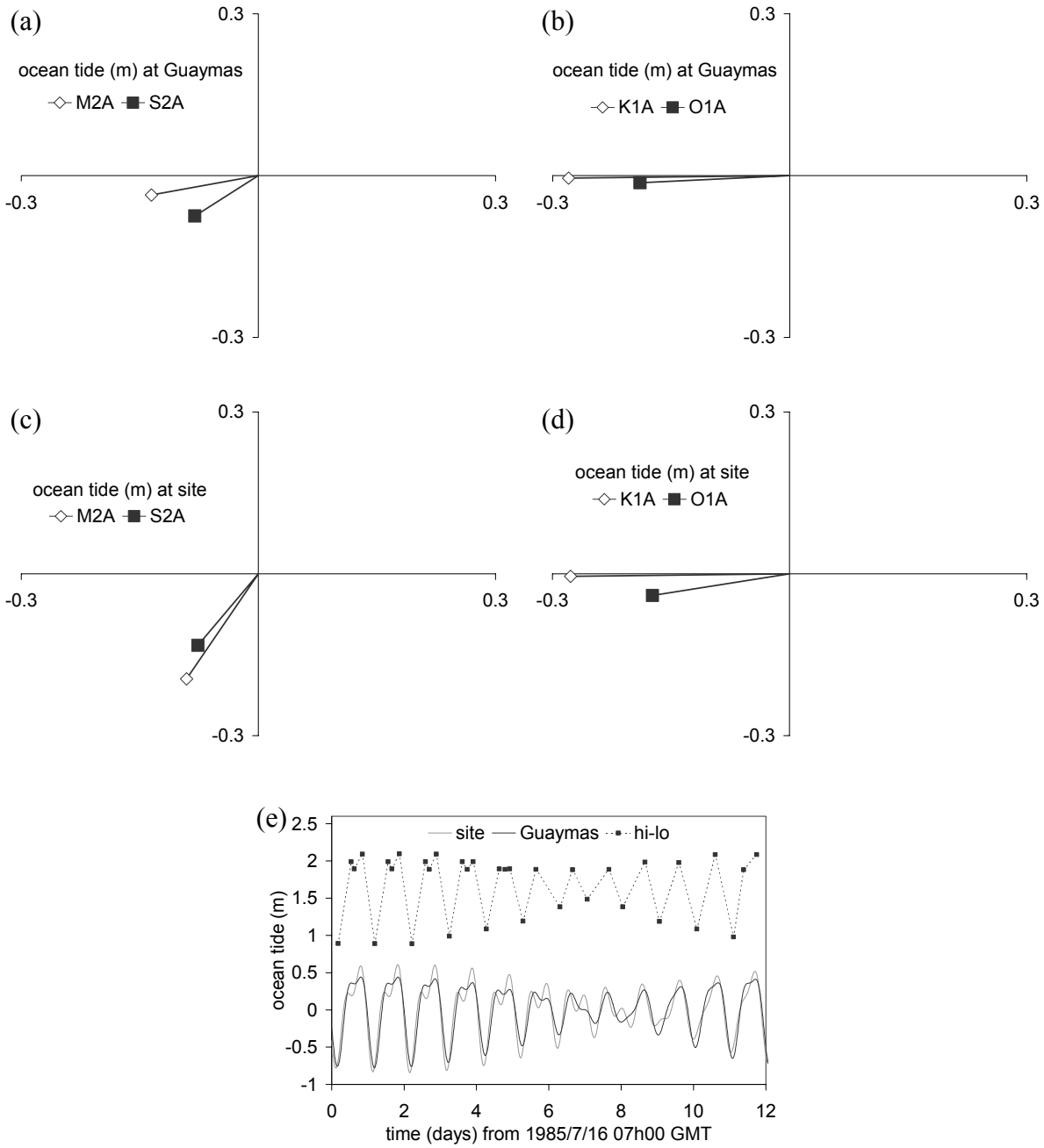

Figure 4.4: The ocean tide at the Guaymas Basin hydrothermal site (27.00°N, 111.40°W), and the town of Guaymas (27.92°N, 110.90°W). (a) – (d) Admiralty Method harmonic constants. (e) Time-domain representation *site* - ocean tide at the hydrothermal site predicted by the CSR code. *Guaymas* – ocean tide at the port of Guaymas from harmonic constants published in tide tables. *hi-lo* – the high and low water points for the port of Guaymas quoted by Little *et al.* (1988, 1989).

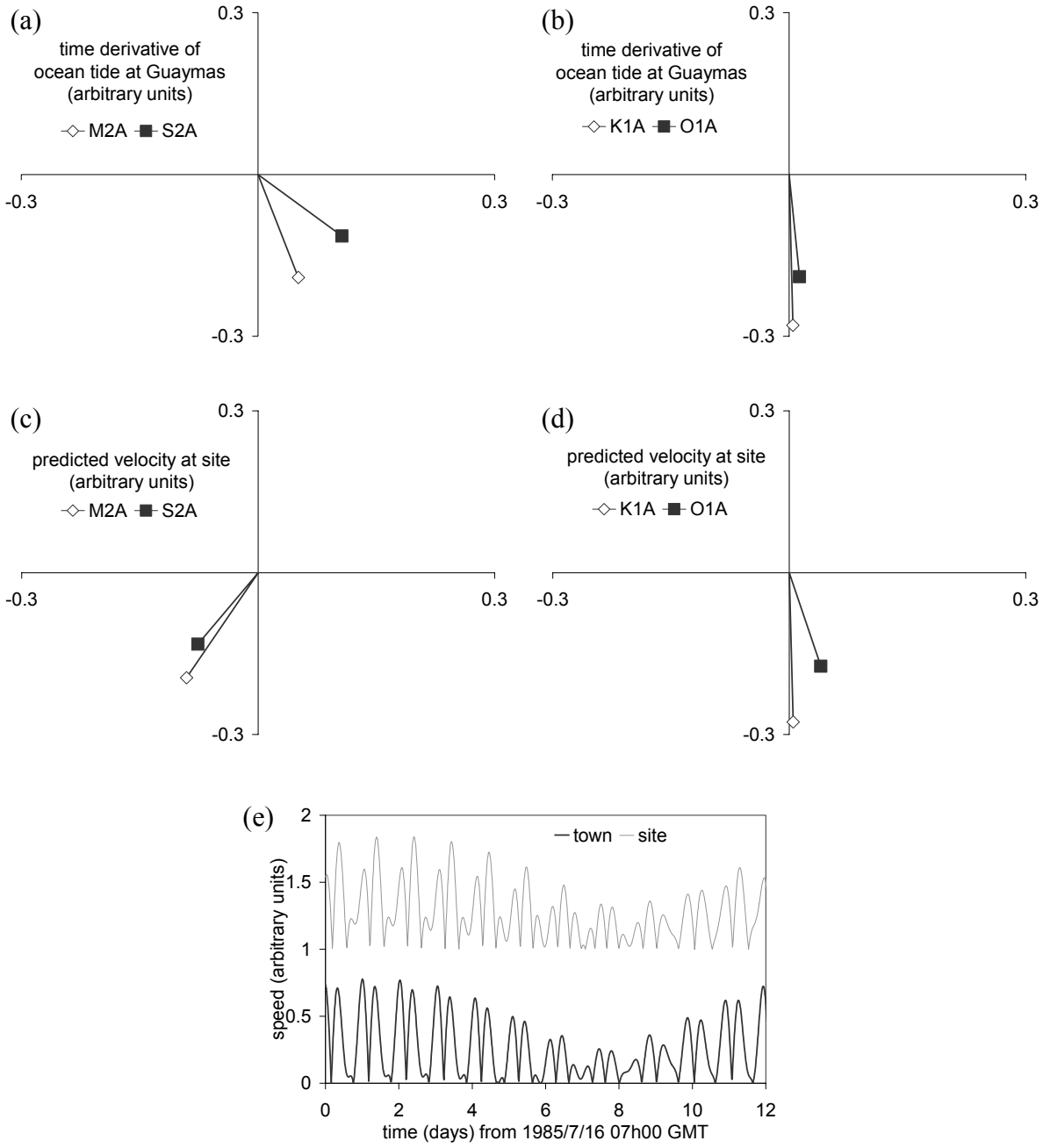

Figure 4.5: Predicted tidal streams at the Guaymas Basin hydrothermal site (27.00°N, 111.40°W), calculated according to the theory of Chapter 2, and at the town of Guaymas (27.92°N, 110.90°W), calculated according to the theory used by Little *et al.* (1988). (a) – (d) Admiralty Method harmonic constants. (e) Time-domain representation. For clarity, the speed for the hydrothermal site is offset by 1 unit on the vertical axis.

In other words, taking a time derivative reduces the phase lag of each component by $\pi/2$ radians (or 90º), and scales the magnitude of each component by its approximate angular frequency ω_j. Therefore the process of differentiation acts as a *high-pass filter*, in which the magnitudes of the semi-diurnal components are doubled relative to the magnitudes of the diurnal components. Figure 4.5 shows harmonic constants for the time derivative of the tidal height at the town of Guaymas, calculated in this way, and expressed in arbitrary units. In other words, the harmonic constants in Figure 4.5a,b were derived from the harmonic constants of the ocean tide at the town of Guaymas (Figure 4.4a,b; Table 4.3) by subtracting 90º from all phase-lags and the doubling the magnitudes of the semi-diurnal components to account for the high-pass filtering. The resulting harmonic constants constitute an Admiralty Method parametric description (in arbitrary units) of the tidal streams as assumed by Little *et al.* (1988). The tidal streams predicted by this model can now be compared with the predictions of a more sophisticated model based on the theory of Section 2.6.

The ocean tide in the Gulf of California has been discussed in some detail by several authors (Filloux, 1973; Quirós *et al.,* 1992; Carbajal & Backhaus, 1998), and a consistent picture emerges from their work. The ocean tide is due to the combination of *standing* diurnal waves and *travelling* semi-diurnal waves, and the associated tidal streams are rectilinear along the gulf. The semi-diurnal waves travel northwestwards (i.e. into the gulf) and are dissipated at the closed northern end. Consequently, the maximum northwestwards semi-diurnal tidal stream coincides with maximum positive semi-diurnal sea surface displacement, and is therefore in phase with the ocean tide (Chapter 2; Doodson & Warburg, 1941). For the diurnal components, which are standing waves, the maximum northwestwards stream coincides with the rising half-tide, and so it leads the ocean tide by 90º. It is therefore possible to derive the harmonic constants of the tidal stream (in arbitrary units) from the harmonic constants of the ocean tide at the hydrothermal site according to this theory (Figure 4.5c,d). There is no high-pass filtering, so the relative magnitudes of the components are the same as for the ocean tide (Figure 4.4c,d). The phase-lags of the travelling semi-diurnal components are unchanged, but the phase-lags of the standing diurnal components must be reduced by 90º. A time-series for the predicted tidal stream magnitude according to this theory is shown in Figure 4.5e alongside a time-series predicted by the simpler theory of Little *et al.* (1988).

It should be noted that the tidal streams predicted by this model differ from those predicted by Little *et al.* (1988) for two reasons. Firstly, the tidal stream has been derived from the ocean tide at the hydrothermal site itself rather than the ocean tide at the town of Guaymas. Secondly, the tidal stream is derived from a rigorous expression taking account of standing and travelling waves, rather than the simple time-derivative of ocean tide height assumed by Little *et al.* (1988).

In summary, it is suggested that the boundary-layer model of Little *et al.* (1988) should be modified to incorporate a more realistic estimate of the tidal streams in the Gulf of California. It would also be desirable to obtain an estimate of the power spectrum of this data using the multiple window method of Section 3.2.2.

4.4 Equatorial East Pacific Rise

4.4.1 Rose Garden Site

Johnson *et al.* (1994) discuss two time-series temperature measurements made at the Rose Garden hydrothermal site at the Galapagos Spreading Centre (0.804167°N, 86.224633°W). Both time-series begin at 1988/4/16 15h00 GMT and are of 18 days duration. The first time-series (Thermistor 2) was obtained from a probe laid on top of a bed of mussels. It reveals semi-diurnal variations of ±1ºC about a mean value of ~3ºC. The second time-series (Thermistor 3) was obtained from a probe which was inserted into a mass of mussels and vestimentiferan worms. Thermistor 3 displayed high temperature peaks at semi-diurnal intervals, although their magnitude varied significantly. For the first 4 days, the high temperature peaks were as much as 12ºC above the baseline temperature of ~4ºC. The magnitude of the peaks dropped to ~1ºC between days 4 and 16, and then increased to ~4ºC. Johnson *et al.* (1994) suggest that this variation in the magnitude of the peaks may be caused by the animals moving the probe, and show that the high temperature peaks from both thermistors occur near the times of low water at the port of Guayaquil (2.20ºN, 79.87ºW). Consequently, Johnson *et al.* (1994) speculate that increased flow of vent fluids occurs when the ocean tide at the Rose Garden site is low.

This conclusion presupposes, however, that the ocean tide at the Rose Garden site is in phase with the ocean tide at the port of Guayaquil. There are at least two reasons why this is unlikely to be the case.

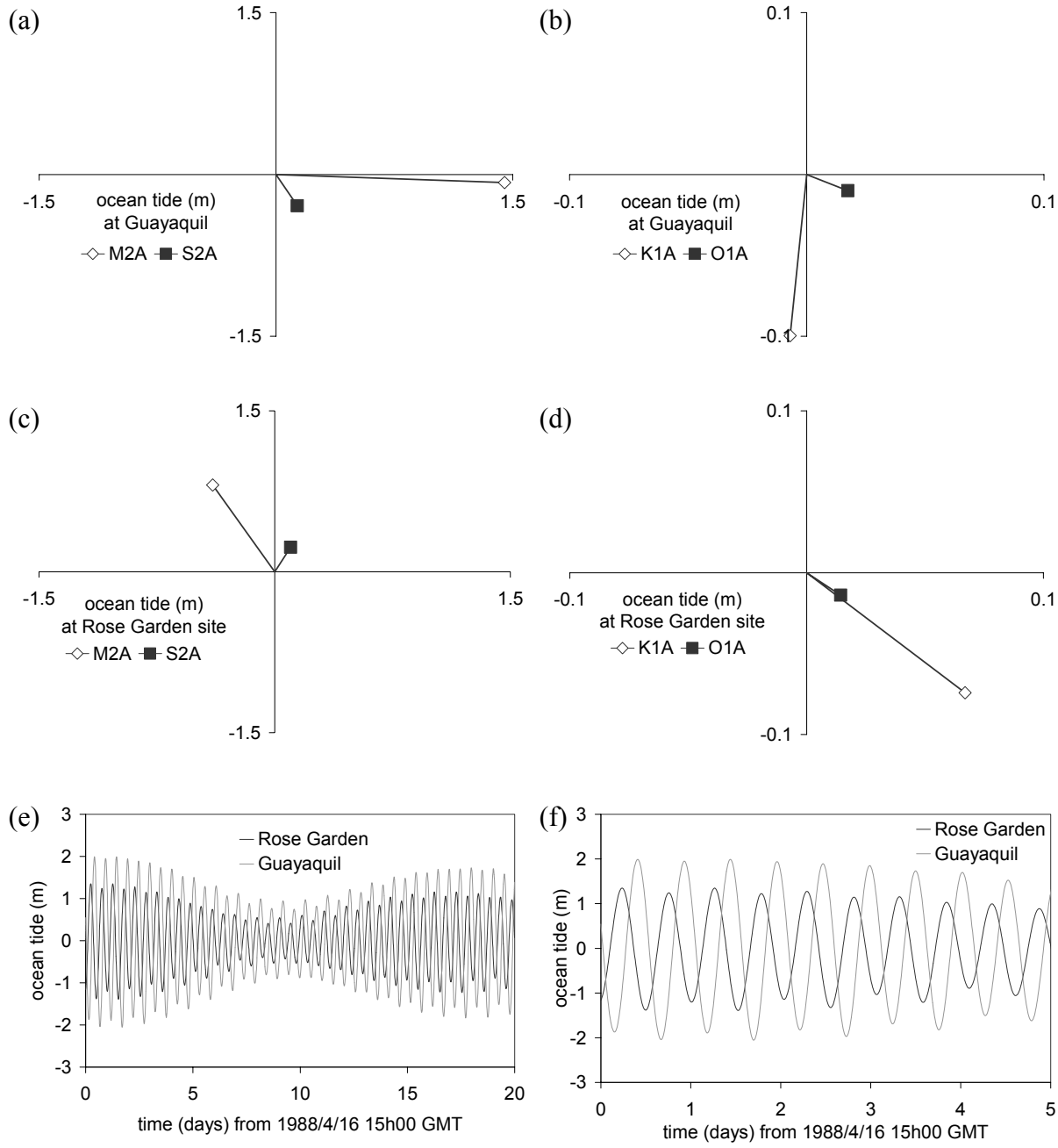

Figure 4.6: Admiralty Method harmonic constants of the ocean tide at the town of Guayaquil (2.20ºN, 79.87ºW), and at the Rose Garden hydrothermal site (0.80°N, 86.22°W). (a) – (d) Admiralty Method harmonic constants. (e),(f) Time-domain representation.

Firstly, the two locations are separated by over 600 km, and secondly the port of Guayaquil lies at the head of a gulf - the Gulf of Guayaquil - where the tide is likely to be very different to that found in the open ocean (Doodson & Warburg, 1941).

The Admiralty Method harmonic constants for the port of Guayaquil (Admiralty Tide Tables, Vol. 4) are compared with those for the Rose Garden Site, which were derived by the HYBRID code from a synthetic time-series created by the CSR code (Table 4.3, Figure 4.6). Table 4.3 shows that semi-diurnal components dominate the ocean tide at both locations, but that the *M2A* and *S2A* components at the Rose Garden site lead those at Guayaquil by 125º.

Rose Garden ocean tides	H_1 (*M2A*)	g_1 (*M2A*)	H_2 (*S2A*)	g_2 (*S2A*)	H_3 (*K1A*)	g_3 (*K1A*)	H_4 (*O1A*)	g_4 (*O1A*)
Guayaquil (m)	1.45	3°	0.32	65°	0.10	94°	0.02	30°
RG site (m)	0.90	244°	0.25	294°	0.10	48°	0.02	44°

Rose Garden ocean tides	$(H_1+H_2)/(H_3+H_4)$	H_1/H_2	g_2-g_1	H_3/H_4	g_4-g_3
Guayaquil	14.8	4.5	62°	5	-64°
RG site	9.6	3.6	50°	5	-4°

Table 4.3: The Admiralty Method harmonic constants for the ocean tide at the port of Guayaquil and at the Rose Garden hydrothermal site.

There are also differences in the diurnal components, but they are of less significance because of their lesser magnitude. The conclusions of Johnson *et al.* (1994) can now be re-examined. They report that high temperature peaks at the Rose Garden site coincide with low tide at the port of Guayaquil. In other words, the temperature signal at the Rose Garden site lags the ocean tide at Guayaquil by ~180°. It follows that the temperature signal at the Rose Garden site lags the *local* ocean tide by a phase angle of ~305°. Thus, the use of the ocean tide at the port of Guayaquil instead of the ocean tide at the Rose Garden site leads to a phase error of 125° (Figure 4.6e,f).

4.4.2 Bio9 Vent Site

Fornari *et al.* (1998) report time-series measurements made at a high-temperature (340ºC) vent at the Bio9 site on the East Pacific Rise (9.83°N, 104.29°W). Their time-series cover periods of between two weeks and ten months, but they find no evidence for tidal influence in their spectral analysis of the data. Unfortunately, they do not report which method of spectral analysis was used. It is possible that the multiple window method might reveal tidal frequencies in their data when other spectral estimators do not. Ocean tide time-series generated by the CSR code show that the ocean tide at the Bio9 site is relatively small, with

a peak amplitude less than 0.4m. It might therefore be speculated that the lack of an obvious tidal signal at the Bio9 vent is a consequence of the fact there is relatively little tidal loading. On the other hand, Shank *et al.* (1995) report that spectral analysis reveals a 'weak ~12.5 h signature' in time-series from temperature probes at the same location.

4.5 Southern East Pacific Rise

4.5.1 The RM24 Site

In 1997, time-series measurements of effluent temperature and velocity were made at the RM24 hydrothermal site on the Southern East Pacific Rise (17.4292ºS, 113.2056ºW) (A. Schultz, *pers. comm.*, 2000). The measurements were made using the Medusa hydrothermal effluent monitoring system developed at the University of Cambridge (Schultz *et al.,* 1996; Dickson, 1997). In the following sections, several references are made to datasets acquired by Medusa systems, and so it is appropriate to review the features of the instrument which are relevant to this dissertation.

4.5.1.1 Overview of the Medusa instrument

The Medusa instrument is essentially a vertical cylinder (~60 cm high, ~10 cm in diameter) which is placed on the seafloor over an area of hydrothermal activity. A gasket system ensures a good seal to the seafloor, and hydrothermal effluent is channeled up the cylinder, where its temperature and velocity are measured. The instrument is also fitted with six 170 ml sample bottles which can draw samples of the effluent at pre-determined times for later chemical analysis. The temperature and velocity sensors are connected to a datalogger which can record time-series of up to one year's duration. The effluent velocity is measured by a propeller mounted inside the instrument. The number of revolutions in a pre-arranged time interval is measured optically and recorded, giving the angular velocity of the propeller. The velocity of the effluent can then be calculated once the system has been calibrated in the laboratory. In this chapter, the symbol v is used to denote an effluent velocity time-series recorded by Medusa.

The Medusa temperature measurements are made as follows. Firstly, a thermistor measures the ambient temperature of the water outside the instrument. The symbol *Th* is used to denote this measurement. Secondly, the temperature of the effluent inside the instrument is measured by two separate thermocouples – a type-K and a type-T. These thermocouples provide two independent measurements of the difference in temperature between the ambient

water outside the instrument and the effluent water inside the instrument. The measurements yielded by the two thermocouples are labelled *Tk* and *Tt*, respectively. It should be noted that the time-series are recorded initially in uncalibrated form, and can only be expressed in dimensional form (i.e. $mm.s^{-1}$ and ºC) after the sensors have been calibrated. Currently, some Medusa time-series remain uncalibrated, but it is still possible to look for tidal signals in the raw, uncalibrated data. In the cases where the thermistor and thermocouple readings have been calibrated to degrees Celsius, the actual temperature of the effluent can be calculated. It is the sum of the thermistor temperature and the temperature difference across either of the thermocouples. There are therefore two measures of effluent temperature, which are labelled *Tefftk* (= *Th* + *Tk*), and *Tefft* (= *Th* + *Tt*).

4.5.1.2 Medusa measurements – time-domain

The data collected by Medusa at the RM24 site span a period of 240 days from 1997/8/5 and are shown in the time-domain in Figure 4.7. The original time-series (sampling interval 15 s) have been low-pass filtered with a moving median filter of length 60 to produce time-series with a sampling interval of 15 min (Schultz *et al.,* 1992). In this dissertation, all Medusa time-series data have been low-pass filtered in this way prior to analysis.

The overview of the *Th*-signal in Figure 4.7a shows that the ambient temperature oscillated around a reasonably constant mean value over the observation period. For the time period between 80 and 120 days there is clear evidence of variation in the magnitude of the oscillations. This is consistent with a springs/neaps tidal cycle. The close-up view in Figure 4.7e shows that there is an underlying semi-diurnal periodicity to the *Th*-signal. The overview of the *Tk*- and *Tt*-signals in Figure 4.7b displays no obvious long-term trend, but shows that the *Tk*- and *Tt*-signals remained proportional to each other throughout the observation period. This proportionality is not surprising since the two signals are independent, uncalibrated measurements of the same physical quantity. Nonetheless, the observation is worthwhile since it provides evidence that neither sensor failed during deployment (cf. Section 4.7). The close-up view of the *Tk*-signal in Figure 4.7f does not reveal any clear tidal periodicity.

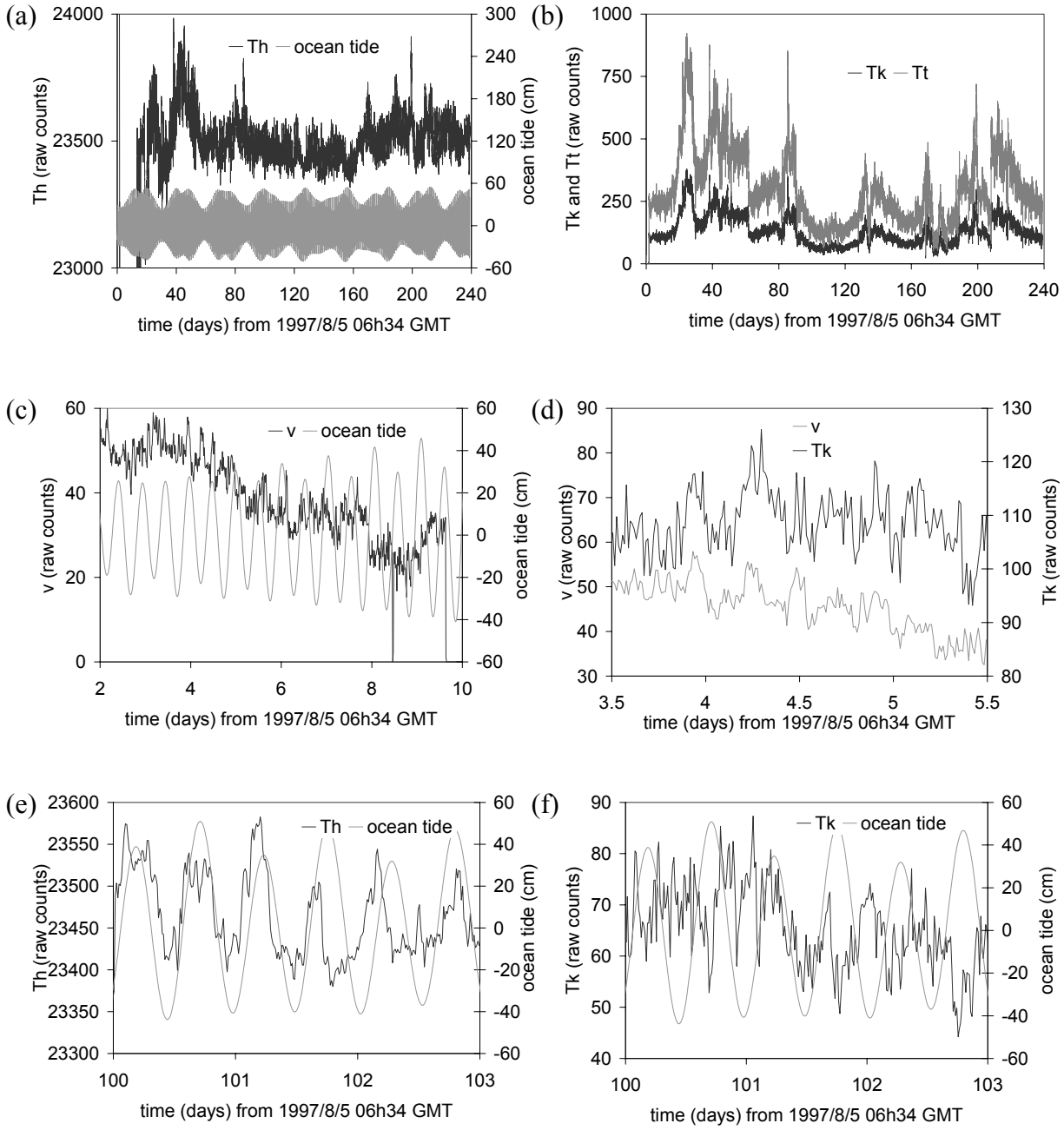

Figure 4.7: Uncalibrated data collected by Medusa at the RM24 site (17.4292ºS, 113.2056ºW) on the Southern East Pacific Rise. *Th* – ambient (thermistor) temperature, *Tk* – temperature difference across thermocouple, *v* – effluent velocity.

The effluent velocity time-series (*v*) is shown in Figure 4.7c. These data cover a much shorter time period (8 days) than the temperature data (240 days) and display a linear downward trend until day 10 when the record stops. It may be that this was caused by a steady increase in the frictional resistance of the propeller of the velocity sensor. Possible

explanations for this friction include thermal expansion in the bearings and/or the precipitation of mineral deposits. There is no obvious diurnal or semi-diurnal periodicity in the record, but there is a short period (between day 4 and day 5) where peaks in the *v*-signal seem to occur at quarter-diurnal intervals, so that they coincide with both high tide and low tide in the ocean. Since the RM24 site is in the open ocean it is expected that peak tidal streams occur at low and high tide (Chapter 2). Consequently, this small section of the record is consistent with a Bernoulli effect explanation of variations in effluent velocity (Schultz & Elderfield, 1997). At low and high tide, when the magnitude of tidal streams is large, the lateral flow of ocean currents across the top of the Medusa might lead to reduced pressure at the top of the instrument and draw fluid upwards. Figure 4.7d shows that increased effluent velocity correlates with an increased temperature difference across the thermocouples. Thus, a highly speculative explanation for this section of the dataset is that warm fluid is drawn upwards through the instrument at high and low tide, driven by tidal streams causing reduced pressure at the top of the Medusa.

4.5.1.3 Medusa measurements – non-parametric analysis

Power spectra for the *Th*-, *Tk*- and *v*-signals are shown in Figure 4.8. All power spectra were obtained from the low-pass filtered (15 min sampling interval) time-series using the MWPS code. The *Th*- and *Tk*-signals each consisted of N=22,937 datapoints (239 days), and the shorter *v*-signal had N=775 datapoints (8 days). Accordingly, the power spectra for the *Th*- and *Tk*-signals were calculated using a time-bandwidth product of 10, with 20 eigenspectra and a 96-point (= 24 h) autoregressive prewhitening filter. The power spectrum for the *v*-signal was calculated using a time-bandwidth product of 1, with 2 eigenspectra and a 96-point autoregressive filter. The low time-bandwidth product was required in order to get reasonable frequency resolution, but means that the variance of the estimated power spectrum is relatively large.

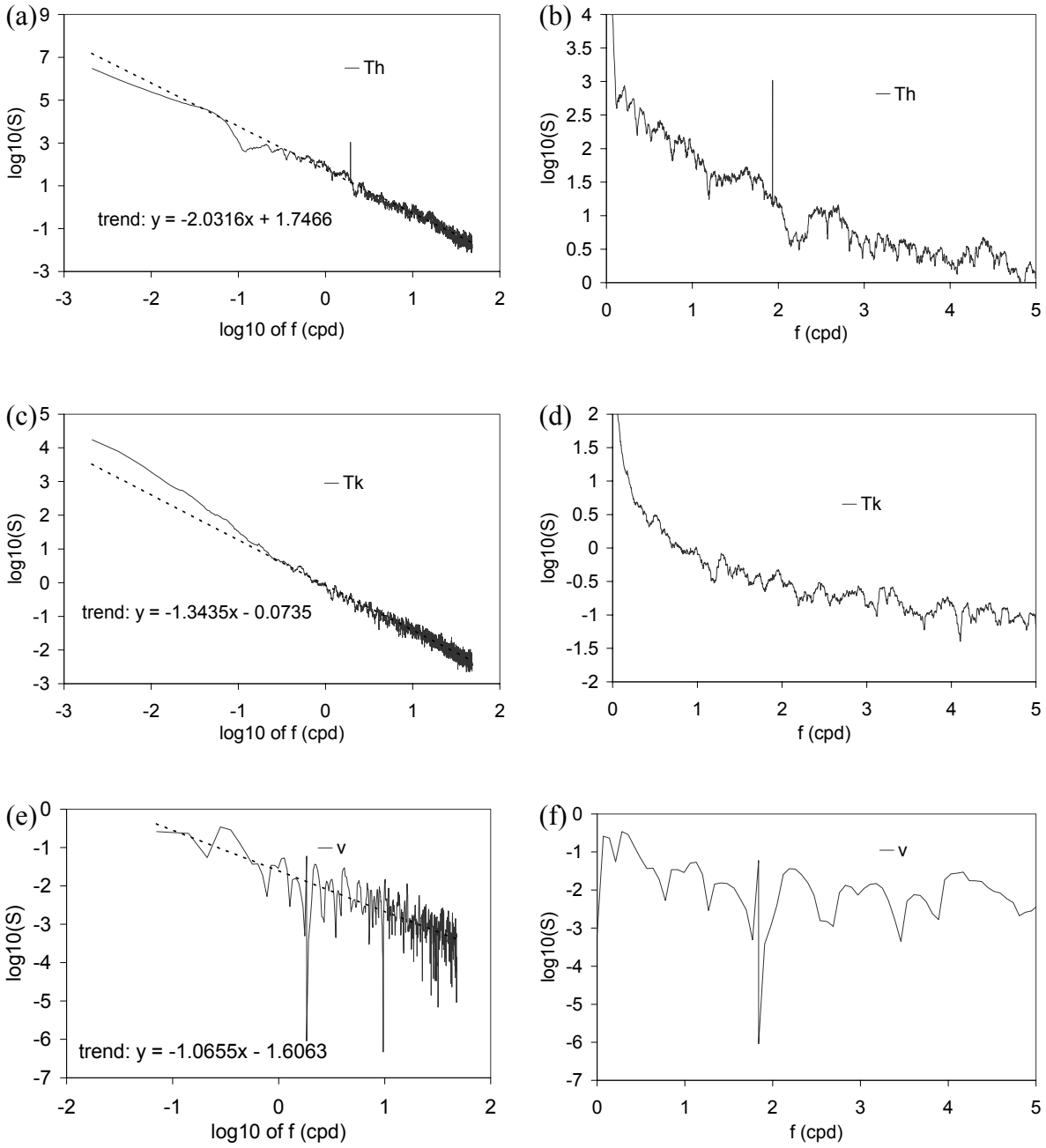

Figure 4.8: Spectral estimates for the data collected by Medusa at the RM24 site (17.4292ºS, 113.2056ºW), calculated using the MWPS code. *Th* – ambient (thermistor) temperature, *Tk* – temperature difference across thermocouple, *v* – effluent velocity.

Figures 4.8a and 4.8b show the estimated power spectrum of the *Th*-signal. The general trend of the spectrum (Figure 4.8a) is of the form $\hat{S}(f) \sim f^{-2}$, which is inconsistent with the $f^{-5/3}$ prediction of the Kolmogorov hypothesis (Section 4.2.5). A close up view of the spectrum (Figure 4.8b) shows that a single significant line component was found at 1.933 ± 0.002 cpd.

(The uncertainty in the location of the line component is equal to the spacing of the frequency bins $1/(N\Delta t)$).This line component can be identified with the *M2* tidal component (1.932 cpd) and provides strong evidence that the *Th*-signal is tidally modulated. There is no evidence of significant power in the diurnal frequency band (Figure 4.8b).

The power spectrum of the *Tk*-signal shows that no significant line components were identified and that it has a general trend $\hat{S}(f) \sim f^{-1.34}$ (Figures 4.8c,d). Since the *Tt*-signal is proportional to the *Tk*-signal in the time-domain (Figure 4.4b), its power spectrum can be expected to exhibit the same features and is not shown here.

The power spectrum of the *v*-signal (Figures 4.8e,f) is of limited use because of the short length of the original time-series. Nonetheless, it is interesting that a single significant line component was identified at 1.84 ± 0.07 cpd. This range includes the *N2* tidal component (1.90 cpd), but not the *M2* component (1.93 cpd) which is usually dominant. Given the shape of the spectrum, the safest conclusion is to say that no positive evidence of tidal modulation is provided by this spectral estimate. On the other hand, the short time-series means that the existence of tidal modulation cannot be ruled out. The general trend of the spectrum, $\hat{S}(f) \sim f^{-1.07}$ is not consistent with the 'five-thirds' law. No strong inferences can be made because of the limited length of the original time-series.

In summary, the non-parametric spectral estimates provide strong evidence for tidal modulation of the *Th*-signal, but no strong evidence for tidal modulation of the *Tk*-, *Tt*- or *v*-signals.

4.5.1.4 Medusa measurements – parametric analysis

Of the time-series collected by Medusa at RM24, only the *Th*-signal shows strong evidence of tidal modulation. Accordingly, it is only for this *Th*-signal that the Admiralty Method harmonic constants are estimated. These estimates are compared with the harmonic constants for the local tidal potential and ocean tide in Table 4.4. The harmonic constants are also shown graphically in the complex plane in Figure 4.9.

An attempt was made to decompose the whole of the *Th*-signal using the Bayesian drift technique (Section 3.3.3) but it was unsuccessful. The algorithm placed a large proportion of the power at semi-diurnal frequencies into the drift component rather than the parametrised tidal component. Consequently, the harmonic constants reported here were estimated by

Huber-weighted section averaging with mean removal using the HYBRID code (Section 3.3.4).

RM24	H_1 (*M2A*)	g_1 (*M2A*)	H_2 (*S2A*)	g_2 (*S2A*)	H_3 (*K1A*)	g_3 (*K1A*)	H_4 (*O1A*)	g_4 (*O1A*)
potential ($m^2.s^{-2}$)	2.57	225°	1.2	226°	0.914	293°	0.647	294°
ocean (m)	0.34	21°	0.06	246°	0.06	358°	0.02	341°
Th (raw counts)	15.98	346°	5.54	357°	16.33	175°	16.95	130°

RM24	$(H_1+ H_2) / (H_3 + H_4)$	H_1 / H_2	$g_2 – g_1$	H_3 / H_4	$g_4 – g_3$
tidal potential	2.42	2.14	< 1°	1.41	< 1°
ocean tide	5	5.67	-135°	3	-17°
Th	0.65	2.88	10.65°	0.96	-44°

Table 4.4 The Admiralty Method harmonic constants of the tidal potential, ocean tide, and those estimated for the Medusa *Th*-signal, at the RM24 site.

The original time-series (of N=22,937 points) was split into 112 overlapping sections of 672 points (= 7 days), giving a 30% offset between sections. Harmonic constants were estimated for each section, following subtraction of the mean value for the section. The final estimates of the harmonic constants are Huber-weighted averages taken over the sections. The error bars represent 95% confidence intervals, assuming that the real and imaginary parts of each harmonic constant are independently normally distributed over the sections (Section 3.3.4).

Using Table 4.4 and Figure 4.9, the harmonic constants of the output signal (*Th*) can be compared with those of the two postulated input signals (the tidal potential and the ocean tide). Within the semi-diurnal band, the *M2A* component dominates the *Th*-signal and is roughly in phase with the *M2A* component of the ocean tide. (For this *M2A* component, the *Th*-signal leads the ocean tide by ~35°). However, this is the only significant point of similarity between the *Th*-signal and the ocean tide. When compared according to the diagnostic measurements listed in Table 4.4, the *Th*-signal seems to bear more similarity to the tidal potential than to the ocean tide. For example, the relative magnitude of semi-diurnal and diurnal components - defined as $(H_1+ H_2)/(H_3 + H_4)$ - is 0.65 for the *Th*-signal, which is indicative of a mixed tide, containing similar proportions of the total power in the diurnal and semi-diurnal bands. The value of 2.42 for the tidal potential is also indicative of a mixed tide, albeit with much more power in the semi-diurnal band. In contrast, the value of 5 for the ocean tide is characteristic of a strongly semi-diurnal signal.

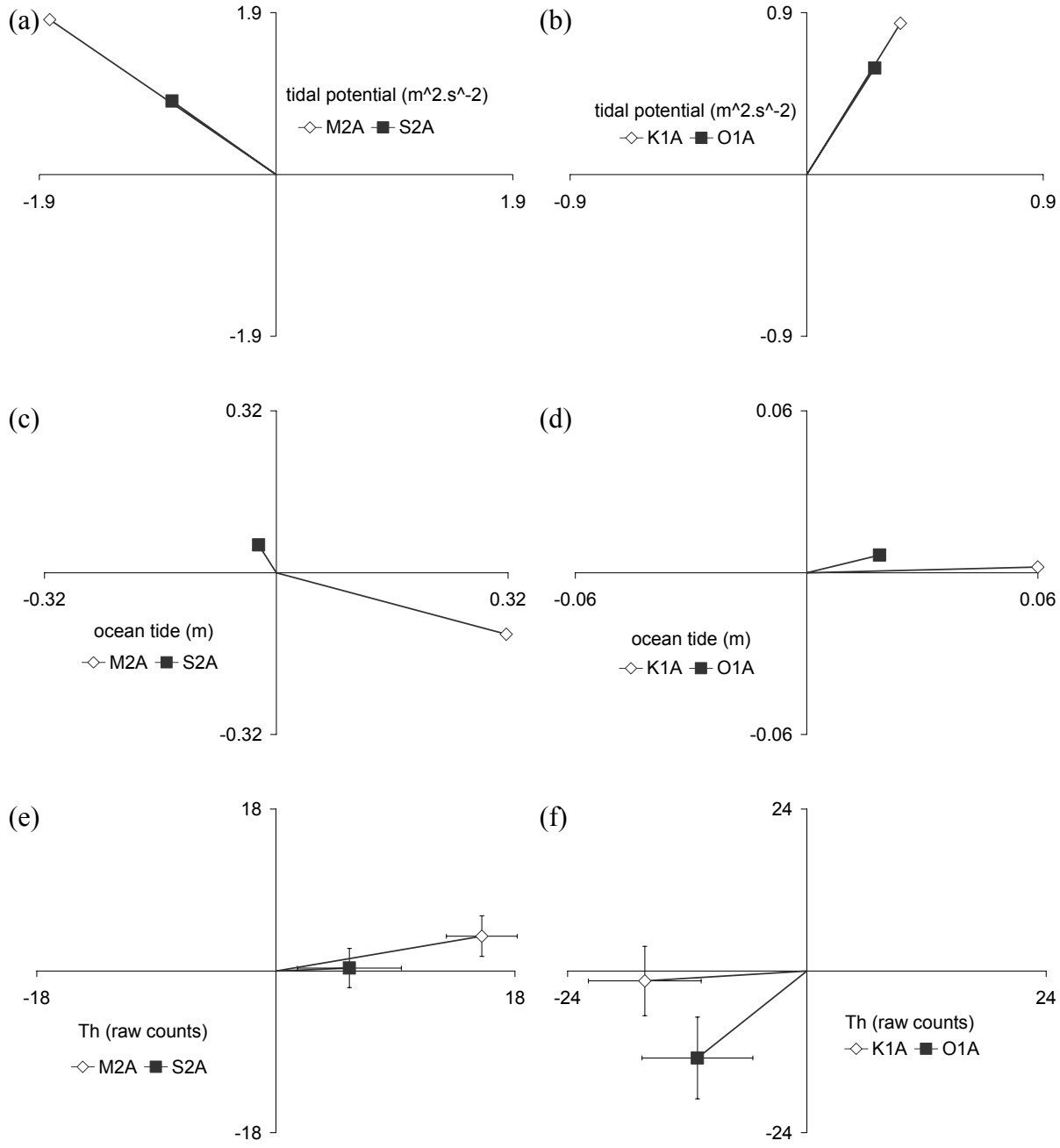

Figure 4.9: Admiralty Method harmonic constants for the RM24 site (17.4292ºS, 113.2056ºW) estimated using the HYBRID code. *Th* – ambient (thermistor) temperature, *Tk* – temperature difference across thermocouple, *v* – effluent velocity.

The relative magnitudes of the semi-diurnal components - defined as the ratio H_1/H_2 - also suggest that the *Th*-signal ((H_1/H_2)=2.88) is more similar to the tidal potential ((H_1/H_2)=2.14) than the ocean tide ((H_1/H_2)=5.67). The difference in phase lag between the semi-diurnal components reinforces this observation. The value obtained for the *Th*-signal ($g_2–g_1$=10.65°) is nearer to that of the tidal potential ($g_2–g_1$<1°) than that of the ocean tide ($g_2–g_1$=-135°).

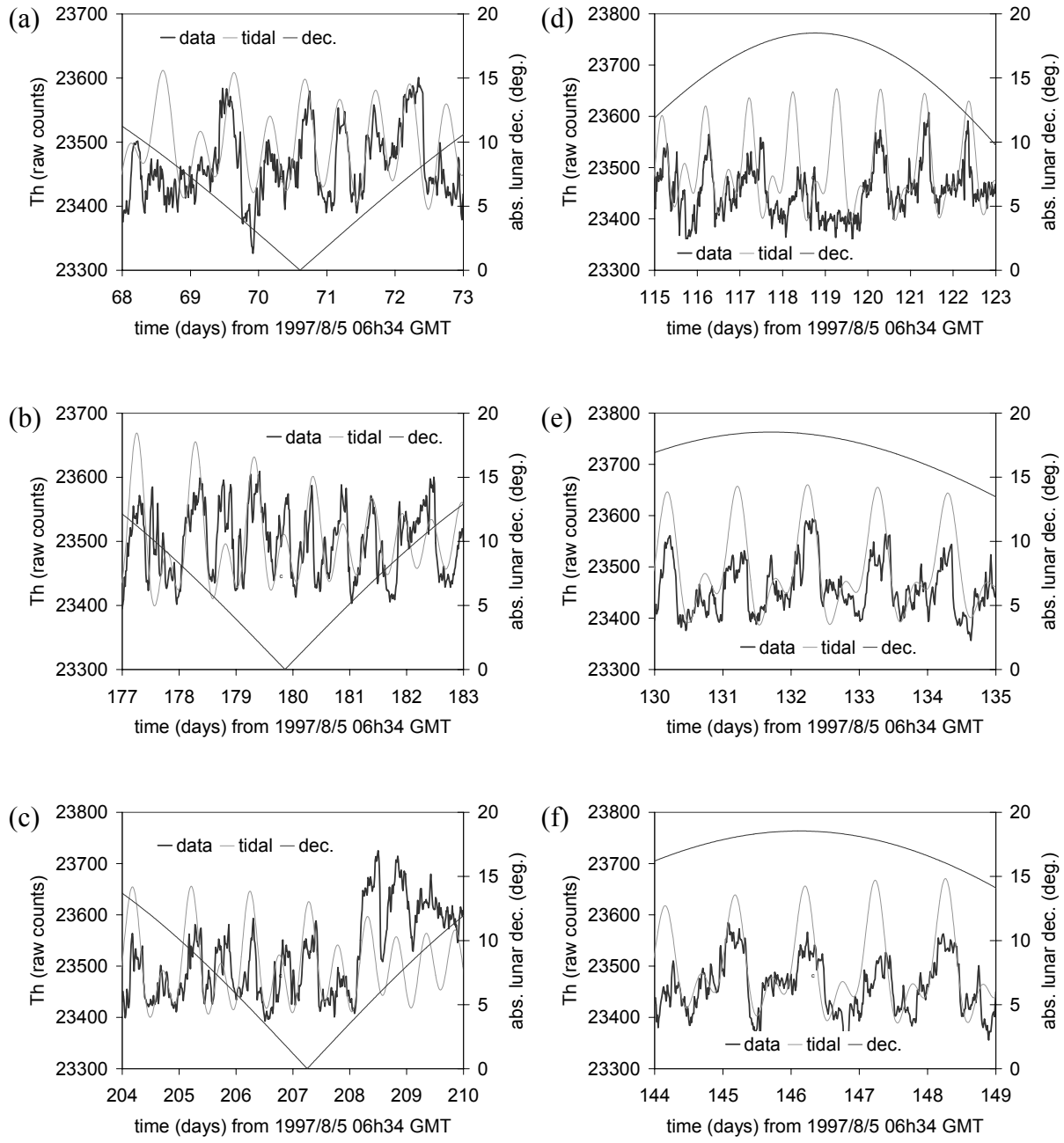

Figure 4.10: The *Th*-signal collected by Medusa at the RM24 site (17.4292ºS, 113.2056ºW). *data* – raw data. *tidal* – the best-fit tidal signal, generated by the harmonic constants of Table 4.4. (For display, this 'tidal' signal has been stretched by a factor of 3 and offset by 23,500.) *dec.* – absolute value of the lunar declination.

Similar observations can be made regarding the relative magnitudes and phases of the diurnal components, but it must be borne in mind that the relative uncertainty in these estimates is much greater, as illustrated by the error bars in Figure 4.9f.

The Admiralty Method harmonic constants derived from the *Th*-signal (Table 4.4) define a tidal signal in the time-domain according to equation (3.15). Figure 4.10 illustrates how well this synthetic tidal signal reflects the original time-series from which the harmonic constants were extracted. The original *Th*-signal (labelled 'data') is plotted alongside the time-series generated by the harmonic constants (labelled 'best fit'). (For display purposes, the 'best fit' signal has been stretched by a factor of 3 and offset by 23,500). The short time periods shown in Figure 4.10 were chosen for display as being those where tidal frequencies were most apparent in the *Th*-signal. It is clear that the data time-series is sometimes predominantly semi-diurnal (Figure 4.10a,b,c) and sometimes predominantly diurnal (Figure 4.10d,e,f). This non-stationary behaviour is closely reflected in the 'best fit' time-series, and can be correlated with the absolute value of the lunar declination which is also shown in Figure 4.10. The 'data' time-series appears to be more strongly semi-diurnal when the lunar declination is small, and more diurnal when the lunar declination is large. This behaviour is predicted by astronomical theory of Section 2.3.2, and provides further evidence that the *Th*-signal is tidally modulated. The existence of time periods where the *Th*-signal exhibits clear diurnal periodicity (Figure 4.10d,e,f) is another illustration of the difference between the *Th*-signal and the local ocean tide. The ocean tide at this site is so strongly semi-diurnal that successive high tides are always separated by ~12 h, and never by ~24 h (e.g. Figure 4.7c).

In summary, the parametric description of the *Th*-signal seems to correlate more closely with the tidal potential than with the ocean tide. This is rather surprising, as there is no obvious mechanism by which the local tidal potential (and hence the solid tide) could influence ambient seafloor temperatures. However, the theory of Little at al. (1988, 1989) provides a plausible link between ambient temperature and tidal streams. If the tidal streams were rectilinear, and not superimposed on a strong background current, this mechanism would lead to frequency-doubling of the temperature signal relative to the ocean tide. The ocean tide at RM24 is strongly semi-diurnal (Table 4.4), and so the associated variations in the *Th*-signal would be quarter-diurnal. However, the *Th*-signal displays virtually no evidence of quarter-diurnal oscillation (Figures 4.7e, 4.8b, 4.10). Thus, if the *Th*-signal is modulated by tidal streams, the streams must be rotating and/or be superimposed on a background current of comparable magnitude.

4.6 Western Pacific

Sato *et al.* (1995) report the results of measurements made using an Ocean Bottom Seismometer with Hydrophone (OBSH) in the South Mariana Trough (13.38°N, 143.92°E). These data were collected at a depth of 1470 m below sea level over a period of 8 days beginning at 1993/10/21. For the first four days of the deployment, the instrument was within 1 m of a hydrothermal vent. It was then moved and spent the remaining four days at a distance of 10 m from the original vent, in an area free from hydrothermal activity. The first four days were marked by a large number of pressure pulses recorded by the hydrophone. These pressure pulses typically lasted between 20 and 60 seconds, and had a negative first break. They were not accompanied by any signal on the seismometers. The frequency with which these pressure events occurred exhibited a periodicity of ~12 h, and appeared to be highest when the local ocean tide was high. During the second 4-day period of the time-series, when the OBSH was placed 10 m from the vent, the pressure events became less frequent and their frequency of occurrence did not exhibit a semi-diurnal periodicity. Sato *et al.* (1995) conclude that the pressure events were caused by the sudden upwelling of hot hydrothermal fluid in the vent. They note that these upwelling events seem more frequent when the local ocean tide is high (i.e. when the hydrostatic pressure on the seafloor is greatest). Therefore these data suggest that episodic hydrothermal activity is most frequent at high tide.

4.7 Mid-Atlantic Ridge

4.7.1 The TAG mound

The TAG hydrothermal mound (26.13°N, 44.82°W) is an active hydrothermal area on the Mid-Atlantic Ridge at a depth of 3700 m below sea level. The mound itself is roughly circular with a diameter of 200 m, and it rises 70 m above the seafloor. At the centre of the mound is an area of vigorous hydrothermal venting known as the Central Black Smoker Complex (CBC) which contains black smokers venting at 360°C - 366°C. In addition to the CBC, there are other areas of the TAG mound where hydrothermal effluent has been observed. This non-CBC effluent ranges from warm, diffuse flow (~20°C), to further high-temperature black smokers.

In 1994, several researchers visited the site and made time-series measurements on the TAG mound, at a time when it was being drilled as part of the Ocean Drilling Program (ODP). As

well as revealing the effect of ocean drilling on hydrothermal effluent, many of these time-series display evidence of tidal modulation. The aim of this section is to collate all of the time-series measurements made at TAG to see if a consistent picture emerges (Kinoshita *et al.,* 1996; Schultz *et al.,* 1996; Fujioka *et al.,* 1997; Kinoshita *et al.,* 1998; Copley *et al.,* 1999).

4.7.1.1 Water column measurements

Kinoshita *et al.* (1996, 1998) report time-series temperature measurements made at TAG using two types of instrument – the Giant Kelp (which measures temperature above the seafloor) and the Daibutsu (which measures temperature on and below the seafloor).

The Giant Kelp records the temperature in the bottom 50 m water column and consists of a vertical string of eight thermistors tethered to the seafloor. Three Giant Kelps were deployed on the periphery of the CBC at TAG, and the resulting time-series display periodic behaviour with a dominant period of ~12 h. After comparing these temperature data with current meter readings (Fujioka *et al.,* 1997), Kinoshita *et al.* (1998) conclude that the hydrothermal plume from the CBC is deflected by tidal currents.

4.7.1.2 Geothermal probe measurements

The Daibutsu instrumented is designed to measure temporal changes in the conductive heat flow from sediments, and consists of eight geothermal probes, each of which is 80 cm long and contains five thermistors mounted at intervals of 17.5 cm. At TAG, an attempt was made to insert the probes at several locations to the south and west of the CBC (Kinoshita *et al.* 1996; Kinoshita *et al.,* 1998). Some of the probes failed to penetrate the sediment and were left on the seafloor to record bottom water temperature. The remaining probes penetrated the sediment partially, so that some of their thermistors were above the seafloor and some below. All of the thermistors which were above the seafloor produced similar time-series showing that bottom water temperature is typically 2.66°C, but with periodic high temperature 'spikes', in which the temperature is raised by between 0.02°C and 0.8°C. These spikes recur at intervals of ~12 h and ~ 24 h. Kinoshita *et al.* (1996, 1998) attribute these variations to the advection of non-buoyant effluent by tidal currents. One interesting feature of the data, which they do not discuss, is the fact that successive spikes are sometimes separated by ~12 h and sometimes separated by ~24 h. A possible explanation for this behaviour lies in the springs/neaps cycle of lunar phases. Kinoshita *et al.* (1998) note that the currents on the seafloor at TAG are predominantly westward. They conclude that there is a background (i.e.

non-tidal) westward current of ~10 cm.s^{-1} upon which tidal streams of the same order of magnitude are superimposed. Thus, the magnitude and direction of the overall current is highly sensitive to the magnitude of the tidal streams. It may be that when tidal streams are large (at springs), they are just sufficient to produce a reversal in the direction of overall current twice per day. However, when tidal currents are small (at neaps), such current reversals may only occur for the larger of that day's tides, or not at all. This tentative explanation for bottom water temperatures is consistent with the published data.

The temperature time-series produced by the subseafloor Daibutsu thermistors appear qualitatively different to those obtained on the seafloor. An example is provided by the subbottom time-series shown in figure 4 of Kinoshita *et al.* (1996), which was obtained at a depth of 44 cm below the seafloor. It is relatively smooth and has the appearance of a pure tidal signal in the sense defined in Chapter 2. In other words, its power spectrum is dominated by diurnal and semi-diurnal oscillations. In contrast, the spiky time-series obtained above the seafloor would have power spectra containing significant power at higher frequency harmonics.

Kinoshita *et al.* (1998) suggest that the subseafloor temperature variations are caused by thermal diffusion of the variations in bottom water temperature down through the sediment. This assertion can be examined more closely with the aid of a simple one-dimensional model of thermal diffusion in seafloor sediment. Let $T(z,t)$ be the temperature perturbation at time t and depth z below the seafloor. Assuming that the seafloor sediment has a constant thermal diffusivity (κ) it then follows that $T(z,t)$ obeys the heat conduction equation:

$$\frac{\partial T}{\partial t} = \kappa \frac{\partial^2 T}{\partial z^2} \quad for \quad z > 0 \tag{4.5}$$

This can be solved subject to a prescribed tidally modulated temperature at the seafloor. The seafloor temperature can be written as a (complex) Fourier series as follows:

$$T(0,t) = \sum_{j=1}^{N} T_j \exp(i\omega_j t) \tag{4.6}$$

It then follows that the temperature in the sediment at depth z is given by:

$$T(z,t) = \sum_{j=1}^{N} T_j \exp\left(-\sqrt{\frac{\omega_j}{2\kappa}}z\right)\exp\left(i\omega_j t - i\sqrt{\frac{\omega_j}{2\kappa}}z\right) \tag{4.7}$$

Considering each harmonic component separately, it is possible to compare the temperature at depth z with the temperature at the seafloor. Equation 4.7 shows that, at depth z, the component at angular frequency ω_j is attenuated in magnitude by a factor:

$$\varepsilon_j(z) = \exp\left(-\sqrt{\frac{\omega_j}{2\kappa}}z\right) \tag{4.8}$$

and delayed in phase by a (radian) angle:

$$\phi_j(z) = \sqrt{\frac{\omega_j}{2\kappa}}z \tag{4.9}$$

It is possible to test whether the measured temperatures fit this simple model. If the data are compatible with the model, empirical values of attenuation and phase-lag (at a given frequency) should obey equations (4.8) and (4.9) so that:

$$\phi_j(z) = -\ln(\varepsilon_j(z)) \tag{4.10}$$

Kinoshita *et al.* (1998) report that amplitudes decrease and phase lags increase with distance below the seafloor, which is in qualitative agreement with the model. Unfortunately, a quantitative test of the model can only be made using the data from a single subseafloor thermistor, as only one suitable time-series is plotted in sufficient detail by Kinoshita *et al.* (1996).

This subseafloor time-series was obtained at a depth z=0.44 m, and is dominated by semi-diurnal oscillations (ω_1=1.45 · 10^{-4} s^{-1}). This semi-diurnal component has an attenuation factor, ε_1, which lies in the range 0.4 to 0.5 (Kinoshita *et al.,* 1996). According to the theory above, this should correspond to a phase-lag, φ_1, of between 0.693 and 0.916 radians (i.e. between 40° and 52°). However, the observed semi-diurnal phase-lag is much larger - its value of 1.57 radians (90°) would be compatible with an attenuation factor of 0.2. Hence, the simple model of equations (4.5) – (4.10) is insufficient to explain the data.

There are many possible explanations for the failure of the model, of which the two simplest are considered here. Firstly, it may be that the subseafloor oscillations are, indeed, caused by the variation in bottom water temperature, but that the thermal diffusivity is not constant with depth. This possibility cannot be ruled out, but there is no obvious reason why the thermal properties of sediment should vary significantly over such a small distance (0.4 m). Secondly, it may be that the tidal variations in subseafloor temperature are not caused by the concurrent tidal variations in bottom water temperature, but by some process which occurs at a deeper level *below* the seafloor. This possibility is discussed in greater detail in Chapter 6.

Here, it is sufficient to note the phase relationship of the subseafloor oscillations to the ocean tide. Kinoshita *et al.* (1996) record that subseafloor temperatures lag the local ocean tide by ~90°. In other words, the highest subseafloor temperatures coincide with the falling half-tide. It should be noted that this phase lag is incompatible with the prediction that tidal variations in temperature at the seafloor lag the ocean tide by a phase angle in the range [135°, 225°] (Section 6.3).

4.7.1.3 Medusa measurements – time-domain

Schultz *et al.* (1996) report time-series measurements made at TAG using a Medusa hydrothermal monitoring system (Section 4.5.1). The Medusa was deployed on an area of vigorous diffuse flow, 50 m East of the CBC and within one metre of a small black smoker chimney. Time-series of ambient bottom water temperature (*Th*) and effluent velocity (*v*) were obtained, along with time-series for the two thermocouples (*Tk* and *Tt*). Following calibration of the temperature data (Dickson, 1997), two time-series for effluent temperature were constructed: *Teffk* = *Th* + *Tk*, and *Tefft* = *Th* + *Tt*. The data shown in figure 4.11 span a period of 100 days from 1994/9/21. The original time-series (sampling interval 15 s) have been low-pass filtered with a moving median filter of length 60 to produce time-series with a sampling interval of 15 min (Schultz *et al.,* 1992).

The overview of the *Th*-signal (Figure 4.11a) shows that the ambient temperatures oscillated about a baseline value throughout the observation period. This baseline temperature displays an upward trend from ~3.5°C at the beginning of the record to ~5°C at the end. Over this period, there is a corresponding increase in the magnitude of the oscillations from 0.5°C to 1.5°C. The close-up view of the *Th*-signal (Figure 4.11e) shows that the oscillations are semi-diurnal and in-phase with the ocean tide. In other words, the highest ambient temperatures coincide with high tide.

The effluent velocity channel (*v*) functioned successfully for only 4 days, after which it operated sporadically (Figure 4.11b). The close-up view of the *v*-signal (Figure 4.11f) covers approximately the same time period as Figure 3 of Schultz *et al.* (1996), and displays essentially the same data. However, the *v*-signal plotted in Schultz *et al.* (1996) appears much smoother because it has been low-pass filtered with a longer moving-average filter. Schultz *et al.* (1996) discern diurnal periodicity in their (more heavily smoothed) *v*-signal. In contrast, the *v*-signal in Figure 4.11f does not display any obvious periodicity at tidal frequencies.

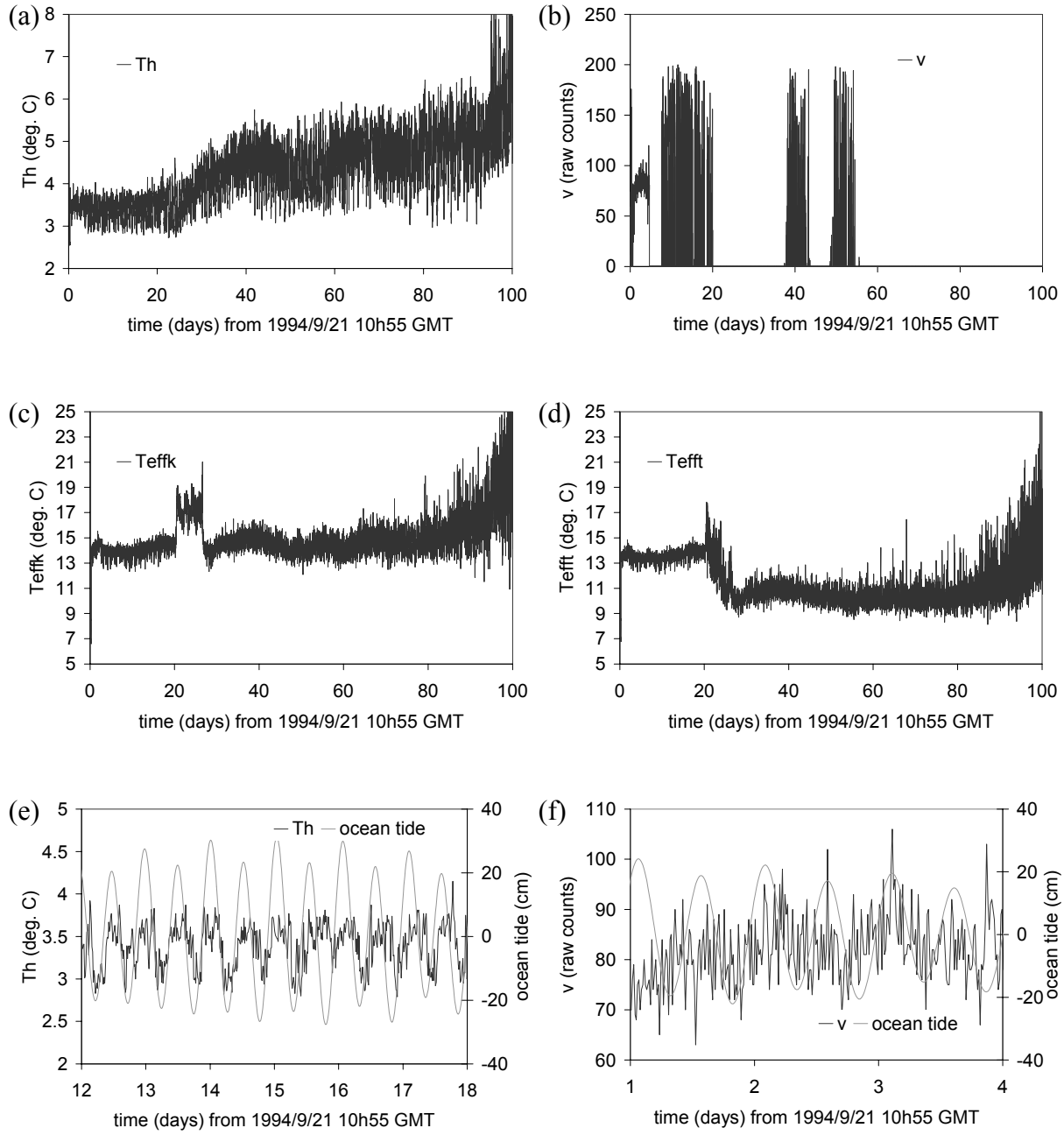

Figure 4.11: Data collected by Medusa at the TAG site (26.13ºN, 44.82ºW) on the Mid-Atlantic Ridge. *Th* – ambient (thermistor) temperature, *Tefffk*, *Tefft* – effluent temperature, *v* – effluent velocity.

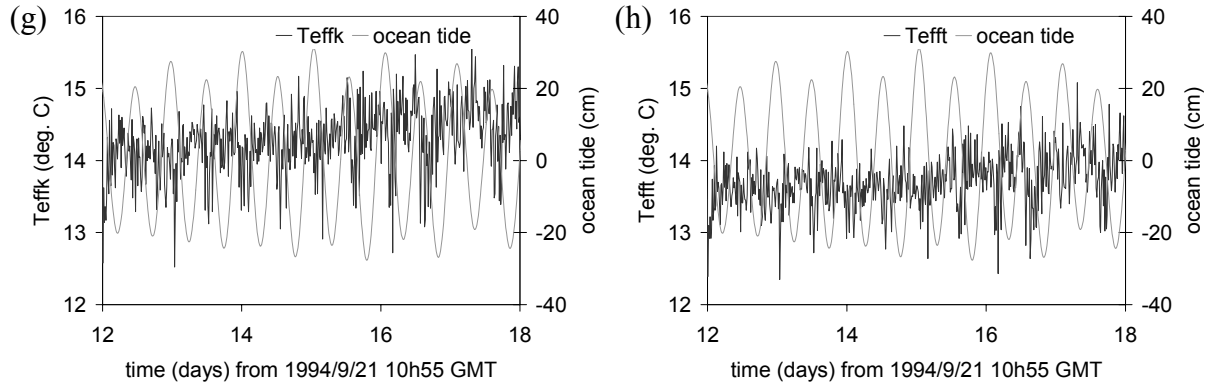

Figure 4.11: (continued) Data collected by Medusa at the TAG site (26.13ºN, 44.82ºW) on the Mid-Atlantic Ridge. *Th* – ambient (thermistor) temperature. *Teffk*, *Tefft* – effluent temperature. *v* – effluent velocity.

Overviews of the two estimates of effluent temperature (*Teffk* and *Tefft*) are shown in Figure 4.11c,d. There is general agreement between the two signals until day 20. In this initial period, the effluent temperature displays semi-diurnal oscillations of ~1°C about a baseline value of ~14°C. On day 20, however, the baseline value of the *Teffk*-signal suddenly jumps to ~17°C while the baseline value of the *Tefft*-signal begins to drift downwards. On day 27, the baseline value of the *Teffk*-signal suddenly returns to ~14°C, while that of the *Tefft*-signal stabilises at ~10°C. Of course, the *Teffk*- and *Tefft*-signals are estimates of the same physical quantity and the fact that they disagree after day 20 suggests that at least one of them is wrong. Examination of the instrument after recovery suggested that the accuracy of the type-T thermocouple had become compromised by leakage (A. Schultz, *pers. comm.*, 2000), and accordingly the *Teffk*-signal is regarded as representing the 'truth'. Schultz *et al.* (1996) note that the 7-day excursion in the *Teffk*-signal correlates with local drilling activity by the Ocean Drilling Program. The close-up views of the *Teffk*- and *Tefft*-signals (Figures 4.11g,h) reveal the semi-diurnal periodicity of the effluent temperature.

4.7.1.4 Medusa measurements – non-parametric analysis

Power spectra for the *Th*-, *Teffk*- and *v*-signals are shown in Figure 4.12. All power spectra were obtained from the low-pass filtered (15 min sampling interval) time-series using the MWPS code. The *Th*- and *Teffk*-signals each consisted of N=10,000 datapoints (104 days), and the shorter *v*-signal had N=384 datapoints (4 days), taken from the beginning of the time-period (Figure 4.11f). The power spectra for the *Th*- and *Teffk*-signals were calculated using

a time-bandwidth product of 5, with 10 eigenspectra and a 96-point (= 24 h) autoregressive prewhitening filter. The power spectrum for the *v*-signal was calculated using a time-bandwidth product of 1, with 2 eigenspectra and a 96-point (=24 h) autoregressive prewhitening filter. The small time-bandwidth product was required in order to get reasonable frequency resolution, but means that the variance of the power spectrum for the *v*-signal is relatively large, and the spectrum should therefore be interpreted with caution.

Figures 4.12a and 4.12b show the estimated power spectrum of the *Th*-signal. The general trend of the spectrum, shown in Figure 4.8a seems to be of the form $\hat{S}(f) \sim f^{-1}$, which is inconsistent with the $f^{-5/3}$ spectrum predicted by the Kolmogorov hypothesis (Section 4.2.5). A close-up view of the spectrum (Figure 4.12b) shows that a single significant line component was found at 3.867 ± 0.004 cpd. This line component can be identified with the 2nd harmonic of the *M2* tidal component (3.864 cpd). At the chosen significance level, no line components were identified in the diurnal or semi-diurnal bands. However there is a spectral peak between 1.9 and 2.0 cpd which can be identified with the *M2* (1.932 cpd) and *S2* (2.000 cpd) components. In the diurnal band, there is a broad concentration of spectral power with two peaks. The first peak lies between 0.80 cpd and 0.95 cpd. It can be identified with the *O1* tidal component (0.930 cpd). The second peak lies between 1.0 and 1.1 cpd, and can be identified with the *K1* tidal component (1.00 cpd). Taken together, these spectral peaks represent very strong evidence of the presence of a tidal signal in the *Th*-signal.

The power spectrum of the *Tefffk*-signal reveals no evidence of any line components, and has a general trend $\hat{S}(f) \sim f^{-0.53}$ (Figures 4.12c,d). The close-up view (Figure 4.12d) shows a large number of spectral peaks, none of which is particularly pronounced. Nonetheless, there is a reasonably strong peak in the semi-diurnal band between 1.9 cpd and 2.0 cpd, and another peak in the diurnal band between 0.94 cpd and 1.13 cpd. Together, these peaks represent fairly strong evidence of tidal modulation of effluent temperature.

The power spectrum of the *v*-signal (Figures 4.12e,f) is of limited use because of the short length of the original time-series. Nonetheless, it is interesting that there appear to be vague spectral peaks at around 1 cpd and 2 cpd, which constitute weak evidence of tidal modulation. There appears to be more spectral power in the diurnal band than the semi-diurnal band. This is consistent with the assertion of Schultz *et al.* (1996) that the *v*-signal is predominantly diurnal.

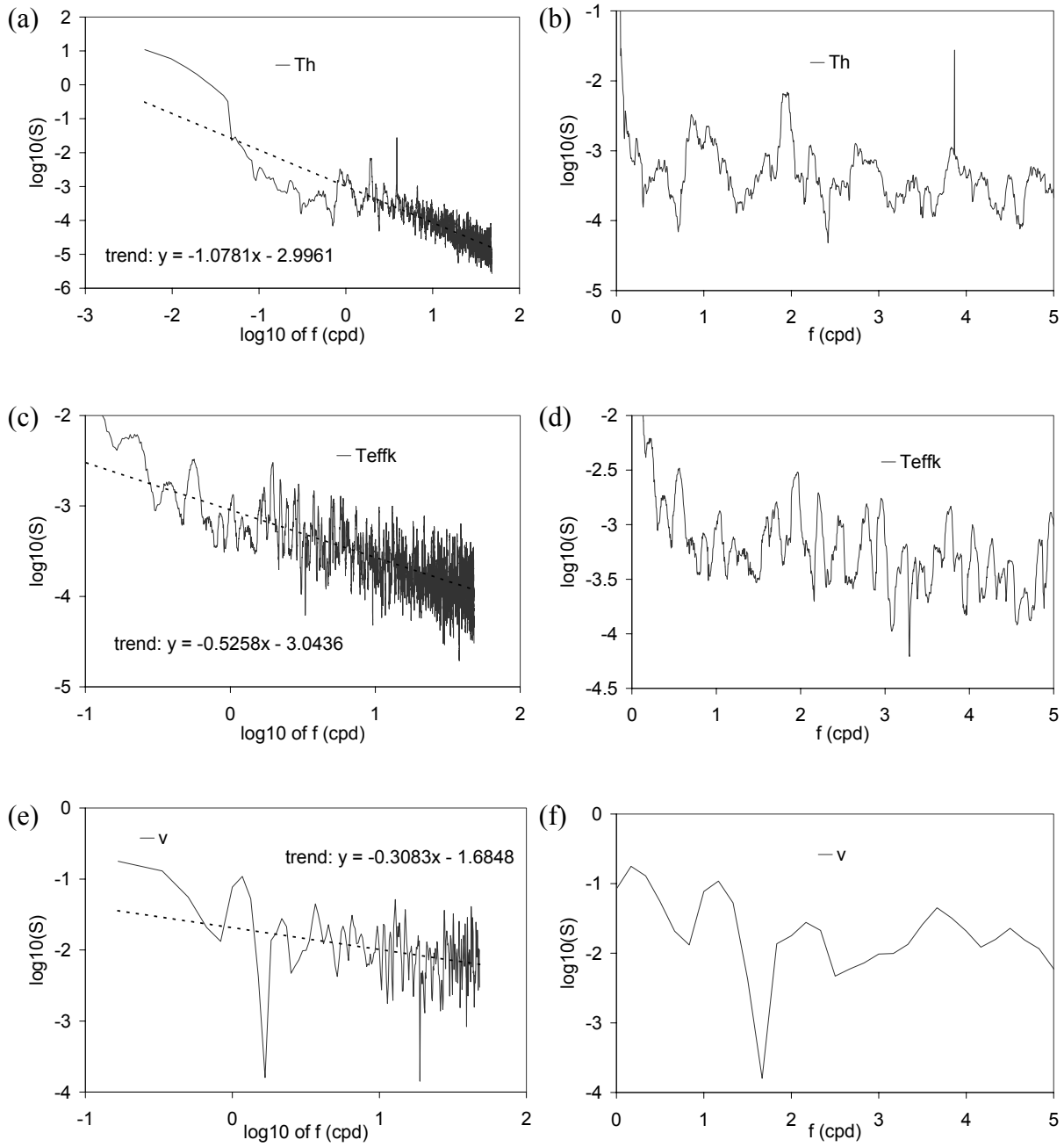

Figure 4.12: Spectral estimates for Medusa collected at the TAG site (26.13ºN, 44.82ºW) calculated using the MWPS code. *Th* – ambient (thermistor) temperature, *Teffk* – effluent temperature, *v* – effluent velocity.

4.7.1.5 Medusa measurements – parametric analysis

The spectral estimates of the previous section provide evidence of tidal modulation in the *Th*-, *Teffk*-, *Tefft*- and *v*-signals. Accordingly, estimates of the Admiralty Method harmonic

constants have been made for each of these signals. These estimates are compared with the harmonic constants for the local tidal potential and ocean tide in Table 4.5 and Figure 4.13.

TAG	H_1 (*M2A*)	g_1 (*M2A*)	H_2 (*S2A*)	g_2 (*S2A*)	H_3 (*K1A*)	g_3 (*K1A*)	H_4 (*O1A*)	g_4 (*O1A*)
potential ($m^2.s^{-2}$)	2.28	88°	1.06	89°	1.23	45°	0.90	45°
ocean (m)	0.15	326°	0.07	1°	0.01	190°	0.03	228°
Th (°C)	0.139	233°	0.094	273°	0.087	71°	0.042	101°
Teffk (°C)	0.156	192°	0.074	256°	0.059	67°	0.005	75°
Tefft (°C)	0.159	191°	0.102	245°	0.035	135°	0.018	237°
v (raw counts)	2.238	175°	2.018	70°	7.244	140°	4.25	18°
shrimp (pixels)	747	245°	2166	335°	2320	182°	1097	357°

TAG	$(H_1+H_2)/(H_3+H_4)$	H_1/H_2	g_2-g_1	H_3/H_4	g_4-g_3
tidal potential	1.57	2.15	< 1°	1.37	< 1°
ocean tide	5.5	2.14	35°	0.33	38°
Th	1.81	1.49	39°	2.11	30°
Teffk	3.65	2.10	64°	12.9	8°
Tefft	4.98	1.56	54°	1.98	102°
v	0.37	1.11	-104°	1.70	-122°
shrimp density	0.85	0.34	90°	2.11	175°

Table 4.5: The Admiralty Method harmonic constants of the tidal potential, ocean tide, Medusa data and shrimp density data at the TAG site estimated using the HYBRID code.

The temperature time-series (*Th*, *Tefffk*, and *Tefft*) each consisted of N=10,000 data points at a sampling interval Δt=15 min. Attempts to extract harmonic constants from the entire time-series using the Bayesian drift technique proved unsuccessful, presumably because the time-series do not conform sufficiently closely to the functional form assumed in Section 3.3.3. Consequently, the harmonic constants reported here were estimated by section averaging, using the HYBRID code, in the manner described in Section 4.5.1. In this case, the temperature time-series were split into 47 overlapping sections of 672 points (= 7 days), giving a 30% offset between sections. The estimated harmonic constants for the *Th*-signal can be compared with those for the tidal potential and the ocean tide (Table 4.5). At TAG, the ocean tide is strongly semi-diurnal, with $(H_1+H_2)/(H_3+H_4)$=5.5, while the tidal potential is more mixed, with $(H_1+H_2)/(H_3+H_4)$=1.57. Thus, the value obtained for the *Th*-signal ($(H_1+H_2)/(H_3+H_4)$=1.81) is more compatible with the tidal potential than with the ocean tide. However, this value should be treated with caution as there is considerable uncertainty in the diurnal harmonic constants (Figure 4.13f).

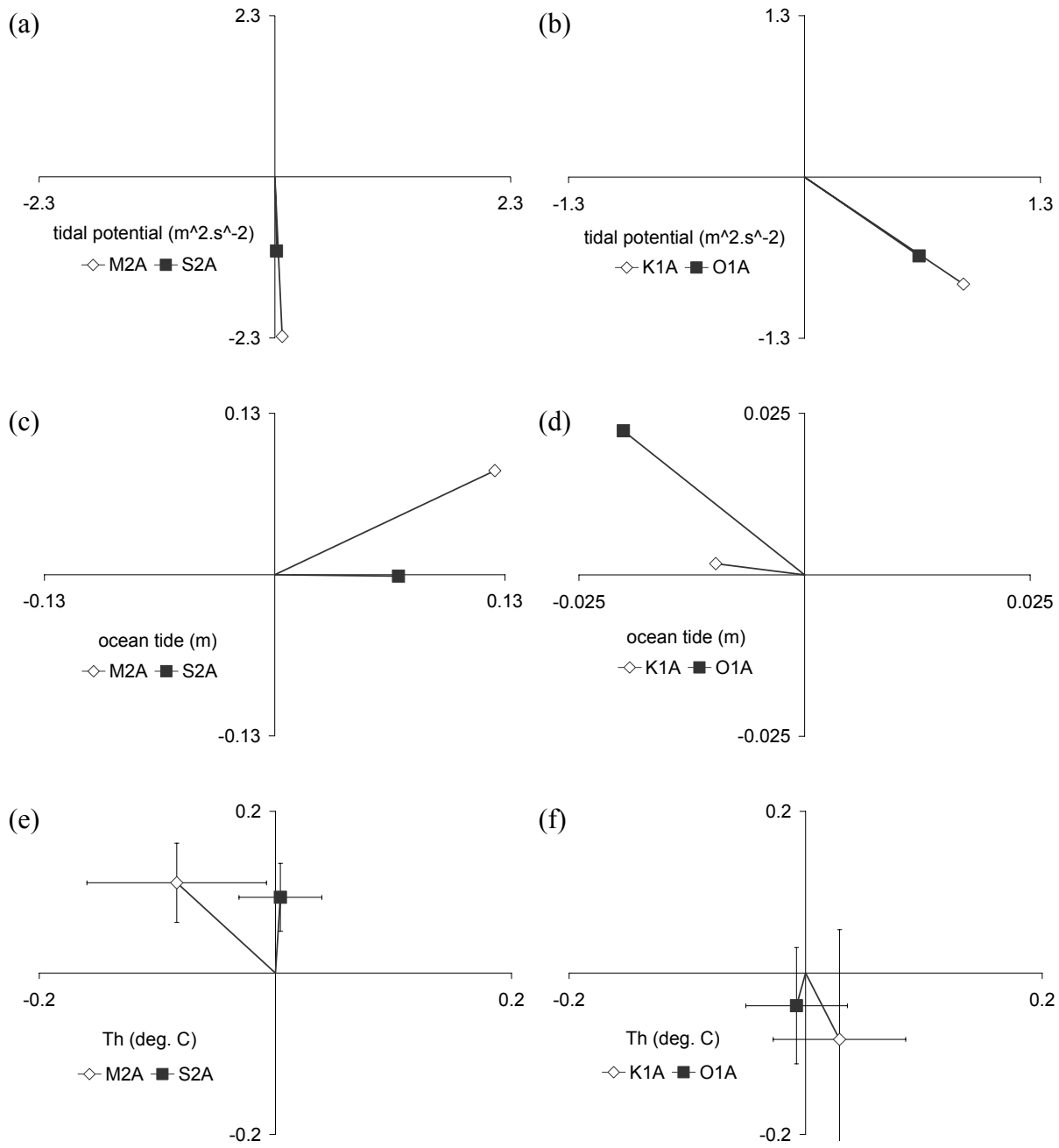

Figure 4.13: Admiralty Method harmonic constants for the TAG site (26.13ºN, 44.82ºW) estimated using the HYBRID code. Tidal potential predicted by ETGTAB code, ocean tide predicted by CSR code. *Th* – ambient (thermistor) temperature.

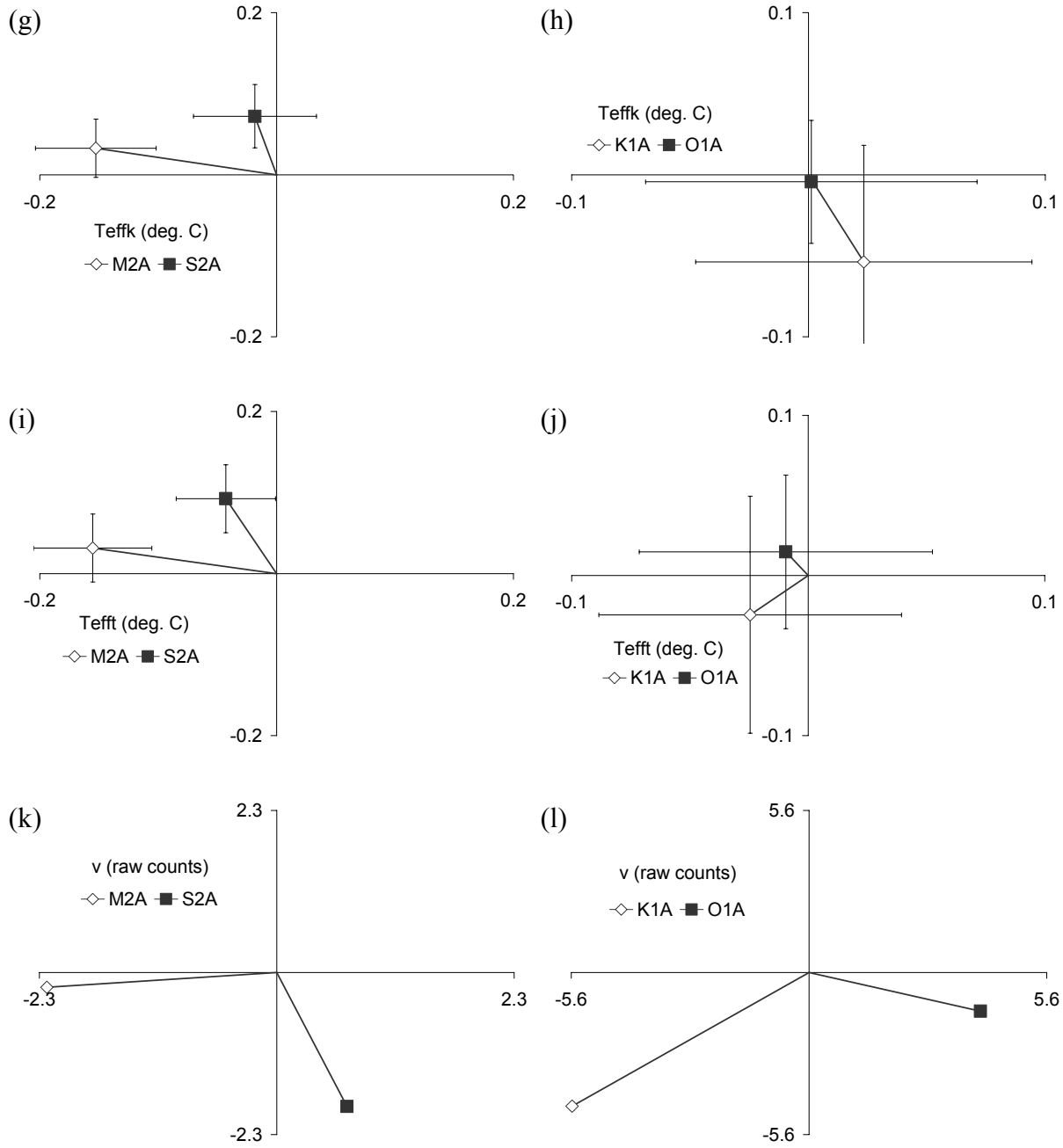

Figure 4.13: (continued) Admiralty Method harmonic constants for the Medusa data at the TAG site (26.13ºN, 44.82ºW) estimated using the HYBRID code. *Teffk*, *Tefft* – effluent temperature. *v* – effluent velocity.

The relative magnitude of the semi-diurnal components is (H_1/H_2)=1.49 for the *Th*-signal, while (H_1/H_2)=2.15 for the tidal potential, and (H_1/H_2)=2.14 for the ocean tide. Therefore the value for the *Th*-signal is equally compatible with both tidal inputs. However, the difference in phase lag of the semi-diurnal components is more diagnostic. The phase difference $(g_2–g_1)$ is negligible for the tidal potential, but $(g_2–g_1)$=35° for the ocean tide and $(g_2–g_1)$=39° for the *Th*-signal. This provides evidence of a correlation between the ocean tide and the *Th*-signal

in the semi-diurnal band, with the *Th*-signal lagging the ocean tide by approximately 270°. In general, therefore, high ambient temperatures occur on the rising half tide. It should be noted, however, that this phase lag does not apply for the entire observation period. For example in the early part of the record (Figure 4.11e), the phase lag between the ocean tide and the *Th*-signal is close to 0°. No inferences are drawn from the diurnal harmonic constants because of the large uncertainties in the estimates (Figure 4.13f).

The estimated harmonic constants for the *Teffk*-signal (Figure 4.13g,h) and the *Tefft*-signal (Figure 4.13i,j) are broadly similar. Since the harmonic constants were derived from section averaging of the entire data record, this is evidence that the tidal parts of the two signals remained similar even after the offset which occurred at day 20 (Figure 4.11c,d). Both signals are dominated by semi-diurnal components, in common with the ocean tide. Table 4.5 shows that the *M2A* components of the effluent temperature signals lag the *M2A* component of the ocean tide by 225° and 226°. In other words high effluent temperatures occur between low tide and rising half-tide. It should be noted that this phase lag is compatible with the theoretical prediction of Section 6.3.1.3. No inferences are drawn from the diurnal harmonic constants because of the large uncertainties in the estimates (Figure 4.13h,j).

The estimation of harmonic constants for the *v*-signal is complicated by the fact that only a very short (384 points, or 4 days) section of data is suitable for analysis (Figure 4.11b). Section-averaging methods are inappropriate for such a short time-series, so this data section was analysed using the HYBRID code with Bayesian drift removal. The results of the analysis are given in Table 4.5 and Figure 4.13k,l. As there is no section averaging, no error bars can be included in the figures. It must be stressed that there is, nonetheless, considerable uncertainty in the estimates. The lack of error bars simply indicates that there is no numerical estimate of this uncertainty. The results suggest that the *v*-signal is dominated by diurnal components. This finding is compatible with the analysis of Schultz *et al.* (1996), which was based on a Harmonic Method decomposition.

The results of the Bayesian drift removal for the *v*-signal are shown in the time-domain in Figure 4.14. Figure 4.14a shows that the algorithm extracts a plausibly smooth drift component. However, it is less clear that the extracted tidal signal (labelled *tide*) constitutes a good representation of the original data. Figure 4.14b shows that this '*tide*' signal has less

than half the amplitude of the residual '*error*' signal. The local ocean tide for the same time period is also shown, for comparison. The ocean tide is strongly semi-diurnal, while the inferred tidal part of the *v*-signal is dominantly diurnal.

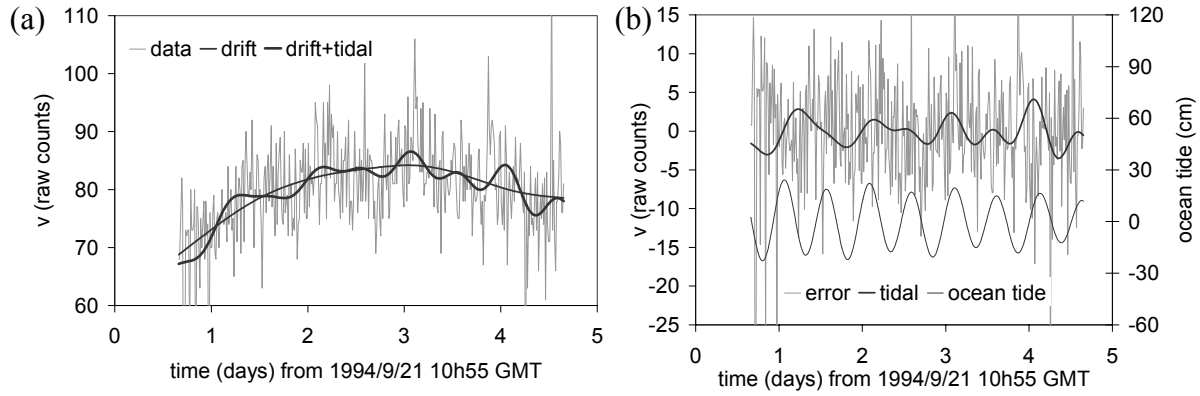

Figure 4.14: The extraction of a tidal signal from the *v*-channel of Medusa at TAG (Schultz *et al.*, 1996), using the HYBRID code with Bayesian drift removal. The data signal is decomposed into *drift*, *tidal* and residual *error*. (a) The original data series (*data*), compared with the *drift* signal and the best-fitting *drift* + *tidal* signal. (b) The tidal part of the *v*-signal (*tidal* – generated by the extracted harmonic constants) compared with the *error*. For comparison, the ocean tide at TAG for the same period is shown on a separate scale.

4.7.1.6 Manatee and OBSH measurements

Fujioka *et al.* (1997) report several time-series obtained at TAG between 1994/8/5 and 1994/8/21. Firstly, several time-series were recorded using a 'Manatee' instrument which was moored 45 m east of the CBC at a height of 2 m above the seafloor. The Manatee is equipped with a current meter, a temperature sensor and a light transmission meter. Secondly, a hydrophone time-series was recorded using an OBSH instrument (Sato *et al.,* 1995) located 30 m east of the CBC.

Fujioka *et al.* (1997) report that the near-bottom current at TAG typically has a magnitude of 0.1 $m.s^{-1}$, which varies only slightly with a semi-diurnal period. Their data show that the direction of this current oscillated with a clear semi-diurnal period between 1994/8/5 and 1994/8/14, but that this oscillation became less regular after 1994/8/14. They note that 'the

former period is co-incident with the flood tide and the latter with the ebb tide'. This cannot be true, since a 'flood' tide is a period of rising sea level and an 'ebb' tide is a period of falling sea level (Manual of Tidal Prediction, 1958). However, it is true that there was a quarter moon on 1994/8/14, which gave rise to neap tides (Yallop & Hohenkerk, 1990). In the presence of a strong background flow, it is possible that tidal streams would be sufficient to reverse the current direction during spring tides, but not during neap tides. It is therefore suggested that Fujioka *et al.* (1997) refer erroneously to 'flood' and 'ebb' tides, instead of 'spring' and 'neap' tides.

The temperature time-series recorded by Manatee shows an ambient temperature of ~2.7°C, interrupted by brief 'spikes' where the temperature rises by ~1°C. These 'spikes' occur with semi-diurnal frequency in the early part of the record (during spring tides), and with erratic frequency in the latter part (during neap tides). Fujioka *et al.* (1997) note that the high temperature spikes do not show a clear pattern of correlation with current direction, and conclude that the temperature variations are due to a combination of changes in currents and hydrothermal venting activity.

The time-series of turbidity displays a similar pattern to the temperature. 'Spikes' of high turbidity (caused by effluent particles suspended in the water) occur with semi-diurnal periodicity in the early part of the record during spring tides. Fujioka *et al.* (1997) note that high turbidity does not always correlate with elevated temperatures. However, on most of the occasions where turbidity and temperature maxima were simultaneous, the current was from south-southeast. The authors note that an active vent was located south-southeast of their Manatee instrument, and suggest that many of the temperature and turbidity anomalies can be attributed to the advection of effluent from this vent.

In summary, the Manatee data suggest that hydrothermal effluent is advected along the ocean floor by the prevailing currents. These currents are strongly influenced by tidal streams, and so contain significant power at the tidal frequencies. However, it appears that these currents are far from being pure tidal streams and contain significant contributions from non-tidal processes. Consequently, any process which depends on the seafloor currents at TAG is likely to exhibit similar behaviour, and have the appearance of a noisy tidal signal.

The pressure pulses recorded by the OBSH hydrophone at TAG (Fujioka *et al.,* 1997), show a similar pattern to those recorded in the Mariana Trough (Sato *et al.,* 1995; Section 4.6), in that their frequency of occurrence varies with a semi-diurnal period. These pressure pulses are interpreted as being due to the periodic upwelling of hot vent fluid. The difference lies in the phase relationship between the local ocean tide and pressure-pulse activity. At the Mariana Trough, pressure-pulse activity was highest at high tide. At TAG, pressure pulse activity seems to peak between falling half-tide and low tide. In other words the TAG OBSH data suggest that the frequency of hydrothermal upwelling events lags the ocean tide by a phase angle in the range [90°, 180°].

4.7.1.7 'Shrimp density' measurements

Copley *et al.* (1999) used a time-lapse video technique to measure the density of shrimp on a section of the TAG hydrothermal mound. The field of view of the camera was static, encompassing ~1.5 m^2 of the mound's surface. At six-hourly intervals, the camera recorded a 15-second segment of video. A single frame was then chosen for image analysis from each of these video segments. The number of pixels in the frame occupied by shrimp was used as a measure of the density of shrimp on the mound. In this way a time-series of 'shrimp density' was constructed with a sampling interval of 6 h. The measurements cover a period of 26 days from 1994/9/21 23h00 GMT. Copley *et al.* (1999) performed a spectral analysis of this time-series using the unwindowed periodogram estimator. The resulting spectrum contains strong peaks covering the diurnal and semi-diurnal frequency bands, and suggests that 'shrimp density' is tidally modulated.

The section of the 'shrimp density' time-series showing the clearest semi-diurnal periodicity is reproduced in Figure 4.15. An attempt was made to find the best-fitting set of Admiralty Method harmonic constants for this section of data using the HYBRID code. Initially, the 15 datapoints of Figure 4.15 were input to the HYBRID code with no modification except subtraction of the mean. The resulting harmonic constants were clearly unrealistic because of their extremely large magnitudes. Strictly, however, they were correct because they generated a time-series which was the best-fit for the data, in a least-squares sense. The problem arose because an attempt was made to fit a parametric function whose fundamental period is 12 h onto a dataset with a 6-h sampling interval. A partial solution is to introduce a fictitious data point before attempting to extract the harmonic constants. Accordingly, 14 separate estimates of each harmonic constant were made. Each of the 14 estimates was made after inserting a fictitious data point, by linear interpolation, halfway between an adjacent

pair of the original data points. A final estimate for each (complex) harmonic constant was then made by taking the mean value of the 14 separate estimates. The harmonic constants estimated in this way are listed in Table 4.5, and were used to create the tidal time-series shown in Figure 4.15.

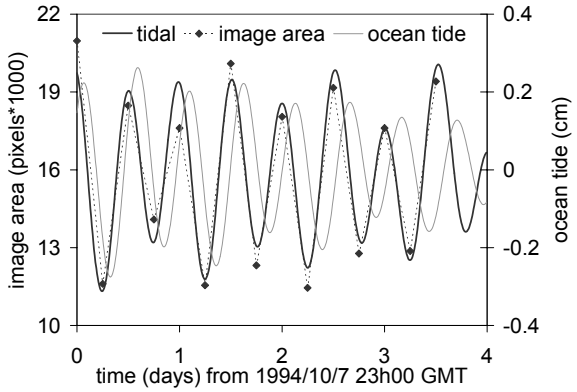

Figure 4.15: A section of the 'shrimp density' time-series collected by Copley *et al.* (1999) at the TAG site. The data points ('image area') record the number of pixels of video frame occupied by shrimp. The data have been fitted with a tidal signal ('tidal') generated by the Admiralty Method harmonic constants given in Table 4.5. The local ocean tide is also reproduced, for comparison.

The original sampling interval of exactly 6 h, coupled with the insertion of fictitious data points based on linear interpolation, probably caused too much power to be attributed to the *S2A* component. (The related *S2* component has a period of exactly 12 h.) Consequently, the harmonic constants extracted here should be regarded as very poorly constrained. Nonetheless, the low quality of the estimate is a useful reminder of the problems inherent in fitting a parametric model to a scant dataset.

Figure 4.15 and Table 4.5 allow the 'shrimp density' to be compared with the local ocean tide. For the *M2A* component, the shrimp density lags the ocean tide by 279°, while for the *S2A* component the phase lag is 334°. It follows that shrimp density is highest at rising half-tide. Since the ambient temperature is also generally greatest on the rising half-tide it can be speculated that the shrimp density is greatest when the ambient temperature is greatest.

4.7.1.8 Summary of tidal modulation observed at TAG

The results of the preceding sections can now be summarised to give an overview of tidal modulation at the TAG hydrothermal mound. The data of Kinoshita *et al.* (1996, 1998) suggest that tidal oscillations in sub-bottom temperatures lag the ocean tide by 90°, while the data of Fujioka *et al.* (1997) suggest that the frequency of episodic venting events lags the ocean tide by an angle between 90° and 180°.

Non-parametric analysis of Medusa data reveals strong evidence of tidal modulation of the ambient (*Th*) and effluent (*Teffk*, *Tefft*) temperatures and weaker evidence of tidal modulation of the effluent velocity (*v*). Parametric analysis using the Admiralty Method suggests that the velocity signal is dominantly diurnal, while the temperature signals are predominantly semi-diurnal. This is consistent with results of Schultz *et al.* (1996) which are based on a Harmonic Method decomposition. The phase lags for the dominant semi-diurnal components in Table 4.5 shows that the *Th*-signal generally lags the ocean tide by 267°. However, there are times during the observation period when the phase lag is close to 0° (Figure 4.11e). This drift in phase lag is probably caused by a change in the properties of the TAG mound and may be due to the ODP drilling which occurred during the observation period. The *M2A* components of the effluent temperature (*Teffk*, *Tefft*) lag the *M2A* component of the ocean tide by 225° and 226°. These phase lags are consistent with the model presented in Section 6.3.1.3.

The density of shrimp observed on a section of the seafloor exhibits tidal modulation (Copley *et al.,* 1999) and is shown to lag the ocean tide by a phase angle of 279° for the *M2A* component and 334° for the *S2A* component. Consequently, high shrimp density occurs at the same phase of the ocean tide as high ambient temperatures.

4.7.2 The Menez Gwen Site

In 1997, time-series data were collected using a Medusa system at the Menez Gwen site (37.83°N, 31.50°W) on the Mid-Atlantic Ridge (A. Schultz, *pers. comm.*, 1997). Time-series of ambient temperature (*Th*), effluent temperature (*Tefft*) and effluent velocity (*v*) were obtained over a period of 11 days from 1997/7/26. In addition, the Medusa sample bottles were used to collect six samples of hydrothermal effluent at a sampling interval of 6 h for later chemical analysis (Cooper, 1999; Cooper *et al.,* 2000).

4.7.2.1 Medusa measurements – time-domain

The data collected by Medusa at the Menez Gwen site are shown in the time-domain in Figure 4.16. The original time-series measurements of velocity and temperature (sampling interval 15 s) have been low-pass filtered with a moving median filter of length 60 to produce time-series with a sampling interval of 15 min (Schultz *et al.,* 1992).

There is some evidence of semi-diurnal periodicity in the overview of the *Th*-signal (Figure 4.16a). This semi-diurnal signal seems strongest in the 2-day period shown in Figure 4.16d, where it appears that the *Th*-signal lags the ocean tide by ~90°, giving the highest ambient temperatures during the falling half-tide. It must be stressed, however, that the time-series is too noisy for any strong inference to be made.

The time-domain view of the *Tefft*-signal provides weak evidence of tidal modulation (Figure 4.16b,e), and the velocity sensor seems to have operated sporadically during the first 3 days of deployment, before failing to record any more data (Figure 4.16c). There is a noticeable downward trend in the *v*-signal which is consistent with a gradual increase in friction slowing down the propeller of the velocity sensor. There is very little evidence of tidal modulation in the time-domain view of the *v*-signal.

Chemical analysis of the six effluent samples shows that they are consistent with a 'mixing' model for diffuse flow (Cooper, 1998: Cooper *et al.,* 2000). According to this model, the diffuse flow passing through Medusa is a mixture of high temperature (~280°C) hydrothermal fluid and cool seawater. The chemical composition of each sample can then be used to calculate the relative proportions of high-temperature fluid and seawater which it contains. The percentage of high temperature (*HT*) fluid in the effluent is graphed against time of sample collection in Figures 4.16f,g.

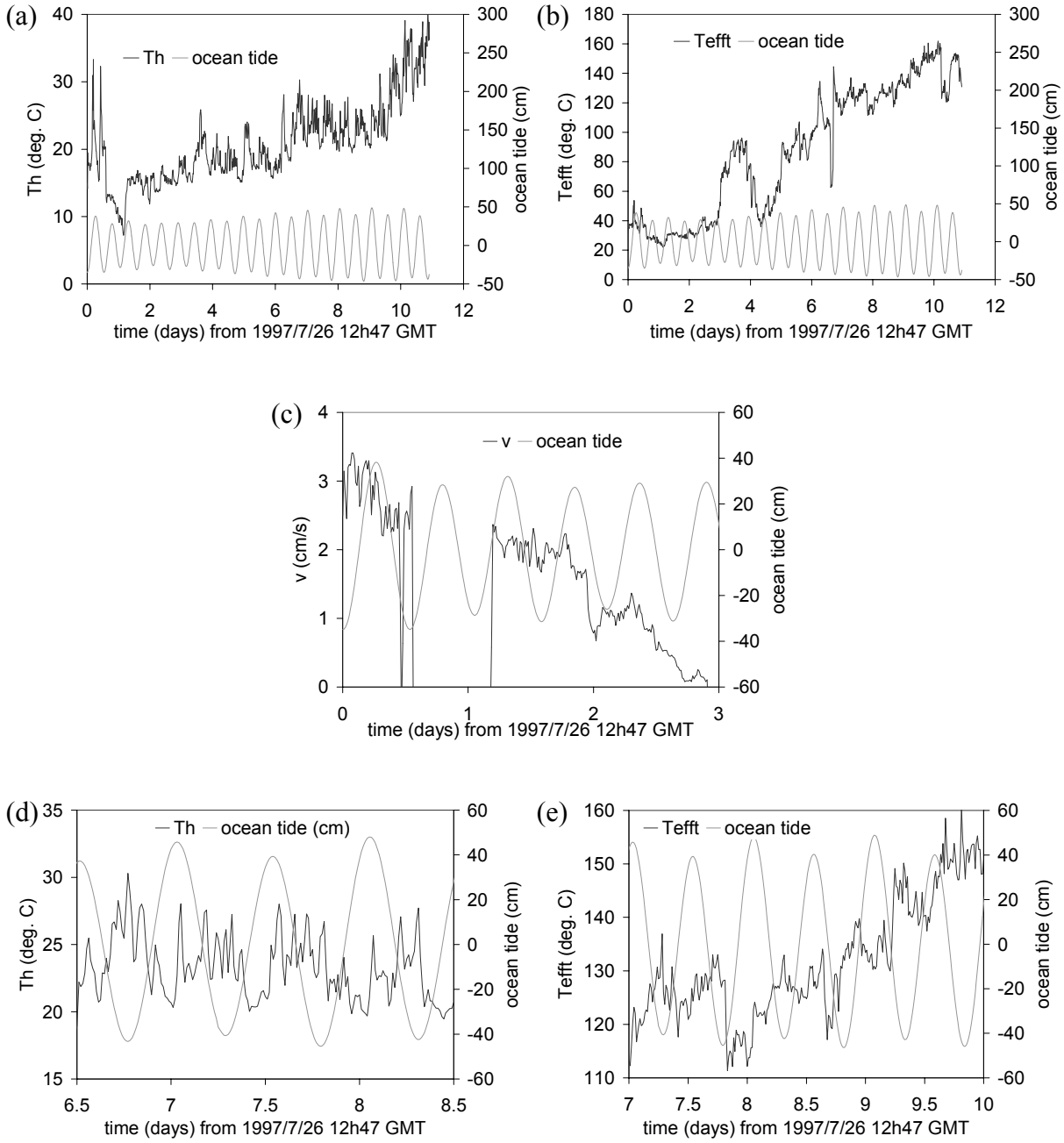

Figure 4.16: Data collected by Medusa at the Menez Gwen site (37.83°N, 31.50°W) on the Mid-Atlantic Ridge. *Th* – ambient (thermistor) temperature, *Tefft* – effluent temperature, *v* – effluent velocity.

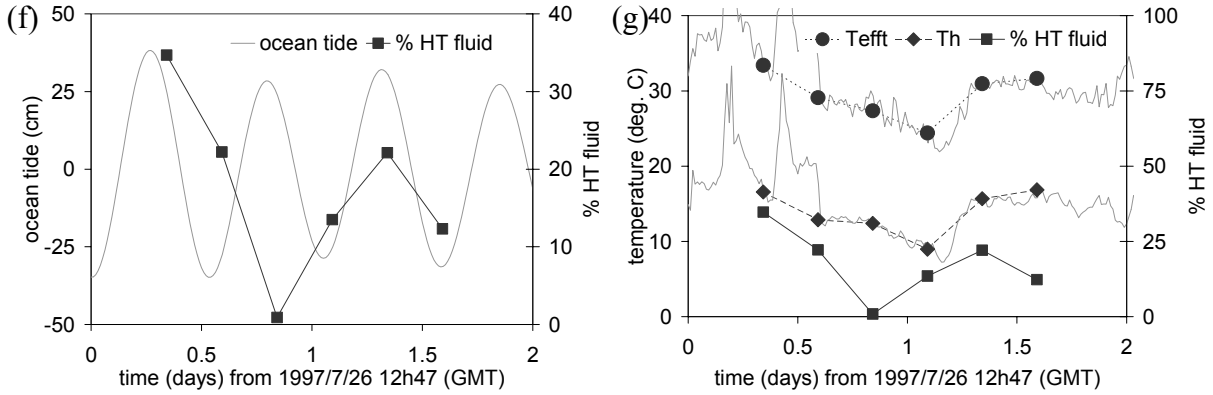

Figure 4.16: (continued) Data collected by Medusa at the Menez Gwen site (37.83°N, 31.50°W) on the Mid-Atlantic Ridge. *Th* – ambient (thermistor) temperature, *Tefft* – effluent temperature, *v* – effluent velocity.

Figure 4.16f shows that the chemical composition of the effluent displays a diurnal periodicity, with no obvious relationship to the semi-diurnal ocean tide. Figure 4.16g compares the inferred effluent composition with the ambient (*Th*) and effluent (*Tefft*) temperatures. The values of the temperatures at the times when the chemical samples were taken are highlighted in the figure. The *Th*- and *Tefft*-signals display similar changes over this period, despite the offset of ~10°C between them. This suggests that the same physical mechanism modulates ambient and effluent temperatures. It is possible to argue from Figure 4.16g that the effluent composition and the temperature channels display roughly similar changes over time, but the sparse data mean that this assertion cannot be made with confidence. However, it is equally true that there is no strong evidence for a *lack* of correlation between effluent temperature and composition in these data.

4.7.2.2 Medusa measurements – non-parametric analysis

The short time-series mean that it would be unjustified to attempt spectral analyses of the *v*-signal or the chemical data obtained by Medusa at Menez Gwen (Figure 4.16c,f). However, power spectra for the *Th*- and *Tefft*-signals, obtained using the MWPS code, are shown in Figure 4.17. The *Th*- and *Tefft*-signals each consist of N=1,047 datapoints (11 days) at a sampling interval of Δt=15 minutes. The power spectra were calculated using a time-bandwidth product of 2, 4 eigenspectra, and with a 96-point (= 24 h) autoregressive prewhitening filter.

Figures 4.17a and 4.17b show the estimated power spectrum of the *Th*-signal. The general trend of the spectrum takes the form $\hat{S}(f) \sim f^{-1.6}$. This is roughly consistent with the Kolmogorov hypothesis of Section 4.2.5, and hence with a model in which ambient temperature is modulated by a turbulent process. No significant spectral lines were detected for the *Th*-signal but there is evidence of broad peaks of spectral power around the semi-diurnal and quarter-diurnal frequency bands.

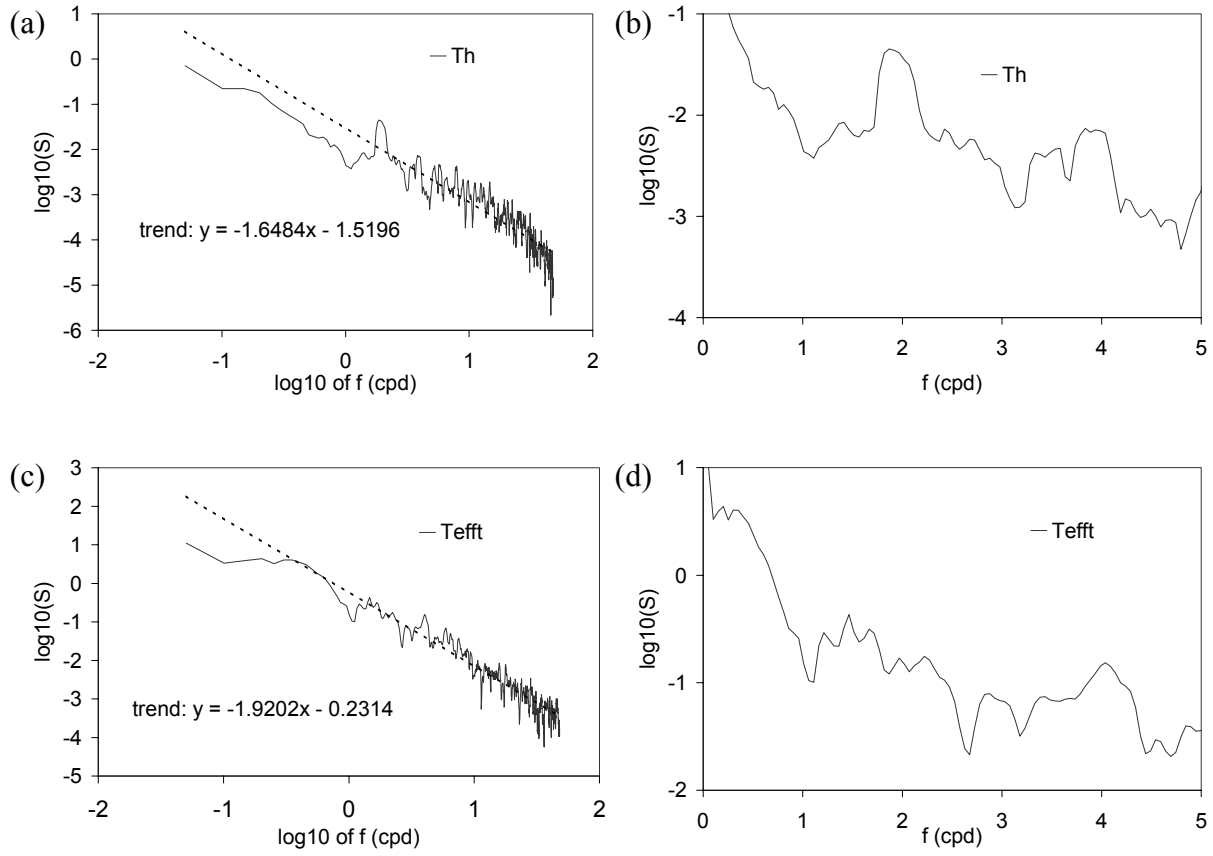

Figure 4.17: Spectral estimates for Medusa data collected at the Menez Gwen site (37.83°N, 31.50°W), calculated using the MWPS code. *Th* – ambient (thermistor) temperature, *Tefft* – effluent temperature.

In contrast, there is no evidence of power at tidal frequencies in the power spectrum of the *Tefft*-signal (Figures 4.17c,d), which has a general trend of the form $\hat{S}(f) \sim f^{-1.9}$.

Neither of these spectral estimates shows strong evidence of tidal modulation. Consequently, no attempt has been made to estimate Admiralty Method harmonic constants for these time-series.

4.7.3 The Lucky Strike site

Between 1997 and 1998, time-series data were collected using a Medusa system at the Lucky Strike site (37.28°N, 32.33°W) on the Mid-Atlantic Ridge (A. Schultz, *pers. comm.*, 1998). Time-series of ambient and effluent temperature were obtained over a period of 240 days from 1997/8/29. It had also been intended to obtain time-series of effluent velocity and composition, but these were not recovered successfully.

The Lucky Strike site is unique amongst the Medusa locations considered in this dissertation because horizontal current measurements for the site are available. A current meter and a temperature sensor were installed on a long-term mooring 20 m above the seafloor. Temperature and current measurements were made at hourly intervals over a period of 408 days from 1994/6/2 (A. Vangriesheim, *pers. comm.*, 1998).

4.7.3.1 Medusa measurements – time-domain

The data collected by Medusa at the Lucky Strike site are shown in the time-domain in Figure 4.18. The original time-series measurements of effluent velocity, effluent temperature and ambient temperature (sampling interval 15 s) have been low-pass filtered with a moving median filter of length 60 to produce time-series with a sampling interval of 15 min (Schultz *et al.,* 1992).

There is clear evidence of tidal modulation in the *Th*-signal (Figure 4.18a,c). A striking feature of the overview (Figure 4.18a) is the presence of an apparent springs/neaps cycle in the *Th*-signal which corresponds with the springs/neaps cycle of the ocean tide. There is clear evidence of semi-diurnal periodicity in the close-up view of Figure 4.18c, where it appears that the *Th*-signal is out of phase with the ocean tide. However, there is less evidence of semi-diurnal periodicity during the period shown in Figure 4.18e. Thus, while the *Th*-signal shows clear evidence of tidal modulation overall, there are times when non-tidal processes dominate the record. The *Tefft*-signal also exhibits semi-diurnal periodicity (Figure 4.18f), but it displays less evidence of a springs/neaps cycle than the *Th*-signal, and has a distinctly non-stationary appearance (Figure 4.18b). This non-stationarity is apparent in the sudden offsets in the record (e.g. at around day 200), and the changing amplitude of the semi-diurnal variations.

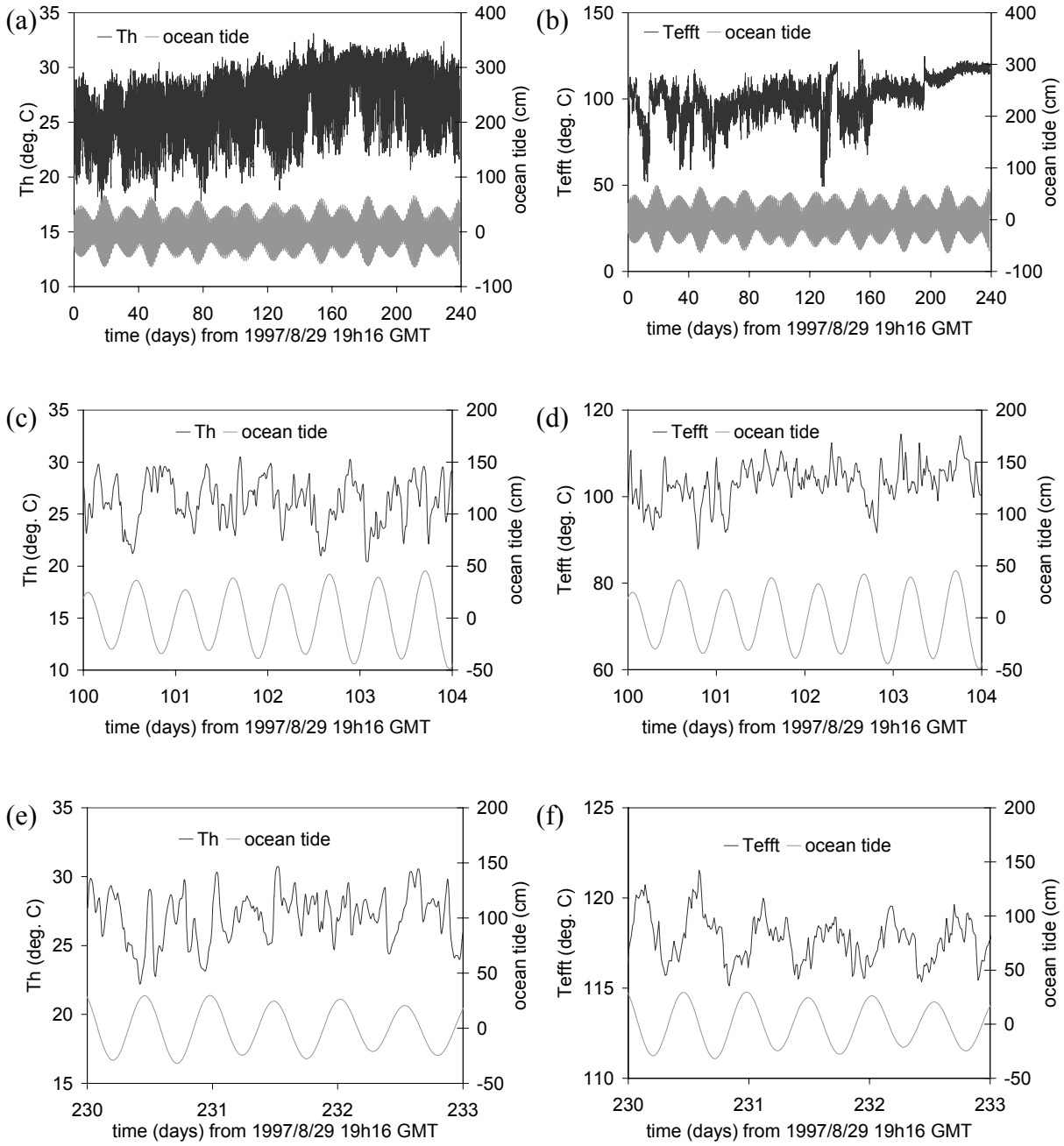

Figure 4.18: Temperature data collected by Medusa at the Lucky Strike site (37.28°N, 32.33°W) on the Mid-Atlantic Ridge. *Th* – ambient (thermistor) temperature. *Tefft* – effluent temperature.

In common with the *Th*-signal, there are times when the semi-diurnal periodicity of the *Tefft*-signal is very clear (Figure 4.18f), and times when it appears to have been swamped by other processes (Figure 4.18d). However, the *Th*- and *Tefft*-signals do not necessarily display strong tidal modulation at the same time. For example, the period between day 230 and day 233 is a time of strong tidal modulation of the *Tefft*-signal, but weak tidal modulation of the

Th-signal (Figure 4.18e,f). From the time-domain graph (Figure 4.18f), the *Tefft*-signal appears to be approximately out of phase with the ocean tide.

4.7.3.2 Medusa measurements – non-parametric analysis

Estimated power spectra for the *Th*- and *Tefft*-signals, obtained using the MWPS code, are shown in Figure 4.19. The power spectra were calculated from the low-pass filtered (15 min sampling interval) time-series which consist of N=22,931 datapoints (239 days). Accordingly, the power spectra were calculated using a time-bandwidth product of 10, using 20 eigenspectra and a 96-point (= 24 h) autoregressive prewhitening filter.

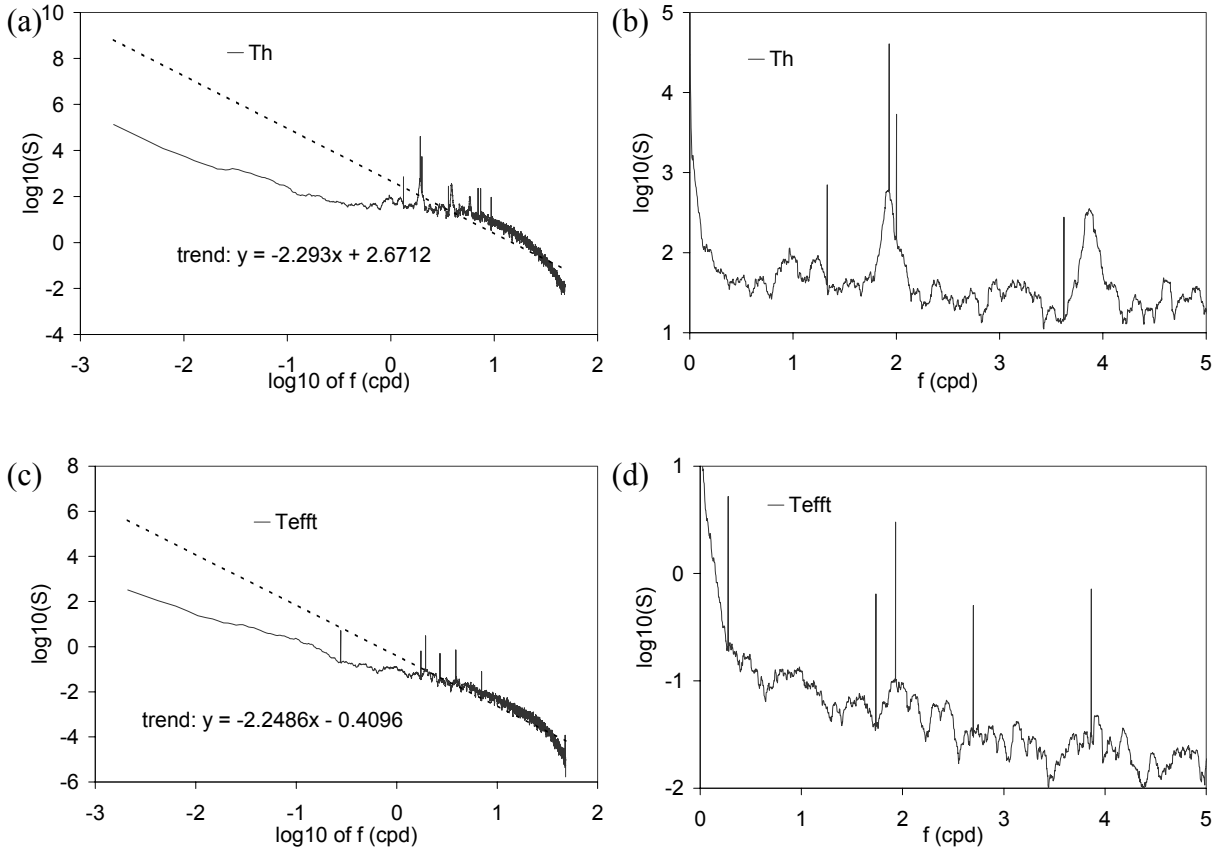

Figure 4.19: Spectral estimates for Medusa data collected at the Lucky Strike site (37.28°N, 32.33°W), calculated using the MWPS code. *Th* – ambient (thermistor) temperature, *Tefft* – effluent temperature.

The estimated power spectrum of the *Th*-signal has a general trend of the form $\hat{S}(f) \sim f^{-2.3}$, although the decay becomes steeper at the highest frequencies (Figure 4.19a). The close-up

view of the spectrum (Figure 4.19b) reveals that several significant line components were detected (Table 4.6).

Low frequency line components – *Th*-signal at Lucky Strike		
frequency of observed line (cpd)	frequency of associated tidal component (cpd)	name of associated tidal component
1.331 ± 0.002		
1.932 ± 0.002	1.932	*M2*
2.001 ± 0.002	2.000	*S2*
3.622 ± 0.002		

Table 4.6: Significant line components identified in the *Th*-signal at Lucky Strike.

The lowest frequency line appears at 1.331 ± 0.002 cpd, and is not tidal in origin. However the lines at 1.932 ± 0.002 cpd and 2.001 ± 0.002 cpd can confidently be identified with the *M2* (1.932 cpd) and *S2* (2.000 cpd) tidal components. The line at 3.622 ± 0.002 cpd lies outside the range of quarter-diurnal frequencies associated with tidal processes, and is unlikely to be tidal in origin. However, there is a broad quarter-diurnal peak centered on 3.87 cpd which corresponds to the 2nd harmonic of the semi-diurnal tidal frequencies, and there is a small peak in the diurnal frequency band (Figure 4.19b). In summary the non-parametric analysis presents very strong evidence of tidal modulation of the *Th*-signal.

The estimated power spectrum of the *Tefft*-signal has a general trend of the form $\hat{S}(f) \sim f^{-2.2}$ (Figure 4.19c), and is broadly similar to the power spectrum of the *Th*-signal. The close-up view of the spectrum (Figure 4.19d) reveals that several significant line components were detected (Table 4.7).

Low frequency line components – *Tefft*-signal at Lucky Strike		
frequency of observed line (cpd)	frequency of associated tidal component (cpd)	name of associated tidal component
0.277 ± 0.002		
1.736 ± 0.002		
1.932 ± 0.002	1.932	*M2*
2.699 ± 0.002		
3.866 ± 0.002	3.865	2nd harmonic of *M2*

Table 4.7: Significant line components detected in the *Tefft*-signal at Lucky Strike.

Three of these lines cannot be tidal in origin because they do not occur at frequencies associated with the tidal potential. These lines occur at 0.277 ± 0.002 cpd, 1.736 ± 0.002 cpd

and 2.699 ± 0.002 cpd. However, the line at 1.932 ± 0.002 cpd corresponds to the *M2* component and the line at 3.866 ± 0.002 cpd corresponds to its 2nd harmonic.

In summary, the estimated power spectra (Figure 4.19) provide strong evidence that both the *Th*- and *Tefft*-signals are tidally modulated. The spectra are dominated by power in the semi-diurnal band and contain significant power in the quarter-diurnal band.

4.7.3.3 Medusa data – parametric description

The Admiralty Method harmonic constants for the *Th*- and *Tefft*-signals are estimated using the HYBRID code. These harmonic constants are compared with the harmonic constants of the local tidal potential and ocean tide in Table 4.8 and Figure 4.20.

An initial attempt was made to decompose the whole of the *Th*- and *Tefft*-signals using the Bayesian drift technique but better results were obtained using section averaging with mean removal. The original time-series (of N=22,931 points) were split into 112 overlapping sections of 672 points (= 7 days), giving a 30% offset between sections.

Using Table 4.8 and Figure 4.20, the harmonic constants of the *Th*-signal can be compared with those of the two postulated input signals (the tidal potential and the ocean tide). The relative magnitude of semi-diurnal to diurnal components $(H_1+H_2)/(H_3+H_4)$ is diagnostic as it differs greatly between the tidal potential and the ocean tide at this location. This ratio takes the value $(H_1+H_2)/(H_3+H_4)=0.998$ for the tidal potential, which indicates a mixed tide. The ocean tide, on the other hand, is strongly a semi-diurnal tide, with $(H_1+H_2)/(H_3+H_4)=9.4$. For the *Th*-signal, $(H_1+H_2)/(H_3+H_4)=3.99$ (Table 4.8). This is sufficiently large for the associated signal to appear semi-diurnal in the domain. Consequently, on the basis of the relative power in the diurnal and semi-diurnal band, it is concluded that the *Th*-signal is more similar to the ocean tide than the tidal potential (Figure 4.20a,c,e).

For example, the difference in phase lag, (g_2-g_1), is 21° for both the *Th*-signal and ocean tide, but it is less than 1° for the tidal potential. Thus, the semi-diurnal components of the *Th*-signal both lag the semi-diurnal components of the ocean tide by 172° (Table 4.8). This is consistent with the observation made in the time-domain that the *Th*-signal and the ocean tide are out of phase.

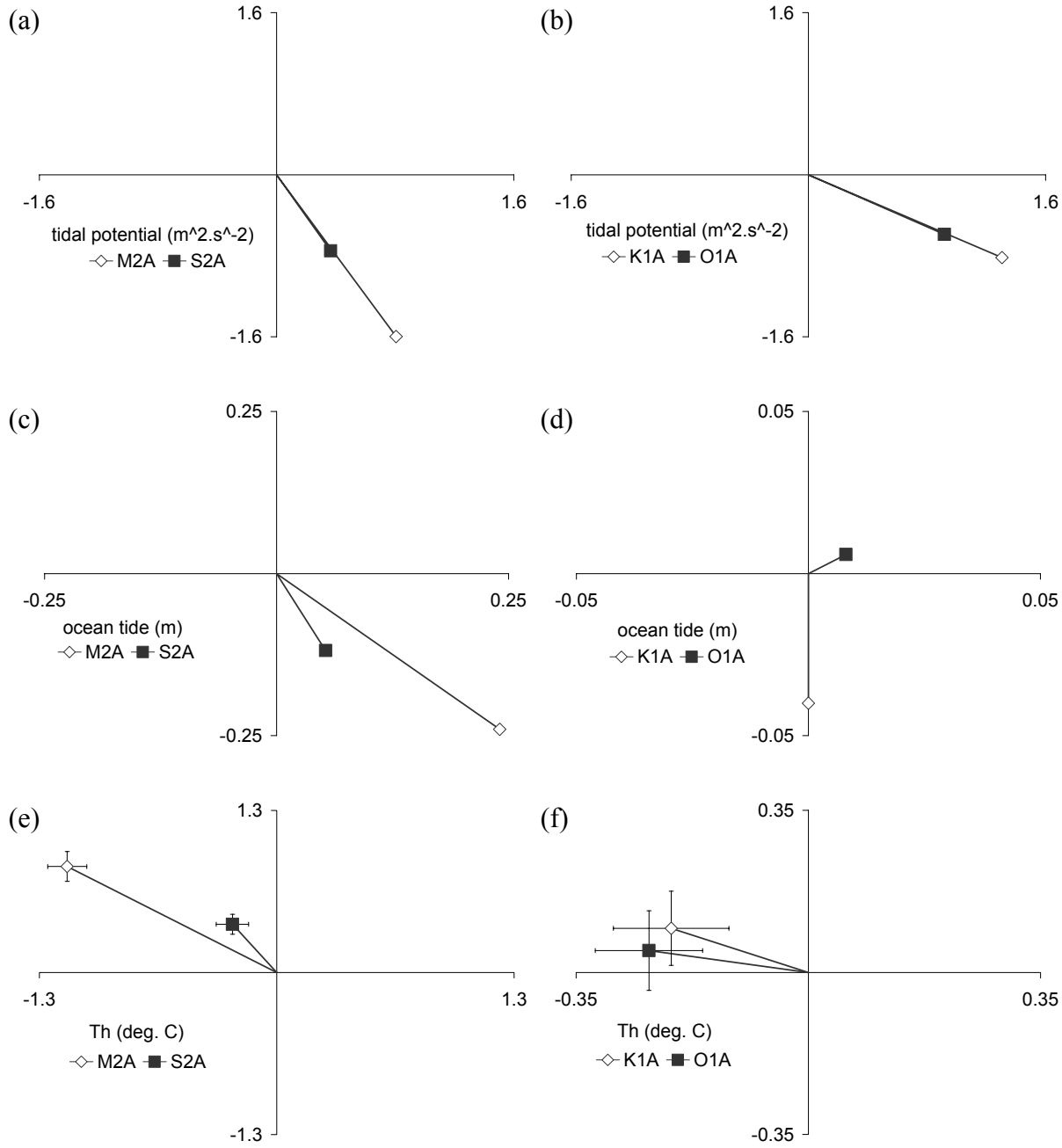

Figure 4.20: Admiralty Method harmonic constants for the Lucky Strike site (37.28°N, 32.33°W) calculated using the HYBRID code. Tidal potential from ETGTAB code, Ocean tide from CSR code, *Th* – ambient (thermistor) temperature measured by Medusa.

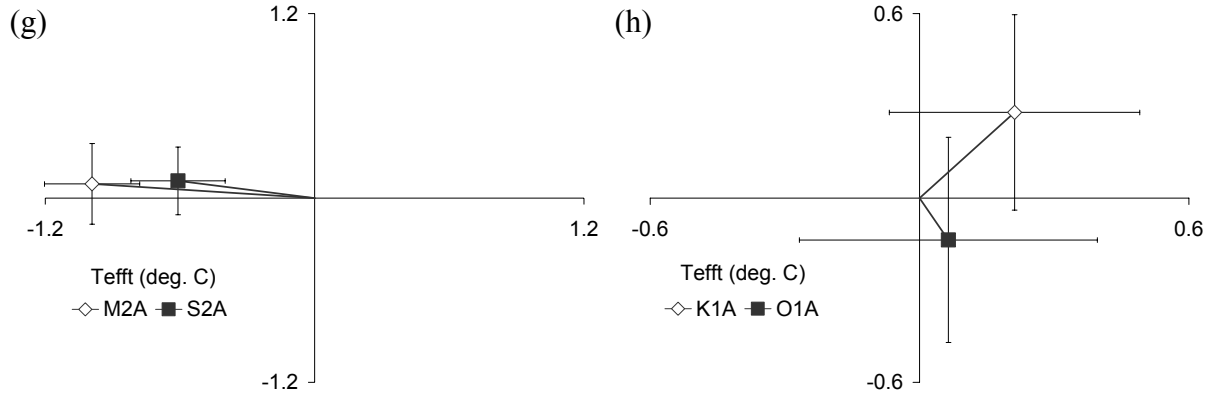

Figure 4.20: (continued) Admiralty Method harmonic constants for the Lucky Strike site (37.28°N, 32.33°W) estimated using the HYBRID code. *Tefft* – Medusa effluent temperature.

The ratio of magnitudes of the semi-diurnal components (H_1/H_2) is 3.13 for the *Th*-signal. This is roughly consistent with both the ocean tide (H_1/H_2=2.62) and the tidal potential (H_1/H_2=2.14).

Lucky Strike	H_1 (*M2A*)	g_1 (*M2A*)	H_2 (*S2A*)	g_2 (*S2A*)	H_3 (*K1A*)	g_3 (*K1A*)	H_4 (*O1A*)	g_4 (*O1A*)
potential ($m^2.s^{-2}$)	1.79	63°	0.835	64°	1.54	32°	1.09	33°
ocean (m)	0.34	45°	0.13	66°	0.04	90°	0.01	324°
Th (°C)	1.43	217°	0.46	238°	0.23	205°	0.24	191°
Tefft (°C)	1.00	185°	0.62	190°	0.35	307°	0.15	65°
ve ($mm.s^{-1}$)	60.6	329°	13.6	3°	3.2	261°	3.9	253°
vn ($mm.s^{-1}$)	74.5	279°	16.2	329°	3.2	213°	3.7	244°
T (°C)	0.096	230°	0.022	226°	0.0042	115°	0.0036	45°

Lucky Strike	$(H_1+H_2)/(H_3+H_4)$	H_1/H_2	g_2-g_1	H_3/H_4	g_4-g_3
potential ($m^2.s^{-2}$)	0.998	2.14	< 1°	1.41	< 1°
ocean (m)	9.4	2.62	21°	4.0	-126°
Th (°C)	3.99	3.13	21°	0.93	-13°
Tefft (°C)	3.23	1.61	5°	2.32	117°
ve ($mm.s^{-1}$)	10.6	4.47	34°	0.82	-8°
vn ($mm.s^{-1}$)	13.17	4.59	50°	0.86	31°
T (°C)	15.12	4.30	-4°	1.17	-71°

Table 4.8: Admiralty Method harmonic constants for the Lucky Strike site, calculated for the tidal potential, ocean tide, Medusa data and water column data.

In the diurnal band, the difference in phase lag of the harmonic constants, (g_4–g_3), is only 13° for the *Th*-signal, and the magnitudes of the diurnal components are approximately equal

($H_3/H_4 \approx 1$). Consequently, the diurnal harmonic constants of the *Th*-signal display more similarity with the tidal potential than with the ocean tide. However, the error bars associated with these estimates are considerable and the spectral estimate (Figure 4.19b) displays significantly more power in the semi-diurnal band than the diurnal. For this reason, it seems reasonable to give more weight to the evidence of the semi-diurnal harmonic constants. Following this line of reasoning, it is concluded that the *Th*-signal has a tidal part which is very similar to the ocean tide, but with the semi-diurnal components delayed by 172°.

A similar interpretation can be made of the harmonic constants of the *Tefft*-signal (Figure 4.20g,h). The diurnal components are poorly resolved (see the error bars in Figure 4.20h) and are not considered further. Within the semi-diurnal band, the difference in phase lag between *M2A* and *S2A*, (g_2-g_1), is 5°, which is closer to the value for the tidal potential (<1°) than to that for the ocean tide (21°). At first glance, this might seem to be evidence linking the effluent temperature more closely to the tidal potential than to the ocean tide. However, the size of the error bars in Figure 4.20g means that such an inference would be unwise. In common with the *Th*-signal, the semi-diurnal components of the *Tefft*-signal are approximately out of phase with the ocean tide. For the *M2A* component, the *Tefft*-signal lags the ocean tide by 140°. For the *S2A* component, the lag is 124°.

4.7.3.4 Water column measurements – time-domain

Current and temperature data collected in the water column at Lucky Strike are shown in the time-domain in Figure 4.21 (A. Vangriesheim, *pers. comm.*, 1998). These data were collected from sensors moored 20 m above the seafloor. Time-series for the eastwards (*ve*) and northwards (*vn*) velocity are shown, along with a time-series of the current speed (*spd*), defined by $spd^2 = ve^2 + vn^2$. The temperature time-series (*T*) was obtained at the same location. All of these series show clear evidence of tidal modulation in the time-domain (Figure 4.21).

The time-series are predominantly semi-diurnal (Figures 4.21b,d), and exhibit a springs/neaps cycle (Figures 4.21a,c). The *spd*-signal displays quarter-diurnal periodicity (Figure 4.21f; Section 2.6.3). Consequently, any physical process which depends on the magnitude of the tidal stream, but not on its direction, is expected to exhibit the same frequency-doubling effect.

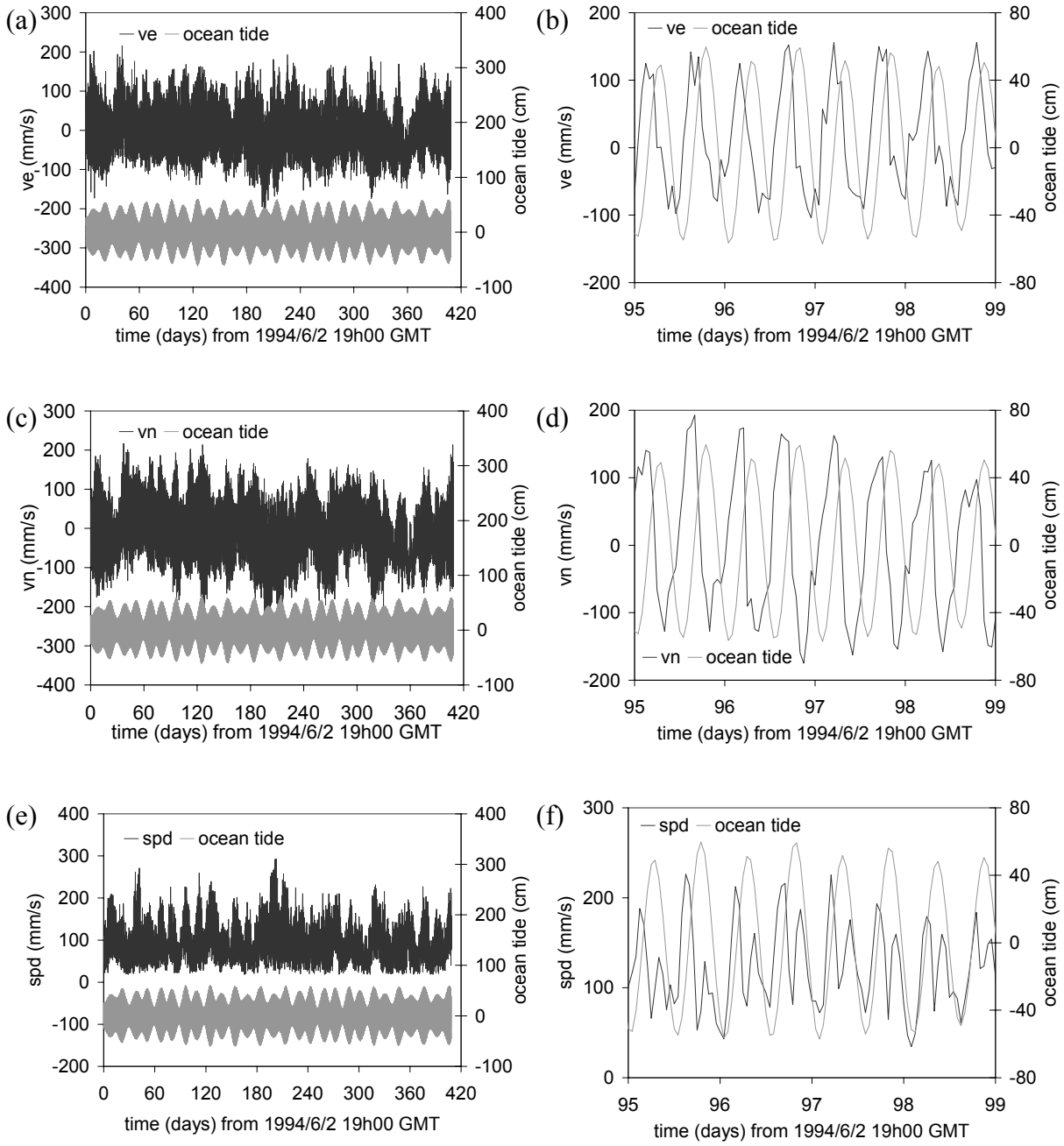

Figure 4.21: Current meter data collected at Lucky Strike (37.28°N, 32.33°W), from a sensor moored 20 m above the seafloor. *ve* – eastward velocity, *vn* – northward velocity, *spd* – speed. Data collected by A. Vangriesheim (*pers. comm.*, 1998).

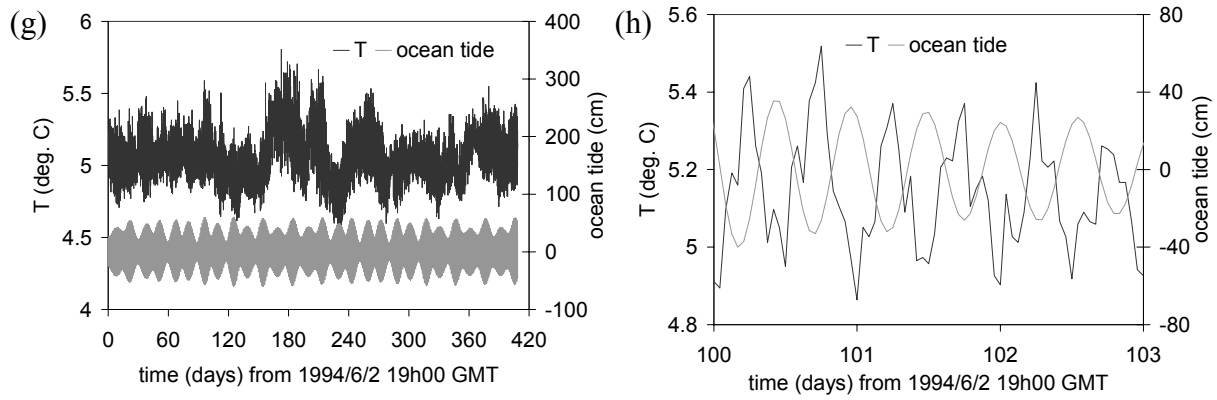

Figure 4.21: (continued) Temperature data (*T*) collected at Lucky Strike (37.28°N, 32.33°W), from a sensor moored 20 m above the seafloor. Data collected by A. Vangriesheim (*pers. comm.*, 1998).

The *T*-signal also displays semi-diurnal periodicity and a clear springs/neaps cycle (Figure 4.21g,h). From Figure 4.21g,h, the *T*-signal lags the ocean tide by ~180°.

4.7.3.5 Water column measurements – non-parametric analysis

Power spectra for the *ve*-, *vn*-, *spd*- and *T*- time-series were calculated using the MWPS code and are shown in Figure 4.22. The time-series cover 408 days and consist of N=9,808 datapoints at a sampling interval of Δt = 1 h. The power spectra were calculated using a time-bandwidth product of 10, using 20 eigenspectra and with a 24-point (=24 h) autoregressive prewhitening filter.

The estimated power spectra of the *ve*- and *vn*-signals both have a general trend of the form $\hat{S}(f) \sim f^{-1.3}$ (Figures 4.22a,c), and contain several significant line components at the low frequency end of the spectrum (Figure 4.22b,d; Tables 4.9, 4.10).

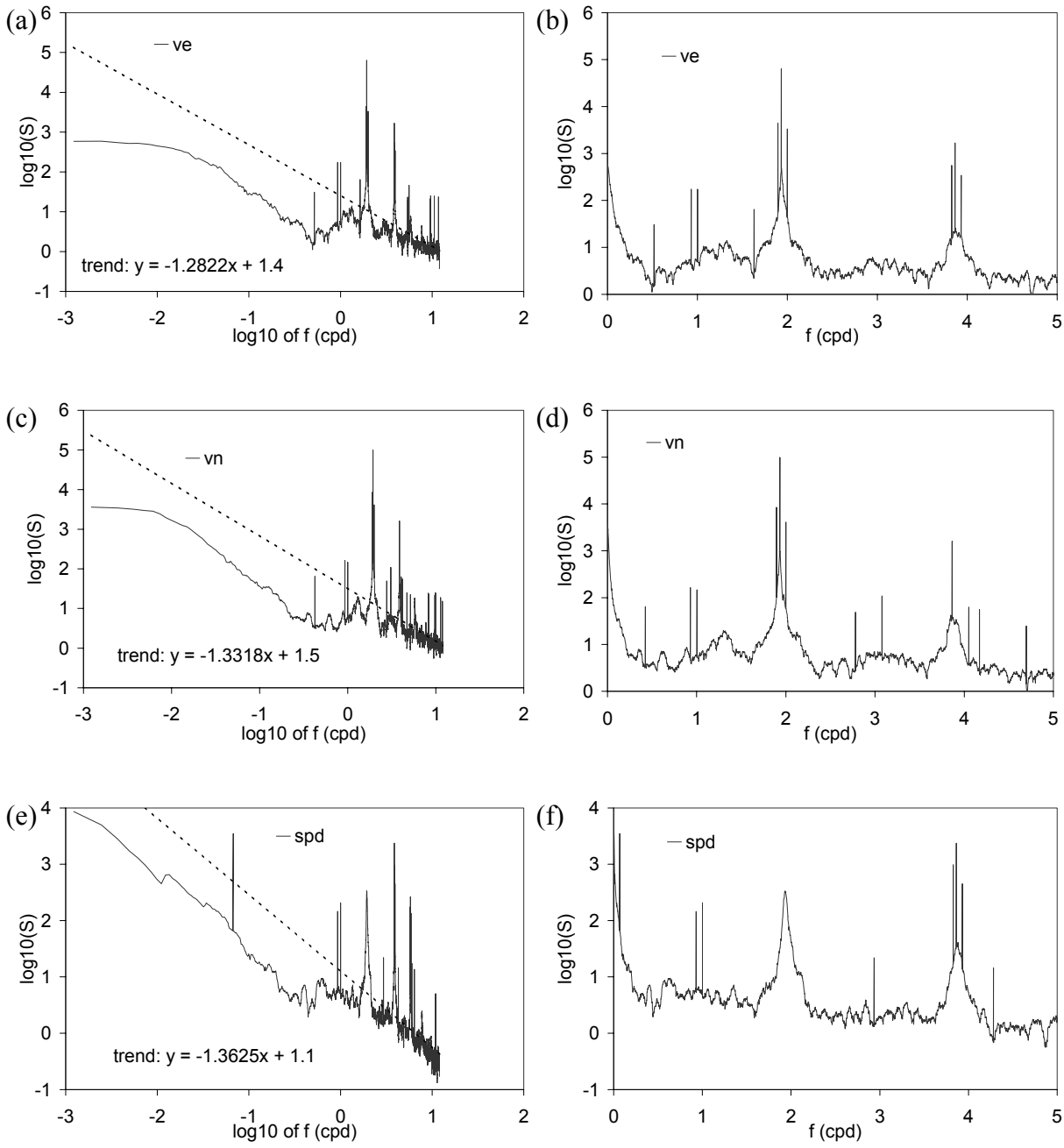

Figure 4.22: Spectral estimates for the water column data collected 20 m above the seafloor at Lucky Strike (37.28°N, 32.33°W) calculated using the MWPS code. *ve* – eastward velocity, *vn* – northward velocity, *spd* – speed. Data collected by A. Vangriesheim (*pers. comm.*, 1998).

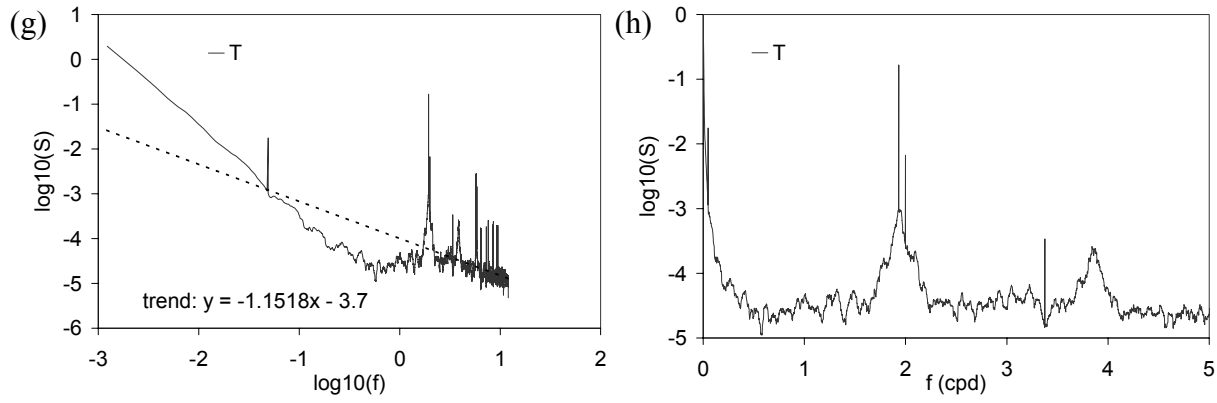

Figure 4.22: (continued) Spectral estimates for the water column data collected 20 m above the seafloor at Lucky Strike (37.28°N, 32.33°W) calculated using the MWPS code. *T* – temperature. Data collected by A. Vangriesheim (*pers. comm.*, 1998).

Most of the observed line components in the two velocity channels coincide with known tidal components. Therefore the estimated spectra constitute very strong evidence of tidal modulation of the velocity signals.

Low frequency line components – *ve* signal at Lucky Strike		
frequency of observed line (cpd)	frequency of associated tidal component (cpd)	name of associated tidal component
0.518 ± 0.001		
0.930 ± 0.001	0.930	*O1*
1.002 ± 0.001	1.003	*K1*
1.630 ± 0.001		
1.896 ± 0.001	1.896	*N2*
1.932 ± 0.001	1.932	*M2*
1.999 ± 0.001	2.000	*S2*
3.828 ± 0.001		
3.865 ± 0.001	3.865	2nd harmonic of *M2*
3.932 ± 0.001		

Table 4.9: Significant line components detected in the *ve*-signal (Figure 4.22b).

The estimated spectrum of the *spd*-signal is shown in Figures 4.22e,f, with the significant line components listed in Table 4.11. Of course, the *spd*-signal is derived from the *ve*- and *vn*-signals, so it is no surprise to find that its spectrum has power concentrated in the same frequency bands and their harmonics. The larger concentration of power in the quarter-diurnal band is caused by the frequency-doubling observed in the time-domain. It is

interesting to note that, despite this effect, the spectrum for the *spd*-signal retains two harmonic lines in the diurnal band (Table 4.11).

Low frequency line components – *vn* signal at Lucky Strike		
frequency of observed line (cpd)	frequency of associated tidal component (cpd)	name of associated tidal component
0.424 ± 0.001		
0.930 ± 0.001	0.930	*O1*
1.002 ± 0.001	1.003	*K1*
1.896 ± 0.001	1.896	*N2*
1.932 ± 0.001	1.932	*M2*
2.001 ± 0.001	2.000	*S2*
2.780 ± 0.001		
3.079 ± 0.001		
3.865 ± 0.001	3.865	2nd harmonic of *M2*
4.052 ± 0.001		
4.172 ± 0.001		
4.697 ± 0.001		

Table 4.10: Significant line components detected in the *vn*-signal (Figure 4.22d).

The estimated spectrum of the *T*-signal is shown in Figures 4.22g,h. It has a general trend of the form $\hat{S}(f) \sim f^{-1.2}$, which is broadly similar to the general trend of the velocity spectra. This is consistent with the hypothesis that temperature changes at this height (20 m above the seafloor) are caused by the lateral movement of hydrothermal plumes. The close-up view of the spectrum (Figure 4.22h) shows no evidence of significant power in the diurnal band, but there is a broad semi-diurnal peak and significant lines were found at the principal semi-diurnal frequencies (Table 4.12).

Low frequency line components – *spd* signal at Lucky Strike		
frequency of observed line (cpd)	frequency of associated tidal component (cpd)	name of associated tidal component
0.067 ± 0.001	0.068	*MSf*
0.930 ± 0.001	0.930	*O1*
1.002 ± 0.001	1.003	*K1*
2.935 ± 0.001		
3.828 ± 0.001		
3.864 ± 0.001	3.865	2nd harmonic of *M2*
3.931 ± 0.001		
4.282 ± 0.001		

Table 4.11: Significant line components detected in the *spd*-signal at Lucky Strike (Figure 4.22f).

Low frequency line components – *T*-signal		
frequency of observed line (cpd)	frequency of associated tidal component (cpd)	name of associated tidal component
0.049 ± 0.001		
1.932 ± 0.001	1.932	*M2*
1.999 ± 0.001	2.000	*S2*
3.377 ± 0.001		

Table 4.12: Significant line components detected in the *T*-signal (Figure 4.22h).

In conclusion, the estimated power spectra for the velocity and temperature data collected in the water column all present strong evidence of tidal modulation. The identification of so many statistically significant harmonic lines by the MWPS code is particularly compelling. The presence of strong quarter-diurnal periodicity in the *spd*-signal (Figure 4.21f) renders it unsuitable for an Admiralty Method analysis. However, the *ve*- *vn*- and *T*-signals appear to be relatively clean tidal signals in the time-domain, and are therefore subjected to an Admiralty Method analysis below.

4.7.3.6 Water column measurements – parametric analysis

Admiralty Method harmonic constants for the *ve*-, *vn*- and *T*-signals are estimated using the HYBRID code. They are listed in Table 4.8 and shown graphically in Figure 4.23, where they are compared with the equivalent harmonic constants for the local ocean tide.

The harmonic constants for the *ve*- and *vn*-signals were estimated using Huber-weighted section averaging with mean removal (Section 3.3.4) because Bayesian drift removal proved unsuccessful in these cases, for the reasons outlined in Section 4.5.1. The original time-series of N=9,808 points was split into 192 overlapping sections of 168 points (= 7 days), giving a 30% offset between sections.

The harmonic constants for the *ve*- and *vn*-signals show a marked similarity with those for the local ocean tide. The relative magnitude of semi-diurnal and diurnal components is similar for all three signals, with $(H_1+H_2)/(H_3+H_4)$=9.4 for the ocean tide, $(H_1+H_2)/(H_3+H_4)$=10.6 for the *ve*-signal and $(H_1+H_2)/(H_3+H_4)$=13.17 for the *vn*-signal (Table 4.8).

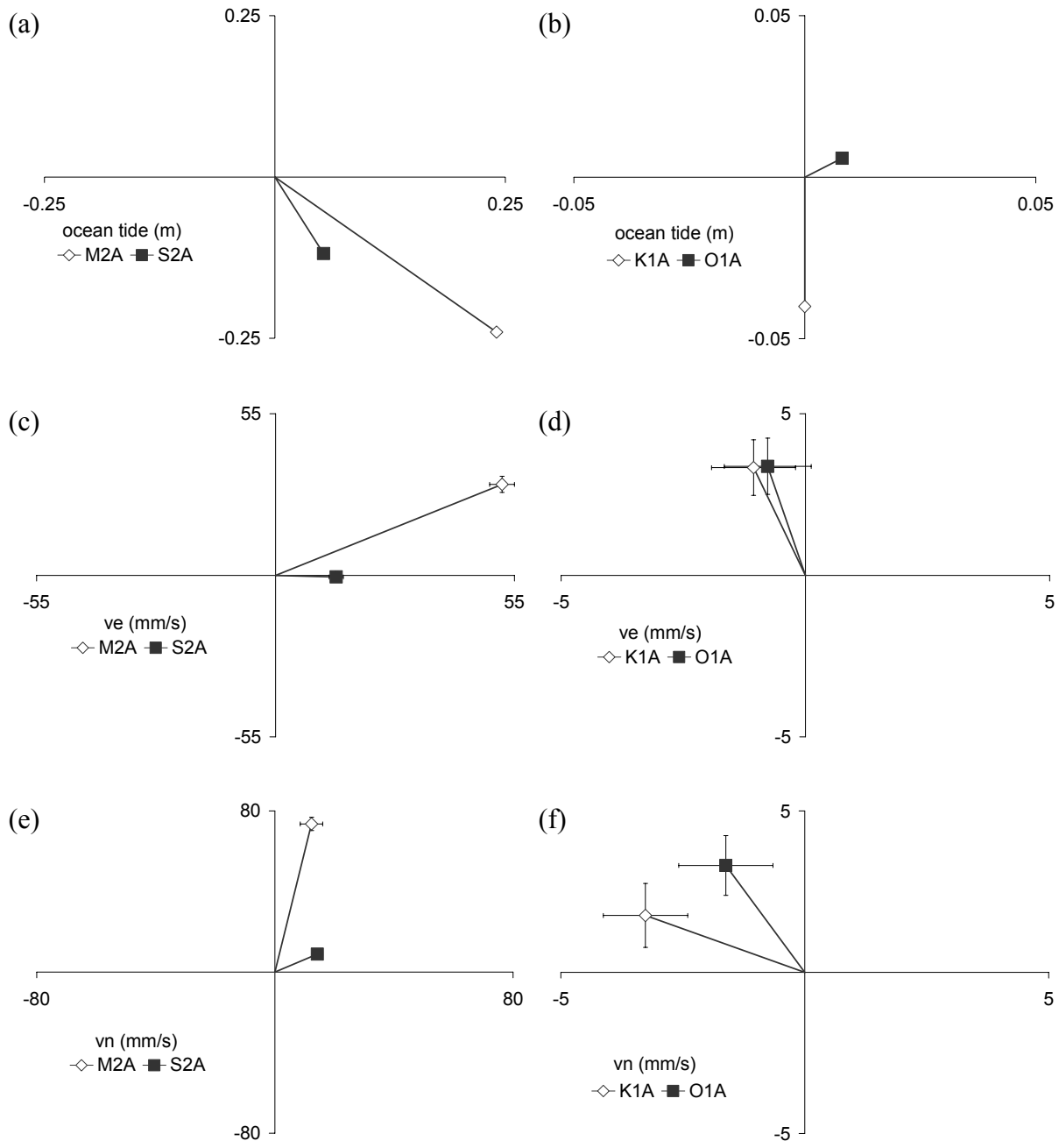

Figure 4.23: The Admiralty Method harmonic constants for the water column data collected at Lucky Strike (37.28°N, 32.33°W) calculated using the HYBRID code, compared with the harmonic constants for the local ocean tide. *ve* – eastward velocity. *vn* – northward velocity.

Furthermore, the relative magnitudes and phases of the semi-diurnal components (H_1/H_2 and (g_2–g_1)) are broadly similar for the three signals, so that the semi-diurnal harmonic constants of the *ve*- and *vn*-signals appear to be rotated versions of their ocean tide equivalents in the complex plane (Figures. 4.23a,c,e).

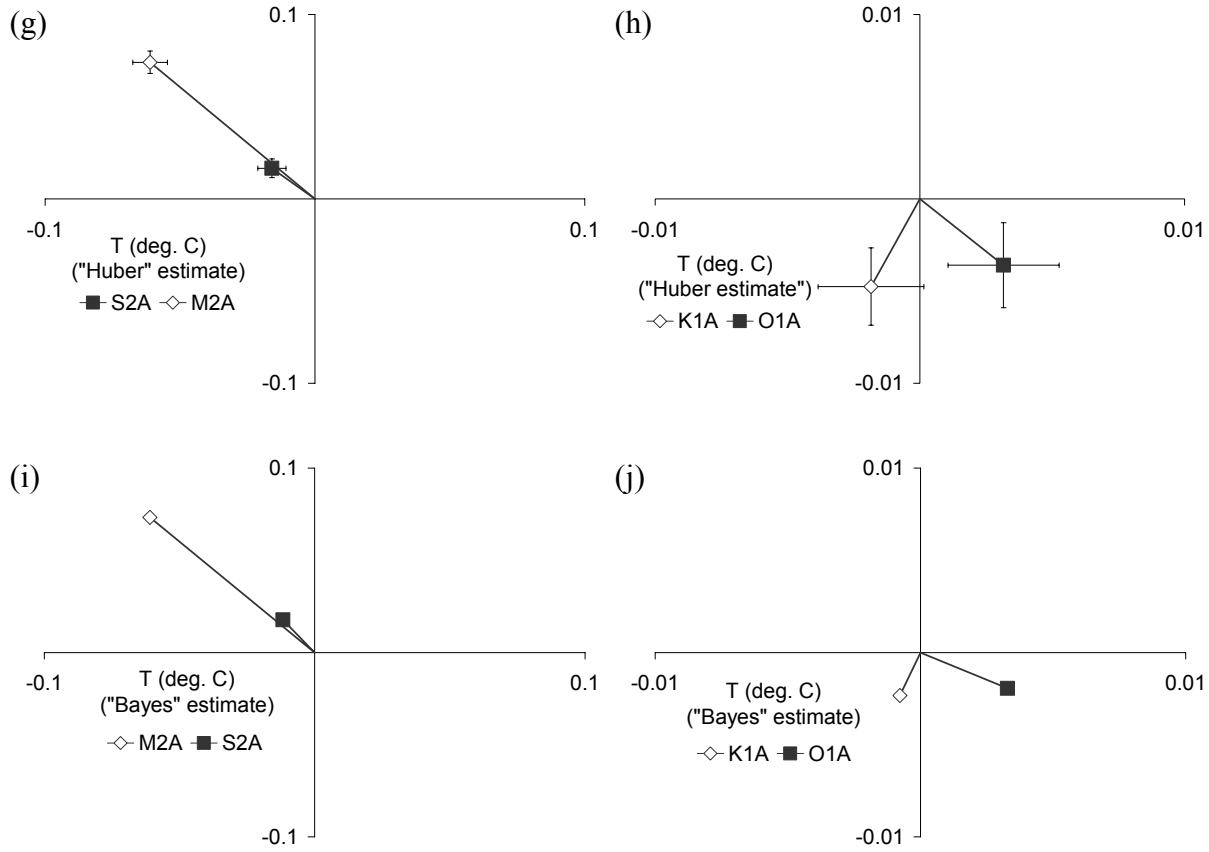

Figure 4.23: (continued) The Admiralty Method harmonic constants estimated for the *T*-signal collected at Lucky Strike (37.28°N, 32.33°W) using the HYBRID code. The "Huber" estimate was made using section averaging with mean removal. The "Bayes" estimate was made using Bayesian drift removal (Section 3.3.4).

This similarity of harmonic constants is not surprising – indeed, it is to be expected from the simple theory of tidal streams presented in Chapter 2 – but it is, nonetheless, worth noting. It increases confidence that the semi-diurnal harmonic constants provide an accurate parametric description of the velocity time-series.

The diurnal harmonic constants of the velocity signals, on the other hand, do not display a similar phase relationship to those of the ocean tide (Figures 4.23b,d,f). They are also much smaller in magnitude than the semi-diurnal harmonic constants. For these reasons, the diurnal harmonic constants are poorly constrained, and no attempt is made to draw inferences from them.

Two sets of harmonic constants for the *T*-signal were estimated using the HYBRID code. The first set (Figures 4.23g,h) was calculated using the same Huber-weighted section averaging technique which is applied to the *ve*- and *vn*-signals above. The second set (Figures 4.23i,j) was calculated using Bayesian drift removal. There is a striking similarity between the two sets of harmonic constants. The *T*-signal is therefore unique, among the datasets considered here, in yielding a credible set of harmonic constants under analysis by the HYBRID code using the Bayesian drift removal procedure. The results of this analysis are shown in the time-domain in Figure 4.24.

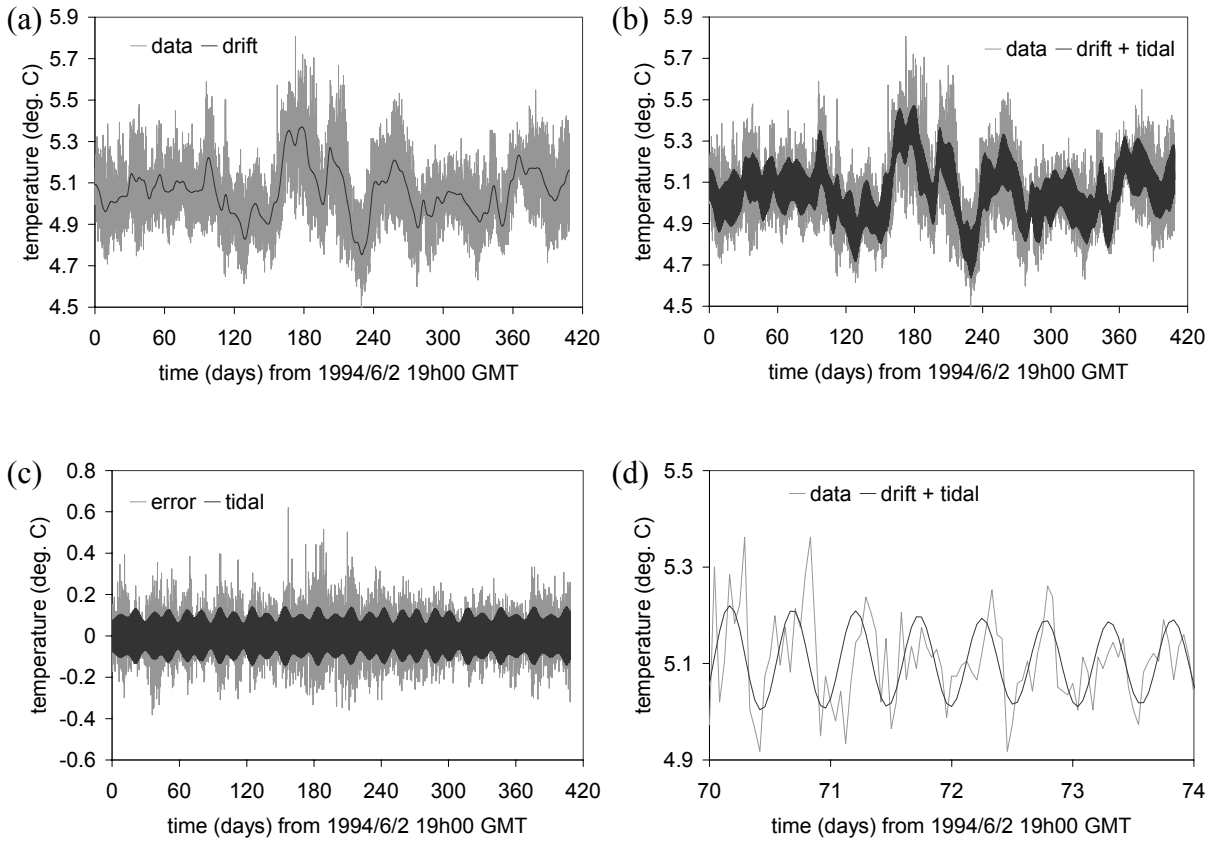

Figure 4.24: The results of the extraction of Admiralty Method harmonic constants from the water column *T*-signal at Lucky Strike (37.28°N, 32.33°W), using the HYBRID code with the Bayesian drift removal technique of Section 3.3.3.

The Bayesian drift removal algorithm of the HYBRID code is designed to decompose the original time-series (*data*) into a sum of three separate time-series (*drift*, *tidal* and *error*). The set of Admiralty Method harmonic constants which generate the *tidal* signal constitute a parametric estimate of the tidal information in the original data (Section 3.3.3). There is a

considerable amount of drift in the *T*-signal, but it has been successfully identified by the algorithm (Figure 4.24a). Figures 4.24b and 4.24d show that the sum of the *drift* and *tidal* signals corresponds well with the original data. For example, the springs/neaps cycle has been reproduced quite well. Since the springs/neaps cycle is caused by the beating of the *M2* and *S2* components, this constitutes evidence that the estimated phases for the *M2A* and *S2A* components are reliable.

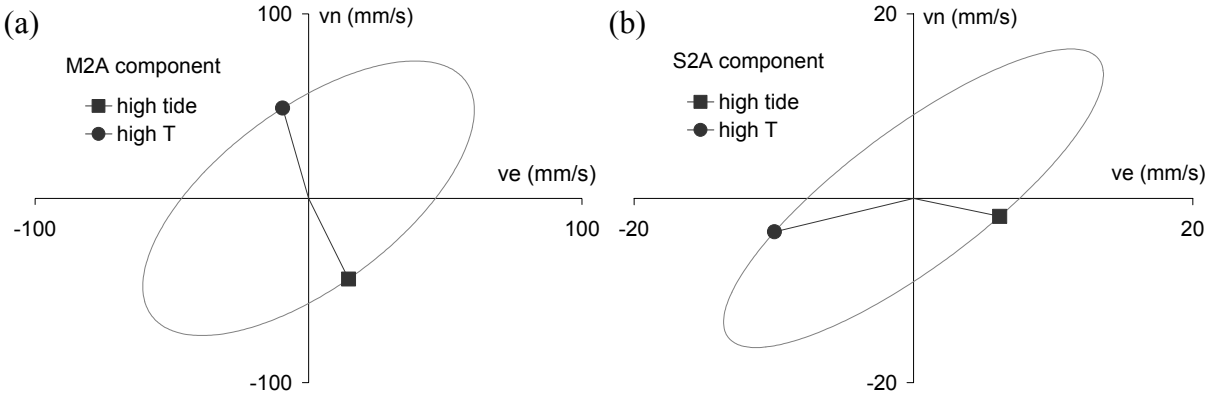

Figure 4.25: Tidal current ellipses extracted from the water column data collected at Lucky Strike (37.28°N, 32.33°W). The Admiralty Method harmonic constants of Table 4.8 were used to generate the ellipses. Also shown on each diagram are the current vector at the time of highest ocean tide ('high tide'), and the current vector at the time of highest measured temperature ('high T').

The phase relationship between velocity (*ve*, *vn*), ocean tide (ζ) and temperature (*T*) can now be examined, making use of the harmonic constants estimated for each series. Firstly, consider the *M2A* component of each time-series. Let *t* be the time (in hours) since the Greenwich passage of the *M2A* component of the tidal potential. Let ω be the angular speed of the *M2A* component (in degrees per hour). The *M2A* components of the four time-series can now be expressed as functions of time, using the harmonic constants of Table 4.6:

$$\left\{\begin{array}{l} ve_{M2A}(t) = 60.6\cos(\omega t - 329) \\ vn_{M2A}(t) = 74.5\cos(\omega t - 279) \\ T_{M2A}(t) = 0.096\cos(\omega t - 230) \\ \zeta_{M2A}(t) = 0.34\cos(\omega t - 45) \end{array}\right\} \tag{4.11}$$

In a horizontal plane where *x* points east and *y* points north, the velocity vector is ($ve(t)$,$vn(t)$), at time *t*. As *t* varies over the course of a tidal cycle, this vector traces a curve in

the *x-y* plane known as the current ellipse. The *M2A* current ellipse for the Lucky Strike velocity data is shown in Figure 4.25a. Hence T_{M2A} is maximised when $\omega t = 230°$, and ζ_{M2A} is maximised when $\omega t = 45°$. The current vectors corresponding to these times are shown in Figure 4.25a. This figure shows that, for the *M2A* component, the current flows slightly west of due north at the time of maximum temperature, and slightly east of due south at the time of high tide. The sensor was moored 400 m due north of the Statue of Liberty hydrothermal vent (A. Vangriesheim, *pers. comm.*, 1998), so it is possible that the tidal temperature variations are due to advection of a plume northwards from the vent site. Figure 4.25b shows the tidal ellipse for the *S2A* component. For this component, the time of highest temperature corresponds to an approximately westward current, which seems inconsistent with the *M2A* result. However, the *S2A* component is much smaller in magnitude and is probably less well constrained.

In summary, the water column data discussed above demonstrate the utility of the Bayesian drift removal technique for sufficiently 'clean' tidal signals. Well constrained Admiralty Method harmonic constants for the tidal streams are extracted for the tidal streams by the HYBRID code. Consequently, the tidal streams at Lucky Strike can be estimated in the time-domain for any date. The harmonic constants are consistent with a model in which the modulation of water column temperature is caused by advection of a plume from the Statue of Liberty hydrothermal vent.

4.8 Other hydrothermal sites

Kadko (1994) reports that a gamma-ray detector placed in diffuse (25°C) flow at the Monolith Vent of the Juan de Fuca Ridge (44.9800°N, 130.2217°W) recorded tidal variations in total radioactivity over a 4 day observation period. It is suggested that these variations are caused by tidally modulated changes in the radon content of the water. No phase relationship with the local ocean tide is given, but it is reported that the oscillations in total radioactivity lag the effluent temperature by ~270° (Kadko, 1994). The simple poroelastic model of Chapter 6 suggests that the effluent temperature at the seafloor lags the ocean tide by a phase angle in the range [135°, 225°]. Under this model, therefore, Kadko's (1994) data imply that the total radioactivity of the effluent lags the ocean tide by a phase angle in the range [45°, 135°]. In comparison, the theory of Chapter 6 predicts that the effluent velocity lags the ocean tide by a phase angle in the range [90°, 135°]. Therefore a new mechanism for the tidal modulation of total radioactivity is proposed here. It may be

that the variations in total radioactivity are not caused by a change in the concentration of radon, but by tidal modulation of the effluent velocity.

Chevaldonné *et al.,* (1991) report time-series measurements made with THYDRO temperature probes. These probes can be inserted a few centimetres into hydrothermal edifices or placed inside clusters of living animals at vent sites. Temperature time-series collected at three separate sites all showed evidence of tidal modulation. The measurements were made at the Totem hydrothermal vent field on the East Pacific Rise (12°49'N, 103°57'W), the Hine Hina vent field in the Lau back-arc basin (22°32'S, 176°43'W), and the White Lady vent field in the North Fiji Basin (16°59'S, 173°55'W). Unfortunately it is not possible to compare the published temperature time-series with predictions of the local ocean tide because the exact start times for the datasets are not published. It is therefore requested that all future reported time-series measurements include the exact location and start time of the dataset to facilitate comparison with the ocean tide.

McDuff & Delaney (1995) and Delaney *et al.* (1997a) report tidal modulation of the temperature of a high temperature vent in the Main Endeavour Field of the Juan de Fuca Ridge. This vent is named "Puffer" because of its periodic step-wise jumps in temperature. These temperature excursions are separated by ~12.5 hours and Delaney *et al.* (1997a) suggest that the phenomenon is due to tidal modulation of subseafloor phase separation.

Most recently, Johnson *et al.* (2000) report tidal modulations in temperature measurements made using thermistors inserted into beds of vestimentiferan tube-worms around diffuse hydrothermal vents. These measurements were made in the Main Endeavour Field of the Juan de Fuca Ridge.

4.9 Conclusions

Evidence of tidal modulation at seafloor hydrothermal systems is provided by a wide variety of time-series collected above, below and on the seafloor. Tidal modulation has been observed in time-series of (1) subseafloor pressure, (2) subseafloor temperature, (3) water column temperature, (4) effluent temperature, (5) effluent velocity (6) effluent composition and (7) the frequency of occurrence of hydrothermal upwelling events. Where possible, the procedure developed in Chapters 2 and 3 is used to re-examine previously published data.

This theory is also used to analyse time-series acquired by the Medusa hydrothermal effluent monitoring system - some of which are presented here for the first time.

The suggested procedure for the analysis of hydrothermal time-series is reiterated below, along with general remarks motivated by the data reported in this chapter.

Firstly, the 'output' data time-series should be viewed in the time-domain alongside the 'input' time-series which is expected to cause tidal modulation which in most cases is the local ocean tide or tidal streams. Ideally the 'input' ocean tide signal would be measured on the seafloor concurrently with the 'output' data time-series. If this is not possible, the ocean tide can be estimated using public domain computer codes such as CSR. It is requested that researchers publish the *exact* time at which their time-series begin to facilitate estimation of the ocean tide. Seafloor hydrothermal systems occur over a wide range of longitudes (i.e. time-zones) and so it is suggested that all future time-series be plotted with Greenwich Mean Time (GMT) as the time ordinate. Furthermore, if a tidally modulated time-series is plotted on an arbitrary timescale which does not record the date, a great deal of valuable information is denied to the analyst. This lost information consists of the positions of the sun and moon during the time-series. These positions are easily predicted from well known astronomical formulae, *provided the date is known*, and are expected to produce a similar non-stationarity in *all* tidal signals. Therefore, knowledge of the date allows any amplitude-modulation or frequency-modulation observed in the data to be compared with astronomical theory.

Secondly, a non-parametric estimate of the power spectrum of the data time-series should be made using the multiple window method (Thomson, 1982). This algorithm identifies statistically significant line components in the spectrum which can be compared with the well known discrete set of tidal frequencies (Table 2.1). If significant line components are identified at several tidal frequencies, it can be concluded with confidence that the time-series is tidally modulated. The multiple window algorithm can produce very different spectral estimates to the simple periodogram estimates which have often been used (e.g. Figure 4.3). The time-bandwidth product ($NW\Delta t$) chosen for a multiple window analysis can be chosen according to the components of the tide which it is hoped to identify. For example, to identify separate line components at frequencies f_1 and f_2 requires that $W < |f_1 - f_2|$. Following Wetzler *et al.* (1998) it is suggested that the overall slope of an estimated spectrum be examined on a log-log plot. An estimated spectrum which takes the form $\hat{S}(f) \sim f^{-5/3}$ at high frequencies is consistent with the turbulence model of the Kolmogorov hypothesis (Section 4.2.5).

Thirdly, a parametric estimate of the tidal part of the time-series should be made using the Admiralty Method. The estimated harmonic constants can be compared with those of the ocean tide and the tidal potential in the complex plane to establish if there is a correlation between the output data signal and either of these two postulated input signals. The results presented here suggest that the tidal modulations observed at seafloor hydrothermal systems are more closely correlated to the local ocean tide than to the local tidal potential. This provides evidence that the tidal modulation of hydrothermal systems due to the load tide is more significant than the tidal modulation due to the solid tide. This observation is consistent with calculations showing that crustal strains due to the load tide are probably about 2 orders of magnitude greater than those due to the solid tide (Section 2.5.4). Consequently, it is concluded that the solid tide has negligible influence on seafloor hydrothermal systems relative to the ocean tide. Consequently, it is only the effect of ocean tide loading which is considered in Chapter 6.

It is demonstrated in Sections 4.2.2 and 4.3.1 that the ocean tide at a seafloor hydrothermal site can differ significantly from the ocean tide at the nearest coastal port. Consequently coastal values of the ocean tide should *not* be considered representative of the tide in the open oceans. It is strongly recommended that global ocean tide models (such as the CSR code) be used whenever it is necessary to infer the ocean tide at a hydrothermal system. Furthermore, it is an oversimplification to assume that the tidal streams on the seafloor are given by the time derivative of the ocean tide. It is shown in Section 4.2.2 that use of the theory of tidal streams (Section 2.6) leads to predicted tidal streams which differ in both magnitude and phase from those obtained by taking the time-derivative of the ocean tide. Ideally, current meter data should be collected concurrently with time-series measurements of hydrothermal systems. In the absence of such direct data, however, great care should be exercised when estimating tidal streams from the ocean tide.

It is postulated that tidal signals in effluent velocity and temperature at seafloor hydrothermal systems are caused by tidal loading of the oceanic crust. Consequently, the phase lag of observed tidal modulations relative to the local ocean tide should be noted. This phase lag can be estimated approximately from examination of the data in the time-domain. In cases where reliable estimates of the Admiralty Method harmonic constants can be found, the phase lags should be estimated from comparison of the harmonic constants. For the data

discussed here, it is generally only possible to make a reliable estimate for the phase of the principal *M2A* component.

Phase lags of data time-series behind local ocean tide (*M2A* component)			
Location	Instrument	Data time-series	Phase lag behind ocean tide (*M2A* component)
ODP Hole 858G	thermistor string	borehole temperature	~180°
RM24	Medusa	ambient bottom water temperature	325°
Mariana Trough	OBSH	episodic venting activity	~0°
TAG	OBSH	episodic venting activity	90° to 180°
TAG	video camera	'shrimp density'	279°
TAG	Medusa	ambient bottom water temperature	267°
TAG	Medusa	effluent temperature	225°
TAG	geothermal probe	sub-bottom temperature	~90°
Menez Gwen	Medusa	ambient bottom water temperature	~90°
Lucky Strike	Medusa	ambient bottom water temperature	172°
Lucky Strike	Medusa	effluent temperature	140°

Table 4.13: The phase lags of observed time-series behind the local ocean for the *M2A* component.

Table 4.13 shows the phase lags of the *M2A* components of seafloor hydrothermal time-series behind the *M2A* component of the local ocean tide. It is predicted in Chapter 6 that effluent temperatures at the seafloor lag the ocean tide by a phase angle in the range [135°, 225°] depending on the assumed thickness and permeability of the seafloor. Table 4.13 shows that this prediction is consistent with the effluent temperatures measured by Medusa at TAG and Lucky Strike. Furthermore, it is diagnostic that the phase lag of effluent temperature behind the ocean tide at TAG lies at the lower end of the predicted range while the corresponding phase lag for Lucky Strike is at the upper end of the predicted range. It is shown in Chapter 6 that the TAG data are consistent with a model of a thin highly permeable

layer just below the seafloor. In contrast, the Lucky Strike data are consistent with a thick, low permeability layer.

Chapter 5: Black smoker temperatures and the structure of subseafloor convection cells

5.1 Introduction

This chapter is concerned with the structure of hydrothermal convection cells in the oceanic crust, associated with mid-ocean ridge spreading centres. The principal aspects of this cell structure – the temperature field and the flow field – are constrained by a variety of physical, chemical and geological observations. The aim of this chapter is to construct the simplest possible convection model which is consistent with these observations. The generally accepted constraints on cell structure, derived from known evidence, are summarised in Figure 5.1

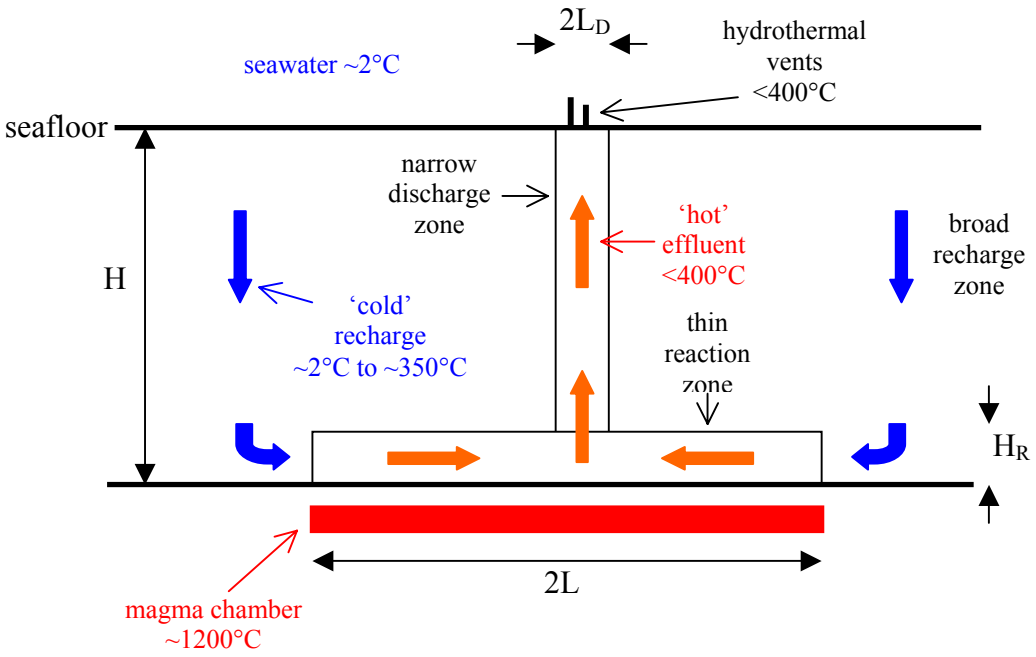

Figure 5.1: Schematic cross-section showing the expected structure of a subseafloor hydrothermal convection cell.

The principal features of this prototype seafloor convection cell (Figure 5.1) are discussed below. The energy required to drive the convection of seawater through the crust is supplied by the top surface of the magma chamber (Cann & Strens, 1982; Richardson *et al.,* 1987). It is known that magma solidifies at ~1200°C, and so it is assumed that this is the temperature of the heat source driving the convection cell (Lowell *et al.,* 1995). In a typical situation, the

magma chamber is located at a depth H ~ 1000 m below the seafloor and has a width $2L$ ~ 1000 m (Detrick *et al.,* 1987). Heat from the magma chamber causes seawater to convect through the crust with the general flow pattern indicated in Figure 5.1.

5.1.1 Recharge zone

The downwelling of cold seawater (~2°C) through the crust occurs through a broad recharge zone where temperatures are relatively low (<<350°C) (Alt, 1995). As the fluid percolates down through the subseafloor, the temperature begins to rise and the fluid interacts chemically with the surrounding rock, leading to an exchange of chemical elements between the evolved seawater and the crust. The nature of these basalt-seawater reactions is temperature dependent. At 70°C, the reactions are relatively slow - Mg, Na and K are removed from the fluid, whilst Ca and silica are added (Seyfried & Bischoff, 1979). At 150°C, the reactions are more rapid - Mg and sulphate are removed from the water, whilst Ca, Na, K, Fe, Mn, Zn, Cu, Ba and silica are all added (Seyfried & Bischoff, 1979; Seyfried & Mottl, 1982). Finally, above 150°C, Ca and sulphate are removed from the water by anhydrite precipitation (Berndt *et al.,* 1988).

5.1.2 Reaction zone

After the recharge zone, which is characterised by descending fluid flow, the convecting fluid enters a region known as the reaction zone above the top of the solidifying magma chamber. This region is generally thought to occur at the maximum penetration depth of the fluid and is characterised by temperatures in excess of 375°C (Berndt *et al.,* 1989) and horizontal fluid flow. The elevated temperatures in the reaction zone lead to extensive seawater-basalt reactions including the exchange of metals and cations and the further removal of sulphate from the water (Seewald & Seyfried, 1990). Estimates of the typical residence time of fluids in the reaction zone can be made from radioisotope studies and range from less than 3 years (Kadko & Moore, 1988) to 20 years (Grasty *et al.,* 1988). These estimated residence times are compared with the predictions of a numerical convection model in Section 5.4. It is expected that the reaction zone spans a temperature range from ~400°C at its top to ~1200°C at its base. The subsequent vertical temperature gradient gives rise to a conductive heat flux which delivers heat from the magma chamber to the water in the convection cell. Thermal calculations show that the reaction zone must be fairly thin (H_R ~ 100 m) in order to maintain the typical power output (~100 MW) of a hydrothermal system (Lowell & Germanovich, 1994). These authors argue that such a thin boundary layer might be maintained by downward migration of the hydrothermal system into freshly frozen

magma. It is argued, however, that these mechanisms are not *necessary* in order to restrict the thickness of the thermal boundary layer (Section 5.3). Rather, it is shown that a thin boundary layer spanning the temperature range ~400°C to ~1200°C is an inevitable consequence of the nonlinear thermodynamic properties of water.

5.1.3 Discharge zone

After the reaction zone, the convecting water enters a discharge zone through which it ascends to the hydrothermal vents on the seafloor. The typical dimensions of a hydrothermally active region of the seafloor (<100 m) are considerably less than the expected dimensions of the magma chamber (L ~ 1000 m) and so the upflow zone is often said to be focussed. It is probable that high permeability pathways, due to fractures, faults or textural inhomogeneities in the crust, serve to focus the upflow in the discharge zone. It must be stressed, however, that these inhomogeneities in crustal permeability are not *necessary* in order to impose the required structure on the cell. Some degree of focussing is inevitable in a convection cell, even in the absence of any high permeability pathways (Sections 5.3 & 5.4). Furthermore, by referring to the thermodynamic properties of water it is possible to estimate the half-width of the discharge zone (L_D) as a function of the width of the magma chamber and the crustal permeability (Section 5.4).

Two mechanisms cause the fluid to cool as it rises through the discharge zone - conductive heat loss and adiabatic cooling. The former is caused by horizontal temperature gradients in the discharge zone while the latter is a consequence of depressurisation. As an example, consider a hydrothermal vent field 2.5 km below sea level, where the pressure is ~25 MPa. If the reaction zone lies a further 1 km below the seafloor, then the upwelling fluid depressurises from ~35 MPa to ~25 MPa during its ascent through the discharge zone. Under adiabatic cooling alone, water leaving the reaction zone at ~400°C would cool to ~352°C on ascent to the seafloor (Haar *et al.,* 1984). The presence of conductive heat loss means that the true degree of cooling in the discharge zone is somewhat greater.

5.1.4 Hydrothermal vents

Finally, after ascending through the discharge zone, the convecting fluid is expelled at hydrothermal vents on the seafloor. The minerals dissolved in the fluid precipitate on contact with the cold ocean waters to form vent chimneys with an internal diameter of ~0.01 m to ~0.1 m (Lowell *et al.,* 1995). The effluent typically exits from these chimneys at a speed of ~1 $m.s^{-1}$. Thus, if these exit speeds are comparable with the speed of ascent in the discharge

zone, the fluid could ascend from the reaction zone to the seafloor (a distance $H \sim 1000$ m) in a matter of a few minutes (Dickson, 1998). This possibility of a 'rapid' ascent is sometimes correlated with the inference that the fluid does not lose much heat on its ascent through the discharge zone (Section 5.2). It might then be argued that a 'rapid' ascent is necessary to ensure that conductive heat losses during ascent are minimal. Qualitatively this is true, but it must be stressed that definition of what constitutes a 'rapid' ascent depends on the rate at which heat is lost conductively by the ascending fluid. Using a numerical model (Section 5.3), it is shown that minimal heat loss can occur during ascent even when there are no high permeability pathways and the ascent time is as large as several years (Section 5.4).

The most rigid constraint on cell structure is provided by the temperature of the fluid expelled at the seafloor. No hydrothermal effluent hotter than 404°C has ever been observed (Campbell *et al.,* 1988), which is particularly remarkable because it is so much less than the temperature (~1200°C) of the heat source (Lister, 1995; Lowell *et al.,* 1995; Wilcock, 1998). Consequently, a successful model for hydrothermal circulation must explain the discrepancy (~800°C) between the inferred temperature of the heat source and the observed temperature of the effluent at the seafloor. For some time it has been suspected that the nonlinear thermodynamic properties of water might be responsible for this temperature difference, but the claim has never been rigorously tested or explained (Bischoff & Rosenbauer, 1985; Johnson & Norton, 1991). In Section 5.3, however, the hypothesis is investigated with reference to a full physical model (Jupp & Schultz, 2000). Numerical simulations, and an analysis of the governing equations, are used to show that the thermodynamic properties of water are *sufficient* to impose the ~400°C cap on effluent temperatures. This cap applies for any sufficiently hot heat source, and it follows that vent temperatures could remain steady even as the magma chamber solidified and cooled to ~500°C (Lowell & Germanovich, 1994).

5.1.5 Summary

In summary, a successful model of hydrothermal convection should have the following features:

i) A magma heat source of width $L \sim 1000$ m and temperature ~1200°C lying at a depth $H \sim 1000$ m below the seafloor. This magma chamber drives convection of seawater in the oceanic crust.

ii) A seafloor pressure in the range 20 MPa – 40 MPa, corresponding to a depth below sea level of 2 km – 4 km.

iii) A relatively thin (H_R ~ 100 m) thermal boundary layer just above the heat source characterised by a temperature range of 400°C - 1200°C and predominantly horizontal fluid flow.

iv) A narrow discharge zone ($2L_D$ < 100 m), through which upwelling fluid at ~400°C ascends to the seafloor

v) Hydrothermal vents on the seafloor, through which fluid emerges at ~350°C to ~400°C.

It is argued in Section 5.3 that the properties of water are sufficient to impose a structure on the convection cell which is consistent with all of these constraints. For simplicity, it is assumed that the porosity and permeability of the seafloor are constant and homogeneous. This is a considerable simplification, but it allows the influence of the thermodynamic properties of water to be considered in isolation. Thus, although the real ocean crust is highly inhomogeneous, this inhomogeneity is not *necessary* to explain convection cell structure. The thermodynamic properties of water are *sufficient*, in themselves, to explain this structure.

5.2 Empirical constraints on convection cell structure

Section 5.1 contained a summary of the generally accepted subseafloor structure of a hydrothermal convection cell. This section is dedicated to a review of the observations on which this conceptual model is built. Evidence for the structure of hydrothermal convection cells comes from two types of location – active seafloor systems, and fossil systems exposed in ophiolites. The evidence from these two sources is considered in turn.

The principal evidence from active seafloor systems consists of measurements of the temperature and chemical composition of hydrothermal effluent. Generally, these measurements are obtained using research submersibles which can be piloted to within a few metres of hydrothermal vents. Probes are used to measure the effluent temperature *in situ* and samples of the fluid are collected for later chemical analysis. Thus, the physical and chemical state of the fluid is known as it leaves the discharge zone. Although these data are collected *on* the seafloor, they can be used to constrain the conditions within the convection cell at depth *below* the seafloor.

An example of this process is illustrated in Figure 5.2, using data from a vent 2.5 km below sea level where the seafloor pressure is 25 MPa or 250 bars (Bischoff & Rosenbauer, 1985). The data consist of the measured temperature of the vent (355°C) and the measured concentration of dissolved silica in the vent fluid (1170 ppm). If it is assumed that the fluid has undergone negligible conductive heat loss and negligible chemical reaction on its ascent to the seafloor, the pressure and temperature of the reaction zone from which it ascended can be estimated.

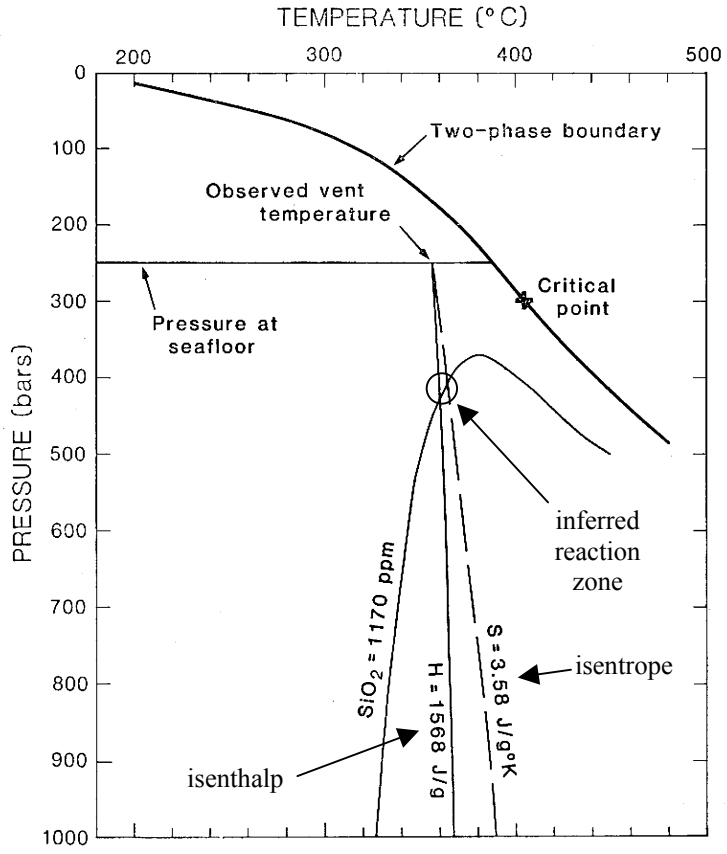

Figure 5.2: An example of the use of geothermometry and geobarometry to infer conditions in the 'reaction zone'. Diagram from Bischoff & Rosenbauer (1985).

Seawater at 25 MPa and 355°C has a specific enthalpy h = 1568 kJ.kg^{-1} and a specific entropy s = 3.58 kJ.kg^{-1}.K^{-1}. The corresponding isenthalp and isentrope are plotted in Figure 5.2. If the ascent through the discharge zone were perfectly isenthalpic, the p-T conditions in the reaction zone would lie somewhere on the isenthalp, while if it were perfectly isentropic,

they would lie on the isentrope. The assumption of negligible heat loss means that the ascent lies somewhere between isentropic and isenthalpic. The contour labelled "SiO_2" is the locus of points in the *p-T* plane for which fluid equilibrated with quartz would have a silica concentration of 1170 ppm. Thus, the assumption of negligible chemical reaction on ascent places the reaction zone somewhere on this contour. Consequently, with the stated assumptions, it can be inferred from Figure 5.2 that the reaction zone occurs at a pressure of ~400 bars (40 MPa) and a temperature of ~360°C. In other words, it must lie ~1.5 km below the seafloor. This example illustrates the use of geothermometry and geobarometry to infer the *p-T* conditions in the reaction zone. Other studies using the same technique have reached the same general conclusion – that the reaction zone is typically ~1 km below the seafloor and a few tens of degrees hotter than the 350°C - 400°C which is typical of the hydrothermal vents themselves (Von Damm *et al.,* 1985; Campbell *et al.,* 1988).

It should be emphasised that this technique analyses the temperature and composition of vent fluid to estimate the *p-T* conditions at which the fluid was most recently in physical and chemical equilibrium with the subseafloor. Thus, in terms of the conceptual model of Figure 5.1, it is only the conditions at the boundary of the reaction zone and the discharge zone which can be estimated. Consequently, a typical geothermometry estimate of ~400°C in the reaction zone would not preclude the possibility that the fluid had reached much higher temperatures elsewhere in the reaction zone. It should also be noted that the reaction zone depths inferred by geobarometry (~1 km) are broadly similar to the magma chamber depths inferred by seismic imaging of the seafloor (Detrick *et al.,* 1987). Thus, it seems likely that the reaction zone lies immediately above the magma chamber and spans a temperature range of 400°C to 1200°C (freezing magma) as represented in Figure 5.1.

Palaeo-oceanic crust exposed on land in ophiolite complexes provides the second type of direct evidence for the subseafloor structure of convection cells. In locations such as Cyprus and Oman, fossil hydrothermal systems are exposed in cross-section. It is therefore possible to infer the temperature structure which existed at depth within the fossil system using fluid inclusion geothermometry (Cowan & Cann, 1988) and by analysing the hydrothermal metamorphic mineral assemblages present (Gillis & Roberts, 1999). In particular, Gillis & Roberts (1999) report measurements made at a section of the Troodos Ophiolite in Cyprus. They interpret this section to represent the conductive boundary layer between the hydrothermal convection cell and its magmatic heat source. Their results (Figure 5.3) suggest

that a linear temperature drop from ~1200°C to ~400°C existed over a vertical distance of ~100 m. Thus, this region can be likened to the reaction zone shown in the prototype hydrothermal system of Figure 5.1. Furthermore, their data are consistent with the reaction zone thickness H_R ~ 100 m inferred from thermal balance calculations.

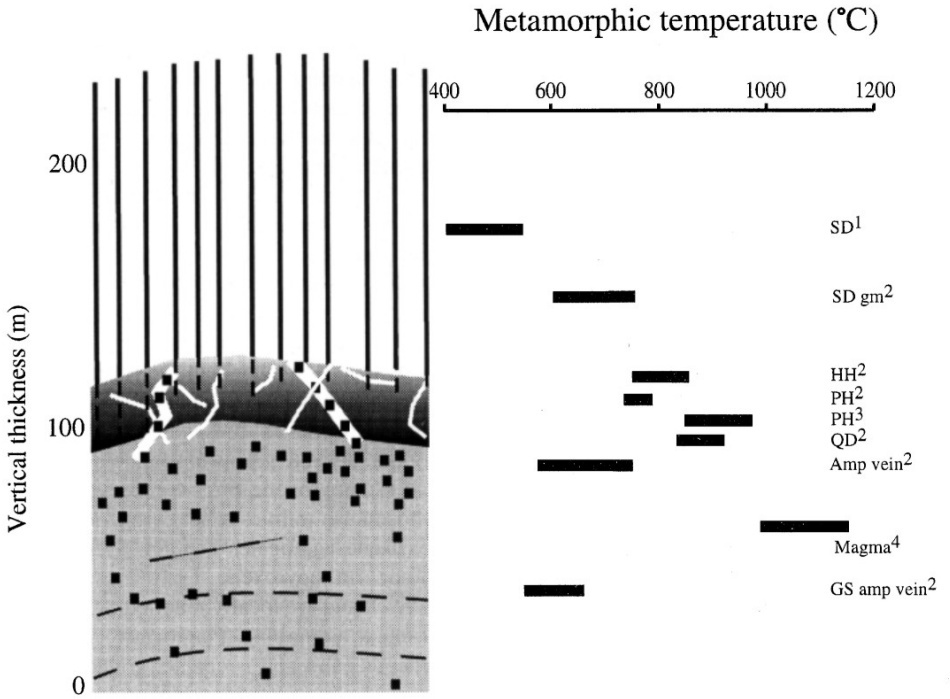

Fig. 3. (Left) Schematic diagram showing typical geological relationships along the sheeted dyke–plutonic transition. Sheeted dykes (vertical lines) are truncated at their base by the gabbronorite sequence (light gray). As the contact aureole is approached, the abundance of felsic melt impregnations (solid squares) within the gabbronorites increases (up to 30%). The contact aureole is cross-cut by quartz diorite (white lines + solid squares) and amphibole (white lines) veins; these veins show no preferred age relationships. (Right) Thermal conditions in the vicinity of the contact aureole. See text for details. Abbreviations: *SD* = sheeted dykes; *HH* = hornblende hornfels; *PH* = pyroxene hornfels; *QD* = quartz diorite; *GS* = gabbronorite series; *gm* = groundmass; *1* = mineral assemblage; *2* = plagioclase–amphibole geothermometer; *3* = orthopyroxene–clinopyroxene geothermometer; *4* = lava chemistry.

Figure 5.3: Metamorphic temperatures inferred in an exposed vertical cross section of the Troodos Ophiolite, Cyprus. It is proposed that the contact (dark-shaded) zone between the sheeted dyke complex and gabbroic sequence represents the fossil reaction zone, which once separated the hydrothermal system from its magmatic heat source. Diagram from Gillis & Roberts (1999).

In summary, the evidence pertinent to the structure of hydrothermal convection cells is remarkably consistent, and it is reasonable to place a high degree of confidence in the schematic model of Figure 5.1. However, it is important to understand why a hydrothermal convection cell should adopt this particular structure, and what imposes the ~400°C cap on vent temperatures. A working numerical model containing the full thermodynamic properties

of water has been constructed and is used to provide an answer to these questions in the following section.

5.3 A simple model of hydrothermal convection

Three mechanisms have been proposed to impose the ~400°C cap to black smoker temperatures. The first suggestion is that high temperature rock (>500°C) is effectively impermeable, because its ductile nature prevents the formation of cracks (Lister, 1974; Fournier, 1991). The second suggestion is that high temperature rock becomes impermeable over time, either by mineral precipitation infilling fracture porosity (Bischoff & Rosenbauer, 1985; Lowell *et al.,* 1993) or by thermal expansion (Germanovich & Lowell, 1992). Finally, the third suggestion is that the temperature cap is imposed by the thermodynamic properties of water. The first two mechanisms restrict effluent temperature by preventing flow through the hotter, deeper crust. In contrast, the third mechanism allows fluid to flow at *all* temperatures throughout the crust but limits the temperature of the fluid expelled at the seafloor. The purpose of this study is to investigate the third mechanism and the validity of the first two mechanisms is not considered.

Previous studies have shown how the thermodynamic properties of water affect the onset of convection (Straus & Schubert, 1977) and the overall rate of heat transfer in cells operating across a *small* temperature difference (~10°C) (Dunn & Hardee, 1981; Ingebritsen & Hayba, 1994). The advantage of assuming a small temperature difference is that the density can legitimately be regarded as a linear function of temperature. For such systems, it has been shown that cells operating near ~22 MPa and ~374°C transfer heat much more rapidly than cells at other temperatures. (The critical point of water, at (~22 MPa, ~374°C) represents the highest pressure and temperature at which phase separation can occur). Since hydrothermal systems frequently encompass the critical point, this 'superconvection' suggests that they might be highly efficient at transferring heat, but it does *not* explain the limit to observed vent temperatures. Real systems operate over a *large* temperature difference (~10°C to ~1200°C) and so the assumption that density depends linearly on temperature is invalid. To explain the narrow range of vent temperatures, no linearising assumptions are made and the focus of the investigation is moved from the overall heat transfer to the internal temperature structure of the cell.

A numerical simulation can be used to illustrate the thermal structure of convection cells (Norton & Knight, 1977). The simulation reported here (Figure 5.4) employs parameter values appropriate to seafloor systems which are outlined below. However, analysis of the governing equations will show that the key features of the cell structure depend solely on the thermodynamics of water, and not on the details of the parametrisation. To isolate the phenomenon under discussion, all previously suggested temperature-limiting mechanisms are excluded, and the crust is taken to be homogeneous and isotropic. Simulations were performed with the package HYDROTHERM (Hayba & Ingebritsen, 1994) (available at http://water.usgs.gov/software/hydrotherm.html), which incorporates a look-up table of the thermodynamic properties of pure water. These thermodynamic properties are tabulated only for temperatures above 0°C, and the program terminates when lower temperatures are encountered. If a cold seawater temperature of 2°C is imposed at the seafloor, numerical inaccuracies mean the program occasionally encounters temperatures below 0°C and crashes. To prevent this, a cold seawater temperature of 10°C is imposed. The thermodynamic properties of seawater vary very little between 2°C and 10°C so this approximation has a negligible effect on the solution. The code required a slight modification in order to enforce a particular thermal boundary condition relevant to seafloor systems (Dickson *et al.,* 1995). Hot effluent emerges from an otherwise cold seafloor, so a fixed temperature boundary condition is not always appropriate. Consequently, the condition $\partial T/\partial z = 0$ is imposed on the seafloor where flow is upwards, while $T = 10$ºC is imposed where flow is downwards.

In Figure 5.4, the top boundary (z = 1000 m) represents the permeable seafloor where the pressure is held at 25 MPa (equivalent to ~2.5 km below sea surface). The side boundaries for the simulation are at x = -1700 m and x = 1700 m (beyond the range of Figure 5.4) and are therefore sufficiently distant that they do not influence the solution near the heat source. The side boundaries are held at T = 10°C and cold hydrostatic pressure throughout the simulation. The bottom boundary (z = 0) is impermeable. Parameters for the simulation are porosity = 10%, permeability $k = 10^{-14}$ m^2, thermal conductivity $\lambda = 2.0$ W.m^{-1}.K^{-1} (Lowell & Germanovich, 1994).

The governing equations are

(i) Darcy's law (Faust & Mercer, 1979)

(ii) An equation of state for pure water (Haar *et al.,* 1984; Watson *et al.,* 1980; Sengers & Kamgar-Parsi, 1984; Sengers & Watson, 1986),

(iii) The conservation of mass and energy in a porous medium (Faust & Mercer, 1979).

Convection is initiated by a 'heater' along part of the bottom boundary (Elder, 1981), which represents the top of the magma chamber. For simplicity, the heater imposes a Gaussian (bell-shaped) temperature profile which runs from 'cold' (T_0 = 10°C) at the sides to 'hot' ($T_0+\Delta T$) at the centre. The heater is 'switched on' at time zero, when the entire domain is cold ($T=T_0$) and at hydrostatic pressure. Time-dependent solutions for the temperature and pressure fields are calculated and allowed to evolve until a steady state is reached.

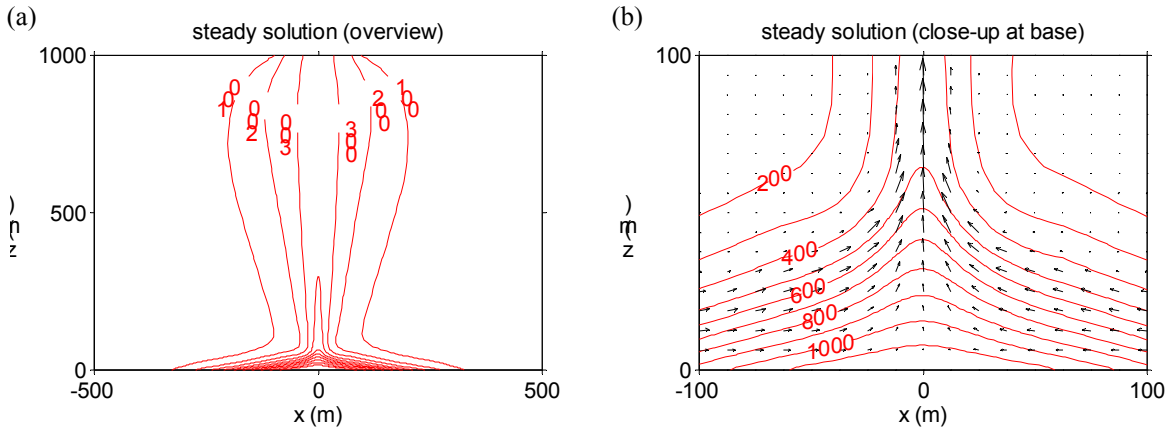

Figure 5.4: The steady state temperature distribution in a convection cell at seafloor pressures, predicted by a HYDROTHERM simulation. (a) The overall temperature structure of the convection cell, showing the distinction between the reaction zone and the discharge zone. Isotherms from 100°C to 1100°C are drawn in red, in increments of 100°C. Flow vectors are omitted for clarity. Flow is downwards at the sides, towards the centre at the base and upwards in the centre. (b) A close-up view of the flow regime and temperature structure inside the boundary layer, showing the bottom 100 m of the domain. Isotherms from 200°C to 1100°C are drawn in increments of 100°C. Vectors are of Darcy velocity.

Figure 5.4 shows a typical steady solution with T_0 = 10°C and ($T_0+\Delta T$) = 1200°C. It is immediately apparent that the main features of the prototype hydrothermal system (Figure 5.1) are reproduced by this simulation. Firstly, there is a thin boundary layer of very hot fluid (~400°C to 1200°C) at the base of the convection cell, which can be likened to the reaction

zone in Figure 5.1. Secondly, there is an upwelling plume of ~400°C which corresponds to the discharge zone. Similar plume temperatures are obtained for other convectively dominated systems with T_0=10°C and ($T_0+\Delta T$) > ~500°C, including systems with anisotropic permeability. It follows that vent temperatures could remain steady as a magma chamber solidified and cooled, dropping only when the heat source fell below ~500°C (Lowell & Germanovich, 1994). Numerical experiments suggest that plumes have a natural tendency to form at ~400°C, given any sufficient heat source and seafloor pressures. The explanation for this phenomenon lies in the balance between conduction and advection, the two mechanisms which transport energy, as the system evolves.

In the model (Figure 5.4), the temperature (T) and pressure (p) are functions of position ($\mathbf{x}=(x,z)$). Thermal gradients produce a conductive heat flux $-\lambda\nabla T$, where λ is the thermal conductivity. Fluid motion creates an advective heat flux $\rho h\mathbf{u}$, for water of density ρ, specific enthalpy h and Darcy velocity $\mathbf{u}$. In the conservation of energy equation (Faust & Mercer, 1979) the rate of change of energy per unit volume is given by the negative divergence of the total heat flux, $-\nabla\cdot(\rho h\mathbf{u}-\lambda\nabla T)$. This can be split into two terms, $-\nabla\cdot(\rho h\mathbf{u})$ and $\lambda\nabla^2 T$, which are the rates of accumulation of energy per unit volume, due to the advection and conduction of heat respectively. At any point in the cell, the relative importance of these two mechanisms can be expressed by the ratio:

$$Ra_L(\mathbf{x},t)=\left|\frac{\nabla\cdot(\rho h\mathbf{u})}{\lambda\nabla^2 T}\right| \tag{5.1}$$

This ratio, which is a function of time and space, measures the influence of fluid motion on the evolution of the local temperature field, and could logically be labelled the 'local Rayleigh number'. (Traditionally, a single fixed parameter - the Rayleigh number - is defined for the whole cell (Straus & Schubert, 1977). Here a 'local Rayleigh number' has been assigned independently to each point in the cell, and is allowed to change with time.) Conduction dominates over advection at any point where $Ra_L \ll 1$ and the temperature evolves independently of any fluid flow. Conversely, where advective heat transfer is strong enough to influence the evolution of the temperature field, $Ra_L \gg 1$ and the isotherms are distorted away from a conductively dominated pattern. Advective distortion of the isotherms marks the separation of the plume from the boundary layer and effectively *defines* the plume in Figure 5.4. To understand where and when plumes initiate as the simulation progresses, it is important to know where and when the local Rayleigh number is maximised.

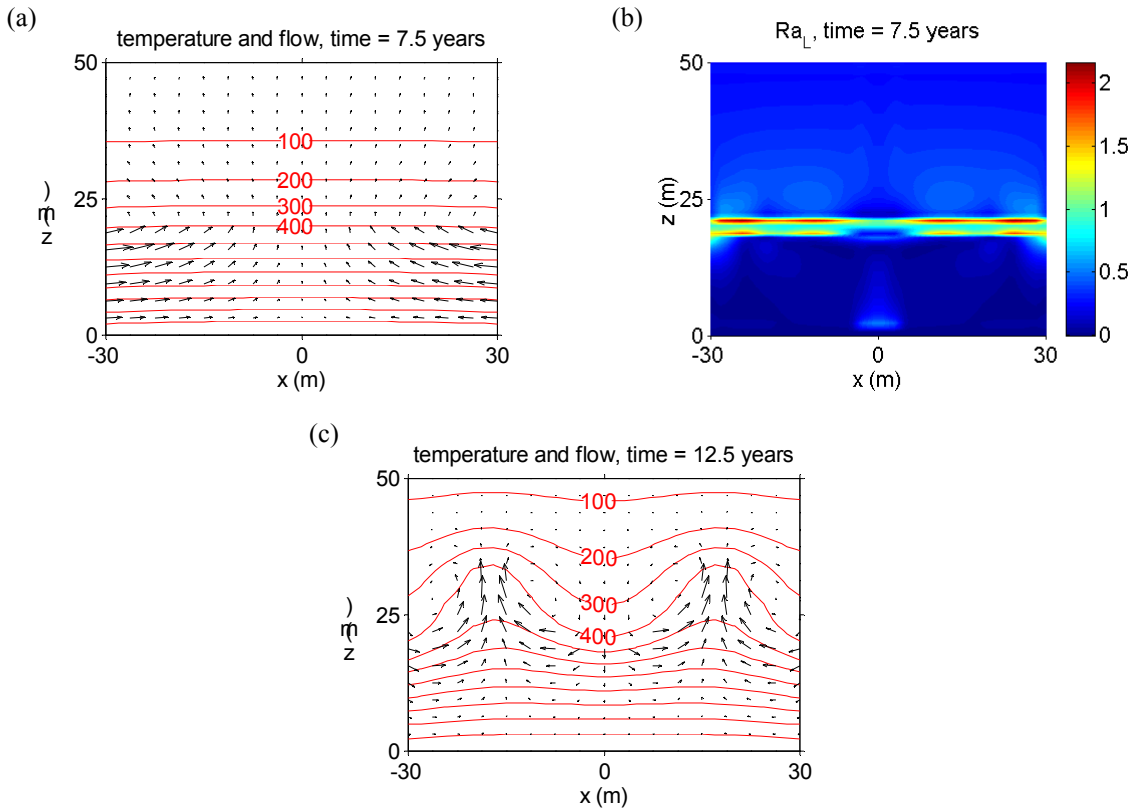

Figure 5.5: The bottom of the domain shown in Figure 5.4, shown at the early stages of the simulation, before a steady state has been reached. (a) The temperature and flow fields just before plume formation. The thermal structure is governed by conduction alone. Convective motion exists, but it does not influence the temperature field. (b) Colour plot of the local Rayleigh number Ra_L, just before plume formation. The regions of greatest Ra_L indicate where plumes are likely to form. (c) The temperature and flow fields just after plume formation. Advection has begun to distort the thermal structure. (As the simulation progresses to steady state, these two plumes coalesce to form the single plume in Figure 5.4). Isotherms are drawn in red from 100°C (top) to 1100°C (bottom) in increments of 100°C. Vectors are of Darcy velocity.

After the heater is switched on, a thermal signal propagates upwards (Figure 5.5). For the period before plume formation (Figures 5.5a,b), the approximate magnitudes of the energy accumulation terms can be calculated. Let d be the distance that the signal has penetrated into the domain, i.e. the vertical range over which the temperature drops from 'hot' (T_0+ΔT) to 'cold' (T_0). Denote by Φ the order of magnitude of the advective heat flux $\left|\rho h \mathbf{u}\right|$. Then,

$|\nabla\cdot(\rho h\mathbf{u})|$ is of order Φ/d, and $|\lambda\nabla^2 T|$ is of order $\lambda(\Delta T)/d^2$. Consequently, the local Rayleigh number (Ra_L) is of order $(\Phi/\lambda(\Delta T))\cdot d$, and therefore scales linearly with the vertical length scale d. Just before plume formation, d is sufficiently small that Ra_L is everywhere of order unity (Figure 5.5b). It is important to note, however, that Ra_L is greatest near the 400°C isotherm. A short time later, when d, and hence Ra_L, have increased slightly, plumes have started to form at about 400°C (Figure 5.5c).

By making some simplifications, it is possible to explain why Ra_L is maximised at ~400°C just before plume formation. At this early stage, when the temperature field is governed by conduction alone, temperature gradients are nearly uniform (Figure 5.5a). It therefore follows, from equation (5.1), that the maximum value of Ra_L is controlled by the maximum value of $|\nabla\cdot(\rho h\mathbf{u})|$. Above the level of horizontal flow, there can be no significant horizontal pressure gradient. It follows that the vertical pressure gradient must be approximately equal in the cold recharge zone, where fluid descends, and the hot discharge zone, where fluid ascends (Pascoe & Cann, 1995). This vertical pressure gradient must be sufficiently small for cold water to descend in the recharge zone, and sufficiently large for hot water to ascend in the discharge zone. Hence, the vertical pressure gradient must lie between hot hydrostatic and cold hydrostatic. The permeability is the same in both limbs, but the total resistance to flow is much greater in the upflow limb because of its smaller cross-sectional area (Figures 5.1, 5.4a). It follows that the vertical pressure gradient is much closer to cold hydrostatic than hot hydrostatic.

Hence, above the level of horizontal flow:

$$\frac{\partial p}{\partial z} \approx -g\rho_0 \tag{5.2}$$

where ρ_0 is the density of cold water. Suppose that the advective heat flux $\rho h\mathbf{u}$ is dominated by its vertical component which, by Darcy's law, is

$$\rho h w = -k\left(\frac{\partial p}{\partial z} + g\rho\right)\frac{\rho h}{\mu} \tag{5.3}$$

for permeability k, gravitational acceleration g, and dynamic viscosity μ. From equations (5.2) and (5.3), an approximate expression for the advective energy accumulation is then

$$-\nabla\cdot(\rho h\mathbf{u}) \approx \left[\frac{\partial}{\partial z}\left(\frac{(\rho_0-\rho)\rho h}{\mu}\right)\right]\cdot[-gk] = -gk\left[\frac{\partial F}{\partial z}\right] \tag{5.4}$$

where the 'fluxibility' of the fluid (F) is defined (Lister, 1995) to be

$$F = \frac{(\rho_0 - \rho)\rho h}{\mu} \tag{5.5}$$

It follows from equations (5.1) and (5.4) that Ra_L should be maximised, and plumes will form, where $|\partial F/\partial z|$ is maximised.

The 'fluxibility' (F) is a function of the thermodynamic state of the fluid (Figures 5.6k,l) and is a scaled version of the vertical advective heat flux in a cold hydrostatic pressure gradient. (The true vertical advective heat flux, in $W.m^{-2}$, is given by the product gkF). Since plumes are expected to form where spatial gradients in fluxibility are greatest, it is important to consider, in detail, the dependence of the fluxibility on pressure and temperature. Figure 5.6 summarises the temperature- and pressure-dependence of the fluxibility and the thermodynamic properties on which it depends. The density of cold water (ρ_0) is a constant and ρ, μ and h are given as functions of pressure and temperature by the steam tables embedded in the HYDROTHERM code (Haar *et al.,* 1984; Watson *et al.,* 1980; Sengers & Kamgar-Parsi, 1984; Sengers & Watson, 1986).

Figures 5.6a,b reveal the variation in fluid density (ρ) over a range of pressures and temperatures relevant to seafloor hydrothermal systems. It is clear that the density varies greatly with temperature and little with pressure, producing a marked density drop at ~400°C to ~500°C for all seafloor pressures. Below the critical pressure of 22 MPa (~2.2km hydrostatic head), this density drop is discontinuous, and is caused by a change of state from liquid to vapour as the water boils. However, above 22 MPa pure water has no boiling point and cannot coexist as two separate phases. Consequently, the density is a continuous function of temperature. There is still a fairly sharp drop in density at ~400°C (Figure 5.6b), but it is not caused by boiling because there is no discontinuity and no phase change. Therefore, for all seafloor pressures above 22 MPa, the water shows a smooth transition from a 'liquid-like' state below ~400°C to a 'gas-like' state above ~400°C.

Figures 5.6c,d reveal the variation in specific enthalpy (h) over the same section of p-T space. The specific enthalpy is a measure of the energy content of the fluid per unit mass and is always quoted relative to some reference state. The reference state for these data, for which h is assigned the value zero, is p = 0.1 MPa, T = 0°C. However, it is clear from the figures that $h \approx 0$ when $T \approx 0$°C for all relevant seafloor pressures. Therefore, it can be

assumed with minimal error that all 'cold' fluid in a hydrothermal convection cell has zero specific enthalpy.

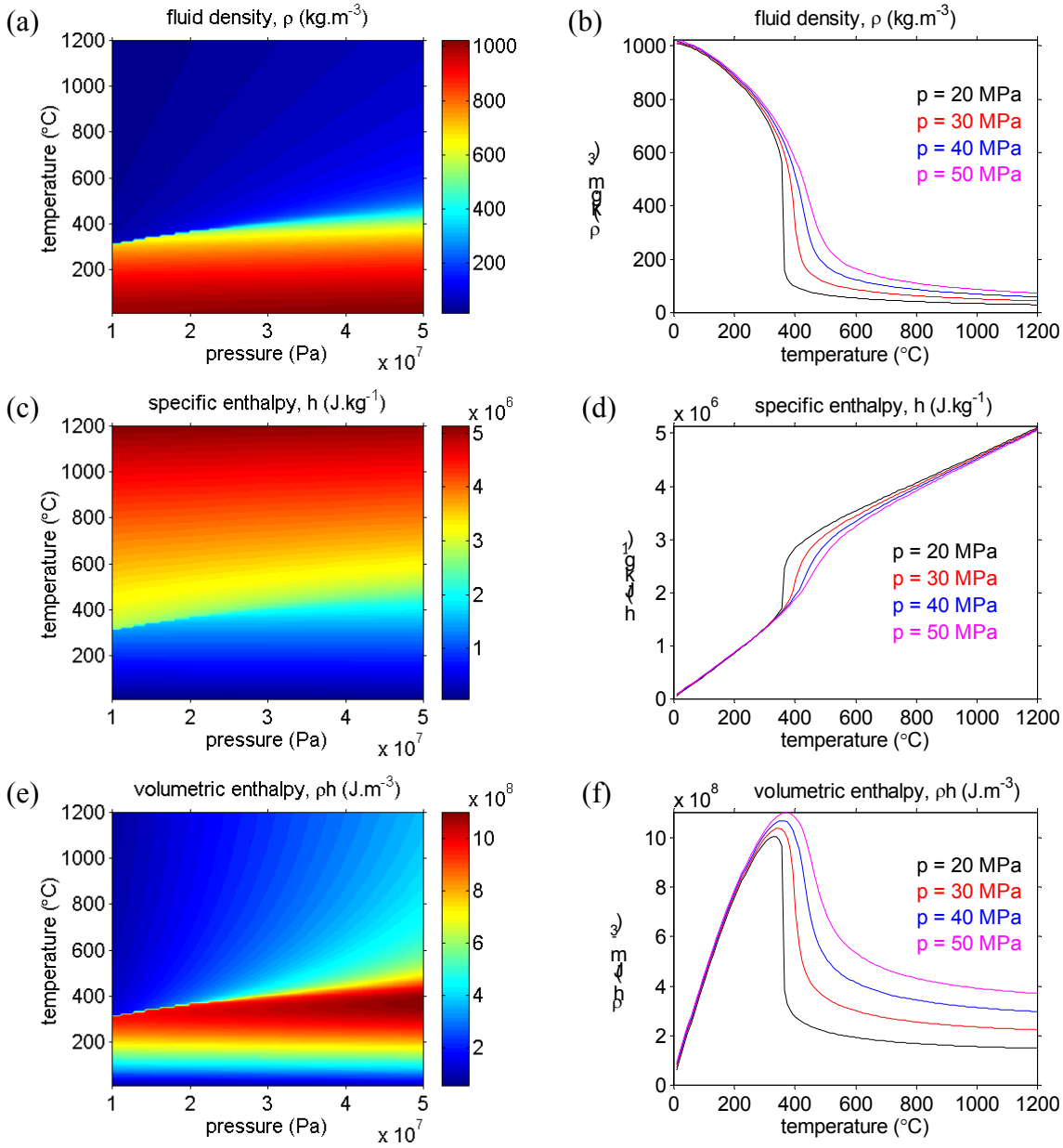

Figure 5.6: The dependence of the thermodynamic properties of pure water on pressure and temperature. Values are taken from the tables embedded in the HYDROTHERM code. The pressure range of 10 MPa to 50 MPa corresponds to depths of between 1km and 5km below sea level. (a) & (b) The density (ρ). (c) & (d) The specific enthalpy (h). (e) & (f) The volumetric enthalpy (ρh).

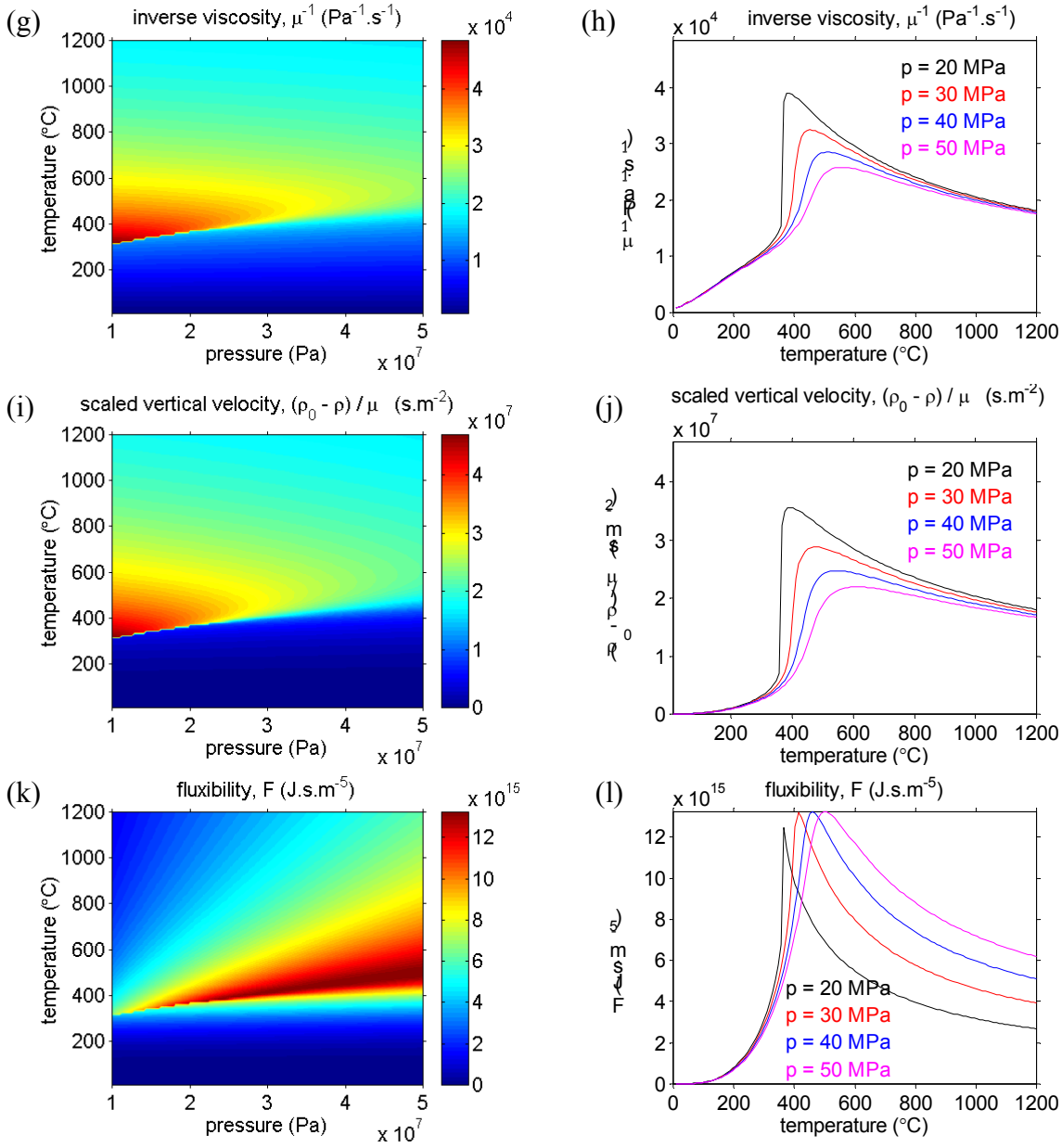

Figure 5.6: (continued) The dependence of thermodynamic variables on the pressure and temperature of the fluid. Values are for pure water and are taken from the tables embedded in the HYDROTHERM code. The pressure range of 10 MPa to 50 MPa corresponds to depths of between 1km and 5km below sea level. (g) & (h) The inverse viscosity (μ^{-1}). (i) & (j) The scaled vertical velocity ($(\rho_0-\rho)/\mu$) of fluid in a cold hydrostatic pressure gradient $g\rho_0$. The true vertical velocity (in $m.s^{-1}$) is $[gk]\cdot[(\rho_0-\rho)/\mu]$. (k) & (l) The fluxibility ($F = (\rho_0-\rho)\rho h/\mu$). In a cold hydrostatic pressure gradient, the buoyancy-driven energy flux (in $W.m^{-2}$) is $[gk]\cdot F$.

Figure 5.6d shows that the specific enthalpy is a monotonic increasing function of temperature for all pressures. It is common in the literature to find references to the specific heat capacity (c_p) of hydrothermal fluid but it is suggested that reference to it is unnecessary and potentially misleading. At a given pressure, the specific heat capacity is defined by the relation $c_p(p,T) = \partial h/\partial T$, and so represents the slope of the lines in Figure 5.6d. For sub-critical pressures (<22 MPa) the phase change associated with boiling causes a discontinuity in the graph of enthalpy (h) against temperature (T). The magnitude of this discontinuity is equal to the latent heat of vaporisation at that pressure, and it is sometimes argued that its existence causes the value of the specific heat capacity to approach infinity as the discontinuity is approached. This is highly misleading as it can lead to the erroneous argument that an infinite amount of energy is required to heat the fluid beyond its boiling point. However, the discontinuity simply means that the specific heat capacity is *undefined* at the boiling point. For this reason, and since the specific enthalpy is a more fundamental quantity (from which the specific heat capacity is derived), no further attention is paid to specific heat capacities in this chapter.

The volumetric enthalpy (ρh) is a measure of the energy content of the fluid *per unit volume* (Figures 5.6e,f). Unlike the specific enthalpy (h) it is not a monotonic increasing function of temperature; on the contrary, for seafloor pressures it is maximised at ~400°C (Figure 5.6f). In other words, at seafloor pressures, 1 m^3 of water at ~400°C contains more energy than 1 m^3 of water at *any other temperature*.

Figures 5.6g,h show the dependence of the inverse fluid viscosity (μ^{-1}) on pressure and temperature. (The figure shows inverse viscosity (μ^{-1}) rather than viscosity (μ) because the resulting graph is clearer.) Figure 5.6h shows that the viscosity is least (equivalently, the inverse viscosity is greatest) at ~400°C. In other words, at seafloor pressures water 'flows more readily' at ~400°C than at *any other temperature*.

Figures 5.6i,j show how the quantity $(\rho_0-\rho)/\mu$ depends on pressure and temperature. This quantity is named the 'scaled vertical velocity' because in a cold hydrostatic pressure gradient ($g\rho_0$) the vertical velocity of upwelling fluid is $w = gk(\rho_0-\rho)/\mu$. Figure 5.6j shows that the scaled vertical velocity is maximised at ~400°C for seafloor pressures. In other words, in a regime of cold hydrostatic pressure water ascends more quickly at ~400°C than at *any other temperature*. This effect is due to a viscosity minimum for water at ~400°C

(Figure 5.6j). Hotter fluid is always less dense than colder fluid and so has greater buoyancy (Figure 5.6a,b). As temperatures rise above ~400°C, however, the viscosity (μ) which resists the flow increases faster than the density drop (ρ_0-ρ) which drives the flow. Above ~400°C, therefore, hotter fluid would actually ascend more slowly than colder fluid.

Finally, Figures 5.6k,l reveal the dependency of the fluxibility (F) on pressure and temperature. The fluxibility is the product of the scaled vertical velocity (Figures 5.6i,j) and the volumetric enthalpy (Figures 5.6e,f). At ~400°C upwelling water displays its maximum vertical velocity (Figure 5.6j) and carries a maximum quantity of thermal energy per unit volume (Figure 5.6f). In summary for seafloor pressures, the fluxibility (F) - and hence the vertical advective heat flux (gkF) - is maximised between ~400°C and ~500°C.

Now that the pressure- and temperature-dependence of fluxibility (F) has been established it is appropriate to return to the subject of plume formation. It is deduced, following equation (5.5), that upwelling plumes are expected to form where $\left|\partial F/\partial z\right|$ is maximised. It is clear from Figure 5.6k that in a seafloor hydrothermal system the fluxibility varies greatly with temperature, but little with pressure. Before the formation of a plume, temperature is approximately a linear function of height (Figure 5.5a). Thus, $\left|\partial F/\partial z\right|$ should be maximised approximately where $\left|\partial F/\partial T\right|$ is maximised.

Figure 5.7a shows $\left|\partial F/\partial T\right|$ as a function of temperature for a range of seafloor pressures. The approximate plume formation temperature ($T_p(p)$) can be defined as the temperature for which $\left|\partial F/\partial T\right|$ is maximised for a given pressure (p). Figure 5.7b shows that $T_p \approx 410$°C for p=35 MPa which is the approximate pressure at the base of the convection cell in Figures 5.4 and 5.5. Thus, 410°C is the temperature at which plumes would separate from the boundary layer, under the simplifying assumptions. The fact that this predicted plume formation temperature is consistent with the numerical simulation (Figure 5.5c) provides *a posteriori* evidence that the various simplifying assumptions (cold hydrostatic pressure gradient, advective flux dominated by vertical component) are justified.

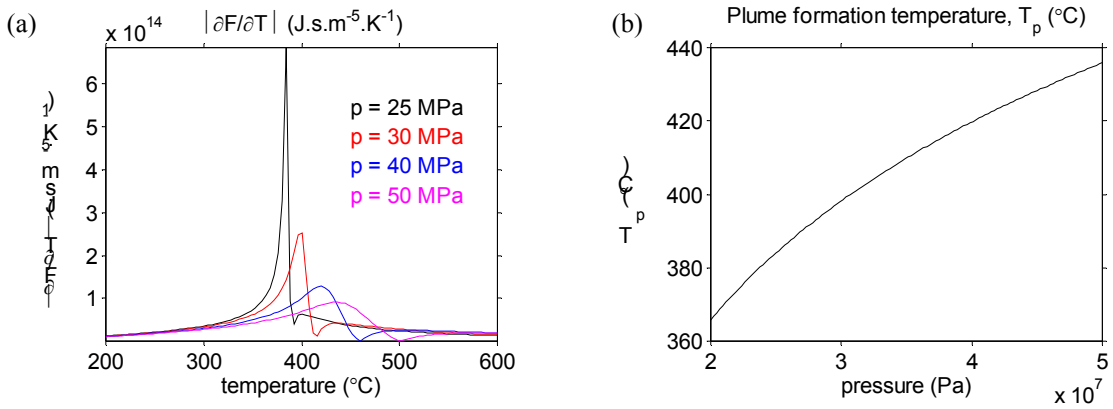

Figure 5.7: The estimated plume formation temperature (T_p) for pure water at seafloor pressures. At a given pressure (p) the plume formation temperature (T_p) is the temperature at which $|\partial F/\partial T|$ is maximised. (a) $|\partial F/\partial T|$ as a function of temperature for a range of seafloor pressures. (b) T_p as a function of pressure.

A highly significant simplification in this analysis has been the assumption that the convecting fluid is pure water rather than salt water. Although the thermodynamic properties of water at *constant* salinity have been known for some time (Bischoff & Rosenbauer, 1985; Anderko & Pitzer, 1993), they are insufficient for use in numerical simulations. If salt is to be included in the calculations, an equation for the conservation of salt must be added to the equations for conservation of mass, energy, and momentum which govern the pure water system. This is a considerable complication. Furthermore, unlike pure water, salt water can boil at *all* seafloor pressures. Therefore it would be necessary to track the progress of two evolving fluids, with varying salinities, at temperatures above ~400°C. The thermodynamic properties of salt water as functions of the *three* independent variables pressure, temperature and salinity have only recently been published (Palliser & McKibbin, 1998a, 1998b, 1998c). Consequently, numerical codes to explore the nature of salt-water convection in the seafloor are in their infancy and have yet to produce conclusive results (Wenyue Xu, *pers. comm.*, 1999). The question of salt water convection is discussed further in Chapter 7, but it is sufficient to note for now that the fluxibility of salt water could, in principle, be defined in exactly the same fashion as for pure water (equation (5.5)). A complication arises, however, because the fluxibility will depend on salinity. Salinity is well constrained in the ocean, but may be considerably different at depth within the seafloor because of phase separation and chemical interaction with the rock. Thus, the results of numerical experiments incorporating the full thermodynamic properties of salt water must be awaited for the issue to be resolved.

As an example, however, the thermodynamic properties of a 3.2% NaCl solution (Bischoff & Rosenbauer, 1985) suggest that T_p would be shifted upwards by ~30ºC compared with the results for pure water.

Although it is a considerable simplification, the use of pure water has the following definite advantage. At pressures greater than 22 MPa (seafloor depth ~2.2 km), pure water is a single-phase fluid. Therefore, the complication of phase separation can be removed from this analysis and it has been possible to demonstrate a temperature-limiting mechanism which is independent of 'phase-separation' or 'two-phase effects'. This suggests that, although phase separation undoubtedly occurs in active hydrothermal systems, it is not *necessary* in order to explain convection cell structure.

Three differences between this approach and classical studies of porous medium convection (Lapwood, 1948) should be noted. Firstly, in this study convection is not generated by a *uniformly* heated lower boundary. The presence of both hot and cold regions at the base of the cell ensures that there is always a horizontal temperature gradient and associated fluid flow. Consequently, the point of interest is not the onset of convective motion, but the onset of convective distortion of the temperature field. Secondly, no use is made of the Boussinesq approximation (Phillips, 1991) under which the advective heat flux would be approximated by $\rho_0 h\mathbf{u}$. The Boussinesq approximation is valid for cells with *small* temperature differences, where $\rho \approx \rho_0$, but in this study the true advective heat flux ($\rho h\mathbf{u}$) is used because ρ can vary from ρ_0 by a factor of 25 (Figures 5.6a,b). Thirdly, this analysis abandons the traditional Rayleigh number, which is an *overall* balance between advection and conduction, in favour of a *local* Rayleigh number which gives the balance at each point in the cell as a function of time. This permits identification of the precise position and temperature at which plumes form.

At a given pressure, and given a sufficient heat source, a plume will form at temperature T_p, the temperature at which $\left|\partial F/\partial T\right|$ is maximised (Figure 5.7). If ambient pressures are known plume formation temperatures can be inferred for single-phase hydrothermal systems. Observed vent temperatures may be cooler than this plume formation temperature because of conductive losses from the ascending fluid, but they cannot be hotter.

5.4 Scaling Analysis

It has been shown that the thermodynamic properties of water can exert a strong influence on the structure of a seafloor convection cell. In the previous section it is supposed, for simplicity, that the permeability of the host rock is constant and homogeneous. Consequently, the observed convection cell structure (Figure 5.4) is governed by the thermodynamic properties of water. Despite the deliberate simplicity of the model, the simulated convection cell displays all three key features required by the existing evidence (Figure 5.1): (i) a thin 'reaction zone', (ii) a narrow 'discharge zone' and (iii) seafloor vents which are limited to ~400°C. This section is concerned with the length- and time-scales associated with the reaction zone and the discharge zone. Phillips (1991) shows how the approximate dimensions of the plume and the basal thermal boundary layer can be calculated for a convection cell in a porous medium. Given that the driving temperature difference is *small*, Phillips assumes that the viscosity (μ) is constant and that the enthalpy (h) and density (ρ) are linear functions of temperature. Phillips also invokes the Boussinesq approximation. The following argument follows that of Phillips (1991), with the difference that the full, nonlinear thermodynamic properties of water are retained.

5.4.1 Cartesian geometry

Suppose that the seafloor convection cell is driven by a magma chamber of half-width L which lies at a depth H below the seafloor, as in Figure 5.1. It has been shown in Section 5.3 that the 400°C isotherm marks the approximate boundary of two important regions of the convection cell – the reaction zone and the discharge zone. The thickness of the reaction zone is denoted by H_R, and the half-width of the discharge zone is denoted by L_D. For the moment, it is assumed that Figure 5.1 represents convection in two spatial dimensions, so that the magma chamber extends indefinitely in the third dimension along the ridge-axis.

There is little horizontal flow above the reaction zone and therefore horizontal pressure gradients are negligible. However, below this level there is considerable horizontal flow from the recharge zone into the reaction zone. Within the reaction zone itself, the flow of hot fluid (of density ρ and viscosity μ) is predominantly horizontal, and so the vertical pressure gradient must be approximately equal to the hot hydrostatic value, $g\rho$. Outside the reaction zone, at the base of the cell, the flow of cold water (of density ρ_0) is also predominantly horizontal. In this region, therefore, the vertical pressure gradient must be approximately

equal to the cold hydrostatic value, $g\rho_0$. At the base of the cell, the difference between the hot and cold hydrostatic pressure regimes - inside and outside the reaction zone - applies over a vertical distance of H_R. Thus, it follows that the horizontal pressure difference driving fluid into the reaction zone is given, approximately, by

$$\Delta p \sim (\rho_0 - \rho) g H_R \tag{5.6}$$

This pressure difference operates over a horizontal distance L, and so by Darcy's law the horizontal velocity of fluid flowing in the reaction zone is

$$u \sim \frac{k}{\mu}\frac{\Delta p}{L} = gk\frac{(\rho_0 - \rho)}{\mu}\frac{H_R}{L} \tag{5.7}$$

The vertical velocity of fluid in the discharge zone is given by

$$w \sim gk\frac{(\rho_0 - \rho)}{\mu} \tag{5.8}$$

Hence, conservation of mass in the reaction zone implies that

$$2\rho u H_R \sim 2\rho w L_D \tag{5.9}$$

Equations (5.7), (5.8) and (5.9) can then be combined to express the mass balance as

$$H_R^2 \sim L_D L \tag{5.10}$$

The energy balance of the reaction zone is a balance between conduction and advection. If the vertical temperature drop across the reaction zone is ΔT, the system is driven by a vertical conductive heat flux of approximate magnitude $\lambda(\Delta T) / H_R$. This heat flux operates over a horizontal distance $2L$ and is balanced by the advective transport of heat into the upflow zone. This advective heat transport consists of 'hot' fluid of specific enthalpy h flowing at a speed w over a horizontal distance $2L_D$. Consequently, the conservation of energy in the reaction zone is expressed by the balance

$$2L\frac{\lambda\Delta T}{H_R} \sim 2\rho h w L_D \tag{5.11}$$

Using the definition of the fluxibility (F) (equation (5.5)) this can be re-arranged to give:

$$\frac{L\lambda(\Delta T)}{L_D H_R} \sim gk\left(\frac{\rho h(\rho_0 - \rho)}{\mu}\right) = gkF \tag{5.12}$$

Equations (5.10) and (5.12) can now be solved to give the approximate magnitudes of the two unknown lengthscales L_D and H_R:

$$L_D \sim \left[\frac{\lambda(\Delta T)}{gF}\right]^{2/3} L^{1/3} k^{-2/3} \tag{5.13}$$

$$H_R \sim \left[\frac{\lambda(\Delta T)}{gF}\right]^{1/3} L^{2/3} k^{-1/3} \tag{5.14}$$

The greatest uncertainty in these expressions resides in the value of the permeability (k) which is very poorly constrained. Plausible values for the permeability of the seafloor range over several orders of magnitude, from 10^{-17} m^2 to 10^{-11} m^2 (Table 6.1), and it is possible that the presence of fractures and fault conduits could make the effective bulk permeability even greater. In contrast, the other parameters on which these scalings depend are relatively accurately known. The gravitational acceleration (g) is constant (g = 9.8 m.s^{-2}), while the thermal conductivity for a water/rock mixture can be estimated with confidence (λ = 2 W.m^{-1}.K^{-1}). The solidifying magma chamber is taken to be at 1200˚C and the boundaries of the upflow and reaction zones are clearly marked by the temperature at which pure water changes from a liquid-like state to a gas-like state. This transition occurs at ~400˚C for all relevant seafloor pressures and therefore the temperature drop across the reaction zone is also well constrained (ΔT = 800 K). Finally, the fluxibility of hot, upwelling water changes little over the relevant temperature range (Figures 5.6k,l) and a value of $F = 1.2 \cdot 10^{16}$ J.s.m^{-5} is typical for all seafloor pressures. Thus, the quantity in square brackets in equations (5.13) and (5.14) takes approximately the same value for all seafloor hydrothermal systems:

$$\left[\frac{\lambda(\Delta T)}{gF}\right] \approx 1.36 \cdot 10^{-14} \quad \text{m}^3 \tag{5.15}$$

It is likely that the half-width of the magma chamber (L) will vary from location to location, but a value of 500 m (i.e. a magma chamber 1 km wide) is probably typical. Taking L = 500 m implies that, in SI units:

$$L_D \sim 4.52 \cdot 10^{-9} \cdot k^{-2/3} \tag{5.16}$$

$$H_R \sim 1.45 \cdot 10^{-3} \cdot k^{-1/3} \tag{5.17}$$

It must be remembered that these are only order of magnitude estimates, because they are derived from approximate balances rather than strict equalities. The values predicted by equations (5.16) and (5.17) can be compared with the results of the numerical simulation of Section 5.3, for which $k = 10^{-14}$ m^2 and $L \approx 500$ m. With these values, equations (5.16) and (5.17) predict that $L_D \approx 10$ m and $H_R \approx 67$ m. Comparison with Figure 5.4 shows that the estimate for H_R is about a factor of 2 too small, while the estimate for L_D is about a factor of 10 too small. Consequently, equations (5.16) and (5.17) can be made more accurate by the introduction of dimensionless factors. The lengthscales, in SI units, then become:

$$L_D \approx 4.52 \cdot 10^{-8} \cdot k^{-2/3} \tag{5.18}$$

$$H_R \approx 2.90 \cdot 10^{-3} \cdot k^{-1/3} \tag{5.19}$$

The graphs in Figure 5.8a show how these lengthscales depend on the permeability (k) according to equations (5.18) and (5.19).

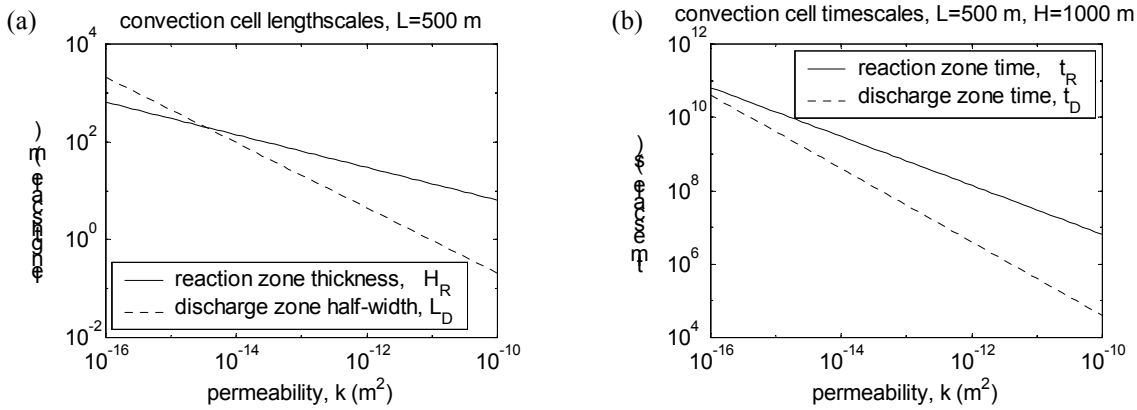

Figure 5.8: The length- and time-scales associated with the reaction and discharge zones in 2-d Cartesian geometry, for a magma chamber of width $2L$ = 1000 m. (a) Lengthscales from equations (5.18) and (5.19). (b) Timescales from equations (5.21) and (5.23).

If it is assumed that the seafloor is homogeneous, these equations could be used to constrain seafloor permeability given a knowledge of the magma chamber width ($2L$). In an active seafloor system seismic imaging may provide this information, whilst in an ophiolite it may be possible to deduce this from direct observation. If either the reaction zone thickness (H_R) or the discharge zone half-width (L_D) could be estimated, an estimate for the bulk permeability could be made.

5.4.2 Residence times in the discharge and reaction zones

The approximate magnitude of the time taken for fluid to ascend the discharge zone is:

$$t_D \sim \frac{H}{w} = \left[\frac{H}{g} \left(\frac{\mu}{\rho_0 - \rho} \right) \right] \cdot k^{-1} \tag{5.20}$$

With H = 1000 m, $(\mu / (\rho_0 - \rho))^{-1} = 2.5 \cdot 10^7$ s.m^{-2} (Figures 5.6i,j) and g = 9.8 m.s^{-2} this gives, in SI units:

$$t_D \sim 4.08 \cdot 10^{-6} \cdot k^{-1} \tag{5.21}$$

Similarly, the approximate magnitude of the residence time of fluid in the reaction zone (t_R) is given by:

$$t_R \sim \frac{L}{u} = \rho h \left[\frac{L^4}{g^2 F^2 \lambda (\Delta T)} \right]^{1/3} \cdot k^{-2/3} \tag{5.22}$$

For hot fluid at ~400°C the volumetric enthalpy is $\rho h \approx 10^9$ J.m^{-3} (Figures 5.6e,f). With L = 500 m, g = 9.8 m.s^{-2}, $F = 1.2 \cdot 10^{16}$ J.s.m^{-5}, λ = 2 W.m^{-1}.K^{-1}, ΔT = 800 K, the reaction zone residence time, in SI units, is:

$$t_R \sim 1.395 \cdot k^{-2/3} \tag{5.23}$$

These residence time estimates are plotted as functions of permeability in Figure 5.8b. For the permeability assumed in Section 5.3 ($k = 10^{-14}$ m^2), the estimates deduced are $t_D \sim 4 \cdot 10^8$ s (≈ 13 years) and $t_R \sim 3 \cdot 10^9$ s (≈ 95 years). The estimate of 13 years residence time for the discharge zone is *much* larger than the estimate of a few minutes obtained by assuming that vent speeds are typical of the discharge zone (Section 5.1). (A discharge zone time of a few minutes would require an effective permeability as high as $4 \cdot 10^{-9}$ m^2, which would have to be provided by fault conduits.) It is important to note that the apparently large ascent time of $t_D \sim$ 13 years is still sufficiently rapid for the fluid to suffer minimal conductive heat loss in the discharge zone and exit with the observed effluent temperatures (Figure 5.4). Elevated temperatures are maintained because the discharge zone has a relatively large half-width L_D ~ 100m creating small horizontal temperature gradients and reducing conductive heat loss. The observation that of little conductive heat loss in the discharge zone confines its position somewhere between the following two extremes. At one extreme, the discharge zone may have large half-width (perhaps up to ~100 m) for much of its height and a long residence time (~10 years). The observation that seafloor vents are so narrow (~0.1 m to ~1 m) suggests that the broad upflow in the discharge zone becomes focussed along fractures near the seafloor. At the other extreme the fractures which focus flow into vents may have deep penetration almost as far as the reaction zone. In the latter case, the discharge zone would have a half-width of the same order of magnitude as the vent diameter over most of its height. In turn, this would create very large horizontal temperature gradients and large conductive heat loss on ascent. This regime would demand correspondingly short residence times in the discharge zone to prevent significant cooling of the fluid on ascent.

The estimate derived for the reaction zone residence time ($t_R \sim$ 95 years when $k = 10^{-14}$ m^2) is comparable on an order of magnitude scale with the radioisotope estimates (Kadko & Moore, 1988; Grasty *et al.,* 1988) of between 3 and 20 years. Assuming L = 500 m, these residence times would be compatible with bulk permeabilities of $1.8 \cdot 10^{-12}$ m^2 and $1.04 \cdot 10^{-13}$ m^2 respectively and support the estimate of bulk permeability used in the model.

5.4.3 Axisymmetric scaling laws

In the previous section, scaling laws are derived for a two-dimensional plume in Cartesian geometry. It is also possible to consider the case of an axisymmetric plume rising above a magma chamber which is circular in plan form. In this case, Figure 5.1 should be interpreted as having an axis of rotational symmetry about the vertical centre line of the discharge zone. The velocity components (u,w) are now in the radial and vertical directions, but take the same form as before (equations (5.7) and (5.8)). However, the conservation of mass is now expressed by:

$$2\pi\rho u L H_R \sim \rho w \pi L_D^2 \tag{5.24}$$

From equations (5.7) and (5.8) for the velocities it follows that:

$$2H_R^2 \sim L_D^2 \tag{5.25}$$

Conservation of energy implies that:

$$\frac{\lambda \Delta T}{H_R}\pi L^2 \sim \rho h w \pi L_D^2 \tag{5.26}$$

from which it follows that:

$$\frac{L^2 \lambda(\Delta T)}{L_D^2 H_R} \sim gkF \tag{5.27}$$

Equations (5.25) and (5.27) can be combined to give:

$$L_D \sim 2^{1/6}\left[\frac{\lambda(\Delta T)}{gF}\right]^{1/3} L^{2/3} k^{-1/3} \tag{5.28}$$

$$H_R \sim 2^{-1/3}\left[\frac{\lambda(\Delta T)}{gF}\right]^{1/3} L^{2/3} k^{-1/3} \tag{5.29}$$

Hence in the axisymmetric case, both the reaction zone thickness (H_R) and the discharge zone half-width (L_D) depend on permeability via the term $k^{-1/3}$. This is in contrast to the case of 2-d Cartesian geometry, where $H_R \sim k^{-1/3}$ (equation (5.14)), but $L_D \sim k^{-2/3}$ (equation (5.13)). Thus, in axisymmetric geometry the reaction zone thickness and discharge zone half-width decay equally quickly as the permeability increases. However, in Cartesian geometry the discharge zone half-width decays faster than the reaction zone thickness. Since the velocities for the axisymmetric case take the same form as for Cartesian geometry (equations (5.7) and (5.8)) it follows that the residence times, t_D and t_R (equations (5.21) and (5.23)), apply equally to both geometries.

5.5 Conclusions

This chapter has been concerned with the control exerted by the nonlinear thermodynamic properties of water on hydrothermal convection cell structure. It has been shown that a very simple model of hydrothermal convection (Section 5.3) is sufficient to reproduce all of the expected features of a hydrothermal convection cell (Sections 5.1 and 5.2), providing the full nonlinear properties of water are retained. The model, which does not rely on inhomogeneous permeability or phase separation, is able to reproduce the thin reaction zone, narrow discharge zone, and temperature limited seafloor vents which are characteristic of all seafloor hydrothermal systems. This suggests that the dynamics associated with inhomogeneous permeability or phase separation are not required to explain convection cell structure, although both phenomena are important in active hydrothermal systems. By introducing a new concept, the 'local Rayleigh number' (Ra_L) it has been possible to predict how the nonlinear properties of pure water dictate the formation of plumes in a porous medium at ~400°C, for seafloor pressures. The 'fluxibility' (F) of water has been shown to be of crucial importance to the formation of convective plumes in the seafloor. It has been argued that seafloor plumes form at the temperature (T_p) for which $\left|\partial F/\partial T\right|$ is maximised. For pure water at seafloor pressures, this plume formation temperature lies between 360°C and 440°C (Figure 5.7). The case of salt water convection is complex and requires thorough investigation. However, it is expected that a similar approach could be adopted.

The scaling analysis presented takes full account of the nonlinear thermodynamic properties of water. It has been shown how the lengthscales and residence times of the reaction zone and discharge zone depend on the permeability, on the assumption that this permeability is homogeneous. In principle, these scalings could be used to constrain bulk permeability if a robust estimate of the lengthscales or residence times could be made from active hydrothermal systems or fossil ophiolite systems.

Chapter 6: Poroelasticity and tidal loading

6.1 Introduction

It is established above, in Chapter 4, that there are many known examples of the tidal modulation of seafloor hydrothermal systems. Variations in temperature, effluent velocity and chemistry can often be correlated to the local ocean tide, and it is therefore expected that the changing tidal pressure field on the seafloor is responsible for a majority of the observed tidal signals. In contrast, Chapter 5 is concerned with the *steady-state* structure of a seafloor convection cell, and in particular its dependence on the properties of water. The aim of this chapter is to establish whether the nonlinear thermodynamic properties of water (Chapter 5) are sufficient to explain the tidal signals which have been observed at mid-ocean ridge hydrothermal systems (Chapter 4).

The effect of tidal loading on subseafloor convection cells is investigated with reference to the equations of poroelasticity, which describe the response of a fluid-filled porous medium to applied stress (Biot, 1941; Rice & Cleary, 1976; Van der Kamp & Gale, 1983; Kümpel, 1991). When a porous medium is placed under load, the resultant stress is borne partly by the solid matrix and partly by the interstitial fluid where it is manifest as a change in fluid pressure known as the incremental pore pressure. The partitioning of the total stress between the fluid and the solid matrix is a function of their elastic properties and the porosity. Consequently, if any one of these properties varies spatially, it is possible for a locally *uniform* load, such as the ocean tide, to produce a *non-uniform* incremental pore pressure field. The subsequent spatial gradients in the incremental pore pressure can then drive interstitial fluid from one region of the fluid-filled medium to another.

For this reason, it is of great interest to consider how the poroelastic properties of a subseafloor convection cell vary spatially. As in Chapter 5, it is assumed for simplicity that the elastic and transport properties of the solid matrix are constant and homogeneous. The only source of spatial variability is the interstitial fluid, whose properties are known to be strongly dependent on temperature. For example, it is shown that the bulk modulus of water changes significantly over the temperature range encountered in a subseafloor hydrothermal system. The partitioning of the total tidal stress between the matrix and the interstitial fluid

differs markedly between regions where the fluid is liquid-like and regions where it is gas-like. When tidal loading is applied at the seafloor, the gradients in incremental pore pressure induce tidally modulated fluid flow between the cold, liquid-like regions and the hot, gas-like regions.

The physical quantities associated with the fluid in a subseafloor convection cell - such as pressure, velocity and temperature (Section 5.3) – are expected to fluctuate as a result of tidal loading. The label 'incremental' is used to refer to the tidally induced variation of any physical quantity about its undisturbed value. For some years, there has been a well-established analytical solution giving the incremental pore pressure in an infinite one-dimensional halfspace subject to uniform tidal loading (Van der Kamp & Gale, 1983; Wang & Davis, 1996). Here, this solution is extended to cover the two physical quantities which are commonly measured on the seafloor – the vertical velocity and the temperature (Chapter 4). For an infinite halfspace, it is shown that the incremental vertical velocity at the seafloor lags the ocean tide by 135°. Consequently, the maximum effluent velocity at the seafloor is predicted to occur ~4.5 h after high tide for semi-diurnal components, and ~9 h after high tide for diurnal components. If the permeable crust is taken to be of finite thickness the corresponding phase lag is shown to lie between 90° and ~135°, depending on the thickness of the permeable layer relative to the lengthscale associated with pore pressure diffusion. Consequently, observed phase lags between the ocean tide and effluent velocity at the seafloor could be used to infer the vertical distance over which the crust is permeable.

An approximate expression for the tidally induced incremental temperature is derived for the case of buoyant fluid ascending through a linear temperature gradient. It is shown that the incremental temperature lags the incremental velocity by 90°. Hence, for an infinite halfspace, the incremental temperature at the seafloor lags the ocean tide by 225° and the hottest effluent is expelled ~7.5 h after high tide for semi-diurnal components, and ~15 h after high tide for diurnal components. If the permeable crust has finite thickness, however, the seafloor effluent temperature lags the ocean tide by an angle between 180° and ~225°, depending on the thickness of the permeable layer. These predicted phase lags are shown to be consistent with many of the seafloor data discussed in Chapter 4.

Analytical solutions of simple one-dimensional models allow the physical processes responsible for seafloor tidal signals to be identified. In Section 6.3.2, some preliminary

numerical simulations are presented in which the two-dimensional convection cell of Section 5.3 is subjected to uniform tidal loading at the seafloor. The results of these simulations are interpreted with reference to the one-dimensional analytical solutions (Section 6.3.1).

6.2 Fundamental concepts of poroelasticity

The purpose of this section is to review the theory of poroelasticity, with particular regard to hydrothermal systems under tidal loading (Biot, 1941; Rice & Cleary, 1976; Van der Kamp & Gale, 1983; Kümpel, 1991). It is assumed that the properties of the crust are constant and homogeneous. Consequently, the objective is to investigate the effect which temperature-dependent fluid properties have on the principal poroelastic parameters.

6.2.1 The dependence of poroelastic parameters on fluid temperature

When a fluid-filled porous medium such as the ocean crust is placed under external load, it experiences incremental stress $(\hat{\sigma}_{ij})$ and incremental strain $(\hat{e}_{ij})$. Prior to loading, the absolute pressure of the fluid in the pores (p) is constant. Under load, however, there is an additional, time-varying pressure known as the incremental pore pressure $(\hat{p})$. The confining pressure $(\hat{p}_c)$ is a scalar measure of the stress, defined by:

$$\hat{p}_c = -\frac{1}{3}\hat{\sigma}_{kk} \tag{6.1}$$

(The Einstein summation convention is used throughout, so that there is an implied summation over a repeated tensor suffix.) Three distinct bulk moduli are relevant to the behaviour of the fluid-filled porous medium and their physical interpretation is summarised in Figure 6.1. Firstly, the grain bulk modulus (K_g) is the bulk modulus of the medium in the absence of any pore space. Secondly, the matrix bulk modulus (K_m) is the bulk modulus of the medium when the pore space exists but is empty. (For this reason, it is sometimes known as the drained bulk modulus.) Values of the grain and matrix bulk moduli for several geological materials are reproduced in Table 6.1.

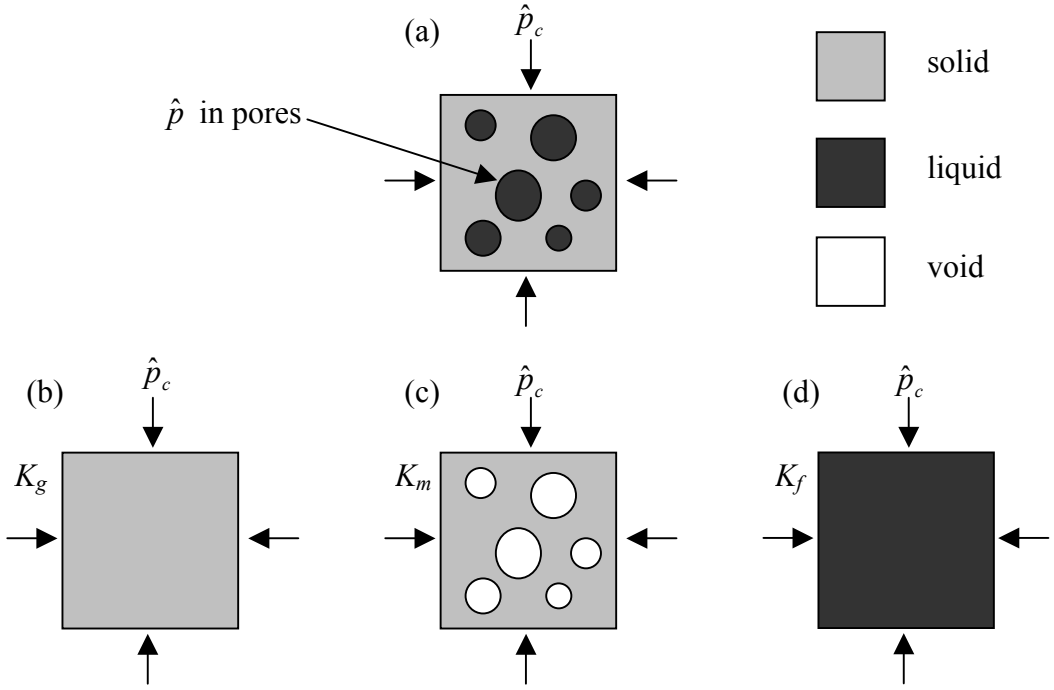

Figure 6.1: Schematic illustrations of the three bulk moduli relevant to poroelasticity. (a) A fluid-filled poroelastic medium subjected to an incremental confining pressure $\hat{p}_c$ has incremental pore pressure $\hat{p}$. (b) Situation defining the grain bulk modulus: $\hat{e}_{kk} = -\hat{p}_c / K_g$. (c) Situation defining the matrix bulk modulus: $\hat{e}_{kk} = -\hat{p}_c / K_m$. (d) Situation defining the fluid bulk modulus: $\hat{e}_{kk} = -\hat{p}_c / K_f$

Thirdly, the fluid bulk modulus (K_f) is the bulk modulus of the fluid which fills the pore space, and is a function of its pressure and temperature. If the pore fluid has temperature T, specific enthalpy h, and density ρ, then the *isenthalpic* fluid bulk modulus (K_{fh}) is defined (Van Wylen & Sonntag, 1978) by:

$$K_{fh} = \left[\left(\frac{1}{\rho} \frac{\partial \rho}{\partial p} \bigg|_{h=const.} \right) \right]^{-1} \tag{6.2}$$

while the *isothermal* fluid bulk modulus (K_{fT}) is defined by:

$$K_{fT} = \left[\left(\frac{1}{\rho} \frac{\partial \rho}{\partial p} \bigg|_{T=const.} \right) \right]^{-1} \tag{6.3}$$

For water, the values of K_{fh} and K_{fT} are sufficiently similar to be regarded as interchangeable, and both may be considered synonymous with the fluid bulk modulus (K_f). (The values quoted in this dissertation are derived from the steam tables embedded in the

HYDROTHERM code and are, strictly, isenthalpic fluid bulk moduli.) Values of K_f are plotted in Figure 6.2 for a range of pressures and temperatures relevant to seafloor hydrothermal systems.

material	K_g (GPa)	K_m (GPa)	v	φ_0	k (m^2)
seafloor sediment[1]	50	0.5	0.10	0.50	$1 \cdot 10^{-17}$ to $1 \cdot 10^{-15}$
seafloor sediment[2]				0.60	$1 \cdot 10^{-15}$
seafloor sediment[3]		2.17		0.80	$5 \cdot 10^{-15}$
Ruhr sandstone[4]	36	13	0.12	0.02	$2 \cdot 10^{-16}$
Berea Sandstone[4]	36	8	0.20	0.19	$2 \cdot 10^{-13}$
Weber sandstone[4]	36	13	0.15	0.06	$1 \cdot 10^{-15}$
Charcoal granite[4]	45	34	0.27	0.02	$1 \cdot 10^{-19}$
Westerly granite[4]	45	25	0.25	0.01	$4 \cdot 10^{-19}$
Tennessee marble[4]	50	40	0.25	0.02	$1 \cdot 10^{-19}$
MOR basement[5]					$9 \cdot 10^{-12}$
"typical" Basalt[6]		30	0.20		

Table 6.1: The transport and elastic properties of various geological materials. K_g – grain bulk modulus. K_m – matrix bulk modulus. v – Poisson's ratio. φ_0 – porosity. k – permeability. References: (1) Wang & Davis (1996). (2) Fang *et al.* (1993). (3) Hurley & Schultheiss (1991). (4) Van der Kamp & Gale (1983). (5) Fisher *et al.* (1997) – MOR refers to 'Mid-Ocean Ridge'. (6) Carmichael (1982), where values for several basalts are given - typical values are reproduced here.

Figure 6.2 shows that K_f depends strongly on temperature but only weakly on pressure in the region of p-T space relevant to seafloor hydrothermal systems. The temperature dependence is similar to that of the thermodynamic properties considered in Chapter 5 (Figure 5.6), in the sense that there is a sharp change in behaviour at ~400°C as water moves from a liquid-like state to a gas-like state. At seafloor pressures, the bulk modulus of water ranges from a cold, liquid-like value of ~2.2 GPa at 2°C to hot, gas-like values between ~0.02 GPa and ~0.05 GPa above ~400°C. (A fluid obeying the laws for a perfect gas has a bulk modulus (K_f) equal to the fluid pressure (p). At seafloor pressures, water above ~400°C approximates this perfect gas behaviour fairly closely.) Comparison of Figure 6.2a with Table 6.1 shows that the bulk modulus of water in the seafloor crust (K_f) is much smaller than the grain bulk modulus (K_g) for all of the listed geological materials. It is therefore assumed that $K_f << K_g$ for all subseafloor convection cells. However, it is not always true that $K_f << K_m$. For example,

Table 6.1 shows that K_f (~2.2 GPa when cold) may even exceed K_m (~0.5 GPa), when the poroelastic medium is sediment.

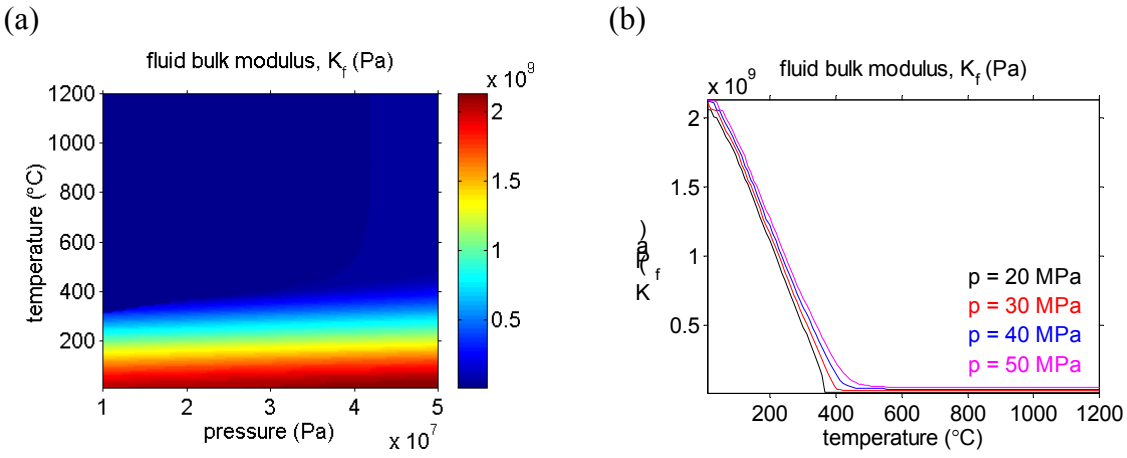

Figure 6.2: The bulk modulus of pure water, K_f. (a) K_f as a function of pressure and temperature. (b) K_f as a function of temperature at a range of typical subseafloor pressures. Data are derived from the steam tables embedded in the HYDROTHERM code. (10^7 Pa corresponds to 1 km below sea level.)

The three bulk moduli (K_g, K_m, and K_f), and the porosity (φ_0) together constitute a set of four fundamental parameters describing the elastic properties of a fluid-filled porous medium. Three further parameters (α, S and β) are often derived from this fundamental set, and their dependence on the thermodynamic state of the pore fluid is considered below.

6.2.1.1 Coefficient of effective stress: α

Firstly, the coefficient of effective stress (α) is defined (Nur & Byerlee, 1971) by:

$$\alpha = 1 - \frac{K_m}{K_g} \tag{6.4}$$

Hence, α is a measure of the relative magnitude of the matrix and grain bulk moduli (Table 6.1). It should be noted that $K_m \leq K_g$, and so α is a dimensionless number in the range [0,1]. The value of α depends solely on the properties of the rock matrix, and *not* on the properties of the interstitial fluid. Consequently, it is assumed for simplicity that α is constant and homogeneous within any particular subseafloor convection cell. For the geological materials listed in Table 6.1, the values of α range from 0.2 (Tennessee marble) to 0.99 (seafloor sediment).

6.2.1.2 Storage compressibility: *S*

The second derived parameter is the storage compressibility (S) defined by:

$$S = \left(\frac{1}{K_m} - \frac{1}{K_g} \right) + \phi_0 \left(\frac{1}{K_f} - \frac{1}{K_g} \right) \tag{6.5}$$

As its name implies, the storage compressibility has units of inverse pressure, and it can be interpreted as the volume of interstitial fluid which is added to the pore space, per unit volume of rock, per unit increase in pore pressure (Kümpel, 1991). Since K_g, K_m, and φ_0 are regarded as constants for any particular problem, it follows that spatial variations in S can only be due to spatial variations in K_f. Figure 6.2 shows that K_f changes little with pressure and is a *decreasing* function of temperature. It therefore follows from equation (6.5) that S changes little with pressure and is an *increasing* function of temperature. Table 6.1 suggests that K_g = 50 GPa and K_m = 30 GPa might be reasonable values for the bulk moduli of the oceanic crust. Unless otherwise stated, these values will be used throughout this chapter.

The fact that S depends on the fluid bulk modulus suggests that there will be a marked change in its value at ~400°C, when water changes from a liquid-like state to a gas-like state. Equation (6.5) shows that the relative magnitude of this change is controlled by the value of the porosity, φ_0. Consequently, a critical porosity, $\varphi_c(p,T)$, can be defined by:

$$\phi_c(p,T) = \frac{\left(\frac{1}{K_m} - \frac{1}{K_g} \right)}{\left(\frac{1}{K_f} - \frac{1}{K_g} \right)} \tag{6.6}$$

It should be noted that this critical porosity depends on the fluid bulk modulus (K_f) and is therefore pressure- and temperature-dependent. The variability of S as a function of fluid temperature can now be classified into one of three regimes corresponding to large, intermediate and small values of the porosity ratio (φ_0 / φ_c). In the intermediate porosity regime - when (φ_0 / φ_c)~1 for all temperatures - the full defining equation for S must be used (equation (6.5)). However, simplifications can be made when the porosity is either large or small in relation to the critical porosity, φ_c. For K_g = 50 GPa and K_m = 30 GPa the critical porosity (φ_c) is 0.03 for cold water (K_f = 2.2 GPa) and 0.0003 for hot water (K_f = 0.02 GPa). The dependence of S on pressure and temperature for the three porosity regimes is illustrated in Figure 6.3.

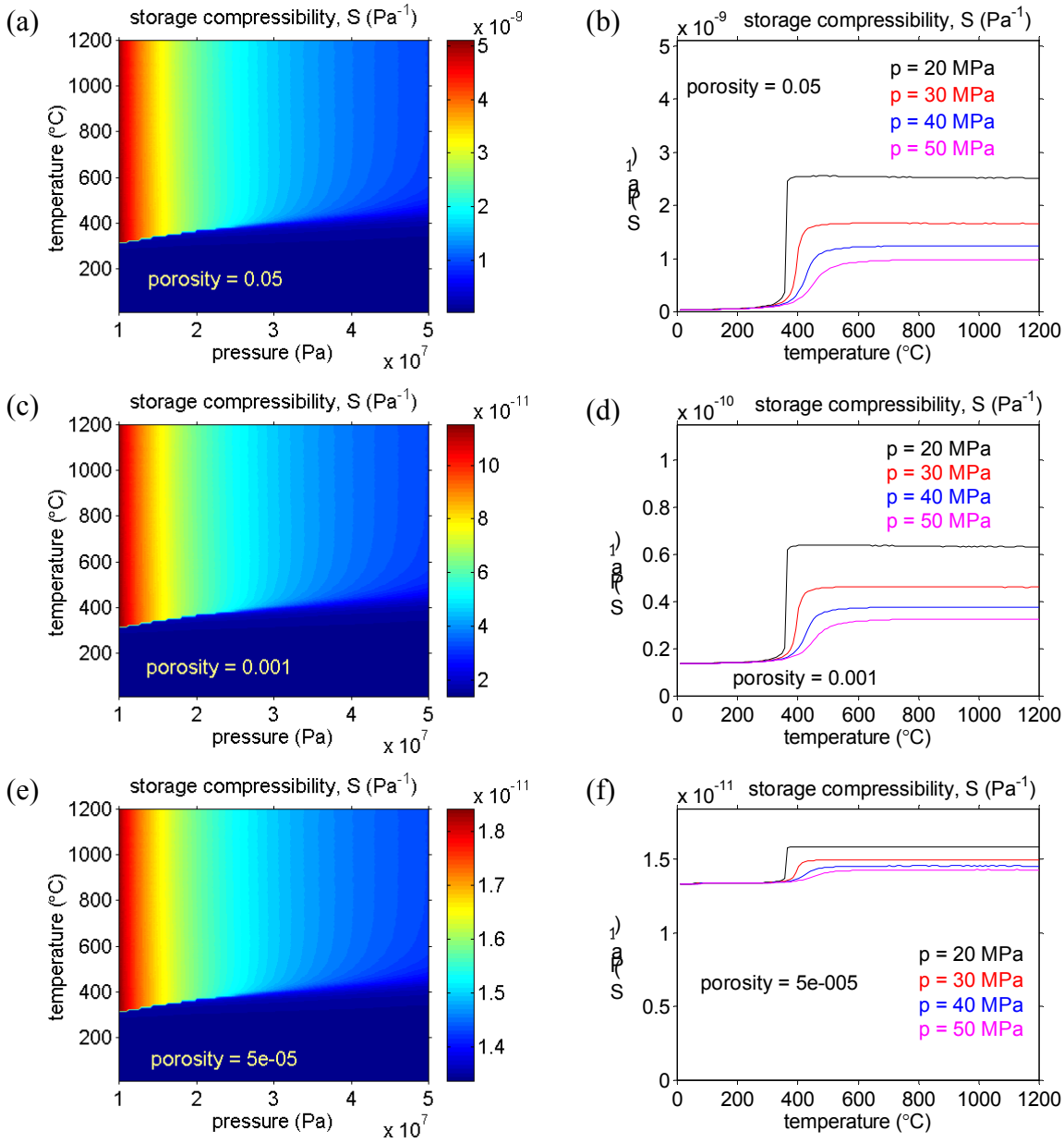

Figure 6.3: The dependence of the storage compressibility (S) on the thermodynamic state of the interstitial fluid in the large, intermediate and small porosity regimes with K_g = 50 GPa, K_m = 30 GPa. The interstitial fluid is assumed to be pure water. Thermodynamic data are taken from the tables embedded in the HYDROTHERM code. (a),(b) φ_0 = 0.05 (large). (c),(d) φ_0 = 0.001 (intermediate). (e),(f) φ_0 = 0.00005 (small). (10^7 Pa corresponds to 1 km below sea level.)

The large porosity regime - when (φ_0 / φ_c) >1 for all temperatures - implies that:

$$S \approx \frac{\phi_0}{K_f} \tag{6.7}$$

Equation (6.7) shows that the storage compressibility (S) is proportional to the fluid compressibility (K_f^{-1}) in the large porosity regime (Figures 6.3a,b).

In contrast, the small porosity regime - when (φ_0 / φ_c) < 1 for all temperatures - implies that

$$S \approx \left(\frac{1}{K_m} - \frac{1}{K_g} \right) = \frac{\alpha}{K_m} \tag{6.8}$$

Hence, the storage compressibility is approximately constant as a function of temperature when the porosity is small (Figures 6.3e,f).

In summary, it should be noted that S is always an *increasing* function of fluid temperature at seafloor pressures. The greatest change in S occurs at ~400˚C, as the water changes from a liquid-like state to a gas-like state. The contrast between the liquid-like and gas-like values of S is greatest when the porosity is large.

6.2.1.3 Skempton ratio: β

Thirdly amongst the derived poroelastic parameters, the Skempton ratio (β) is defined by

$$\beta = \frac{\left(\frac{1}{K_m} - \frac{1}{K_g} \right)}{\left(\frac{1}{K_m} - \frac{1}{K_g} \right) + \phi_0 \left(\frac{1}{K_f} - \frac{1}{K_g} \right)} \tag{6.9}$$

The Skempton ratio is a dimensionless parameter taking values in the range [0,1]. When a poroelastic medium is loaded isotropically, the Skempton ratio (β) can be interpreted as the ratio of the incremental pore pressure $\left(\hat{p}\right)$ to the applied incremental confining pressure $\left(\hat{p}_c\right)$ (Figure 6.1a). Equivalently, β is the proportion of the total applied stress which is borne by the pore fluid. Equations (6.4), (6.5) and (6.9) imply that $\beta = (\alpha / K_m) / S$. Since α and K_m are constant properties of the rock matrix, it follows that the variation of β with the thermodynamic state of the fluid can be divided into the same three porosity regimes as the variation of S.

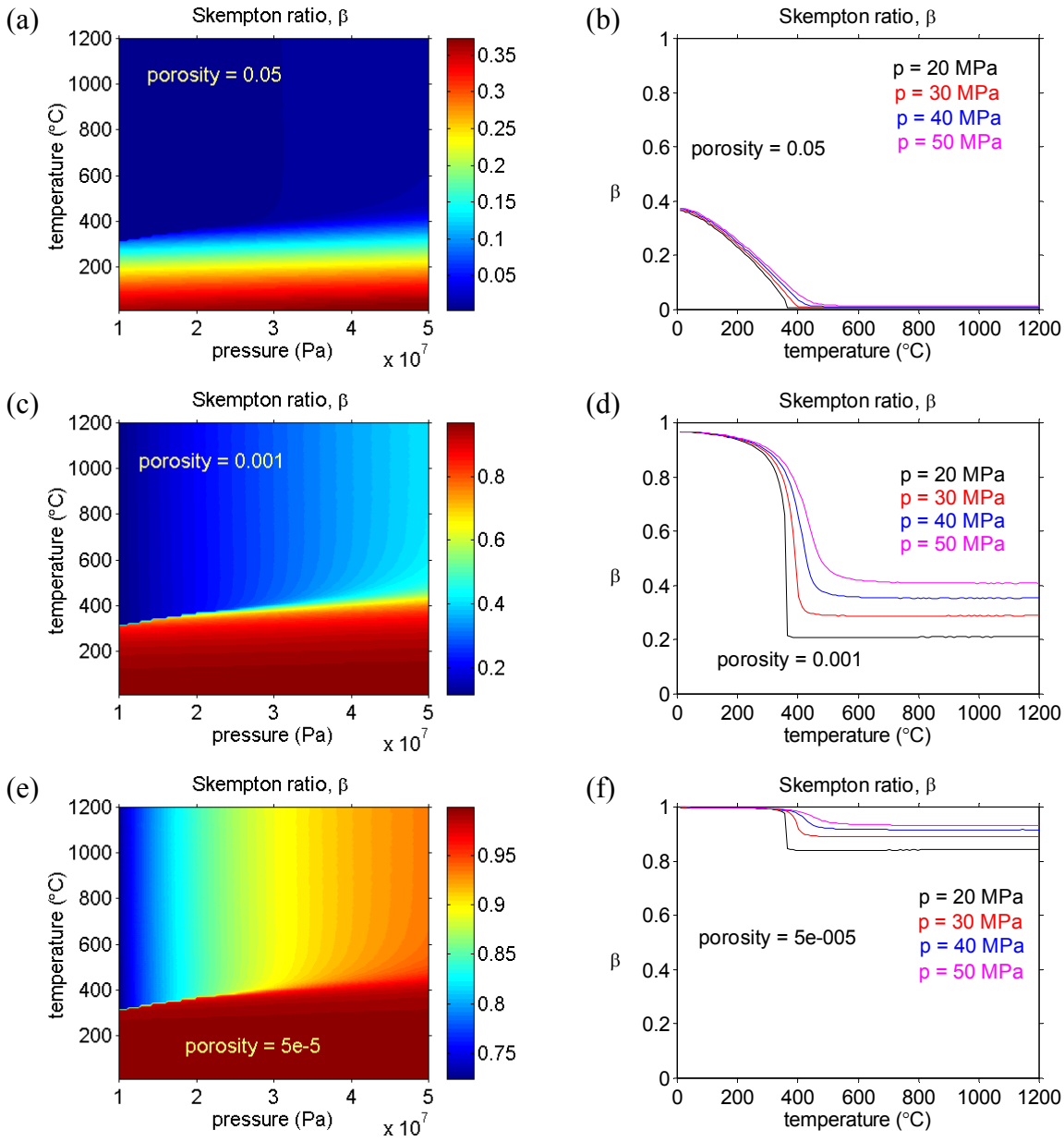

Figure 6.4: The dependence of the Skempton ratio (β) on the thermodynamic state of the interstitial fluid in the large, intermediate and small porosity regimes with K_g = 50 GPa, K_m = 30 GPa. Interstitial fluid is pure water. Thermodynamic data from the tables embedded in the HYDROTHERM code. (a), (b) φ_0 = 0.05 (large). (c), (d) φ_0 = 0.001 (intermediate). (e), (f) φ_0 = 0.00005 (small). (10^7 Pa corresponds to 1 km below sea level.)

For intermediate porosity - when $(\varphi_0 / \varphi_c) \sim 1$ - the full defining equation for β (equation (6.9)) must be used. However, for large porosity - when $(\varphi_0 / \varphi_c) > 1$ - equation (6.9) reduces to:

$$\beta \approx \left[\frac{\alpha}{\phi_0 K_m}\right] K_f \tag{6.10}$$

Hence the Skempton ratio (β) is a scaled version of the fluid bulk modulus (K_f) when the porosity is large and it is therefore highly temperature dependent (Figures 6.2a,b, 6.4a,b).
In contrast, for small porosity - when (φ_0 / φ_c) < 1 - the temperature dependence of the Skempton ratio is much reduced (Figures 6.4e,f) and equation (6.9) reduces to

$$\beta \approx 1 \tag{6.11}$$

In summary, β is a *decreasing* function of fluid temperature for all seafloor pressures, with the greatest change occurring at ~400°C, where water changes from a liquid-like state to a gas-like state. The contrast between the liquid-like and gas-like values of β is greatest when the porosity is large. Since β represents the proportion of the applied stress borne by the interstitial fluid, it follows that uniform tidal loading at the seafloor can create incremental pore pressures which differ between the hot and cold parts of a hydrothermal convection cell. In general terms, when the ocean tide is high, cold regions of the cell (where β is large) will have greater pore pressures than hot regions (where β is small). Consequently, fluid is expected to flow from cold regions to hot regions at high tide. The pressure difference which drives the flow is particularly large if the hot fluid is gas-like (>~400°C) and the cold fluid is liquid-like (<~400°C). The magnitude of the induced flow is determined by the spatial gradient of the incremental pore pressure. Consequently, the induced tidally modulated flow is expected to be large where spatial gradients in temperature are large. This heuristic argument is investigated with greater rigour in Section 6.3.

6.2.2 The governing equations of poroelasticity

Given a value for the Poisson's ratio of the solid matrix (ν) it can be shown (Rice & Cleary, 1976; Van der Kamp & Gale, 1983) that the stress-strain relationship for a fluid-filled porous medium is:

$$\hat{e}_{ij} = \frac{1}{3K_m}\left[\frac{(1+\nu)}{(1-2\nu)}\hat{\sigma}_{ij} - \frac{\nu}{(1-2\nu)}\hat{\sigma}_{kk}\delta_{ij} + \alpha\hat{p}\delta_{ij}\right] \tag{6.12}$$

Typically, the Poisson's ratio takes a value $\nu \approx 0.2$ for geological materials (Table 6.1), and so $\nu = 0.2$ is assumed throughout this chapter. With the convention that a repeated suffix indicates summation, equation (6.12) yields:

$$\hat{e}_{kk} = \frac{1}{3K_m}\left[\hat{\sigma}_{kk} + 3\alpha\hat{p}\right] = -\frac{1}{K_m}\left[\hat{p}_c - \alpha\hat{p}\right] \tag{6.13}$$

Equation (6.13) can be used to provide a physical interpretation for the effective stress ratio (α). For a solid medium, the volume dilatation $(\hat{e}_{kk})$ is proportional to the confining pressure $(\hat{p}_c)$ (Figure 6.1b). For a poroelastic medium, however, equation (6.13) shows that the volume dilatation is proportional to the so-called effective pressure $(\hat{p}_c - \alpha\hat{p})$.

This dissertation is concerned with the effect of tidal loading at periods of ~12 h and greater. This timescale is much greater than the time taken for seismic waves (speed > 1 km.s^{-1}), to cover the lengthscales appropriate to hydrothermal systems (< 10 km). Consequently, the stresses due to tidal loading of the seafloor are, effectively, transmitted instantaneously throughout a subseafloor convection cell. The equations of compatibility for an elastic medium (Love, 1927) can be applied to equation (6.12) to give an equation expressing elastic equilibrium:

$$\nabla^2\left[(1+\nu)\hat{\sigma}_{ij} - \nu\hat{\sigma}_{kk}\delta_{ij}\right] + \frac{\partial^2}{\partial x_i \partial x_j}\hat{\sigma}_{kk} + \alpha(1-2\nu)\left[\nabla^2\hat{p}\,\delta_{ij} + \frac{\partial^2}{\partial x_i \partial x_j}\hat{p}\right] = 0 \qquad (6.14)$$

Equation (6.14) can be contracted on the suffices to yield:

$$\nabla^2\hat{\sigma}_{kk} + \left[\frac{2\alpha(1-2\nu)}{(1-\nu)}\right]\nabla^2\hat{p} = 0 \qquad (6.15)$$

The conservation of pore fluid is expressed by the equation:

$$\left[\frac{k}{\mu S}\right]\nabla^2\hat{p} = \frac{\partial\hat{p}}{\partial t} + \frac{\partial}{\partial t}\left(\beta\cdot\frac{\hat{\sigma}_{kk}}{3}\right) \qquad (6.16)$$

where k is the permeability of the rock matrix and μ is the dynamic viscosity of the interstitial fluid.

In general, solutions to problems of poroelastic loading are found by solving equations (6.14) and (6.16) for the incremental pore pressure $(\hat{p})$ and the incremental stress tensor $(\hat{\sigma}_{ij})$. In certain simple cases, however, the number of unknowns reduces to two - $\hat{p}$ and $\hat{\sigma}_{kk}$ - and solutions are found by solving equations (6.15) and (6.16). Furthermore, if $\hat{\sigma}_{kk}$ is known, equation (6.16) becomes a forced conduction equation for the incremental pore pressure $(\hat{p})$ with a diffusivity (κ) defined by

$$\kappa = \frac{k}{\mu S} \qquad (6.17)$$

The permeability of the seafloor (k) is very poorly constrained (Table 6.1). Consequently, it is helpful to define a scaled diffusivity ((μS)$^{-1}$) in order to examine the dependence of the diffusivity (κ) on the temperature (T) of the interstitial fluid.

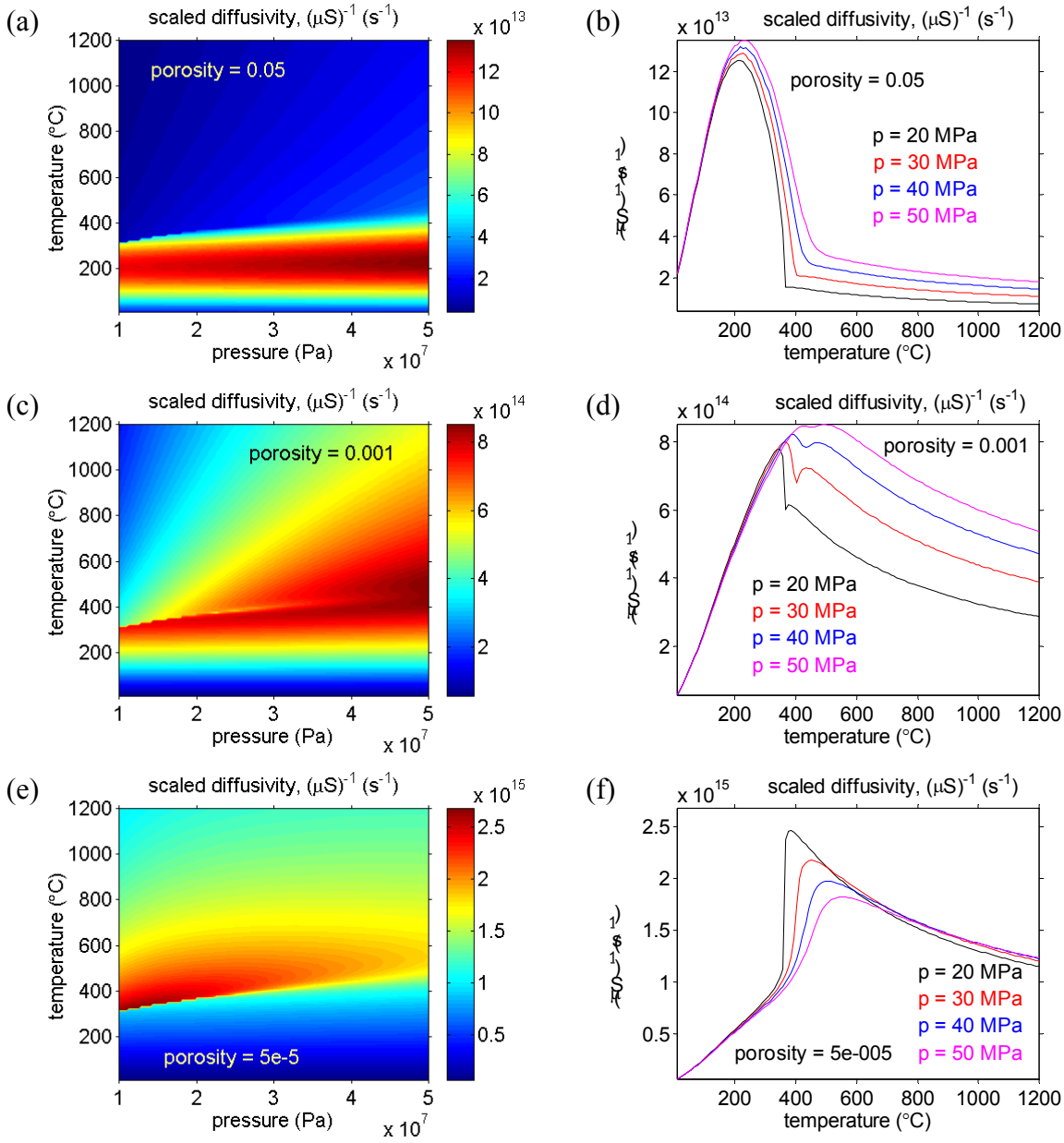

Figure 6.5: The dependence of the scaled diffusivity ($(\mu S)^{-1}$) on the thermodynamic state of the interstitial fluid in the large, intermediate and small porosity regimes with K_g = 50 GPa, K_m = 30 GPa. (The true diffusivity, in $m^2.s^{-1}$ is $k\cdot(\mu S)^{-1}$). The interstitial fluid is assumed to be pure water. Thermodynamic data from the tables embedded in the HYDROTHERM code. (a),(b) φ_0 = 0.05 (large). (c),(d) φ_0 = 0.001 (intermediate). (e),(f) φ_0 = 0.00005 (small). (10^7 Pa corresponds to 1 km below sea level.)

Figure 6.5 shows how the scaled diffusivity depends on pressure and temperature in each of the three porosity regimes for K_g = 50 GPa and K_m = 30 GPa. In the large porosity regime - when $(\varphi_0 / \varphi_c) > 1$ - equations (6.7) and (6.17) imply that:

$$\frac{1}{\mu S} \approx [\phi_0] \frac{K_f}{\mu} \tag{6.18}$$

Consequently the diffusivity is proportional to (K_f / μ) (Figures 6.5a,b), and is maximised at ~200°C for seafloor pressures.

Conversely, in the small porosity regime - when (φ_0 / φ_c) > 1 - equations (6.8) and (6.17) imply that:

$$\frac{1}{\mu S} \approx \left[\frac{K_m}{\alpha} \right] \frac{1}{\mu} \tag{6.19}$$

Consequently, the diffusivity is proportional to the inverse viscosity (μ^{-1}) (Figures 6.5e,f), and is maximised at ~400°C for seafloor pressures.

In summary, Figure 6.5 shows that the scaled diffusivity is maximised somewhere between ~200°C and ~400°C for all seafloor pressures, depending on the value of the porosity. Hence, assuming that crustal permeability is homogeneous, diffusive incremental pore pressures due to tidal loading will tend to propagate furthest in regions of a subseafloor convection cell where the temperature is between ~200°C and ~400°C.

Equations (6.16) and (6.17) show that the propagation of incremental pore pressure is described by a diffusion equation with diffusivity κ. When tidal loading is applied to the seafloor at angular frequency ω, diffusion occurs over a characteristic lengthscale known as the skindepth (d) defined by:

$$d = \sqrt{\frac{2\kappa}{\omega}} = \sqrt{k} \sqrt{\frac{2}{\omega}} \sqrt{\frac{1}{\mu S}} \tag{6.20}$$

It has already been remarked that the crustal permeability (k) is very poorly constrained for seafloor hydrothermal systems. Nonetheless, using equation (6.20) it is possible to make some general deductions concerning the magnitude of the skindepth (d). Figure 6.6 shows how the skindepth for semi-diurnal loading (ω = $1.4 \cdot 10^{-4}$ s^{-1}) depends on permeability for typical values of $(\mu S)^{-1}$ taken from Figure 6.5. In broad terms, the minimum plausible skindepth for a semi-diurnal tidal signal in seafloor crust is d ~ 1 m when k = 10^{-17} m^2 and the fluid is at ~2°C. Conversely, the maximum plausible skindepth is d ~ 10,000 m when k = 10^{-10} m^2 and the fluid is at ~400°C. It is important to note that this range of skindepths spans a very wide range. A skindepth of 1 m is very much less than the typical dimensions of a seafloor convection cell (H ~ 1000 m, L ~ 500 m) while a skindepth of 10,000 m is considerably larger. The dependence of the skindepth on angular frequency (ω) in equation

(6.20) implies that the skindepths for diurnal components are greater than those for semi-diurnal components by a factor of √2.

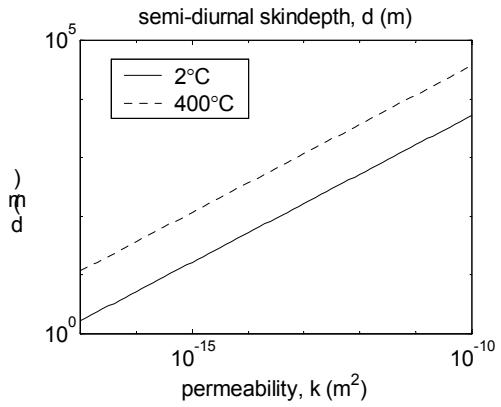

Figure 6.6: The variation of the skindepth (d) for semi-diurnal tidal loading as a function of permeability, k. Using the values from Figure 6.5c,d it is assumed that $(\mu S)^{-1}=2\cdot10^{-13}$ s^{-1} at ~2°C, and $(\mu S)^{-1}=10^{-15}$ s^{-1} at 400°C. Note the logarithmic scales on both axes.

It is now possible to describe qualitatively the nature of solutions of equation (6.16) in a seafloor under tidal loading, according to the size of the skindepth (d). By considering the case of a layered seafloor, Wang & Davis (1996) demonstrated that a diffusive pressure signal is induced wherever there is a sharp contrast in the elastic properties of the seafloor. In the case of the idealised convection cell of Chapter 5, there are two such sharp boundaries in elastic properties– the seafloor itself, and the boundary separating liquid-like water from gas-like water which is approximated by the 400°C isotherm. The amplitude of the diffusive pressure signal decays exponentially over a lengthscale d away from the boundaries in elastic properties. In fact at distances greater than $2d$ from these boundaries, the diffusive pressure signal is negligible and the solution is dominated by the 'instantaneous pressure signal':

$$\hat{p} \approx -\beta \frac{\hat{\sigma}_{kk}}{3} = \beta \hat{p}_c \tag{6.21}$$

It should be noted that the approximate solution of equation (6.21) applies at every point of the cell which is more than a distance $2d$ from a sharp boundary in elastic properties. Consequently, the magnitude of the skindepth (d) is of great importance. In regions more than a few skindepths from boundaries in elastic properties, the incremental pore pressure is in phase with the tidal loading. Therefore, if the skindepth is very small (d < 10 m) the incremental pore pressure is well approximated by equation (6.21) over almost all of the

subseafloor. It follows that the incremental pore pressure will be in phase with the ocean tide over most of the cell, although its amplitude varies according to any spatial variations in the Skempton ratio (β). In contrast, if the skindepth is comparable with the lengthscales of the cell (d > 100 m), then the incremental pore pressure at depth is generally not in phase with the ocean tide.

In Section 6.3, these qualitative remarks above concerning the incremental pore pressure response to tidal loading are illustrated with analytical solutions and numerical simulations.

6.3 Tidal loading of the seafloor

This section is concerned with the effect of loading by the ocean tide on a poroelastic seafloor. The nature of the global ocean tide is discussed in Chapter 2, where it is illustrated with the use of cotidal maps (Figure 2.8). The area of seafloor associated with an individual hydrothermal system typically has a lengthscale of at most 1 km. This is much smaller than the typical wavelength of the ocean tide. Consequently, it is reasonable to suppose that at any time the tidal loading is uniform over the area of seafloor associated with an individual hydrothermal convection cell.

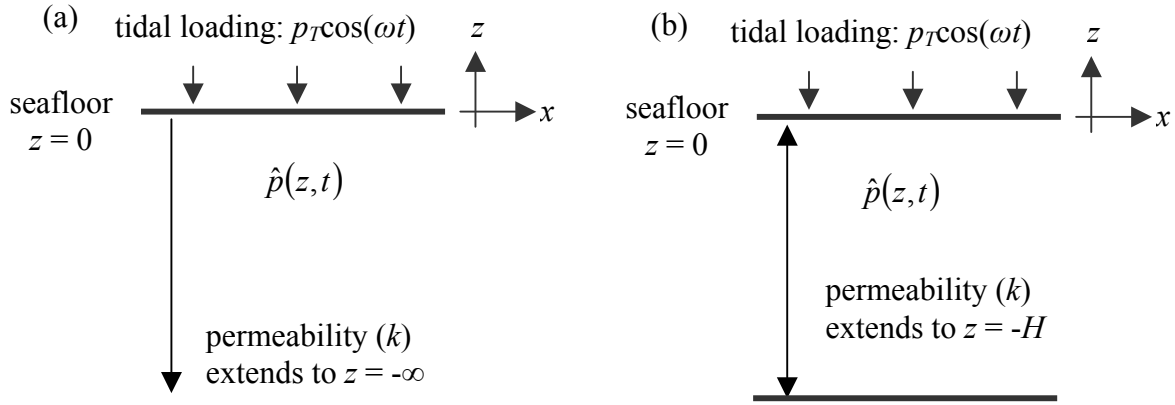

Figure 6.7: The loading of a 1-d seafloor by the ocean tide. It is supposed that there is no horizontal spatial variation. (a) Infinite 1-d halfspace. (b) Finite permeable layer of depth H.

6.3.1 Tidal loading of a 1-d seafloor

Consider the uniform tidal loading of a seafloor in which the poroelastic properties are homogeneous and the incremental pore pressure is $\hat{p}(z,t)$ (Figure 6.7a,b). Symmetry implies

that there is no horizontal strain $\left(\hat{e}_{11} = \hat{e}_{22} = 0\right)$. Since the governing equations are linear, the incremental pore pressure due to a single component of the ocean tide can be considered in isolation (Table 2.1). The imposed pressure on the seafloor is therefore taken to be a time-harmonic oscillation of magnitude p_T and angular frequency ω. In complex notation, the seafloor boundary condition on the incremental pore pressure is:

$$\hat{p}(0,t) = p_T \exp(i\omega t) \tag{6.22}$$

The tides in the open oceans generally have an amplitude of ~1 m (Figure 2.8), and so p_T typically has an amplitude of about 10 kPa.

6.3.1.1 Incremental pore pressure in an infinite halfspace

The simplest model is one in which the permeable crust is of infinite extent below the seafloor (Figure 6.7a). The solution for this infinite halfspace is derived by Van der Kamp & Gale (1983) and is discussed in detail by Wang & Davis (1996). It is of fundamental importance, and is reproduced below.

Van der Kamp & Gale (1983) show that the incremental vertical stress is the same for all depths:

$$\hat{\sigma}_{33} = -p_T \exp(i\omega t) \quad \forall z \tag{6.23}$$

Consequently, equation (6.16) can be re-arranged to read:

$$\left[\frac{3(1-\nu)k}{(3(1-\nu)-2\alpha\beta(1-2\nu))\mu S}\right]\frac{\partial^2 \hat{p}}{\partial z^2} = \frac{\partial \hat{p}}{\partial t} + \left[\frac{(1+\nu)\beta}{3(1-\nu)-2\alpha\beta(1-2\nu)}\right]\frac{\partial}{\partial t}(\hat{\sigma}_{33}) \tag{6.24}$$

Since $\hat{\sigma}_{33}(z,t)$ is known from equation (6.23), equation (6.24) constitutes a forced diffusion equation for the incremental pore pressure $(\hat{p})$.

From equation (6.24), it is possible to define a '1-d diffusivity' (κ_{1d}) according to:

$$\kappa_{1d} = \left[\frac{3(1-\nu)}{3(1-\nu)-2\alpha\beta(1-2\nu)}\right]\frac{k}{\mu S} \tag{6.25}$$

The assumption of a 1-d seafloor leads to the introduction of the dimensionless factor in square brackets, which distinguishes κ_{1d} (equation (6.25)) from κ (equation (6.17)).

Equation (6.24) also suggests the definition of a '1-d loading efficiency' (γ_{1d}) according to:

$$\gamma_{1d} = \left[\frac{(1+\nu)}{3(1-\nu)-2\alpha\beta(1-2\nu)}\right]\beta \tag{6.26}$$

The assumption a 1-d seafloor leads to the introduction of the dimensionless factor in square brackets which distinguishes γ_{1d} (equation (6.26)) from the Skempton ratio, β (equation (6.9)).

Referring to the 1-d parameters of equations (6.25) and (6.26), equation (6.24) yields an equation governing the diffusion of incremental pore pressure in a homogeneous 1-d seafloor:

$$\kappa_{1d}\frac{\partial^2 \hat{p}}{\partial z^2} = \frac{\partial \hat{p}}{\partial t} + \gamma_{1d}\frac{\partial}{\partial t}\left(-p_T \exp(i\omega t)\right) \tag{6.27}$$

By analogy with the skindepth (d) (equation (6.20)), a '1d-skindepth', representing the lengthscale of diffusion of the incremental pore pressure, can be defined by:

$$d_{1d} = \sqrt{\frac{2\kappa_{1d}}{\omega}} \tag{6.28}$$

Since κ_{1d} and γ_{1d} are not here functions of space, equations (6.22) and (6.27) have the (complex) solution:

$$\hat{p}(z,t) = p_T\left[(1-\gamma_{1d})\exp\left(\left(\frac{1+i}{d_{1d}}\right)z\right) + \gamma_{1d}\right]\exp(i\omega t) \tag{6.29}$$

Equation (6.29) can be written in real notation as:

$$\hat{p}(z,t) = p_T\left[(1-\gamma_{1d})\exp\left(\frac{z}{d_{1d}}\right)\cos\left(\frac{z}{d_{1d}} + \omega t\right) + \gamma_{1d}\cos(\omega t)\right] \tag{6.30}$$

Typical depth profiles associated with this solution are shown in Figure 6.8. It is conceptually useful to split the solution of equation (6.30) into the sum of an instantaneous signal ($p_T\gamma_{1d}\cos(\omega t)$) and a diffusive signal ($p_T(1 - \gamma_{1d})\exp(z/d_{1d})\cos(z/d_{1d} + \omega t)$). The instantaneous signal is in phase with the ocean tide and has magnitude $p_T\gamma_{1d}$ for all depths. In contrast, the diffusive signal decays exponentially from the seafloor over a lengthscale d_{1d} and is generally not in phase with the ocean tide. Figure 6.8 shows that the nature of the incremental pore pressure solution depends on the value of z/d_{1d}. Close to the seafloor (i.e. within one or two skindepths) the incremental pore pressure contains a significant diffusive component. Further from the seafloor, however, the incremental pore pressure is dominated by the instantaneous signal ($p_T\gamma_{1d}\cos(\omega t)$). Therefore the 1-d loading efficiency (γ_{1d}) represents the proportion of the tidal load which is borne by the interstitial fluid at depths greater than 2 skindepths.

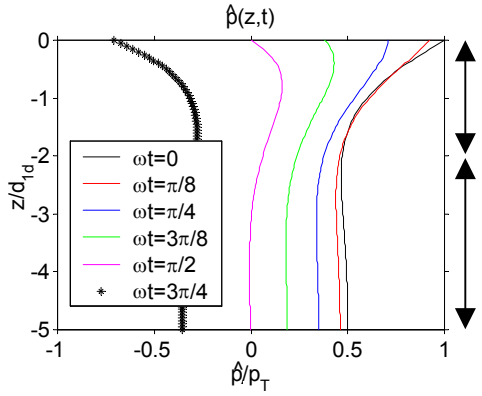

$$\frac{\hat{p}(z,t)}{p_T} = \gamma_{1d}\cos(\omega t) + (1-\gamma_{1d})\exp\left(\frac{z}{d_{1d}}\right)\cos\left(\frac{z}{d_{1d}} + \omega t\right)$$

$$\frac{\hat{p}(z,t)}{p_T} \approx \gamma_{1d}\cos(\omega t)$$

Figure 6.8: Typical depth profiles of the incremental pore pressure $(\hat{p}(z,t))$ as a function of dimensionless depth ($-z/d_{1d}$) in an infinite halfspace at various times during the tidal cycle with $\gamma_{1d} = 0.5$. High tide occurs when $\omega t=0$. Half tide occurs when $\omega t=\pi/2$. Maximum vertical velocity at the seafloor occurs when $\omega t=3\pi/4$. The diffusive pressure signal is limited to depths for which $(-z/d_{1d}) < \sim 2$.

6.3.1.2 Incremental velocity in an infinite halfspace

Previous authors have been concerned solely with the incremental pore pressure (Van der Kamp & Gale, 1983; Wang & Davis, 1996). In contrast, the aim here is to investigate the flow of interstitial fluids induced by the incremental pore pressure. In other words, the point of interest is the *spatial gradient* of the incremental pore pressure rather than the incremental pore pressure itself. The tidally induced incremental velocity at the seafloor ($z = 0$) is of particular interest since it can be measured by instruments such as Medusa (Chapter 4).

Applying Darcy's law to equation (6.29), the incremental vertical velocity (in complex notation) is:

$$\hat{w}(z,t) = -\frac{k}{\mu}\frac{\partial \hat{p}}{\partial z} = -\frac{k}{\mu}p_T(1-\gamma_{1d})\left(\frac{1+i}{d_{1d}}\right)\exp\left(\left(\frac{1+i}{d_{1d}}\right)z + i\omega t\right) \qquad (6.31)$$

Therefore the tidally induced incremental velocity at the seafloor is:

$$\hat{w}(0,t) = -\frac{k}{\mu}p_T(1-\gamma_{1d})\left(\frac{1+i}{d_{1d}}\right)\exp(i\omega t) \qquad (6.32)$$

Equation (6.32) shows that the tidally induced outflow of water at the seafloor *leads* the ocean tide by a radian angle $\arg(-(1+i)) = -3\pi/4$ radians. In other words, the tidally induced outflow of pore water at the seafloor *lags* the ocean tide by $+3\pi/4$ radians (or 135°). Therefore peak outflow occurs ~4½ hours after high tide for the semi-diurnal components,

and ~9 hours after high tide for diurnal components. In principle, this predicted phase lag of 135° could be compared with observed effluent velocity time-series from the seafloor for each harmonic component of the tide (Table 2.1). However, the effluent velocity time-series which have been collected to date are too short and too noisy to allow the extraction of individual harmonic components (Chapter 4). Comparison of this theory with observation will therefore have to await the collection of higher quality data.

The tidally modulated effluent velocities observed on the seafloor take the form of a small incremental velocity $(\hat{w})$ imposed on a steady background flow (w). From equation (6.32), the amplitude of the velocity variations is:

$$|\hat{w}| = \frac{p_T k}{\mu} \frac{(1-\gamma_{1d})}{d_{1d}} \tag{6.33}$$

Assuming that the background flow consists of fluid of density ρ ascending a cold hydrostatic pressure gradient ($g\rho_0$), the steady velocity (w) is given by:

$$w = \frac{gk(\rho_0 - \rho)}{\mu} \tag{6.34}$$

From equations (6.33) and (6.34), it is possible to define the dimensionless magnitude of the incremental seafloor velocity as follows:

$$\frac{|\hat{w}|}{w} = \left(\frac{p_T}{g}\right) \frac{(1-\gamma_{1d})}{(\rho_0 - \rho) d_{1d}} \tag{6.35}$$

Equation (6.35) expresses the magnitude of the tidal oscillations in effluent velocity as a fraction of the background steady velocity. Using the fact that $S = \alpha / (K_m \beta)$, and equations (6.25), (6.26) and (6.28), it can be shown that:

$$d_{1d} = \frac{1}{\sqrt{\omega}} \sqrt{k} \sqrt{\frac{6K_m(1-\nu)}{\alpha(1+\nu)}} \sqrt{\frac{\gamma_{1d}}{\mu}} \tag{6.36}$$

Equations (6.35) and (6.36) then imply that the dimensionless magnitude of the incremental seafloor velocity is:

$$\frac{|\hat{w}|}{w} = \underbrace{\left[\frac{p_T}{g}\sqrt{\frac{\alpha(1+\nu)}{6K_m(1-\nu)}}\right]}_{(a)} \cdot \underbrace{\left[\sqrt{\omega}\right]}_{(b)} \cdot \underbrace{\left[\frac{1}{\sqrt{k}}\right]}_{(c)} \cdot \underbrace{\left[\frac{\sqrt{\mu}(1-\gamma_{1d})}{(\rho_0 - \rho)\sqrt{\gamma_{1d}}}\right]}_{(d)} \tag{6.37}$$

The terms in square brackets in equation (6.37) can be considered in turn, to reveal how variations in parameter values affect the magnitude of the velocity perturbations observed at the seafloor. Term (a) contains quantities which are either fixed constants or elastic parameters of the rock matrix, while term (b) shows that the dimensionless incremental velocity increases with the frequency of the loading. Consequently, under this theory,

seafloor velocity signals are predicted to be *high-pass filtered* relative to the ocean tide. Equation (6.37) predicts that the ratio of semi-diurnal to diurnal amplitudes in the outflow velocity signal is greater than that in the ocean tide by a factor of √2. Term (c) shows that the dimensionless magnitude of the incremental velocity decreases as the permeability increases. Term (d) reveals the dependence of the velocity perturbations on the thermodynamic state of the pore water and can be used to define a 'tidal flow magnitude parameter' (M_T) as follows:

$$M_T = \left[\frac{(1-\gamma_{1d})}{\sqrt{\gamma_{1d}}}\right]\frac{\sqrt{\mu}}{(\rho_0-\rho)} \tag{6.38}$$

Graphs of M_T are presented in Figure 6.9 over a range of *p*-*T* conditions appropriate to hydrothermal systems. When the porosity (φ_0) is very small, $\gamma_{1d} \approx 1$ and so:

$$M_T \approx \frac{\sqrt{\mu}}{(\rho_0-\rho)} \tag{6.39}$$

Figure 6.9 shows that M_T is minimised at ~400°C for all seafloor pressures. Hence, the ratio of the tidally induced incremental velocity to the buoyancy driven background velocity is a *decreasing* function of temperature for the temperatures below ~400°C which characterise the discharge zone of a subseafloor convection cell (Chapter 5). Therefore equations (6.37) and (6.38) predict that the tidal variations in effluent velocity are most significant as a fraction of the steady flow for:

(1) cool effluent
(2) high frequency loading
(3) low permeabilities

The observation that effluent velocity variations are greatest for high frequency loading implies that the relative magnitudes of semi-diurnal to diurnal components will be greater in an effluent velocity time-series than in the local ocean tide. It has already been remarked (Chapter 2) that the semi-diurnal components of the ocean tide are typically larger than the diurnal components. For these two reasons, it is expected that tidal variations in effluent velocity will, in general, be dominated by semi-diurnal frequencies. In the subsequent sections it is assumed for simplicity that the load at the seafloor is a pure sine wave of angular frequency ω. By linearity, the diurnal and semi-diurnal components may be considered separately. In the case of semi-diurnal loading $\omega = 1.408 \cdot 10^{-4}$ rad.s^{-1}, while for diurnal loading $\omega = 7.038 \cdot 10^{-5}$ rad.s^{-1}.

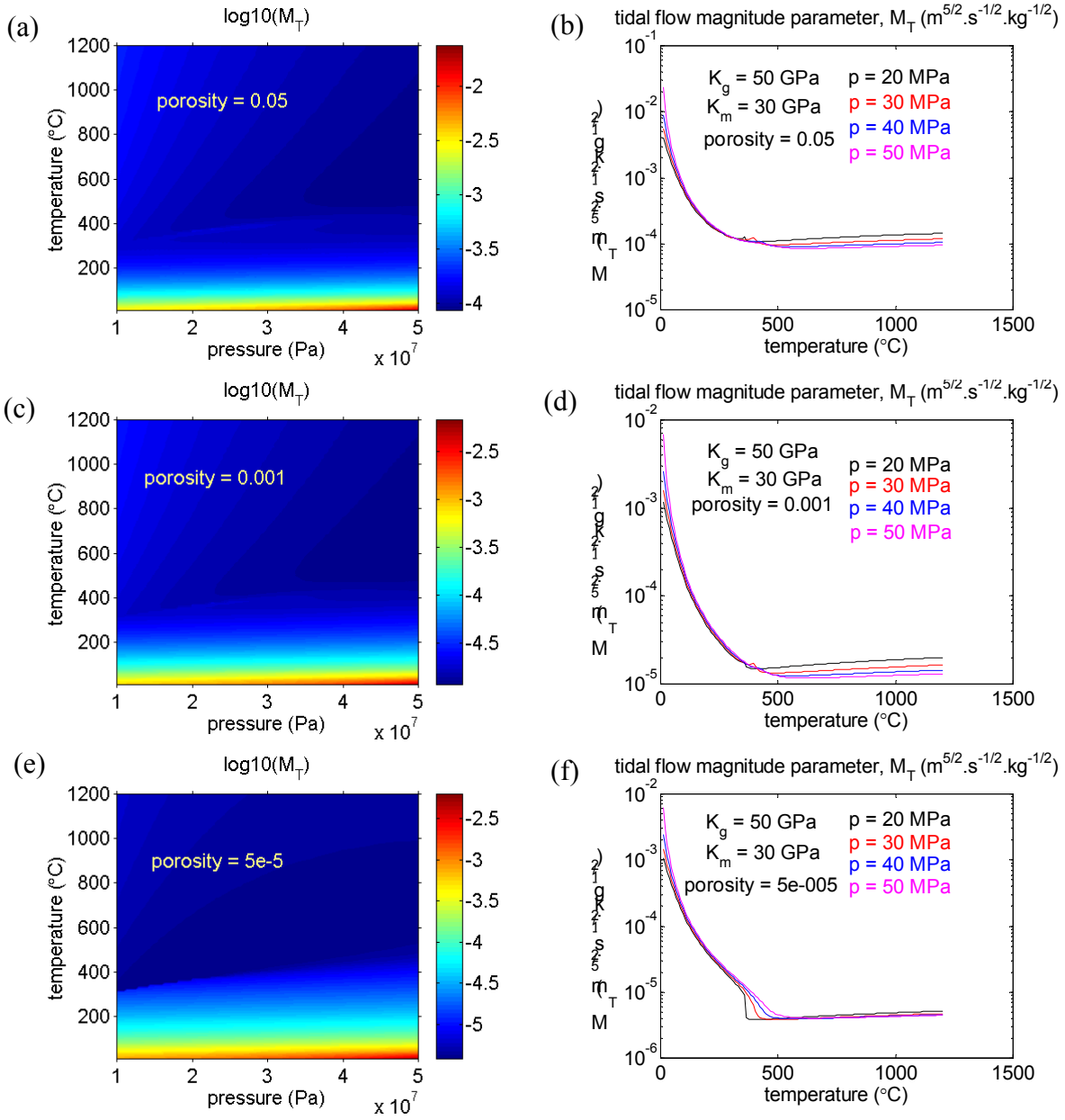

Figure 6.9: The dependence of the tidal flow magnitude parameter (M_T) on the thermodynamic state of the interstitial fluid in the large, intermediate and small porosity regimes with K_g = 50 GPa, K_m = 30 GPa. The magnitude of the velocity perturbations at the seafloor, relative to the background velocity, is proportional to M_T. Interstitial fluid is pure water. Thermodynamic data from the tables embedded in the HYDROTHERM code. (a), (b) φ_0 = 0.05 (large). (c), (d) φ_0 = 0.001 (intermediate). (e), (f) φ_0 = 0.00005 (small). (10^7 Pa corresponds to 1 km below sea level.)

6.3.1.3 Incremental temperature in an infinite halfspace

In the previous section, the incremental pore pressure solution of Van der Kamp & Gale (1983) $\left(\hat{p}(z,t)\right)$ is extended to yield an expression for the incremental velocity $\left(\hat{w}(z,t)\right)$. In this section, an expression for a third quantity of interest - the incremental temperature $\left(\hat{T}(z,t)\right)$ - is derived.

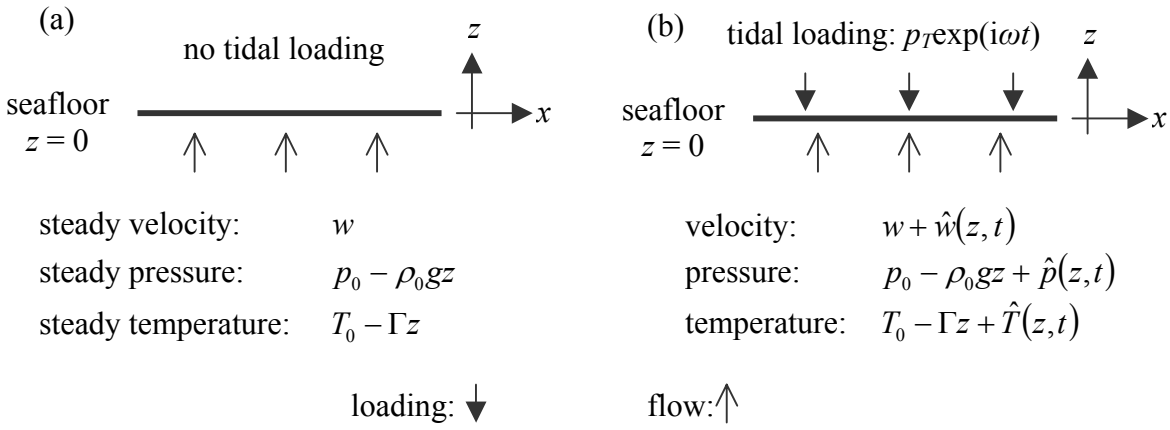

Figure 6.10: The incremental temperature $\left(\hat{T}(z,t)\right)$ due to tidal loading, just below the seafloor. (a) In the absence of tidal loading, the vertical velocity is assumed to be constant while the pressure and temperature are linear functions of depth. (b) Under tidal loading, the pressure, velocity and temperature are all tidally modulated.

For simplicity, it is supposed that pressure and temperature are linear functions of depth in the absence of tidal loading (Figure 6.10a). This is approximately true in the section of the hydrothermal discharge zone which lies just below the seafloor (Figure 5.1). If the pressure gradient is cold hydrostatic (Section 5.3) and the temperature gradient is denoted by Γ, then:

$$p(z) = p_0 - g\rho_0 z \tag{6.40}$$

$$T(z) = T_0 - \Gamma z \tag{6.41}$$

It is supposed for simplicity that the density (ρ) and dynamic viscosity (μ) do not vary with depth. The buoyancy-driven vertical velocity (in the absence of tidal loading) therefore has the constant value:

$$w = \frac{-k}{\mu}\left[\frac{dp}{dz} + g\rho\right] = \frac{gk(\rho_0 - \rho)}{\mu} \tag{6.42}$$

This steady state flow (Figure 6.10a) satisfies mass conservation because:

$$\frac{\partial}{\partial z}(\rho w) = 0 \tag{6.43}$$

However, the advective energy accumulation per unit volume (Q) is non-zero because:

$$Q = -\frac{\partial}{\partial z}(\rho h w) = -\rho w \frac{\partial h}{\partial z} \tag{6.44}$$

Supposing for simplicity that enthalpy is a linear function of temperature - $h(p,T) = c_p T$ - it then follows that:

$$Q = \rho c_p w \Gamma \tag{6.45}$$

In a real seafloor system, the advective energy accumulation of equation (6.45) would be balanced by the lateral conductive flow of heat away from the discharge zone. It is not possible to incorporate lateral conduction into this model explicitly because it is assumed that there is only one spatial dimension. However, energy can be balanced by assuming that heat is removed at a rate Q per unit volume at all depths below the seafloor. In other words, heat sinks must be introduced to simulate the effect of conductive heat loss and ensure that energy is balanced in the steady state.

It is supposed that the steady, one-dimensional solution described above is disturbed by tidal loading ($p_T \exp(i\omega t)$) on the seafloor ($z = 0$) (Figure 6.10b). The pressure, velocity and temperature are then perturbed from their steady values as follows:

$$\begin{aligned} p(z) &\rightarrow p_0 - g\rho_0 z + \hat{p}(z,t) \\ w &\rightarrow w + \hat{w}(z,t) \\ T(z) &\rightarrow T_0 - \Gamma z + \hat{T}(z,t) \end{aligned} \tag{6.46}$$

Assuming that the incremental pressure $\left(\hat{p}(z,t)\right)$ and incremental velocity $\left(\hat{w}(z,t)\right)$ are given by the 1-d solutions discussed in previous sections (equations (6.29) and (6.31)), an expression for the incremental temperature $\left(\hat{T}(z,t)\right)$ can be derived.

If tidally induced changes in fluid density are negligible, the conservation of energy under tidal loading is expressed by the advection-diffusion equation:

$$\frac{\partial}{\partial t}\left(T + \hat{T}\right) + \left(w + \hat{w}\right)\frac{\partial}{\partial z}\left(T + \hat{T}\right) = -\frac{Q}{\rho c_p} \tag{6.47}$$

Equation (6.47) can be linearised by neglecting the product of any two incremental properties. Using equations (6.41) and (6.45), this linearisation yields:

$$\frac{\partial \hat{T}}{\partial t} + w\frac{\partial \hat{T}}{\partial z} = \Gamma \hat{w} \tag{6.48}$$

The steady state velocity (w) and the steady state temperature gradient (Γ) are both constant. Therefore equation (6.48) can be used to derive an expression for the incremental temperature $\left(\hat{T}(z,t)\right)$ in terms of the incremental velocity $\left(\hat{w}(z,t)\right)$. Equation (6.31) shows that the tidally induced incremental velocity has the form:

$$\hat{w}(z,t) = A\exp\left(\left(\frac{1+i}{d_{1d}}\right)z + i\omega t\right) \tag{6.49}$$

where A is a complex number expressing the amplitude and the phase relative to the ocean tide.

Equation (6.48) suggests that the incremental temperature has a similar form to equation (6.49). Accordingly, it is postulated that:

$$\hat{T}(z,t) = B\exp\left(\left(\frac{1+i}{d_{1d}}\right)z + i\omega t\right) \tag{6.50}$$

where the value of the unknown complex constant (B) remains to be calculated.

Equations (6.48), (6.49) and (6.50) together yield an expression linking the complex amplitudes A and B:

$$B\frac{w}{d_{1d}}\left[1+\left(1+\frac{\omega d_{1d}}{w}\right)i\right] = \Gamma\cdot A \tag{6.51}$$

Equation (6.51) shows that the incremental temperature $\left(\hat{T}(z,t)\right)$ lags the incremental velocity $\left(\hat{w}(z,t)\right)$ by the radian angle:

$$\arg(A) - \arg(B) = \arg\left[1+\left(1+\frac{\omega d_{1d}}{w}\right)i\right] \tag{6.52}$$

Since ω, d_{1d}, and w are all positive real numbers, equation (6.52) implies that the incremental temperature lags the incremental velocity by an angle in the range $[\pi/4, \pi/2]$ (i.e. between 45° and 90°). The exact value of this phase lag depends on the value of the dimensionless parameter:

$$\frac{\omega d_{1d}}{w} = \left[\frac{1}{g(\rho_0-\rho)}\sqrt{\frac{2\omega\mu}{S}}\sqrt{\frac{3(1-\nu)}{3(1-\nu)-2\alpha\beta(1-2\nu)}}\right]\frac{1}{\sqrt{k}} \tag{6.53}$$

For semi-diurnal tidal loading, $\omega = 1.4\cdot10^{-4}$ s^{-1} and all parameters except the permeability (k) are known accurately. Assuming typical values ($g = 9.8$ m.s^{-2}, $(\rho_0-\rho) = 500$ kg.m^{-3}, $\mu = 5\cdot10^{-5}$ Pa.s, $S = 5\cdot10^{-9}$ Pa^{-1}, $\nu = 0.2$, $\alpha = 0.5$, $\beta = 0.5$), suggests that, in SI units:

$$\frac{\omega d_{1d}}{w} \approx 7\cdot10^{-4}\frac{1}{\sqrt{k}} \tag{6.54}$$

Using equations (6.52) and (6.54), the phase difference between the incremental velocity and the incremental temperature can be graphed as a function of permeability (k) (Figure 6.11). Table 6.1 suggests that the permeability of the seafloor lies between 10^{-17} m^2 and 10^{-10} m^2. Figure 6.11 shows that the incremental temperature lags the incremental velocity by almost exactly 90° within this range. Phase lags significantly smaller than 90° are only possible for permeabilities greater than 10^{-9} m^2. Such high permeabilities could only exist if there were considerable cracking of the discharge zone. Consequently, seafloor measurements of the phase lag between effluent velocity and temperature are diagnostic. Phase lags significantly below 90° present evidence for unusually high seafloor permeability.

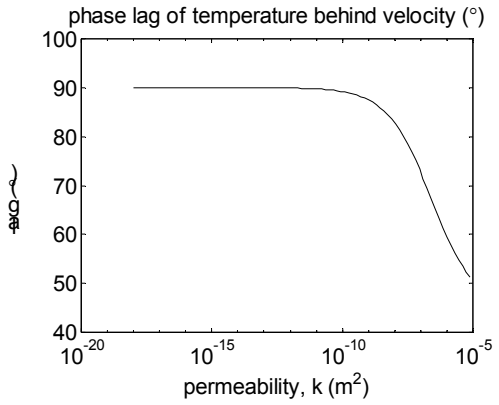

Figure 6.11: The predicted phase lag of the incremental temperature $\left(\hat{T}(z,t)\right)$ behind the incremental velocity $\left(\hat{w}(z,t)\right)$ as a function of permeability (k) for typical seafloor parameter values. Note the logarithmic scale on the horizontal axis.

In the infinite halfspace model, it has been shown that the incremental velocity at the seafloor lags the ocean tide by 135°. Consequently, the infinite halfspace model predicts that the incremental temperature at the seafloor lags the ocean tide by an angle in the range [180°, 225°]. Furthermore, for semi-diurnal loading and permeabilities less than 10^{-10} m^2, the phase lag is predicted to be almost exactly equal to 225° (Figure 6.11).

6.3.1.4 Incremental pore pressure in a finite permeable layer

The assumption of an infinite halfspace is a significant simplification, and it is of interest to extend the well-established halfspace model of Van der Kamp & Gale (1983) to the case of a

finite permeable layer. It is therefore supposed in this section that the crust is only permeable between $z = 0$ and $z = -H$ (Figure 6.6b).

The new boundary condition $\left(\hat{w}(-H,t)=0\right)$ means that the solution of equation (6.27), which is given by equation (6.29) for an infinite halfspace, is now given by:

$$\hat{p}(z,t)=p_T\left[(1-\gamma_{1d})\frac{\cosh\left((1+i)\left(\frac{z+H}{d_{1d}}\right)\right)}{\cosh\left((1+i)\left(\frac{H}{d_{1d}}\right)\right)}+\gamma_{1d}\right]\exp(i\omega t) \tag{6.55}$$

6.3.1.5 Incremental velocity in a finite permeable layer

By Darcy's law, it follows from equation (6.55) that the incremental velocity for a finite permeable layer is given (in complex notation) by:

$$\hat{w}(z,t)=-\frac{k}{\mu}p_T(1-\gamma_{1d})\frac{(1+i)}{d_{1d}}\frac{\sinh\left((1+i)\left(\frac{z+H}{d_{1d}}\right)\right)}{\cosh\left((1+i)\left(\frac{H}{d_{1d}}\right)\right)}\exp(i\omega t) \tag{6.56}$$

The incremental velocity on the seafloor is then:

$$\hat{w}(0,t)=-\frac{k}{\mu}p_T(1-\gamma_{1d})\frac{(1+i)}{d_{1d}}\tanh\left((1+i)\left(\frac{H}{d_{1d}}\right)\right)\exp(i\omega t) \tag{6.57}$$

It should be noted that the presence of the impermeable boundary at $z = -H$ affects both the magnitude and phase of the outflow at the seafloor (equation (6.57)), compared with the solution for an infinite halfspace (equation (6.32)).

It can be shown that:

$$\left|\tanh\left((1+i)\left(\frac{H}{d_{1d}}\right)\right)\right|=\sqrt{\frac{\sinh^2\left(\frac{H}{d_{1d}}\right)+\sin^2\left(\frac{H}{d_{1d}}\right)}{\sinh^2\left(\frac{H}{d_{1d}}\right)+\cos^2\left(\frac{H}{d_{1d}}\right)}} \tag{6.58}$$

and that:

$$\arg\left[\tanh\left((1+i)\left(\frac{H}{d_{1d}}\right)\right)\right]=\tan^{-1}\left[\frac{\sin\left(\frac{2H}{d_{1d}}\right)}{\sinh\left(\frac{2H}{d_{1d}}\right)}\right] \tag{6.59}$$

Therefore the tidally induced outflow at the seafloor has magnitude:

$$\frac{p_T k}{\mu}\frac{(1-\gamma_{1d})}{d_{1d}}\sqrt{\frac{\sinh^2\left(\frac{H}{d_{1d}}\right)+\sin^2\left(\frac{H}{d_{1d}}\right)}{\sinh^2\left(\frac{H}{d_{1d}}\right)+\cos^2\left(\frac{H}{d_{1d}}\right)}} \tag{6.60}$$

It has already been shown (equation (6.32)) that the effluent velocity at the seafloor lags the ocean tide by a radian angle (3π / 4) in the case of an infinite halfspace. It follows from equation (6.59) that the presence of an impermeable boundary at z = -H means that the effluent velocity at the seafloor lags the ocean tide by a radian angle:

$$\frac{3\pi}{4}-\tan^{-1}\left[\frac{\sin\left(\frac{2H}{d_{1d}}\right)}{\sinh\left(\frac{2H}{d_{1d}}\right)}\right] \tag{6.61}$$

The predicted magnitude (equation (6.60)) and phase lag (equation (6.61)) of the incremental velocity at the seafloor are shown in Figure 6.12 as functions of the dimensionless depth of the impermeable boundary (H / d_{1d}).

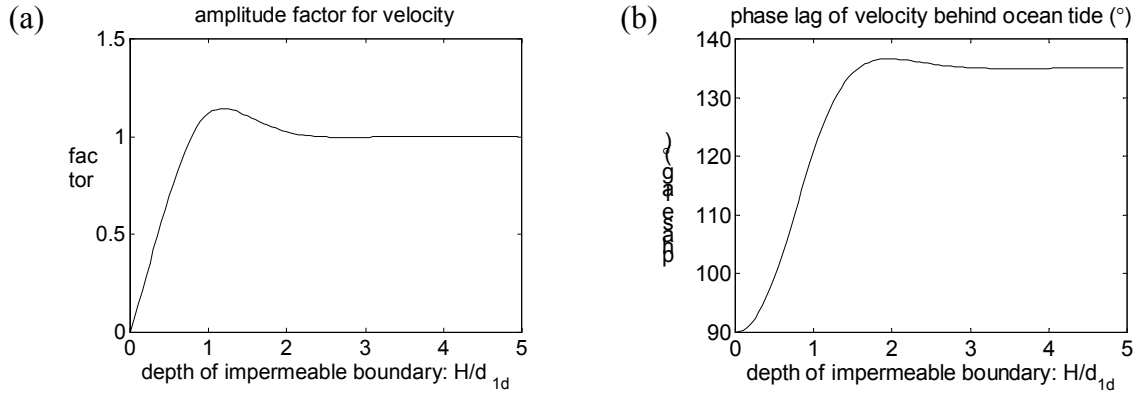

Figure 6.12: The effect of an impermeable layer at depth H on the magnitude and phase of the incremental velocity at the seafloor. The horizontal axes measure the dimensionless depth of the impermeable layer (H/d_{1d}). (a) The amplitude of the outflow as a fraction of the infinite halfspace solution, which is approached as $H/d_{1d} \rightarrow \infty$. (b) The lag of the outflow behind the ocean tide in degrees, which approaches the infinite halfspace value of 135° as $H/d_{1d} \rightarrow \infty$.

In summary, the incremental velocity at the seafloor lags the ocean tide by an angle between 90° and 135°, depending on the relative magnitude of the 1-d skindepth (d_{1d}) and depth over which the seafloor crust is permeable (H). If the skindepth is much smaller than the thickness of the permeable layer ($H / d_{1d} >> 1$) the incremental velocity follows the infinite halfspace solution and lags the ocean tide by 135°. In contrast, if the skindepth is greater than $H/2$ (so that $H / d_{1d} < 1$), then the incremental velocity at the seafloor is reduced in magnitude compared to the infinite halfspace solution (Figure 6.12a), and its phase lag behind the ocean tide takes a value in the range [90°, 135°]. When sufficient high quality data are available, observed values of the phase lag between the ocean tide and the effluent could be used to constrain the ratio (H / d_{1d}).

6.3.2 Tidal loading of a 2-d seafloor

In Section 6.3.1, the investigation of tidal loading is restricted to one spatial dimension for simplicity. In this section, the same principles are extended to two dimensions by considering the tidal loading of the simulated convection cell of Chapter 5. The numerical steady state solution (Figure 5.4) defines the properties of the interstitial fluid as functions of space. Figure 6.13 shows the distribution of pressure (p), temperature (T), density (ρ) and fluid compressibility (K_f^{-1}) within the simulated convection cell. It should be noted that the seafloor is placed at z = 0 m in these figures in common with the convention followed throughout this chapter. (In Chapter 5, however, it is more convenient to place the seafloor at z = 1000 m). The division between the cold, dense, liquid-like region below ~400°C and the hot, buoyant, gas-like region above ~400°C is clearly shown in Figure 6.13c,d. Under tidal loading, it is expected that the differing incremental pore pressures in these regions will drive a tidally modulated flow. In the following sections, a numerical simulation is used to examine this flow.

6.3.2.1 Governing equations in 2-d

In Section 6.3.1.1 the equations governing the propagation of incremental pore pressure in one dimension are derived (Van der Kamp & Gale, 1983). In this section, the analogous equations governing the incremental stress $\left(\hat{\sigma}_{ij}(x,z,t)\right)$ and incremental pore pressure $\left(\hat{p}(x,z,t)\right)$ in two spatial dimensions are derived. In this case, the assumption of only two spatial dimensions implies that $\hat{e}_{22} = 0$. Therefore equations (6.12) and (6.13) imply that:

$$\hat{\sigma}_{kk} = (1+\nu)(\hat{\sigma}_{11} + \hat{\sigma}_{33}) - \alpha(1-2\nu)\hat{p} \tag{6.62}$$

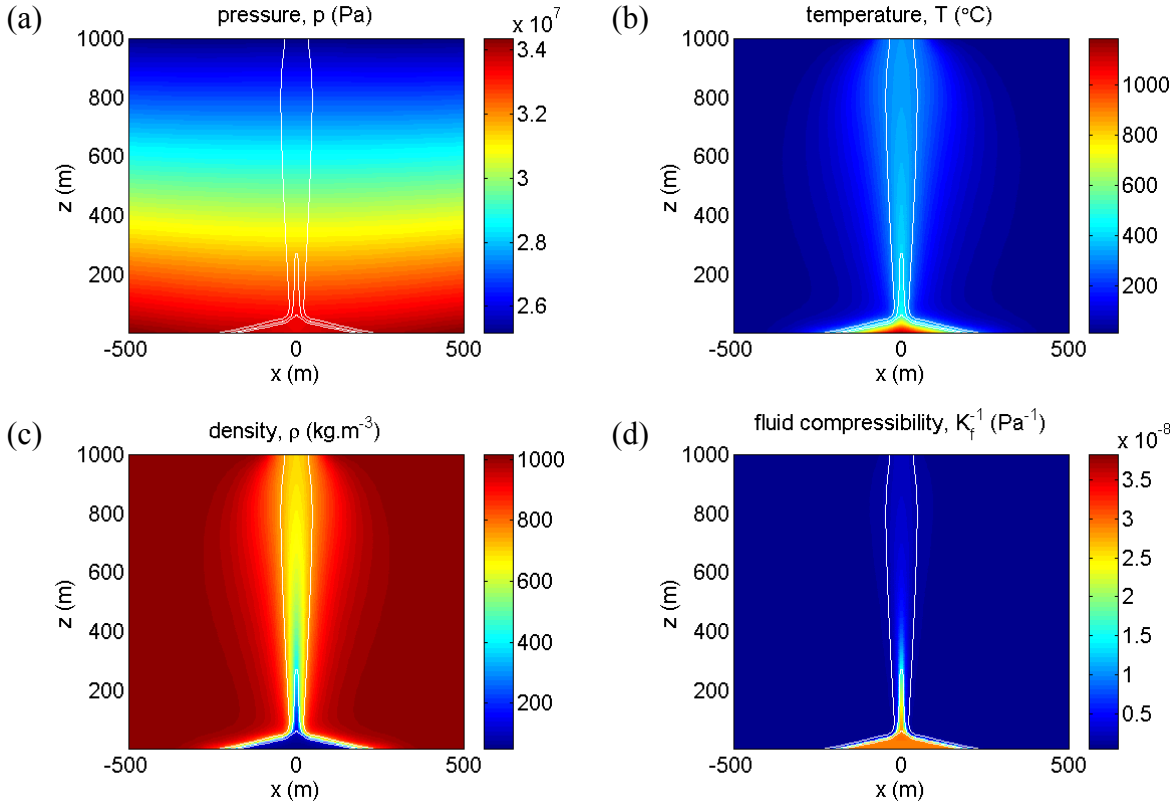

Figure 6.13: The thermodynamic properties of the fluid in the numerically simulated convection cell of Section 5.3. In each plot, the domain is the same as that shown in Figure 5.4a. The seafloor is at z = 0 m and a magma chamber lies at z = -1000 m. On all plots the isotherms at 300°C, 400°C and 500°C are shown in white. The change from liquid-like properties to gas-like properties occurs at ~400°C. (a) The pore pressure, p. (b) The temperature, T. (c) The density, ρ. (d) The fluid compressibility, K_f^{-1}.

It then follows from equation (6.14) that:

$$\alpha(1-2\nu)\left[\frac{\partial^2}{\partial x^2}+\frac{\partial^2}{\partial z^2}\right]\hat{p}+\left[(2-\nu)\frac{\partial^2}{\partial x^2}+(1-\nu)\frac{\partial^2}{\partial z^2}\right]\hat{\sigma}_{11}+\left[(1-\nu)\frac{\partial^2}{\partial x^2}-\nu\frac{\partial^2}{\partial z^2}\right]\hat{\sigma}_{33}=0 \quad (6.63)$$

$$\alpha(1-2\nu)\left[\frac{\partial^2}{\partial x^2}+\frac{\partial^2}{\partial z^2}\right]\hat{p}+\left[-\nu\frac{\partial^2}{\partial x^2}+(1-\nu)\frac{\partial^2}{\partial z^2}\right]\hat{\sigma}_{11}+\left[(1-\nu)\frac{\partial^2}{\partial x^2}(2-\nu)\frac{\partial^2}{\partial z^2}\right]\hat{\sigma}_{33}=0 \quad (6.64)$$

Equation (6.16) implies that:

$$\left[\frac{3k}{(3-\alpha\beta(1-2\nu))\mu S}\right]\frac{\partial^2\hat{p}}{\partial z^2}=\frac{\partial\hat{p}}{\partial t}+\left[\frac{(1+\nu)\beta}{3-\alpha\beta(1-2\nu)}\right]\frac{\partial}{\partial t}(\hat{\sigma}_{11}+\hat{\sigma}_{33}) \quad (6.65)$$

Equation (6.65) suggests the definition of a 2-d diffusivity according to:

$$\kappa_{2d} = \left[\frac{3}{3-\alpha\beta(1-2\nu)}\right]\frac{k}{\mu S} \tag{6.66}$$

and a 2-d loading efficiency according to:

$$\gamma_{2d} = \left[\frac{(1+\nu)}{3-\alpha\beta(1-2\nu)}\right]\beta \tag{6.67}$$

It then follows that conservation of fluid mass is expressed by:

$$\kappa_{2d}\frac{\partial^2 \hat{p}}{\partial z^2} = \frac{\partial \hat{p}}{\partial t} + \gamma_{2d}\frac{\partial}{\partial t}\left(\hat{\sigma}_{11} + \hat{\sigma}_{33}\right) \tag{6.68}$$

Equations (6.63), (6.64) and (6.68) are the governing equations for the three scalar fields $\hat{p}(x,z,t)$, $\hat{\sigma}_{11}(x,z,t)$ and $\hat{\sigma}_{33}(x,z,t)$. A numerical solution for these fields can be found when tidal loading ($p_T\cos(\omega t)$) is applied to the seafloor ($z = 0$).

6.3.2.2 Numerical simulation

Boundary conditions are required in order to obtain a numerical solution to equations (6.63), (6.64) and (6.68). Considering first the incremental pore pressure, the tidal loading on the seafloor imposes the condition:

$$\hat{p} = p_T \exp(i\omega t) \quad (z = 0) \tag{6.69}$$

The bottom boundary (z = -1000 m) is taken to be impermeable, which implies that:

$$\left.\frac{\partial \hat{p}}{\partial z}\right|_{z=-1000} = 0 \tag{6.70}$$

It is expected that the one dimensional solution of Section 6.3.1.1 will apply on the side boundaries (x = ±500 m). If the 1-d skindepth and 1-d loading efficiency for cold water are labelled d_c and γ_c respectively, then equation (6.27) implies the boundary conditions:

$$\hat{p}(\pm 500, z, t) = \gamma_c p_T \exp(i\omega t) + (1-\gamma_c)p_T \exp\left(\frac{(1+i)z}{d_c} + i\omega t\right) \tag{6.71}$$

Following Van der Kamp & Gale (1983) it is assumed that the boundary condition for the vertical stress is the same on all four boundaries:

$$\sigma_{33} = -p_T \exp(i\omega t) \tag{6.72}$$

Finally, in order to ensure that $\hat{e}_{22} = 0$, the following condition must be met on all four boundaries:

$$\sigma_{11} = \frac{\nu}{1-\nu}\sigma_{33} - \frac{\alpha(1-2\nu)}{1-\nu}p \tag{6.73}$$

Since the tidal loading is assumed to occur at a single angular frequency ω, it follows that the incremental pressure and stress can be written in the form:

$$\left.\begin{aligned} \hat{p}(x,z,t) &= P(x,z)\exp(i\omega t) \\ \hat{\sigma}_{11}(x,z,t) &= \Sigma_{11}(x,z)\exp(i\omega t) \\ \hat{\sigma}_{33}(x,z,t) &= \Sigma_{33}(x,z)\exp(i\omega t) \end{aligned}\right\} \tag{6.74}$$

The governing equations (6.63), (6.64), (6.68) and the boundary conditions (6.69) – (6.73) can then be solved using standard finite difference techniques (Press *et al.,* 1986) to find the complex amplitudes $P(x,z)$, $\Sigma_{11}(x,z)$ and $\Sigma_{33}(x,z)$.

Unfortunately, only a very limited amount of computer time was available to perform calculations of this nature, and the parameters used (K_m = 0.5 GPa, K_g = 50 GPa, ν = 0.1, φ_0 = 0.1, k = 10^{-12} m^2) are not consistent with those assumed elsewhere in this dissertation (Chapter 5). Computer facilities were not available to rerun the simulations with consistent parameter values. The results (Figures 6.14 – 6.16) should therefore be viewed as illustrative of a general principle rather than definitive. Nonetheless, the simulations cover a sufficiently wide range of parameter values to illustrate the different incremental pore pressure regimes which apply according to the size of the cold skindepth d_c. The subscript 'c' is used to denote the values of the loading efficiency (γ_c) and skindepth (d_c) obtained for cold water from equations (6.26) and (6.28). Similarly, the subscript 'h' is used to denote the values (γ_h and d_h) obtained for hot (~400°C), gas-like water. In these numerical examples, $\gamma_c \approx 0.93$ and $\gamma_h \approx 0.14$. The seafloor parameter known to the least precision is the permeability (k), which can vary over several orders of magnitude (Table 6.1). Equation (6.28) shows that cold skindepth d_c depends on the ratio (k / ω), and so the effect of varying k is simulated numerically by varying ω.

Figure 6.14 shows the calculated incremental pore pressure for tidal loading with k = 10^{-12} m^2, ω = 0.1 s^{-1}. In this case the cold skindepth (d_c = 2.6 m) is much smaller than the dimensions of the cell, and so the diffusive part of the incremental pore pressure is restricted to a region of lengthscale $2d_c$ = 5.2 m around the seafloor and the boundary between the liquid-like and gas-like regions. At distances greater than $2d_c$ from these boundaries in elastic properties, the solution takes a form equivalent to the instantaneous pressure signal of equation (6.21). In other words the solution is approximately $\hat{p} \approx \gamma_c p_T \exp(i\omega t)$ in the liquid-like region of the cell and $\hat{p} \approx \gamma_h p_T \exp(i\omega t)$ in the gas-like region of the cell. Therefore the incremental pore pressure is in phase with the tidal loading over most of the convection cell.

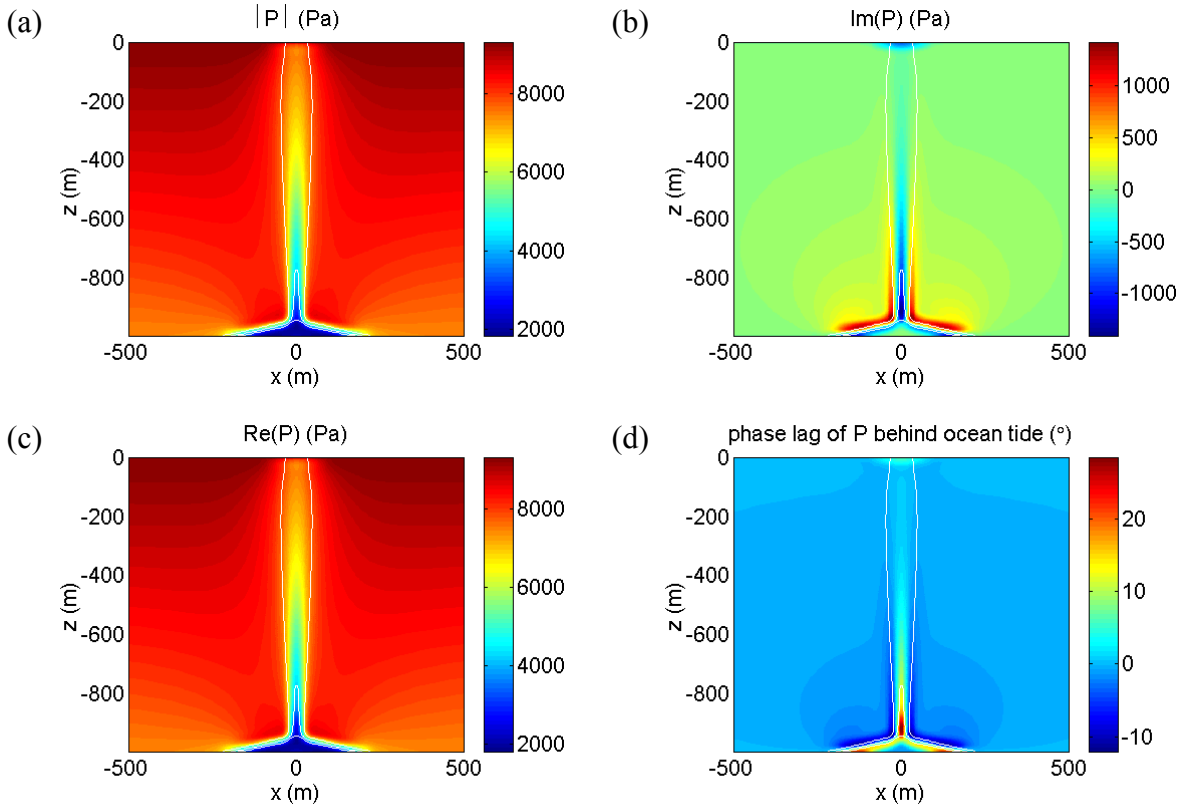

Figure 6.14: The complex incremental pore pressure amplitude $P(x,z)$ with p_T = 10 kPa, d_c = 2.6 m, γ_c = 0.94 and γ_h = 0.14. (a) The real part of the solution, representing the incremental pore pressure at high tide. (b) The imaginary part of the solution, representing the incremental pore pressure at rising half tide. (c) The magnitude of the incremental pore pressure. (d) The phase of the incremental pore pressure – expressed as a phase lag behind the ocean tide in degrees. In all figures, the isotherms at 300°C, 400°C and 500°C are drawn in white to illustrate the structure of the underlying convection cell (Figure 5.4).

Figure 6.15 shows the incremental pore pressure results with $k = 10^{-12}$ m^2, $\omega = 0.001$ s^{-1}. In this case, the larger value of the cold skindepth (d_c = 26 m) explains why the incremental pore pressure response of Figure 6.15 does not follow the boundaries in fluid properties (Figure 6.13) as closely as in Figure 6.14. The larger skindepth has led to a 'smearing' of the response across the boundary between the liquid-like and gas-like regions.

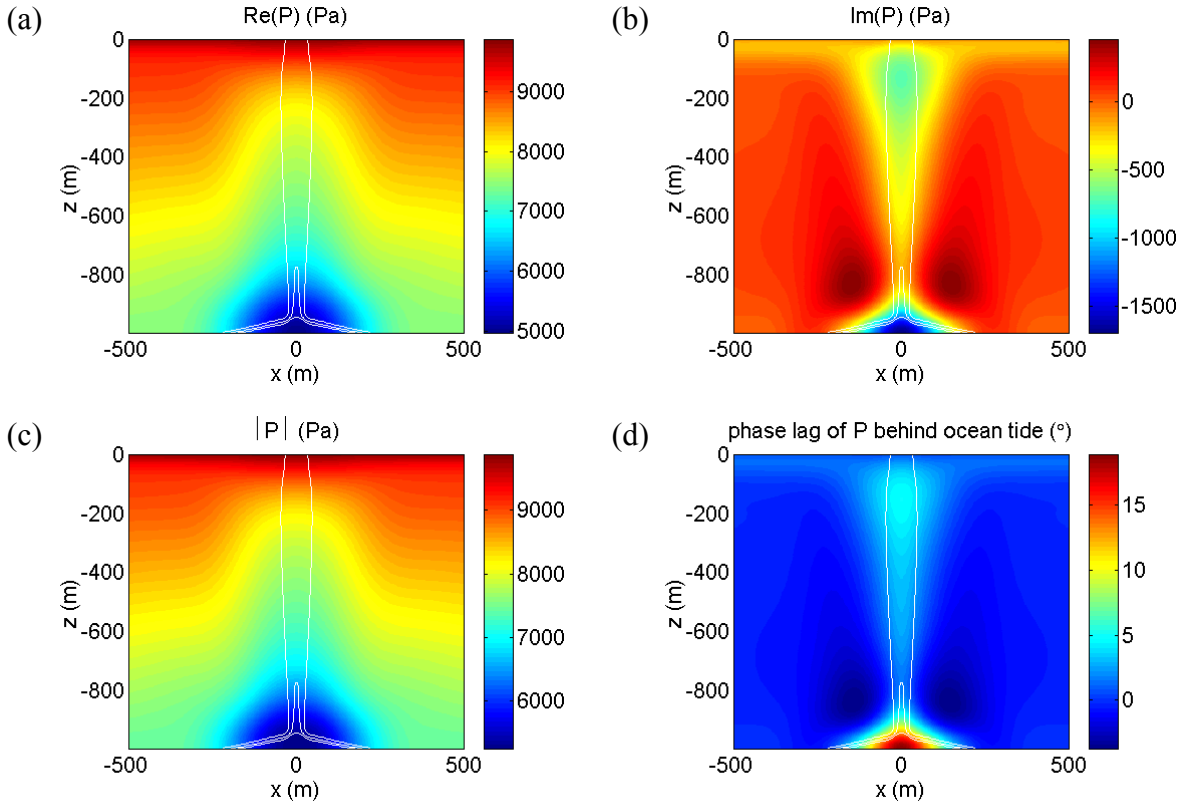

Figure 6.15: The complex incremental pore pressure amplitude $P(x,z)$ with p_T = 10 kPa, d_c = 26 m, γ_c = 0.94 and γ_h = 0.14. (a) The real part of the solution, representing the incremental pore pressure at high tide. (b) The imaginary part of the solution, representing the incremental pore pressure at falling half tide. (c) The magnitude of the incremental pore pressure. (d) The phase of the incremental pore pressure – expressed as a phase lag behind the ocean tide in degrees. In all figures, the isotherms at 300°C, 400°C and 500°C are drawn in white to illustrate the structure of the underlying convection cell (Figure 5.4).

Finally, Figure 6.16 shows the incremental pore pressure results with $k = 10^{-12}$ m^2 and ω = 0.000001 s^{-1}. In this case, the cold skindepth (d_c = 816 m) is sufficiently large that incremental pore pressure response is dominated by the diffusive component over the entire convection cell.

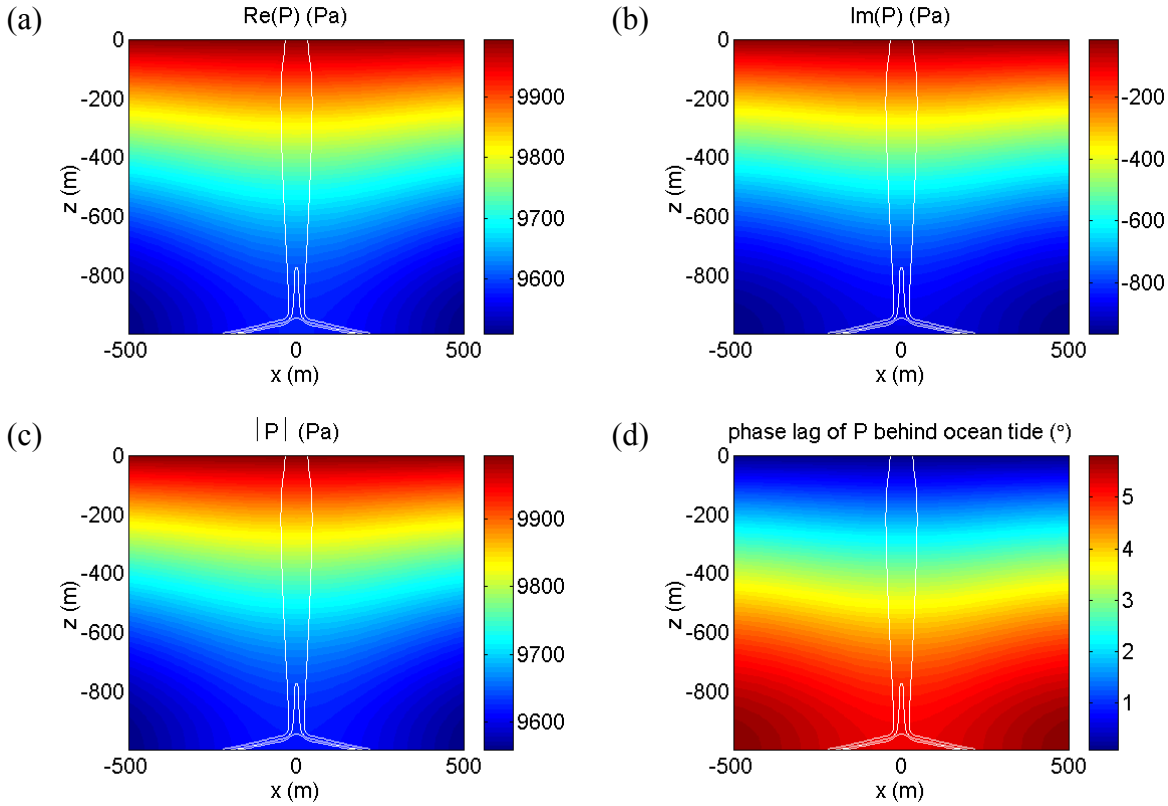

Figure 6.16: The complex incremental pore pressure amplitude $P(x,z)$ with p_T = 10 kPa, d_c = 816 m, γ_c = 0.94 and γ_h = 0.14. (a) The real part of the solution, representing the incremental pore pressure at high tide. (b) The imaginary part of the solution, representing the incremental pore pressure at rising half tide. (c) The magnitude of the incremental pore pressure. (d) The phase of the incremental pore pressure – expressed as a phase lag behind the ocean tide in degrees. In all figures, the isotherms at 300°C, 400°C and 500°C are drawn in white to illustrate the structure of the underlying convection cell (Figure 5.4).

In summary, Figures 6.14 – 6.16 illustrate the importance of the magnitude of the skindepth to the nature of the incremental pore pressure solution.

6.4 Conclusions

In this chapter, the application of the theory of poroelasticity to the tidal loading of subseafloor hydrothermal convection cells has been investigated.

The thermodynamic properties of water exert an important influence on the principal parameters of poroelasticity. At seafloor pressures, there is a marked difference between the properties of liquid-like water below ~400°C and gas-like water above ~400°C. Consequently, it is predicted that the incremental pore pressure response to tidal loading in a hydrothermal convection cell varies spatially. The difference in response between the liquid-like and gas-like regions is greatest when the porosity is large.

The characteristic lengthscale of pore pressure diffusion induced by tidal loading is the skindepth (d). The skindepth depends on the permeability (k) which is very poorly constrained. For semi-diurnal loading, the skindepth can range from d = 1 m ($k = 10^{-17}$ m^2) to d = 10,000 m ($k = 10^{-10}$ m^2). The nature of the incremental pore pressure response depends on the magnitude of the skindepth compared with the lengthscales of the subseafloor convection cell. When the skindepth is much smaller than the lengthscales of the cell, the incremental pore pressure is given, over most of the cell, by the instantaneous response which is in phase with the ocean tide.

Van der Kamp & Gale (1983) derived an analytical solution for the incremental pore pressure in an infinite halfspace subject to tidal loading. In Section 6.3.1 their solution is extended in a number of ways. Firstly, it is used to provide expressions for the incremental velocity and temperature in an infinite halfspace. Secondly, an analogous incremental pore pressure solution is derived for the case of a permeable layer of finite vertical extent. This solution is also used to derive expressions for the incremental velocity and temperature in a finite permeable layer.

In the case of an infinite halfspace, it is shown that the tidally induced outflow at the seafloor lags the ocean tide by 135° for each tidal component. The magnitude of this tidally induced velocity is considered as a fraction of the steady effluent velocity. It is shown that the tidal modulations are greatest (as proportion of the steady effluent velocity) when the effluent is cool, the permeability is low and the frequency of the tidal loading is high. This last observation implies that the tidal modulations of effluent velocity measured at the seafloor are *high-pass filtered* relative to the ocean tide. In other words, semi-diurnal components should be amplified at the expense of diurnal components in comparison with the ocean tide. The incremental temperature in an infinite halfspace is calculated for the region just below the seafloor where the pressure and temperature are both linear functions of depth. It is

shown that the incremental temperature lags the incremental velocity by an angle which lies between 45° and 90°. The exact value of the phase lag depends on the permeability. For most plausible values of crustal permeability, the phase lag is almost exactly 90°. However, if the presence of cracks in the seafloor has led to a greatly enhanced seafloor permeability ($>10^{-10}$ m^2), the phase lag can take lower values in the range [45°, 90°]. For the infinite halfspace model, it follows that the incremental temperature lags the ocean tide by an angle in the range [180°, 225°]. The phase lag is almost exactly 225° for when the permeability is less than $\sim 10^{-10}$ m^2, but it approaches 180° as the permeability increases above $\sim 10^{-10}$ m^2.

In the case of a finite permeable layer of depth H, the behaviour of the analytical solutions is controlled by the parameter (H / d_{1d}) which expresses the thickness of the permeable layer in skindepths. The tidally induced effluent velocity at the seafloor is shown to lag the ocean tide by an angle in the range [90°, 135°]. The phase lag is almost exactly 135° for (H / d_{1d}) > 2, but it approaches 90° as (H / d_{1d}) → 0. The amplitude of the tidally induced effluent velocity at the seafloor is compared with the result for an infinite halfspace. The amplitude of the outflow differs significantly from infinite halfspace result when (H / d_{1d}) < 2 and tends to zero as (H / d_{1d}) → 0. The incremental temperature in a finite permeable layer lags the incremental velocity by an angle in the range [45°, 90°] in exactly the same way as for an infinite halfspace. Consequently, the tidally induced temperature variations at the seafloor lag the ocean tide by an angle in the range [135°, 225°] when the permeable layer is of finite thickness.

Consequently, the simple poroelastic results derived here are sufficient to explain effluent velocities which lag the ocean tide by an angle in the range [90°, 135°], and effluent temperatures which lag the ocean tide by an angle in the range [135°, 225°]. This last range is consistent with the general (but by no means universal) observation that effluent temperatures tend to be low when the ocean tide is high – a situation that corresponds to a phase lag of 180°.

The theoretical predictions outlined above can now be compared with the phase-lags derived from real seafloor time-series (Table 4.13). It should be noted that these data refer to several different types of seafloor measurement which must be considered separately, and that the theory developed in this chapter does not apply to the majority of these signals.

The two hydrophone signals concern a physical process (episodic venting) which is not considered in any of the models developed in this dissertation. Consequently, no attempt is made to explain the phase-lags in these signals. Similarly, the measurements of 'ambient bottom water temperature' and 'sub-bottom temperature' are probably modulated by tidal streams and so the tidal loading mechanism explored above is not relevant. The estimated phase-lag for the 'shrimp density' time-series should be treated with *extreme* caution because the sampling interval of 6 h leads to unreliable estimates of the harmonic constants (Chapter 4). Consequently, there remain only three signals in Table 4.13 for which the phase-lags can be estimated with confidence and for which the theoretical model developed above is relevant - the two Medusa measurements of 'effluent temperature' and the thermistor measurements of 'borehole temperature'. For these signals, the estimated phase-lags of the *M2A* component behind the local ocean tide are ~180º, 225º and 140º (Table 4.13). These values all lie within the predicted range of [135°, 225°] and are therefore consistent with the model.

Chapter 7: Conclusions and suggested future work

A series of simple theoretical models has been developed in an attempt to explain the structure of a subseafloor hydrothermal convection cell and its response to tidal loading at the seafloor. In addition, a discussion of the nature of tidal signals has led to the development of a new technique for the analysis of tidally modulated time-series obtained at seafloor hydrothermal systems.

The purpose of this chapter is to review the results of the preceding chapters and to suggest ways in which the work presented here could be extended in the future.

7.1 Directions for future research

7.1.1 Collection of further hydrothermal time-series

The discussion of the nature of tidal signals in Chapters 2 and 3 shows that an understanding of tidal processes can be used to advantage in the analysis of a tidally modulated data set. It is therefore hoped that future analyses of time-series data from seafloor hydrothermal systems will refer where necessary to the theory of tides. Many of the time-series examined in Chapter 4 are noisy and difficult to interpret with certainty. It may be that such noise is unavoidable but it is hoped that it will be possible to collect longer, cleaner time-series from hydrothermal systems in the future. In particular, there is a need for time-series measurements of effluent temperature which cover a time period longer than a few days. The collection of such data, however, presents considerable technical difficulties.

7.1.2 Less simplistic convection models

The convection model of Chapter 5 is deliberately simplistic but could usefully be extended in a number of ways. The assumption of a homogeneous, isotropic subseafloor is clearly an idealisation and it would be interesting to see how important these assumptions are. Thermal expansion of the rock and the subsequent alteration of porosity and permeability could also be included in future models. The most important simplification imposed in Chapter 5, however, involves the use of pure water as the convecting fluid. Pure water is a single-phase fluid at all seafloor temperatures for pressures in excess of 22 MPa (~2.2 km cold hydrostatic head), and so the considerable complication of phase separation is avoided by placing the

seafloor at a depth below sea level greater than 2.2 km. It would be interesting to extend the model of Chapter 5 in two stages. Firstly, hydrothermal convection of pure water at pressures below 22 MPa could be studied to investigate the effect of phase separation on convection cell structure. Secondly, salt water could be used as the convecting fluid in place of pure water for a range of seafloor pressures. It should be noted that the second extension represents a much larger jump in physical complexity than the first.

The thermodynamic state of pure water can be fully described by two thermodynamic variables such as the pressure (p) and specific enthalpy (h). Consequently, the convection of pure water in a porous medium is governed by two conservation equations – the conservation of mass and energy – in addition to Darcy's law which expresses conservation of momentum. Furthermore, phase separation of pure water occurs at a unique temperature – the boiling point – for any given pressure below the critical pressure of 22 MPa.

In contrast to pure water, the thermodynamic state of salt water depends on a greater number of thermodynamic variables. An extra thermodynamic parameter – the salinity – is added for each extra salt which is dissolved in the water. The convection of seawater at mid-ocean ridge hydrothermal systems involves the exchange of a number of dissolved chemical species between the pore fluid and the rock. Consequently, modelling the convection of salt water in a porous medium requires that the mass of each salt be conserved in addition to fluid mass, momentum and energy. Furthermore, a full numerical simulation would need to track the exchange of dissolved salts with the rock matrix and model the subsequent changes in porosity and permeability. It is clear that the numerical modelling of reacting salt water flows constitutes a considerable challenge.

Recently, the thermodynamic properties of a salt solution containing a single salt (NaCl) have been tabulated from theoretical and experimental data (Palliser & McKibbin, 1998a: Palliser & McKibbin, 1998b: Palliser & McKibbin, 1998c). The thermodynamic properties of the solution are given as functions of the temperature (T), pressure (p) and salinity (X). The salinity is expressed a mass fraction of salt in the solution and is therefore a dimensionless number taking values between 0 and 1. Numerical codes making use of these salt water properties are currently in development and have been applied to convection at the sub-critical temperatures for which the solution remains a single phase fluid (Lowell & Xu, 2000). The modelling of salt water convection at temperatures sufficient to cause phase separation is currently being investigated (W. Xu, *pers. comm.*, 1999)

To give an idea of the extra physics implied by the presence of salt in the convecting fluid, the equations of Palliser & McKibbin (1998a) are used to generate the state-space diagram shown in Figure 7.1. Palliser & McKibbin (1998a) publish isothermal cross-sections of the state-space which display the state of the solution as a function of pressure (p) and salinity (X). In the context of seafloor convection, however, it is more useful to examine isobaric cross-sections of the state-space which show the state of the solution as a function of pressure (p) and temperature (T), and so the diagrams in Figure 7.1 take this form. It should be noted that the salinity is shown on a logarithmic scale. The diagrams are divided into three regions. In region (1) the solution is a single phase fluid, while in region (2) it is a two-phase mixture of gas and liquid. In general the liquid and gas have different salinities, and the vertical co-ordinate represents the overall salinity of the mixture. In region (3) the system consists of solid salt and a saturated fluid solution. In other words, if salt solution is taken into region (3) of the state-space, solid salt precipitates out of solution.

It is now possible to consider the trajectory of a fluid particle through the state-space as it is heated over the range temperatures found in a seafloor convection cell. It is supposed for simplicity that the process is isobaric so that an individual diagram from Figure 7.1 can be used, and that the fluid is initially cold seawater. Bischoff & Rosenbauer (1985) suggest that a NaCl solution of salinity $X = 0.032$ is a good analogue for seawater. Consequently it is supposed that the fluid begins its passage through the convection cell at $T = 2°C$ and $\log_{10}(X) = -1.5$. As the fluid is heated at constant pressure it travels along a horizontal line in the state-space (Figure 7.1) until it reaches region (2) where phase separation occurs. At this point the fluid dynamics become complicated. The two-phase mixture is represented overall by a single point in the state-space at temperature T and salinity X, which lies in region (2). The individual gas and liquid phases, however, must lie at two distinct points on the boundary of region (2) in the state-space. At phase separation, the liquid and gas phase must both have the same temperature (T) but the liquid has a salinity X_l and the gas has a salinity X_g. If the mixture is subjected to further heating, the liquid and gas phases must be tracked separately through the state-space. Furthermore, in a convection cell, the liquid and gas phases are subject to contrasting body forces because of their different densities and could therefore move separately to regions of the seafloor with different temperatures. In the absence of numerical simulations it is not clear what the subsequent trajectory of convecting salt water through the state-space would be at super-critical temperatures. The results of numerical simulations are therefore awaited with considerable interest.

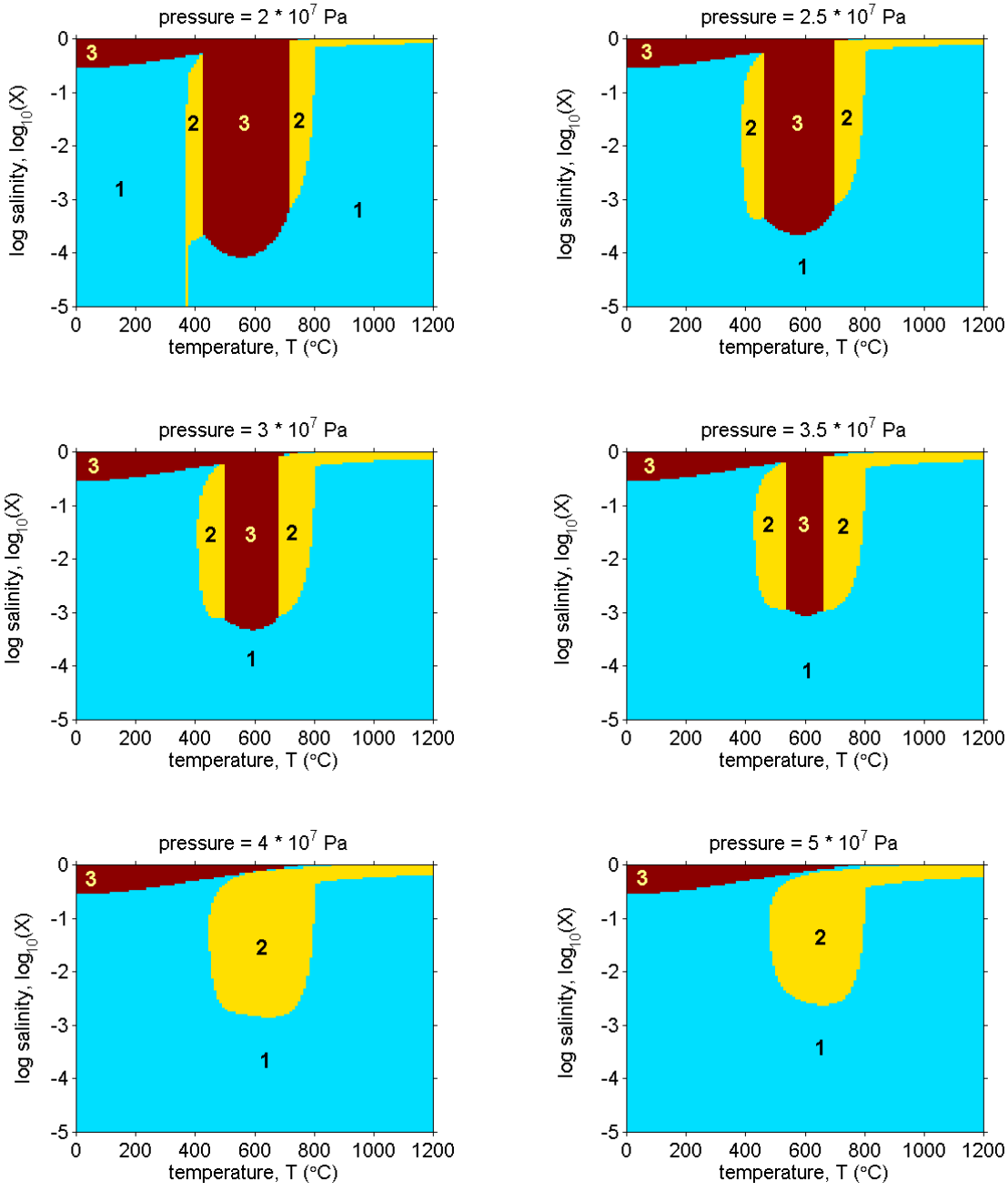

Figure 7.1: Isobaric cross-sections of the H_2O-NaCl state -pace for a range of seafloor pressures (10^7 Pa corresponds to a depth 1 km below sea level). Regions of state space are labelled as follows: **(1)** – Unsaturated single phase fluid. **(2)** – Unsaturated two-phase fluid (liquid + gas). **(3)** – Saturated single-phase fluid. Thermodynamic data from Palliser & McKibbin (1998a).

7.1.3 Direct imaging of subseafloor flow and temperature

Another area of active research relevant to this dissertation concerns the direct imaging of the subseafloor. Seismic tomography has been used for some years to constrain the depth of axial magma chambers but it does not reveal the flow or temperature structure of hydrothermal convection cells (e.g. Detrick *et al.*, 1987). However, there are two techniques which may be able to image flow and temperature structure - controlled-source electromagnetic tomography and measurement of the ζ-potential.

Controlled-source electromagnetic tomography has been used to infer the resistivity structure at an axial volcanic ridge segment of the Reykjanes Ridge at 57°45'N on the Mid-Atlantic Ridge (Sinha *et al.*, 1998; MacGregor *et al.*, 1998). If the temperature (T) is measured in °C, the resistivity of seawater (ρ_{SW}), measured in Ω.m, is given by the formula:

$$\rho_{SW} = \left(3 + \frac{T}{10}\right)^{-1} \tag{7.1}$$

for temperatures between 0°C and 350°C (Nesbitt, 1993). Consequently, tomographic estimates of crustal resistivity could be used to infer the temperature of the interstitial fluid, and hence the flow structure below the seafloor. A tomographic estimate of the width of the upflow zone could also be combined with the scaling analysis of Chapter 5 to infer subseafloor permeability. It remains to be seen whether this technique will prove practical. The structures which have been imaged previously using this method are on a significantly larger scale (1 km) than the expected width of the upflow zone (<100 m). High frequency electromagnetic signals would be required in order to resolve smaller structures, but they would attenuate more rapidly within the crust (L.M. MacGregor, *pers. comm.*, 1999).

The second technique which might be used to image subseafloor flow structure makes use of the theory of the ζ-potential (Revil & Pezard, 1998; Revil *et al.*, 1999a; Revil *et al.*, 1999b). The ζ-potential is the name given to the electrical potential generated when a charge carrying fluid is forced to move through a potential gradient. In the case of hydrothermal systems, the pore water functions as an electrolyte. The fluid motion is forced by thermal buoyancy and the potential gradient is created by polarisation due to the drag of the excess charge located at the grain-water interface of the porous medium (Revil *et al.*, 1999b). Measurements of the ζ-potential have been made at land-based geothermal systems, and are manifest as a positive potential anomaly in the ground above a discharge zone and a negative potential anomaly in the ground above a recharge zone. It is suggested that surveys of the electrical potential of the seafloor at hydrothermal sites might reveal similar behaviour and be used to infer the

widths of recharge and discharge zones in hydrothermal convection cells. Revil *et al.* (1999b) point out that the magnitude of the ζ-potential is smaller for saline fluids than for fresh water, which might mean that the technique is unsuitable for seafloor use. On the other hand, phase separation in a seafloor hydrothermal system can result in the upwelling fluid having a reduced salinity.

In summary, it will be interesting to see whether electromagnetic tomography and the ζ-potential prove practical in the imaging of subseafloor flow structure.

7.2 Conclusions

In this section, the results of the preceding chapters are reviewed.

Chapter 2 contains a thorough review of the common features shared by all tidal signals. It is demonstrated that the astronomical positions of the sun and moon influence the relative magnitudes of the diurnal and semi-diurnal oscillations of which all tidal signals are composed, as well modulating their magnitudes according to the springs/neaps cycle of lunar phases. For this reason, it is recommended that time-series from hydrothermal systems be analysed with the positions of the sun and moon in mind. It is also recommended that the date and GMT time be given for all reported data so that comparison with tidal predictions can be made. The three postulated tidal inputs to a seafloor hydrothermal system – the solid tide, ocean tide and tidal streams are considered in turn. Order of magnitude calculations suggest that dilatation of the crust due to the ocean tide is far more significant than that due to the solid tide. The phase relationship between the ocean tide and tidal streams is discussed so that tidal streams may be deduced from ocean tide models when no direct measurements are available.

Chapter 3 is concerned with finding the optimal numerical techniques for the analysis of tidally modulated time-series collected at seafloor hydrothermal systems. Among non-parametric techniques for estimating power spectra, the periodogram methods used previously by some authors are shown to be unsuitable for the short, noisy time-series collected at hydrothermal systems. It is recommended that the multiple window method of Thomson (1982) be used instead. The MWPS code of A. Chave (*pers. comm.*, 1999) is ideal for this purpose. Among parametric methods for describing the tidal part of a time-series, it is argued that the Admiralty Method (Admiralty Tidal Handbook, No. 3) is optimal. This parametric description of tidal signals is used to describe the ocean tides in the world's ports

and can be adapted for use with seafloor time-series. A new code – HYBRID – has been written for this purpose. Since seafloor time-series are often contaminated by drift and noise, methods to deal with these problems have been incorporated into the code. A technique derived from Bayesian statistics (Tamura *et al*., 1991) is used to remove the drift component of the time-series, while robust section averaging methods (Chave et al. 1987) are incorporated to reduce the effect of outlier data on the estimated parameters. The HYBRID code produces a set of 8 harmonic constants which describe the tidal component of a time-series. These harmonic constants can be visualised as 4 phasors in the complex plane. Consequently, the tidal components of two time-series can be examined in terms of their phasors. It is therefore possible to compare the phasor representations of the three postulated 'input signals' (solid tide, ocean tide and tidal streams) with the tidal component of an observable 'output signal'. It can then be decided (in principle) which 'input signal' is responsible for the modulation of the 'output signal'.

Chapter 4 comprises a review of the previously observed tidal modulations observed in time-series collected at seafloor hydrothermal systems. The chapter also contains the results obtained when the principles of Chapter 2 and the techniques of Chapter 3 are applied to real data collected on the seafloor. It is shown that use of the multiple window method of spectral estimation can result in very different power spectra than are obtained from a simple periodogram analysis. It is also demonstrated that the ocean tide at a hydrothermal site may be very different from the ocean tide at the nearest coastal port. It is therefore unwise to infer the nature of the ocean tide at a hydrothermal site from coastal tide tables. Furthermore the tidal streams on the seafloor cannot necessarily be obtained simply by differentiating the ocean tide with respect to time. The theory of tidal streams quoted in Chapter 2 should be consulted before an estimation of seafloor currents is attempted. The HYBRID code is used to estimate the Admiralty Method harmonic constants of a number of data time-series. The quality of the results is variable and depends to a large extent of the noisiness of the original signal. The Bayesian drift removal technique, in particular, is shown to be inappropriate when the signal-to-noise ratio of the data is low. However, the estimation of Admiralty Method harmonic constants using the Bayesian drift removal technique is shown to be very successful for the clean tidal signal obtained from current meter measurements at the Lucky Strike hydrothermal site. In general it is shown that effluent temperatures display greater similarity with the ocean tide than with the solid tide. This conclusion is consistent with the order of magnitude argument presented in Chapter 2. It is therefore proposed that the tidal modulation of effluent temperature at seafloor hydrothermal systems is caused by the tidal

loading of the seafloor. The tidal modulation of ambient bottom water temperatures, on the other hand, is often caused by the lateral advection of warm water by tidal streams. The time-series data for effluent velocity are insufficiently comprehensive for any firm conclusion to be drawn.

Chapter 5 examines the effect which the nonlinear thermodynamic properties of water have on the steady-state structure of a subseafloor hydrothermal convection cell. It is shown that these thermodynamic properties are sufficient to impose a structure on the convection cell which is consistent with the known constraints. For simplicity, a homogeneous isotropic seafloor is assumed and the convecting fluid is taken to be pure water above the critical pressure of 22 MPa. A numerical simulation and analysis of the governing equations are used to explain how the thermodynamic properties of water impose an upper limit of ~400°C on the temperature of black smokers. It is predicted that temperatures greater than ~400°C are confined to a thin boundary layer at the base of the convection cell which can be identified with the reaction zone observed in ophiolites. A scaling analysis is presented which calculates the width of the discharge zone and the thickness of the reaction zone as functions of the bulk permeability. The predicted residence times of fluid in the reaction and discharge zones are also estimated.

Chapter 6 investigates the tidal loading of a hydrothermal convection cell by the changing tidal pressure field on the seafloor. The convection cell structure derived in Chapter 5 is shown to lead to a dichotomy between regions of the cell where water is liquid-like (<400°C) and regions of the cell where water is gas-like (>400°C). The dependence of the important poroelastic parameters on fluid temperature is discussed. In general terms, the interstitial fluid bears a high proportion of the applied load when cold and a low proportion of the applied load when hot. Consequently, at high tide, the incremental pore pressure is highest where the fluid is cold and a flow is induced from cold regions to hot regions. The one-dimensional incremental pore pressure solution of Van der Kamp and Gale (1983) is extended to yield expressions for the incremental fluid velocity and incremental temperature due to tidal loading. In the case of an infinite halfspace, the incremental fluid velocity at the seafloor is shown to lag the ocean tide by a phase angle of 135°. If the permeable seafloor is of finite vertical extent, this phase lag is shown to lie in the range [90°, 135°]. A simple model in which temperature and pressure are linear with depth predicts that the incremental temperature lags the incremental velocity by a phase angle in the range [45°, 90°] depending on the permeability. Consequently, the incremental temperature is predicted to lag the ocean

tide by a phase angle in the range [180°, 225°] for an infinite half-space, and a phase angle in the in the range [135°, 225°] for a finite permeable layer. These predictions are shown to be consistent with some of the data presented in Chapter 4.

It is hoped that the theoretical principles outlined in this dissertation will prove useful to future investigators. The physics of seafloor hydrothermal systems are only partially understood, and it is certain that the coming years will see the publication of new data and more sophisticated models. There is much to learn.

Appendix: Nomenclature

Chapter 2: Roman letters

Symbol	Meaning	Unit
A	amplitude of surface wave	m
A_j	(complex) amplitude of tidal component	[various]
a	right ascension	rad or °
a	magnitude of tidal stream in x-direction	$m.s^{-1}$
b	magnitude of tidal stream in y-direction	$m.s^{-1}$
d	declination of tide-raising body	rad or °
e	eccentricity of ellipse	-
h	depth of ocean	m
h	Love number, $h \approx 0.60$	-
G	gravitation constant = $6.670 \cdot 10^{-11}$ $N.m^2.kg^{-2}$	$N.m^2.kg^{-2}$
g	gravitational acceleration = 9.80665 $m.s^{-2}$	$m.s^{-2}$
g_j	phase lag of tidal component	rad or °
H_j	amplitude of tidal component	[various]
k	wave-number in x-direction	$rad.m^{-1}$
l	Love number, $l \approx 0.07$	-
t	time	s
M_B	mass of tide-raising body	kg
M_E	mass of the Earth $\approx 5.97 \cdot 10^{24}$ kg	kg
N	number of harmonic components in a decomposition	-
P	point at which tide is evaluated	-
r	distance from centre of Earth	m
r_B	distance of tide-raising body from centre of Earth	m
r_E	radius of the Earth $\approx 6.4 \cdot 10^6$ m	m
t	time	s
u	velocity in x-direction	$m.s^{-1}$
v	velocity in y-direction	$m.s^{-1}$
W	tidal potential	$m^2.s^{-2}$
W_2	2^{nd} order spherical harmonic, approximating W	$m^2.s^{-2}$
w	velocity in z-direction	$m.s^{-1}$
x	ecliptic longitude of moon	rad or °
x'	ecliptic longitude of sun	rad or °
x	horizontal spatial co-ordinate	m
y	ecliptic latitude	rad or °
y	horizontal spatial co-ordinate	m
Z	terrestrial longitude with respect to lower transit	rad or °
z	vertical spatial co-ordinate	m

Chapter 2: Greek letters

Symbol	Meaning	Unit
ε	strain	-
ζ	arbitrary tidal signal	[various]
ζ_{eq}	vertical displacement of sea-surface ('equilibrium tide')	m

ζ_O	vertical displacement of sea-surface ('ocean tide')	m
ζ_S	vertical displacement of Earth's surface ('solid tide')	m
λ	(terrestrial) latitude – angle above equator	rad or °
ν	Poisson's ratio or Earth, $\nu \approx 0.25$	-
ρ_0	average density of seawater ≈ 1025 kg.m^{-3}	kg.m^{-3}
Φ_L	lunar phase parameter	-
Ω	angular frequency	rad.s^{-1}
ω	angular frequency	rad.s^{-1}
ω_j	angular frequency of tidal component	rad.s^{-1}

Chapter 3: Roman letters

Symbol	Meaning	Unit
A	matrix used in Bayesian drift algorithm	-
$A_j(t)$	j'th (complex) harmonic constant (Admiralty Method)	-
$b_j(t)$	j'th basis function (Admiralty Method)	-
$\hat{b}_j(t)$	j'th basis function (Harmonic Method)	-
D	matrix used in Bayesian drift algorithm	-
d_j	drift signal in the time domain	[various]
$d_k(f)$	weights used in derivation of $\hat{S}_{MWPS}(f)$	-
f	frequency	s^{-1}
$F_j(t)$	amplitude of j'th basis function (Admiralty Method)	-
g_j	phase lag of j'th harmonic constant (Admiralty Method)	rad or °
$\hat{g}_j$	phase lag of j'th harmonic constant (Harmonic Method)	rad or °
H_j	magnitude of j'th harmonic constant (Admiralty Method)	[various]
$\hat{H}_j$	magnitude of j'th harmonic constant (Harmonic Method)	[various]
i	$\sqrt{-1}$	-
K	number of eigenspectra used to define $\hat{S}_{MWPS}(f)$	-
$K(f)$	arbitrary kernel function	-
$K_F(f)$	Fejer kernel function	-
$L(\nu)$	marginal posterior likelihood	-
M	number of data sections used for section-averaging	-
N	number of data points in time-series	-
$\underline{P}$	extended parameter vector	[various]
$S(f)$	true power spectrum	[various]
$\hat{S}_{BA}(f)$	band-averaged estimate of power spectrum	[various]
$\hat{S}_{MWPS}(f)$	multiple window estimate of power spectrum	[various]
$\hat{S}_P(f)$	(unwindowed) periodogram estimate of power spectrum	[various]
$\hat{S}_{SA}(f)$	section-averaged estimate of power spectrum	[various]
$\hat{S}_{WP}(f)$	windowed periodogram estimate of power spectrum	[various]
t	time	s
t_j	time of j'th data point	s
T	matrix of Admiralty Method basis functions	-
W	bandwidth in frequency domain	s^{-1}
$W_S(f)$	spectral window	-
$v_j^{(m)}$	mth discrete prolate spheroidal sequence	-
w_j	data window in the time domain	-
w_m	Huber weights used in robust section-averaging	-

$\underline{X}$	extended data vector	[various]
x_j	data series in the time domain	[various]

Chapter 3: Greek letters

Symbol	Meaning	Unit
Δt	sampling interval	s
$\varepsilon(t)$	error component of time-series	[various]
$\zeta(t)$	time-series to be analysed	[various]
$\underline{\theta}$	vector expressing harmonic constants	[various]
μ	median of several estimates of a harmonic constant	[various]
ν	hyperparameter controlling smoothness of drift signal	[various]
π	3.141592	-
σ	interquartile distance of estimates of a harmonic constant	[various]
σ^2	variance of random variable	[various]
$\sigma_B{}^2$	data variance	[various]
$\varphi_j(t)$	phase of j'th basis function (Admiralty Method)	rad or °
ω_j	angular frequency of j'th tidal component	$rad.s^{-1}$

Chapter 4: Roman letters

Symbol	Meaning	Unit
T	temperature	ºC
t	time	s
Teffk	Medusa effluent temperature (Teffk = Th + Tk)	ºC
Tefft	Medusa effluent temperature (Teffk = Th + Tt)	ºC
Th	Medusa thermistor channel (calibrated)	ºC
Th	Medusa thermistor channel (uncalibrated)	-
Tk	Medusa type-K thermocouple channel (calibrated)	ºC
Tk	Medusa type-K thermocouple channel (uncalibrated)	-
Tt	Medusa type-T thermocouple channel (calibrated)	ºC
Tt	Medusa type-T thermocouple channel (uncalibrated)	-
v	Medusa velocity channel (calibrated)	$mm.s^{-1}$
v	Medusa velocity channel (uncalibrated)	-
ve	eastward velocity measured by current meter	$mm.s^{-1}$
vn	northward velocity measured by current meter	$mm.s^{-1}$
z	depth below seafloor	m

Chapter 4: Greek letters

Symbol	Meaning	Unit
ε_j	attenuation factor	-
κ	thermal diffusivity	$m^2.s^{-1}$
φ_j	phase lag	rad

Chapter 5: Roman letters

Symbol	Meaning	Unit
c_p	specific heat capacity	$J.kg^{-1}.K^{-1}$
d	vertical distance of penetration of thermal signal	m
F	fluxibility	$J.s.m^{-5}$
g	gravitational acceleration = 9.80665 $m.s^{-2}$	$m.s^{-2}$
H	depth of magma chamber below seafloor	m
H_R	thickness of reaction zone	m
h	specific enthalpy	$J.kg^{-1}$
k	permeability	m^2
L	half-width of magma chamber	m
L_D	half-width of discharge zone	m
p	pressure	Pa
Ra_L	local Rayleigh number	-
s	specific entropy	$J.K^{-1}.kg^{-1}$
T	temperature	°C
T_0	temperature of 'cold' water in convection cell	°C
t	time	s
t_D	residence time in discharge zone	s
t_R	residence time in reaction zone	s
$\boldsymbol{u}$	(vector) Darcy velocity	$m.s^{-1}$
u	horizontal Darcy velocity	$m.s^{-1}$
w	vertical Darcy velocity	$m.s^{-1}$
x	horizontal spatial coordinate	m
z	vertical spatial coordinate	m

Chapter 5: Greek letters

Symbol	Meaning	Unit
Δp	pressure difference	Pa
ΔT	temperature difference	°C
λ	thermal conductivity	$W.m^{-1}.K^{-1}$
μ	dynamic viscosity of fluid	Pa.s
π	3.141592	-
ρ	fluid density	$kg.m^{-3}$
ρ_0	density of cold water	$kg.m^{-3}$
Φ	order of magnitude of advective heat flux	$W.m^{-2}$

Chapter 6: Roman letters

Symbol	Meaning	Unit
A	complex amplitude of incremental velocity	$m.s^{-1}$
B	complex amplitude of incremental enthalpy	$J.kg^{-1}$
d	skindepth	m
d_{1d}	1-d skindepth	m
d_{2d}	2-d skindepth	m

$\hat{e}_{ij}$	incremental strain tensor of fluid-filled porous medium	-
g	gravitational acceleration = 9.80665 $m.s^{-2}$	$m.s^{-2}$
H	depth below seafloor of impermeable layer	m
h	steady specific enthalpy	$J.kg^{-1}$
h_0	steady specific enthalpy on seafloor	Pa
$\hat{h}$	incremental specific enthalpy	$J.kg^{-1}$
K_f	fluid bulk modulus	Pa
K_{fh}	isenthalpic fluid bulk modulus	Pa
K_{fT}	isothermal fluid bulk modulus	Pa
K_g	grain bulk modulus	Pa
K_m	matrix bulk modulus	Pa
k	permeability	m^2
L	half-width of magma chamber	m
M_T	tidal flow magnitude parameter	$m^{5/2}.s^{-1/2}.kg^{-1/2}$
p	steady pore pressure	Pa
p_0	steady pressure on seafloor	Pa
$\hat{p}$	incremental pore pressure	Pa
$\hat{p}_c$	incremental confining pressure	Pa
p_T	magnitude of tidal pressure oscillation on seafloor	Pa
Q	heat sink	$W.m^{-3}$
S	storage compressibility	Pa^{-1}
T	steady temperature	°C
t	time	s
w	steady vertical velocity	$m.s^{-1}$
$\hat{w}$	incremental vertical velocity	$m.s^{-1}$
x	horizontal spatial coordinate	m
x_i	(1^{st} rank tensor) spatial coordinate	m
z	vertical spatial coordinate	m

Chapter 6: Greek letters

Symbol	Meaning	Unit
α	coefficient of effective stress	-
β	Skempton ratio	-
Γ	vertical enthalpy gradient	$J.kg^{-1}.m^{-1}$
γ_{1d}	1-d loading efficiency	-
γ_{2d}	2-d loading efficiency	-
δ_{ij}	Kronecker delta tensor	-
κ	diffusivity	$m^2.s^{-1}$
κ_{1d}	1-d diffusivity	$m^2.s^{-1}$
κ_{2d}	2-d diffusivity	$m^2.s^{-1}$
μ	dynamic viscosity of fluid	Pa.s
ν	Poisson's ratio	-
π	3.141592	-
ρ	steady fluid density	$kg.m^{-3}$
$\hat{\rho}$	incremental fluid density	$kg.m^{-3}$
$\hat{\sigma}_{ij}$	incremental stress tensor of fluid-filled porous medium	Pa
φ_0	porosity	-
φ_c	critical porosity	-

ω	angular frequency	$rad.s^{-1}$

Chapter 7: Roman letters

Symbol	Meaning	Unit
p	pressure	Pa
T	temperature	°C
X	salinity (wt % NaCl)	-
X_g	salinity of gas phase (wt % NaCl)	-
X_l	salinity of liquid phase (wt % NaCl)	-

Chapter 7: Greek letters

Symbol	Meaning	Unit
ρ_{SW}	seawater resitivity	Ω.m

References

Books, papers and conference abstracts

Admiralty Tidal Handbook No.1, *The Admiralty Method of Harmonic Tidal Analysis for Long Period Observations (over a period of 1 or 12½ months)*, Published by the Hydrographer of the Navy (1985).

Admiralty Tidal Handbook No.3, *The Admiralty Method of Harmonic Tidal Analysis for Short Period Observations (for periods of less than 1 months)*, Published by the Hydrographer of the Navy (1986).

Admiralty Tide Tables Volume 4, Pacific Ocean 2000, Published by the Hydrographer of the Navy (1999).

Agnew, D.C. (1997), NLOADF: A program for computing ocean-tide loading, *Journal of Geophysical Research*, Vol. 102, No. B3, pp. 5109 – 5110.

Alt, J.C. (1995), Subseafloor processes in mid-ocean ridge hydrothermal systems, in *"Seafloor hydrothermal systems: Physical, Chemical, Biological and Geological interactions"*, (ed. Humphris, S.E. et al.), Geophysical Monograph Series, Vol. 91, pp. 85 – 114.

Akaike, H. (1980), Likelihood and the Bayes procedure, in *"Bayesian Statistics"*, (ed. Bernardo, J.M. et al.), *University Press, Valencia*, pp. 143 – 166.

Anderko, A. & Pitzer, K.S. (1993), Equation-of-state representation of phase equilibria and volumetric properties of the system NaCl-H_2O above 573 K, *Geochimica et Cosmochimica Acta*, Vol. 57, pp. 1657 – 1680.

Berndt, M.E., Seyfried, W.E. & Beck, J.W. (1988), Hydrothermal alteration processes at mid-ocean ridges: experimental and theoretical constraints from Ca and Sr exchange reactions and isotopic ratios, *Journal of Geophysical Research*, Vol. 93, pp. 4573 – 4583.

Berndt, M.E., Seyfried, W.E. & Janecky, D.R. (1989), Plagioclase and epidote buffering of cation ratios in mid-ocean ridge hydrothermal fluids: experimental results in and near the supercritical region, *Geochimica et Cosmochimica Acta*, Vol. 53, pp. 2283 – 2300.

Biot, M.A. (1941), General theory of three-dimensional consolidation, *Journal of Applied Physics*, Vol. 12, pp. 155 – 164.

Bischoff, J.L. & Rosenbauer, R.J. (1985), An empirical equation of state for hydrothermal seawater (3.2 percent NaCl), *American Journal of Science*, Vol. 285, pp. 725 – 763.

Bredehoeft, J.D. (1967), Response of well-aquifer systems to earth tides, *Journal of Geophysical Research*, Vol. 72, No. 12, pp.3075 – 3087.

Campbell, A.C., Palmer, M.R., Klinkhammer, G.P., Bowers, T.S., Edmond, J.M., Lawrence, J.R., Casey, J.F., Thomson, G., Humphris, S., Rona, P. & Karson, J.A. (1988), Chemistry of hot springs on the Mid-Atlantic Ridge, *Nature*, Vol. 335, pp. 514 – 519.

Cann, J.R. & Strens, M.R. (1982), Black smokers fuelled by freezing magma, *Nature*, Vol. 298, pp. 147 – 149.

Carbajal, N. & Backhaus, J.O. (1998), Simulation of tides, residual flow and energy budget in the Gulf of California, *Oceanologica Acta*, Vol. 21, No. 3, pp. 429 – 446.

Carmichael, R.S. (1966), *Handbook of Physical Properties of Rocks, Vol. II*, 345 pp., (CRC press, Boca Raton, Florida).

Cartwright, D.E. & Tayler, R.J. (1971), New computations of the tide-generating potential, *Geophysical Journal of the Royal Astronomical Society*, Vol. 23, pp. 45 – 74.

Cartwright, D.E. & Edden, A.C. (1973), Corrected tables of tidal harmonics, *The Geophysical Journal of the Royal Astronomical Society*, Vol. 33, No. 3, pp. 253.

Chave, A.D., Thomson, D.J. & Ander, M.E. (1987), On the robust estimation of power spectra, coherences, and transfer functions, *Journal of Geophysical Research*, Vol. 92, No. B1, pp. 633 – 648.

Chevaldonné, P, Desbruyères, D. & Le Haître, M. (1991), Time-series of temperature from three deep-sea hydrothermal vent sites, *Deep-Sea Research*, Vol. 38, No. 11, pp. 1417 – 1430.

Cooper, M.J. (1999), *Geochemical investigations of hydrothermal fluid flow at mid-ocean ridges*, Ph.D. thesis, University of Cambridge, 218 pp.

Cooper, M.J., Elderfield, H. & Schultz, A. (2000), Diurnal variability in the chemistry of diffuse flow fluids from the Menez Gwen hydrothermal site, *[Manuscript in preparation]*.

Copley, J.T.P., Tyler, P.A., Van Dover, C.L., Schultz, A., Dickson, P., Singh, S. & Sulanowska, M. (1999), Subannual temporal variation in faunal distributions at the TAG hydrothermal mound (26°N, Mid-Atlantic Ridge), *Marine Ecology*, Vol. 20, pp. 291 – 306.

Cowan, J & Cann J. (1988), Supercritical two-phase separation of hydrothermal fluids in the Troodos ophiolite, *Nature*, Vol. 333, pp. 259 – 261.

Davis, E.E. & Becker, K. (1994), Formation temperatures and pressures in a sedimented rift hydrothermal system: 10 months of CORK observations, holes 857D and 858G, *Proceedings of the Ocean Drilling Program, Scientific Results*, Vol. 139, pp. 649 – 666.

Davis, E.E., Becker, K., Wang, K. & Carson, B. (1995), Long-term observations of pressure and temperature in hole 892B, Cascadia accretionary prism, *Proceedings of the Ocean Drilling Program, Scientific Results,* Vol. 146, pp. 299 – 311.

Davis, E. & Becker, K. (1999), Tidal pumping of fluids within and from the oceanic crust: new observations and opportunities for sampling the crustal hydrosphere, *Earth and Planetary Science Letters*, Vol. 172, pp. 141 – 149.

Delaney, J.R., Butterfield, D.A., Lilley, M.D., Kelley, D.S., Baross, J.A.& McDuff, R.E. (1997a), The Third Fluid: tidally forced entrainment of a non-seawater mixing component below the seafloor, *Eos, Trans. AGU, Fall Supplement*.

Delaney, J.R., Kelley, D.S., Lilley, M.D., Butterfield, D.A., McDuff, R.E. & Baross, J.A. (1997b), Temporal/spatial exploration of physical, chemical and biological linkages in a submarine hydrothermal laboratory: the Endeavour Ridge, *Eos, Trans. AGU, Fall Supplement*.

Detrick, R.S., Buhl, P., Vera, E., Mutter, J., Orcutt, J., Madsen, J. & Brocher, T. (1987), Multi-channel seismic imaging of a crustal magma chamber along the East Pacific Rise, *Nature*, Vol. 326, pp. 35 – 41.

Dickson, P., Schultz, A., Woods, A. (1995), Preliminary modelling of hydrothermal circulation within mid-ocean ridge sulphide structures, in *"Hydrothermal Vents and Processes"*, (ed. Parson, L.M. et al.), *Geological Society Special Publication*, Vol. 87, pp. 145 – 157.

Dickson, P.C. (1997), *Modelling fluid flow in seafloor hydrothermal systems*, Ph.D. thesis, University of Cambridge, 218 pp.

Doodson, A.T. (1921): The harmonic development of the tide generating potential, *Proceedings of the Royal Society*, Series A, Vol. 100, pp. 306 – 328.

Doodson, A.T. & Warburg, H.D. (1941), *Admiralty Manual of Tides*, Her Majesty's Stationery Office, 270 pp.

Dunn, J.C. & Hardee, H.C. (1981), Superconvecting geothermal zones, *Journal of Volcanology and Geothermal Research*, Vol. 11, pp. 189 – 201.

Egbert, G.D., Bennett, A.F. & Foreman, M.G.G. (1994), TOPEX/POSEIDON tides estimated using a global inverse model, *Journal of Geophysical Research*, Vol. 99, No. C12, pp. 24821 – 24852.

Elder, J.E. (1981), *Geothermal Systems*, pp. 180 – 187 (Academic Press, London).

Elderfield, H. & Schultz, A. (1996), Mid-ocean ridge hydrothermal fluxes and the chemical composition of the ocean, *Annual Review of Earth and Planetary Sciences*, Vol. 24, pp. 191 – 224.

Fang, W.W. & Langseth, M.G. (1993), Analysis and application of in situ pore pressure measurements in marine sediments, *Journal of Geophysical Research*, Vol. 98, No. B5, pp. 7921 – 7938.

Farrell, W.E. (1972a), Global calculations of tidal loading, *Nature*, Vol. 238, pp. 43 – 44.

Farrell, W.E. (1972b), Deformation of the earth by surface loads, *Reviews of Geophysics and Space Physics*, Vol. 10, pp. 761 – 797.

Farrell, W.E. (1973), Earth tides, ocean tides and tidal loading, *Philosophical Transactions of the Royal Society of London*, Vol. 274, pp. 253 – 259.

Faust, C.R. & Mercer, J.W. (1979), Geothermal Reservoir Simulation 1. Mathematical Models for Liquid- and Vapor-Dominated Hydrothermal Systems, *Water Resources Research*, Vol. 15, pp. 23 – 30.

Filloux, J.H. (1973) Tidal patterns and energy balance in the Gulf of California, *Nature*, Vol. 243, pp. 217 – 221.

Fisher, A.T., Becker, K. & Davis, E.E. (1997), The permeability of young oceanic crust east of Juan de Fuca Ridge determined using borehole thermal measurements, *Geophysical Research Letters*, Vol. 24, No. 11, pp. 1311 – 1314.

Fornari, D.J., Shank, T., Von Damm, K.L., Gregg, T.K.P., Lilley, M., Levai, G., Bray, A., Haymon, R.M., Perfit, M.R. & Lutz, R. (1998), Time-series measurements at high temperature hydrothermal vents, East Pacific Rise 9°49'-51'N: evidence for monitoring a crustal cracking event, *Earth and Planetary Science Letters*, Vol. 160, pp. 419 – 431.

Fournier, R.O. (1991), The transition from hydrostatic to greater than hydrostatic fluid pressure in presently active continental hydrothermal systems in crystalline rock, *Geophysical Research Letters*, Vol. 18, pp. 955 – 958.

Francis, O. & Mazzega P. (1990), Global charts of ocean tide loading effects, *Journal of Geophysical Research*, Vol. 95, No. C7, pp. 11411 – 11424.

Fujioka, K., Kobayashi, K., Kato, K., Aoki, M., Mitsuzawa, K., Kinoshita, M. & Nishizawa, A. (1997), Tide-related variability of TAG hydrothermal activity observed by deep-sea monitoring system and OBSH, *Earth and Planetary Science Letters*, Vol. 153, pp. 239 – 250.

Germanovich, L.N. & Lowell, R.P. (1992), Percolation theory, thermoelasticity, and discrete hydrothermal venting in the Earth's crust, *Science*, Vol. 255, pp. 1564 – 1567.

Germanovich, L.N., Lowell, R.P. & Astakhov, D.K. (2000), Stress-dependent permeability and the formation of seafloor event plumes, *Journal of Geophysical Research*, Vol. 105, No. B4, pp. 8341 – 8354.

Gillis, K.M. & Roberts, M.D. (1999), Cracking at the magma-hydrothermal transition: evidence from the Troodos Ophiolite, Cyprus, *Earth and Planetary Science Letters*, Vol. 169, pp. 227 – 244.

Grant, H.L., Stewart, R.W. & Moilliet, A. (1962), Turbulence spectra from a tidal channel, *Journal of Fluid Mechanics*, Vol. 12, p. 241 – 263.

Grasty, R.L., Smith, C.W., Franklin, J.M. & Jonasson, I.R. (1988), Radioactive orphans in barite-rich chimneys, Axial Caldera, Juan de Fuca Ridge, *Canadian Mineralogist*, Vol. 26, pp. 627 – 636.

Haar, L., Gallagher, J.S. & Kell, G.S. (1984), *NBS/NRC Steam Tables,* 320pp. (Hemisphere, New York).

Hayba, D.O. & Ingebritsen, S.E. (1994), The computer model HYDROTHERM, a three-dimensional finite-difference model to simulate ground-water flow and heat transport in the temperature range of 0 to 1,200 degrees Celsius, *U.S. Geological Survey Water-Resources Investigations Report* No. 94-4045**.**

Herzig, P.M. & Hannington, M.D. (1995), Massive polymetallic sulfides at the modern seafloor: A review, *Ore Geology Reviews*, Vol. 10, pp. 95 – 115.

Hsieh, P.A. & Bredehoeft, J.D. (1987), Determination of aquifer transmissivity from earth tide analysis, *Water Resources Research*, Vol. 23, No. 10, pp. 1824 – 1832.

Hsieh, P.A., Bredehoeft, J.D. & Rojstaczer, S.A. (1988), Response of well aquifer systems to earth tides: problem revisited, *Water Resources Research*, Vol. 24, No. 3, pp. 468 – 472.

Hurley, M.T. & Schultheiss, P.J. (1991), Sea-bed shear modulus from measurements of tidally induced pore pressures, in *"Shear waves in marine sediments"*, (ed. Hovem, J. et al.), Kluwer Academic, Norwell, Mass., pp. 411 – 418.

Hyde, R.A. & Pettigrew, N.A. (1993), A modification of the response method of tidal analysis, *Journal of Geophysical Research*, Vol. 98, No. C12, pp. 22753 – 22757.

Ingebritsen, S.E. & Rojstaczer, S.A., (1993), Controls on geyser periodicity, *Science*, Vol. 262, pp. 889 – 892.

Ingebritsen, S.E. & Hayba, D.O. (1994), Fluid flow and heat transport near the critical point of H_2O, *Geophysical Research Letters*, Vol. 21, pp. 2199 – 2202.

Ingebritsen, S.E. & Rojstaczer, S.A., (1996), Geyser periodicity and the response of geysers to deformation, *Journal of Geophysical Research*, Vol. 101, No. B10 pp. 21891 – 21905.

Johnson, H.P. & Tunnicliffe, V. (1985), Time-series measurements of hydrothermal activity on northern Juan de Fuca Ridge, *Geophysical Research Letters*, Vol. 12, No. 10, pp. 685 – 688.

Johnson, J.W. & Norton, D. (1991), Critical phenomena in hydrothermal systems: state, thermodynamic, electrostatic, and transport properties of H_2O in the critical region, *American Journal of Science*, Vol. 291, pp. 541 – 648.

Johnson, K.S., Childress, J.J., Beehler, C.L. & Sakamoto, C.M. (1994), Biogeochemistry of hydrothermal vent mussel communities: the deep-sea analogue to the intertidal zone, *Deep-Sea Research I,* Vol. 41, No. 7, pp. 993 – 1011.

Johnson, H.P. (1998), Tidal modulation of hydrothermal circulation; bare rock heat flow from the summit of Baby Bare seamount, Juan de Fuca ridge, *Eos, Trans. AGU, Fall Supplement*.

Johnson, H.P., Hutnak, M., Dziak, R. Fox, C.G., Urcuyo, I., Cowens, J.P., Nabelek, J. & Fisher, C. (2000), Earthquake-induced changes in a hydrothermal system on the Juan de Fuca mid-ocean ridge, *Nature*, Vol. 407, pp. 174 – 177.

Jupp, T. & Schultz, A. (1999), Plume formation in the oceanic lithosphere – a natural cap on black smoker temperatures, *Eos, Trans. AGU, Fall Supplement,* Vol. 80, p. F931.

Jupp, T. & Schultz A. (2000), A thermodynamic explanation for black smoker temperatures, *Nature*, Vol. 403, pp. 880 – 883.

Kadko, D. (1994), Time-series gamma spectrometry of diffuse flow from the North Cleft segment of the Juan de Fuca Ridge, *Eos, Trans. AGU, Fall Supplement,* Vol. 75, p. 307.

Kadko, D. & Moore, W. (1988), Radiochemical constraints on the crustal residence time of submarine hydrothermal fluids: Endeavour Ridge, *Geochimica et Cosmochimica Acta*, Vol. 52, pp. 659 – 668.

Kinoshita, M., Matsubayashi, O. & Von Herzen, R.P. (1996), Sub-bottom temperature anomalies detected by long-term temperature monitoring at the TAG hydrothermal mound, *Geophysical Research Letters*, Vol. 23, No. 23, pp. 3467 – 3470.

Kinoshita, M., Von Herzen, R.P., Matsubayashi, O. & Fujioka, K. (1998), Erratum to 'Tidally-driven effluent detected by long-term temperature monitoring at the TAG hydrothermal mound, Mid-Atlantic Ridge', *Physics of the Earth and Planetary Interiors*, Vol. 109, pp. 201 – 212.

Kümpel, H.-J. (1991), Poroelasticity: parameters reviewed, *Geophysical Journal International*, Vol. 105, pp. 783 – 799.

Lamb, H. (1932), *Hydrodynamics*, (6th edition), 738 pp., (Cambridge University Press, Cambridge).

Lambert, A. (1974), Earth tide analysis and prediction by the response method, *Journal of Geophysical Research*, Vol. 79, No. 32, pp. 4952 – 4960.

Lapwood, E.R. (1948), Convection of a fluid in a porous medium, *Proceedings of the Cambridge Philosophical Society*, Vol. 44, pp. 508 – 521.

Lavelle, J.W., Wetzler, M.A., Baker, E.T. & Embley, R.W. (1999), Prospecting for hydrothermal vents using moored current and temperature data: Axial Volcano on the Juan de Fuca Ridge, Northeast Pacific, *Eos, Trans. AGU, Fall Supplement*.

Le Prevost, C., Genco, M.L., Lyard, F., Vincent, P., Canceil, P. (1994), Spectroscopy of the world ocean tides form a finite element hydrodynamic model, *Journal of Geophysical Research*, Vol. 99, No. C12, pp. 24777 – 24797.

Le Prevost, C., Bennett, A.F. & Cartwright, D.E. (1995), Ocean tides for and from TOPEX/POSEIDON, *Science*, Vol. 267, pp. 639 – 642.

Lister, C.R.B. (1974), On the penetration of water into hot rock, *Geophysical Journal of the Royal Astronomical Society*, Vol. 39, pp. 465 – 509.

Lister, C.R.B. (1995), Heat transfer between magmas and hydrothermal systems, or, six lemmas in search of a theorem, *Geophysical Journal International*, Vol. 120, pp. 45 – 59.

Little, S.A., Stolzenbach, K.D. & Grassle, F.J. (1988), Tidal current effects on temperature in diffuse hydrothermal flow: Guaymas Basin, *Geophysical Research Letters*, Vol. 15, No. 13, pp.1491 – 1494.

Little, S.A., Stolzenbach, K.D. & Grassle, F.J. (1989), Correction to "Tidal current effects on temperature in diffuse hydrothermal flow: Guaymas Basin", *Geophysical Research Letters*, Vol. 16, No. 8, pp.985 – 986.

Longman, I.M. (1962), A Green's function for determining the deformation of the earth under surface mass loads, 1. Theory, *Journal of Geophysical Research*, Vol. 67, No. 2, pp. 845 – 850.

Longman, I.M. (1963), A Green's function for determining the deformation of the earth under surface mass loads, 2. Computations and numerical results, *Journal of Geophysical Research*, Vol. 68, No. 2, pp. 485 – 496.

Love, A.E.H. (1927), *A treatise on the mathematical theory of elasticity*, Cambridge University Press, 643 pp.

Lowell, R.P., Van Cappellen, P. & Germanovich, L. (1993), Silica precipitation in fractures and the evolution of permeability in hydrothermal upflow zones, *Science*, Vol. 260, pp. 192 – 194.

Lowell, R.P. & Germanovich, L.N. (1994), On the temporal evolution of high-temperature hydrothermal systems at ocean ridge crests, *Journal of Geophysical Research*, Vol. 99, pp. 565 - 575.

Lowell, R.P., Rona, P.A. & Von Herzen, R.P. (1995), Seafloor hydrothermal systems, *Journal of Geophysical Research*, Vol. 100, pp. 327 – 352.

Lowell, R.P. & Xu, W. (2000), Sub-critical two-phase convection near a dike, *Earth and Planetary Science Letters*, Vol. 174, pp. 385 – 396.

McDuff R.E. & Delaney, J.R. (1995), Periodic variability in fluid temperature at a seafloor hydrothermal vent, *Eos, Trans. AGU, Fall Supplement,* Vol. 76, p. 710.

MacGregor, L.M., Constable, S. & Sinha, M.C. (1998), The RAMESSES experiment – III, Controlled-source electromagnetic sounding of the Reykjanes Ridge at 57°45'N, *Geophysical Journal International*, Vol. 135, pp. 773 – 789.

Manual of Tidal Prediction (3rd edition, 1958), Brown, Son & Ferguson, Glasgow.

Marine, I.W. (1975), Water level fluctuations due to Earth tides in a well pumping from slightly fractured crystalline rock, *Water Resources Research*, Vol. 11, No. 1, pp. 165 – 173.

Melchior, P. (1983), *The Tides of the Planet Earth (2nd edition)*, 641 pp. (Pergamon Press, Oxford).

Morton, J.L. (1984), *Oceanic spreading centers: axial magma chambers, thermal structure, and small scale ridge jumps*, Ph.D. thesis, Stanford University.

Morton, J.L. & Sleep, N.H. (1985), A mid-ocean ridge thermal model: constraints on the volume of axial hydrothermal heat flux, *Journal of Geophysical Research*, Vol. 90, No. 13, pp. 11345 – 11353.

Munk, W.H. & Cartwright, D.E. (1966), Tidal spectroscopy and prediction, *Philosophical Transactions of the Royal Society of London, Series A*, Vol. 259, pp. 533 – 581.

Nesbitt, B.E. (1993), Electrical resistivities of crustal fluids, *Journal of Geophysical Research,* Vol. 98, No. B3, pp. 4301 – 4310.

Norton, D. & Knight, J. (1977), Transport phenomena in hydrothermal systems: cooling plutons, *American Journal of Science*, Vol. 277, pp. 937 – 981.

Nur, A. & Byerlee, J.D. (1971), An exact effective stress law for elastic deformation of rock with fluids, *Journal of Geophysical Research*, Vol. 76, No. 26, pp. 6414 – 6419.

Palliser, C. & McKibbin, R. (1998a), A model for deep hydrothermal brines, I: T-p-X state-space description, *Transport in Porous Media,* Vol. 33, pp. 65 – 80.

Palliser, C. & McKibbin, R. (1998b), A model for deep hydrothermal brines, II: Thermodynamic properties – density, *Transport in Porous Media,* Vol. 33, pp. 129 – 154.

Palliser, C. & McKibbin, R. (1998c), A model for deep hydrothermal brines, III: Thermodynamic properties – enthalpy and viscosity, *Transport in Porous Media,* Vol. 33, pp. 155 – 171.

Pascoe, A.R. & Cann, J.R. (1995), Modelling diffuse hydrothermal flow in black smoker vent fields, in *"Hydrothermal Vents and Processes"*, (ed. Parson, L.M. et al.), *Geological Society Special Publication*, Vol. 87, pp. 159 – 173.

Phillips, O.M. (1966), *The dynamics of the upper ocean*, 336 pp., (Cambridge University Press, Cambridge).

Phillips, O.M. (1991), *Flow and reactions in permeable rocks*, pp. 245-264 (Cambridge University Press, Cambridge).

Phillips, O.M. (1991a), The Kolmogorov spectrum and its oceanic cousins: a review, *Proceedings of the Royal Society of London,* Series A, Vol. 434 pp. 125 – 138.

Press, W.H., Flannery, B.P., Teukolsky, S.A. & Vetterling, W.T. (1986), *Numerical Recipes: The Art of Scientific Computing*, 818pp. (Cambridge University Press, Cambridge).

Quirós, G., Badan-Dangon, A. & Ripa, P. (1992), M2 currents and residual flow in the Gulf of California, *Netherlands Journal of Sea Research*, Vol. 28, No. 4, pp. 251 – 259.

Revil, A. & Pezard, P.A. (1998), Streaming electrical potential anomaly along faults in geothermal areas, *Geophysical Research Letters*, Vol. 25, No. 16, pp. 3197 – 3200.

Revil, A., Pezard, P.A. & Glover, P.W.J. (1999), Streaming potential in porous media 1. Theory of the zeta potential, *Journal of Geophysical Research*, Vol. 104, No. B9, pp. 20021 – 20031.

Revil, A., Schwaeger, H., Cathles, L.M. & Manhardt, P.D. (1999), Streaming potential in porous media 2. Theory and application to geothermal systems, *Journal of Geophysical Research*, Vol. 104, No. B9, pp. 20033 – 20048.

Rice, J.R. & Cleary, M.P. (1976), Some basic stress diffusion solutions for fluid-saturated elastic porous media with compressible constituents, *Reviews of Geophysics and Space Physics*, Vol. 14, No. 2, pp. 227 – 241.

Richardson, C.J., Cann, J.R., Richards, H.G. & Cowan, J.G. (1987), Metal-depleted toot zones of the Troodos ore-forming system, *Earth and Planetary Science Letters*, Vol. 84, pp. 243 – 253.

Rojstaczer, S. (1988), Determination of fluid flow properties from the response of water levels in wells to atmospheric loading, *Water Resources Research*, Vol. 24, No. 11, pp. 1927 – 1938.

Rojstaczer, S. & Agnew, D.C. (1989), The influence of formation material properties on the response of water levels in wells to earth tides and atmospheric loading, *Journal of Geophysical Research*, Vol. 94, No. B9, pp. 12403 – 12411.

Rojstaczer, S. & Riley, F.S. (1990), Response of the water level in a well to earth tides and atmospheric loading under unconfined conditions, *Water Resources Research*, Vol. 26, No. 8, pp. 1803 – 1817.

Rudnicki, M.D., James, R.H. & Elderfield, H. (1994), Near-field variability of the TAG non-buoyant plume, 26°N, Mid-Atlantic Ridge, *Earth and Planetary Science Letters*, Vol. 127, pp. 1 – 10.

Sato, T., Kasahara, J. & Fujioka, K. (1995), Observation of pressure change associated with hydrothermal upwelling at a seamount in the south Mariana Trough using an ocean bottom seismometer, *Geophysical Research Letters*, Vol. 22, No. 11, pp. 1325 – 1328.

Schrama, E.J.O. & Ray, R.D. (1994), A preliminary tidal analysis of TOPEX/POSEIDON altimetry, *Journal of Geophysical Research*, Vol. 99, No. C12, pp. 24,799 – 24,808.

Schultz, A., Delaney, J.R. & McDuff, R.E. (1992), On the partitioning of heat flux between diffuse and point source seafloor venting, *Journal of Geophysical Research*, Vol. 97, No. B9, pp. 12,299 – 12,314.

Schultz, A., Dickson, P. & Elderfield, H. (1996), Temporal variations in diffuse hydrothermal flow at TAG, *Geophysical Research Letters*, Vol. 23, No.23, pp. 3471 – 3474.

Schultz, A. & Elderfield, H. (1997), Controls on the physics and chemistry of seafloor hydrothermal circulation, *Philosophical Transactions of the Royal Society of London*, Series A, Vol. 355, pp. 387 – 425.

Schultz, A. & Jupp, T. (1999), The tidal modulation of seafloor hydrothermal flow, *Eos, Trans. AGU, Fall Supplement,* Vol. 80, p. F922.

Schwiderski, E.W. (1980), On charting global ocean tides, *Reviews of Geophysics and Space Physics*, Vol. 18, No. 1, pp. 243 – 268.

Seewald, J.S. & Seyfried, W.E. (1990), The effect of temperature on metal mobility in subseafloor hydrothermal systems: constraints from basalt alteration experiments, *Earth and Planetary Science Letters*, Vol.101, pp. 388 – 403.

Sengers, J.V. & Kamgar-Parsi, B. (1984), Representative equations for the viscosity of water substance, *Journal of Physical and Chemical Reference Data*, Vol. 13, pp. 185 – 205.

Sengers, J.V. & Watson J.T.R. (1986), Improved international formulation for the viscosity and thermal conductivity of water substance, *Journal of Physical and Chemical Reference Data*, Vol. 15, pp. 1291 – 1314.

Seyfried, W.E. & Bischoff, J.L. (1979), Low temperature basalt alteration by seawater: an experimental study at 70°C and 150°C, *Geochimica et Cosmochimica Acta*, Vol. 43, pp. 1937 – 1947.

Seyfried, W.E. & Mottl, M.J. (1982), Hydrothermal alteration of basalt by seawater under seawater-dominated conditions, *Geochimica et Cosmochimica Acta*, Vol. 46, pp. 985 – 1002.

Shank, T.M., Fornari D.J., Von Damm, K., Lilley, M., Van Dover, C.L., Levai, G. & Lutz, R.A. (1995), Dynamic fluctuations and cyclic periodicities of low-T hydrothermal venting: time-lapse multi-probe temperature measurements and vide imaging at 9° 49.8'N, *Eos, Trans. AGU, Fall Supplement*.

Shank, T.M., Fornari D.J.& Lutz, R.A. (1997), Periodicities and variability of high- and low-temperature hydrothermal venting along the Biotransect (9° 50'N) on the East Pacific Rise: three years of continuous synchronous temperature monitoring, *Eos, Trans. AGU, Fall Supplement,* Vol. 76, No. 46, p. F701.

Sinha, M.C., Constable, S. C., Peirce, C., White, A., Heinson, G., MacGregor, L.M., & Navin, D.A. (1998), Magmatic processes at slow spreading ridges: implications of the RAMESSES experiment at 57°45'N on the Mid-Atlantic Ridge, *Geophysical Journal International*, Vol. 135, pp. 731 – 745.

Slepian, D. (1978), Prolate spheroidal wave functions, Fourier analysis, and uncertainty – V: the discrete case, *Bell Systems Technical Journal*, Vol. 57, pp. 1371 – 1429.

Stein, C.A. & Stein, S. (1992), A model for the global variation in oceanic depth and heat flow with lithospheric age, *Nature*, Vol. 359, pp. 123 – 129.

Stein, C.A. & Stein, S. (1999), Constraints on hydrothermal heat flux through the oceanic lithosphere from global heat flow, *Journal of Geophysical Research*, Vol. 99, pp. 3081 – 3095.

Straus, J.M. & Schubert, G. (1977), Thermal convection of water in a porous medium: effects of temperature- and pressure-dependent thermodynamic and transport properties, *Journal of Geophysical Research*, Vol. 82, pp. 325 – 333.

Tamura, Y. (1987), A harmonic development of the tide-generating potential, *Bulletin D'Information Des Marées Terrestres*, Vol. 99, pp. 6813 – 6855.

Tamura, Y., Sato, T., Ooe, M. & Ishiguro, M. (1991), A procedure for tidal analysis with a Bayesian information criterion, *Geophysical Journal International*, Vol. 104, pp. 507 – 516.

Thomson, D.J. (1982), Spectrum estimation and harmonic analysis, *Proceedings of the IEEE*, Vol. 70, No. 9, pp. 1,055 – 1,096.

Thomson, D.J., Lanzerotti, L.J., Medford, L.V. & Maclennan, C.G. (1986), Study of tidal periodicities using a transatlantic telecommunications cable, *Geophysical Research Letters*, Vol. 13, No. 6, pp. 525 – 528.

Tryon, M.D., Brown, K.M., Dorman, L.M. & Sauter, A.W. (1996), Instrument development and results from seafloor flux meter deployments off N. California and the EPR, *Eos, Trans. AGU, Fall Supplement*.

Turner, J.S. (1973), *Buoyancy effects in fluids*, 368 pp., (Cambridge University Press, Cambridge).

Van der Kamp, G. & Gale, J.E. (1983), Theory of earth tide and barometric effects in porous formations with compressible grains, *Water Resources Research*, Vol. 19, No. 2, pp. 538 – 544.

Van Wylen, G.J. & Sonntag, R.E. (1978), *Fundamentals of classical thermodynamics*, *SI version, 2nd edition*, 744 pp., (John Wiley & Sons, New York).

Vera, E.E. & Diebold, J.B. (1994), Seismic imaging of oceanic layer 2A between 9°30' and 10°N on the East Pacific Rise from two-ship wide-aperture profiles, *Journal of Geophysical Research*, Vol. 99, pp. 3031 – 3041.

Von Damm, K.L., Edmond, J.M., Grant, B., Measures, C.I., Walden, B. & Weiss, R.F. (1985), Chemistry of submarine hydrothermal solutions at 21°N, East Pacific Rise, *Geochimica et Cosmochimica Acta*, Vol. 49, pp. 2197 – 2220.

Wang, K. & Davis, E.E. (1996), Theory for the propagation of tidally induced pore pressure variations in layered subseafloor formations, *Journal of Geophysical Research*, Vol. 101, No. B5, pp. 11483 – 11495.

Wang, K., Davis, E.E. & Van der Kamp, G. (1998), Theory for the effects of free gas in subsea formations on tidal pore pressure variations and seafloor displacements, *Journal of Geophysical Research*, Vol. 103, No. B6, pp. 12339 – 12353.

Wang, K., Van der Kamp, G. & Davis, E.E. (1999), Limits of tidal energy dissipation by fluid flow in subsea formations, *Geophysical Journal International*, Vol. 139, pp. 763 – 768.

Watson, J.T.R., Basu, R.S. & Sengers, J.V. (1980), An improved representative equation for the dynamic viscosity of water substance, *Journal of Physical and Chemical Reference Data*, Vol. 9, pp. 1255 – 1290.

Wetzler, M.A., Lavelle, J.W., Cannon, G.A. & Baker, E.T. (1998), Variability of temperature and currents measured near Pipe Organ hydrothermal vent site, *Marine Geophysical Researches*, Vol. 20, No. 6, pp. 505 – 516.

Wilcock, W.S.D. (1998), Cellular convection models of mid-ocean ridge hydrothermal circulation and the temperatures of black smoker fluids, *Journal of Geophysical Research*, Vol. 103, pp. 2585 – 2596.

Yallop, B.D. & Hohenkerk, C.Y. (1990), *Compact data for navigation and astronomy for the years 1991 – 1995*, 70 pp., (Cambridge University Press, Cambridge).

Computer codes by other authors

The following computer codes were kindly made available by their authors over the internet. The internet addresses given are those from which the codes were obtained and may no longer be valid.

Code & Programmer	Description and internet location
CSR (R. Eanes)	Calculates the ocean tide at any location based on satellite altimetry (Schrama & Ray, 1994). ftp://ftp.csr.utexas.edu/pub/tide/csr_2.0/
ETGTAB (H.-G. Wenzel)	Calculates the tidal potential (and hence solid tide) at any point on the Earth's surface. http://www-gik.bau-verm.uni-karlsruhe.de/~iagetc/
HYDROTHRERM (D. Hayba)	Finite difference code to calculate Darcy flow in a porous medium. Uses the full non-linear properties of water. http://water.usgs.gov/software/hydrotherm.html
MWPS (A. Chave)	Implements the multiple window power spectrum technique described in Thomson (1982). ftp://faraday.whoi.edu/pub
SPOTL (D.C. Agnew)	A suite of programs to calculate the load tide (Agnew, 1997). ftp://bilby.ucsd.edu/pub/spotl

In addition, a selection of codes to predict the ocean tide is currently available from http://podaac-www.jpl.nasa.gov/cdrom/tide/Document/html/models.htm

Computer codes written for this dissertation

The following computer codes were written by the author for use in this dissertation.

Code & Programmer	Description
PREDICT (T. Jupp)	Calculates the time-domain representation of a tidal signal from its Admiralty Method harmonic constants.
HYBRID (T. Jupp)	Extracts the Admiralty Method harmonic constants from a tidally modulated time-series
DIFFUSE (T. Jupp)	Calculates the response of a two dimensional poroelastic subseafloor convection cell to tidal loading at the seafloor.